

Assessment of Analysis Methods for Seismic Shear Wall Capacity Using JNES/NUPEC Multi-Axial Cyclic and Shaking Table Test Data

Brookhaven National Laboratory

**U.S. Nuclear Regulatory Commission
Office of Nuclear Regulatory Research
Washington, DC 20555-0001**



Assessment of Analysis Methods for Seismic Shear Wall Capacity Using JNES/NUPEC Multi-Axial Cyclic and Shaking Table Test Data

Manuscript Completed: December 2006
Date Published: January 2007

Prepared by
J. Xu, J. Nie, J. Braverman and C. Hofmayer

Brookhaven National Laboratory
Upton, NY 11973-5000

S. Ali, NRC Project Manager

Prepared for
Division of Fuel, Engineering, and Radiological Research
Office of Nuclear Regulatory Research
U.S. Nuclear Regulatory Commission
Washington, DC 20555-0001
Job Code N6076



ABSTRACT

As part of a program (JCN N-6076) sponsored by the U. S. Nuclear Regulatory Commission (NRC), a study is performed by Brookhaven National Laboratory (BNL) to assess the performance of analysis methods for computing the seismic response of shear wall structures subjected to strong ground motions and their ultimate seismic failure capacities. The BNL study is accomplished using the multi-axial cyclic and shaking table test data provided by the Japan Nuclear Energy Safety Organization (JNES) and Nuclear Power Engineering Corporation (NUPEC) as part of collaborative efforts between NRC and JNES/NUPEC to study seismic issues important to the safe operation of commercial nuclear power plant (NPP) structures, systems and components (SSC). It is the subject of this report to present and discuss the results and insights of the BNL study.

The BNL study described in this report includes: 1) an assessment of simplified methods for seismic shear wall failure capacity estimates against the JNES/NUPEC cyclic and shaking table test data, 2) an ANACAP finite element (FE) prediction of JNES single and multi-axial cyclic test data, 3) an ANACAP FE 3-D simulation of the JNES/NUPEC shaking table test, and 4) an assessment of the effect of prior damage history on the FE analyses of the seismic response of shear wall structures. This study concluded that both the simplified and FE methods investigated in this report are capable of predicting the ultimate seismic capacity of the JNES/NUPEC shear wall specimens with reasonable accuracy from a practical standpoint. The progressive degrading characteristics of the shear wall specimens were also captured by the BNL analyses, especially the ANACAP FE 3-D dynamic simulation analysis. The NRC staff concludes that the JNES/NUPEC cyclic and shaking table test data discussed in this report can be used as a benchmark for future validations or confirmations of the adequacy of other alternative analytical methods or computer programs for the seismic response analysis of NPP shear wall structures, which were not included in this report for the BNL study.

FOREWORD

This report documents the collaborative efforts of the U.S. Nuclear Regulatory Commission (NRC) and the Japan Nuclear Energy Safety Organization (JNES) and Nuclear Power Engineering Corporation (NUPEC) under the NRC-JNES agreement in the area of seismic engineering research. Specifically, the shear wall test program addressed in this report is one of a series of large-scale seismic testing programs of nuclear power plant (NPP) structures, systems, and components conducted by JNES/NUPEC. The research conducted and information exchanged under this collaborative agreement have allowed the NRC to gain access to valuable data from large-scale seismic test programs that are not available anywhere else in the world. In addition, this program has enhanced interactions with various Japanese organizations to promote the exchange of information and awareness of ongoing seismic research in Japan.

The JNES/NUPEC reinforced concrete (RC) shear wall test program was a multi-year program to investigate the behavior of NPP RC shear walls subjected to strong earthquake motions, and to assess the capabilities of various methodologies for RC shear wall capacity analysis. The test program included element tests, diagonal cyclic loading tests of box walls, multi-directional simultaneous cyclic loading tests of box and cylinder walls, and shaking table tests of box and cylinder walls. In both cyclic and shaking table tests, the specimens were loaded to the level of incipient failure, and in the shaking table tests, the specimens were shaken to levels well above typical design earthquake excitation levels. This report includes a summary description of these tests and their results.

Under contract to the NRC, Brookhaven National Laboratory (BNL) participated in this program and performed this study. The primary objectives of the BNL study were as follows:

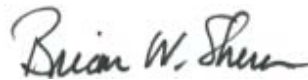
- (1) Assess analysis methods for seismic shear wall capacity calculations against the JNES/NUPEC multi-axial cyclic loading and shaking table test data.
- (2) Determine the effect of out-of-plane loads on the in-plane shear capacity calculations.
- (3) Gain technical insights from the JNES/NUPEC data for use in evaluating methodologies for assessing the seismic capacity of RC shear walls.

To achieve those objectives, the following numerical methods were selected for the BNL study:

- simplified methods based on code-type equations for shear wall capacity calculations, as recommended in the following consensus standards developed by the American Concrete Institute (ACI) and the American Society of Civil Engineers:
 - o ACI 349-01, “Code Requirements for Nuclear Safety-Related Concrete Structures and Commentary”
 - o ASCE 43-05, “Seismic Design Criteria for Structures, Systems, and Components in Nuclear Facilities”
- simplified methods based on code-type equations used in seismic fragility calculations
- three-dimensional (3-D) finite element (FE) analysis using ANACAP (an FE program with a detailed RC material model)

Based on the correlation analyses performed against the JNES/NUPEC test data, the BNL study has provided both qualitative and quantitative assessments of the applicability and limitations of these numerical methods. Insights developed in this report provide valuable information that can be used for safety assessments of NPP shear wall structures.

From a regulatory standpoint, it is essential to understand the limitations and sensitivities of these analysis methods and the importance of validating these methods against test data. As affirmed by the BNL study, the JNES/NUPEC tests have yielded valuable data, which, together with insights gained from the various correlation analyses presented in this report, will serve as an excellent resource for seismic fragility estimates of RC shear wall structures. In addition, the BNL study confirmed that (for the range of parameters considered) when the bi-axial shear components are treated as uncorrelated, it is acceptable to neglect the effect of out-of-plane loads on the in-plane shear capacity estimate, as is the current practice of the nuclear industry. Finally, on the basis of the BNL study, the NRC concluded that the JNES/NUPEC data can be used to benchmark analytical models and methods for seismic response analysis of NPP low-rise shear wall structures with comparable aspect ratios.



Brian W. Sheron, Director
Office of Nuclear Regulatory Research
U.S. Nuclear Regulatory Commission

TABLE OF CONTENTS

ABSTRACT.....	iii
FOREWORD	v
TABLE OF CONTENTS.....	vii
LIST OF FIGURES	ix
LIST OF TABLES	xv
EXECUTIVE SUMMARY	xvii
ACKNOWLEDGMENTS	xxi
1 INTRODUCTION	1
1.1 Background.....	1
1.2 Scope and Objectives	1
1.3 Report Organization	1
2 DESCRIPTION OF JNES CYCLIC AND SHAKING TABLE TESTS.....	3
2.1 Test Specimens.....	3
2.1.1 Uni-Directional Cyclic Loading Test Specimens.....	3
2.1.2 Multi-Axis Cyclic Loading Test Specimens	3
2.1.3 Shaking Table Test Specimens	4
2.2 Test Instrumentation and Procedures	5
2.2.1 Cyclic static tests.....	5
2.2.2 Shaking Table Tests	6
2.3 Summary of JNES Test Results.....	7
2.3.1 Cyclic Static Test Results.....	7
2.3.2 Shaking Table Test Results	9
3 ASSESSMENT OF SIMPLIFIED METHODS FOR ESTIMATING SHEAR WALL SEISMIC STRENGTH AGAINST TEST DATA.....	41
3.1 Methods for Calculating Ultimate Capacity and Comparison to Test Results	41
3.1.1 ACI Design Code Method.....	41
3.1.2 ASCE 43-05 (Barda et al.) Method.....	45
3.1.3 Relevant Information of the JNES/NUPEC Specimens.....	48
3.1.4 Application of ASCE 43-05 Method to All Test Specimens	49
3.1.4.1 Strength Capacities Using the ASCE 43-05 Method.....	49
3.1.4.2 Strength Adjustment Based on a Single-Wall Approach	50
3.1.4.3 Strength Adjustment Based on an Overall-Box Structure Approach	52
3.1.4.4 Discussions	53
3.1.5 Application of ACI Methods to All Test Specimens	54
3.2 Methods for Calculating Inelastic Energy Absorption Factor and Comparison to Test Results.....	55
3.2.1 Estimation of Inelastic Energy Absorption Factor for JNES Shaker Table Test	55
3.2.2 Ridell-Newmark Method.....	57
3.2.3 Effective Frequency/Effective Damping Methods (EFED)	61
4 ANACAP 3-D FINITE ELEMENT ANALYSIS OF STATIC CYCLIC TESTS.....	79
4.1 Specimens and Loadings	79
4.1.1 The NUPEC Specimens	79
4.1.2 Cyclic Loading Scenarios.....	80
4.2 Finite Element Model	82
4.2.1 ANACAP Constitutive Models.....	82

4.2.2	Shear Wall Model	82
4.2.3	Static Analysis.....	83
4.3	Results and Comparisons.....	84
4.4	Summary of the Static Cyclic Analyses	87
5	ANACAP 3-D FINITE ELEMENT SIMULATION OF DYNAMIC SHAKING	
	TABLE TESTS.....	113
5.1	Description of ANACAP Dynamic Shear Wall Model.....	113
5.2	ANACAP Simulation of Shaking Table Shear Wall Tests	115
5.2.1	ANACAP Analysis for Run-1.....	115
5.2.2	ANACAP Analysis for Run-2.....	116
5.2.3	ANACAP Analysis for Run-2'	117
5.2.4	ANACAP Analysis for Run-3.....	118
5.2.5	ANACAP Analysis for Run-3'	118
5.2.6	ANACAP Analysis for Run-4.....	119
5.2.7	ANACAP Analysis for Run-5.....	120
5.2.8	ANACAP Analysis for Run-6.....	121
5.3	ANACAP Analysis of Test Run 6 without Considering Prior Damages	122
5.4	ANACAP Analysis of Test Run 6 using Only X-Input Motion.....	123
6	CONCLUSIONS AND RECOMMENDATIONS	173
7	REFERENCES	177

LIST OF FIGURES

Figure 2-1 Uni-Directional Cyclic Test specimens (SD-08 Series).....	11
Figure 2-2 Proportions of Different Deformation Components at Cycle Peaks	11
Figure 2-3 Box-Type Shear Wall Specimen for Multi-axis Cyclic Tests	12
Figure 2-4 Cylindrical-Type Shear Wall Specimen for Multi-Axis Cyclic Tests.....	12
Figure 2-5 Reinforcement Arrangement for Box-Type Shear Wall Specimen.....	13
Figure 2-6 Reinforcement Details for both Box- and Cylindrical-type Walls.....	13
Figure 2-7 Proportions of Deformation Components for Specimen SB-B-01	14
Figure 2-8 Dimensions of Shaking Table Test Specimens in mm unit.....	15
Figure 2-9 Rebar Arrangements and Details of Test Specimens	16
Figure 2-10 Rebar Details at Corners of Box-Type Specimens.....	16
Figure 2-11 Loading Apparatus Schematics for Uni-Directional Cyclic Tests	17
Figure 2-12 Loading Cycle Schematics for Uni-Directional Cyclic Tests	18
Figure 2-13 Loading Apparatus schematics for Multi-axis Cyclic Tests.....	18
Figure 2-14 Loading Patterns for Multi-axis Cyclic Tests.....	19
Figure 2-15 Loading Cycle Schematics for Multi-axis Cyclic Tests	19
Figure 2-16 Shear Force and Deformation Schematics for Multi-axis Cyclic Tests	19
Figure 2-17 Computed Shear Force Orbits for Multi-Axis Tests	20
Figure 2-18 Response Spectra for Input Motions to Shaking Table	20
Figure 2-19 Input Motion Acceleration Time Histories to Shaking Table	21
Figure 2-20 Low-Pass High Cut Filter Applied to Recorded Response Data.....	21
Figure 2-21 Schematic Locations of Accelerometers on Top and Base Slabs.....	22
Figure 2-22 Schematic Locations of Accelerometers on Table Top and Top Weight.....	23
Figure 2-23 Schematic Locations of Displacement Gauges on Top of Walls	24
Figure 2-24 Schematic Locations of Displacement Gauges on Mid-Height of Walls.....	25
Figure 2-25 Schematic Locations of Strain Gauges of Vertical Rebars of Walls (A & B).....	26
Figure 2-26 Schematic Locations of Strain Gauges of Vertical Rebars of Walls (C & D).....	27
Figure 2-27 Schematic Locations of Strain Gauges of Bolts Fastening Slab to Table	28
Figure 2-28 Hysteresis Loops for SD-08 Series Specimens Subjected to Uni-Directional Cyclic loading.....	28
Figure 2-29 Envelopes of Hysteresis Loops for SD-08 Series Specimens Subjected to Uni-Directional Cyclic loading	29
Figure 2-30 Crack Patterns of Shear Walls for SD-08 Series Specimens at Onset of Failure.....	29
Figure 2-31 Comparison of JEAG Calculations of Shear Forces with Test Data.....	29
Figure 2-32 Comparison of JEAG Calculations of Hysteresis Loops with Test Data.....	30
Figure 2-33 Shear-Deformation Hysteresis Loops for Specimen SB-B-01 (Rectangular Loading).....	30
Figure 2-34 Shear-Deformation Hysteresis Loops for Specimen SB-B-02 (Cross Loading).....	31
Figure 2-35 Shear-Deformation Hysteresis Loops for Specimen SB-B-03 (Diagonal Cross Loading)	31
Figure 2-36 Shear-Deformation Hysteresis Loops for Specimen SB-C-01 (Rectangular Loading).....	32
Figure 2-37 Comparisons of Shear-Deformation Envelop Curves for Different Loading Patterns.....	32
Figure 2-38 Crack Patterns of Shear Walls at Onset of Failure for Specimens Subjected to Different Loading Patterns	33
Figure 2-39 Schematic Notations employed in Displays of Shaking Table Test Results	36
Figure 2-40 Horizontal Acceleration Response of Upper Slab for Specimen DT-B-02.....	36
Figure 2-41 Three Orthogonal Components of Acceleration Response of Upper Slab for Specimen DT-B-02.....	36
Figure 2-42 Horizontal Acceleration Response of Upper Slab for Specimen DT-C-01.....	37
Figure 2-43 Three Orthogonal Components of Acceleration Response of Upper Slab for Specimen DT-C-01	37

Figure 2-44 Horizontal Acceleration and Displacement Orbits from Run 3 for DT-B-02	37
Figure 2-45 Horizontal Hysteresis Loops from Run 3 for DT-B-02.....	37
Figure 2-46 Horizontal Acceleration and Displacement Orbits from Run 4 for DT-B-02	38
Figure 2-47 Horizontal Hysteresis Loops from Run 4 for DT-B-02.....	38
Figure 2-48 Horizontal Acceleration and Displacement Orbits from Run 6 for DT-B-02	38
Figure 2-49 Horizontal Hysteresis Loops from Run 6 for DT-B-02.....	38
Figure 2-50 X-Z Plane Acceleration and Displacement Orbits from Run 36 for DT-B-02.....	39
Figure 2-51 Progressive Development of Shear Wall Cracks for DT-B-02	39
Figure 2-52 Progressive Development of Shear Wall Cracks for DT-C-01	40
Figure 3-1 Concrete Shear Wall Strength as a Function of Aspect Ratio.....	70
Figure 3-2 Regression Analysis of V_U/V_{MT} vs. V_{VT}/V_{MT}	70
Figure 3-3 Contour Plot of Eq. 3-19	71
Figure 3-4 Contour Plot of Eq. 3-19 in Terms of Loading Angle.....	72
Figure 3-5 Maximum Vector Shear Forces Normalized by V_U	73
Figure 3-6 Maximum Vector Shear Forces Normalized by V_U/F	73
Figure 3-7 JNES Shaker Table Input Spectra X Direction, 5% Damping	74
Figure 3-8 JNES Shaker Table Input Spectra Y Direction, 5% Damping	74
Figure 4-1 Box-shaped Shear Wall Dimension	88
Figure 4-2 Rebar Configuration (Unit mm) [after Hiroshi, 2001]	89
Figure 4-3 1-D Displacement Loading Pattern	89
Figure 4-4 Rectangular Displacement Loading Pattern	90
Figure 4-5 A Typical X-Y Displacement Orbit for Rectangular Loading [after Hiroshi, 2001]	90
Figure 4-6 Cross Displacement Loading Pattern	91
Figure 4-7 A Typical X-Y Displacement Orbit for Cross Loading [after Hiroshi, 2001]	91
Figure 4-8 Diagonal Cross Displacement Loading Pattern.....	92
Figure 4-9 A Typical X-Y Displacement Orbit for Diagonal Cross Loading [after Hiroshi, 2001].....	92
Figure 4-10 Displacement History at the Top of Shear Wall for SB-B-01	93
Figure 4-11 Displacement History at the Top of Shear Wall for SB-B-02.....	93
Figure 4-12 Displacement History at the Top of Shear Wall for SB-B-03.....	94
Figure 4-13 ANACAP Unconfined Concrete Compression Model.....	94
Figure 4-14 Criteria Curve for ANACAP Crack Initiation [from ANATECH 2004, Courtesy of ANATECH	95
Figure 4-15 ANACAP Concrete Tension Stiffening Model [from Dunham R.S. and Rashid Y.R., 2003, Courtesy of ANATECH]	95
Figure 4-16 ANACAP Shear Retention Model [from Dunham R.S. and Rashid Y.R., 2003, Courtesy of ANATECH].....	96
Figure 4-17 ANACAP Shear Wall Model	96
Figure 4-18 ANACAP Shear Wall Mesh.....	97
Figure 4-19 ANACAP Rebars Model for the Shear Wall.....	97
Figure 4-20 Shear Force – Displacement Relation For 1-D Cyclic Loading	98
Figure 4-21 Cycle-By-Cycle Shear Force – Displacement Relation For 1-D Cyclic Loading	99
Figure 4-22 $Q_x - D_x$ Relation for Rectangular Loading	100
Figure 4-23 $Q_y - D_y$ Relation for Rectangular Loading	100
Figure 4-24 Cycle-By-Cycle $Q_x - D_x$ Relation For Rectangular Loading.....	101
Figure 4-25 Cycle-By-Cycle $Q_y - D_y$ Relation For Rectangular Loading.....	102
Figure 4-26 Shear Force Orbits for Rectangular Loading	103
Figure 4-27 Cycle-By-Cycle Shear Force Orbits For Rectangular Loading.....	103
Figure 4-28 $Q_x - D_x$ Relation for Cross Loading.....	104
Figure 4-29 $Q_y - D_y$ Relation for Cross Loading.....	104
Figure 4-30 Cycle-By-Cycle $Q_x - D_x$ Relation For Cross Loading.....	105
Figure 4-31 Cycle-By-Cycle $Q_y - D_y$ Relation For Cross Loading.....	106

Figure 4-32 Shear Force Orbits for Cross Loading.....	106
Figure 4-33 Qx – Dx Relation for Diagonal Cross Loading.....	107
Figure 4-34 Qy – Dy Relation for Diagonal Cross Loading.....	107
Figure 4-35 Cycle-By-Cycle Qx – Dx Relation For Diagonal Cross Loading.....	108
Figure 4-36 Cycle-By-Cycle Qy – Dy Relation For Diagonal Cross Loading.....	109
Figure 4-37 Shear Force Orbits for Diagonal Cross Loading.....	110
Figure 4-38 Cycle-By-Cycle Shear Force Orbits For Diagonal Cross Loading.....	111
Figure 5-1 Elevation of DT-B-02 Model (Unit: mm).....	125
Figure 5-2 Shear Wall Model for Dynamic Simulation.....	125
Figure 5-3 Shear Wall Mesh for Dynamic Simulation.....	126
Figure 5-4 Shear Wall Mesh for Dynamic Simulation (Elevation, Unit mm).....	127
Figure 5-5 Shear Wall Rebars for Dynamic Simulation.....	127
Figure 5-6 X-Input Motions for ANACAP Simulation Analysis.....	128
Figure 5-7 Y-Input Motions for ANACAP Simulation Analysis.....	128
Figure 5-8 Z-Input Motions for ANACAP Simulation Analysis.....	129
Figure 5-9 Comparison of X-Direction Response between ANACAP Analysis at Upper Corners of Shear Walls and Measured Data for Run-1.....	129
Figure 5-10 Comparison of Y-Direction Response between ANACAP Analysis at Upper Corners of Shear Walls and Measured Data for Run-1.....	130
Figure 5-11 Comparison of Z-Direction Response between ANACAP Analysis at Upper Slab Corner No. 1 and Measured Result for Run-1.....	130
Figure 5-12 Comparison of Z-Direction Response between ANACAP Analysis at Upper Slab Corner No. 2 and Measured Result for Run-1.....	131
Figure 5-13 Comparison of Z-Direction Response between ANACAP Analysis at Upper Slab Corner No. 3 and Measured Result for Run-1.....	131
Figure 5-14 Comparison of Z-Direction Response between ANACAP Analysis at Upper Slab Corner No.4 and Measured Result for Run-1.....	132
Figure 5-15 Comparison of X-Direction Response between ANACAP Analysis at Upper Corners of Shear Walls and Measured Data for Run-2.....	132
Figure 5-16 Comparison of Y-Direction Response between ANACAP Analysis at Upper Corners of Shear Walls and Measured Data for Run-2.....	133
Figure 5-17 Comparison of Z-Direction Response between ANACAP Analysis at Upper Slab Corner No.1 and Measured Result for Run-2.....	133
Figure 5-18 Comparison of Z-Direction Response between ANACAP Analysis at Upper Slab Corner No.2 and Measured Result for Run-2.....	134
Figure 5-19 Comparison of Z-Direction Response between ANACAP Analysis at Upper Slab Corner No.3 and Measured Result for Run-2.....	134
Figure 5-20 Comparison of Z-Direction Response between ANACAP Analysis at Upper Slab Corner No.4 and Measured Result for Run-2.....	135
Figure 5-21 Comparison of X-Direction Response between ANACAP Analysis at Upper Corners of Shear Walls and Measured Data for Run-2'.....	135
Figure 5-22 Comparison of Y-Direction Response between ANACAP Analysis at Upper Corners of Shear Walls and Measured Data for Run-2'.....	136
Figure 5-23 Comparison of Z-Direction Response between ANACAP Analysis at Upper Slab Corner No.1 and Measured Result for Run-2'.....	136
Figure 5-24 Comparison of Z-Direction Response between ANACAP Analysis at Upper Slab Corner No.2 and Measured Result for Run-2'.....	137
Figure 5-25 Comparison of Z-Direction Response between ANACAP Analysis at Upper Slab Corner No.3 and Measured Result for Run-2'.....	137
Figure 5-26 Comparison of Z-Direction Response between ANACAP Analysis at Upper Slab Corner No.4 and Measured Result for Run-2'.....	138

Figure 5-27 Comparison of Hysteresis Loops in X-Direction for Run-2'	138
Figure 5-28 Comparison of Hysteresis Loops in Y-Direction for Run-2'	139
Figure 5-29 ANACAP Calculated SRSS Base Shear vs. SRSS Shear Strain for Run-2'	139
Figure 5-30 Comparison of X-Direction Response between ANACAP Analysis at Upper Corners of Shear Walls and Measured Data for Run-3.....	140
Figure 5-31 Comparison of Y-Direction Response between ANACAP Analysis at Upper Corners of Shear Walls and Measured Data for Run-3.....	140
Figure 5-32 Comparison of Z-Direction Response between ANACAP Analysis at Upper Slab Corner No.1 and Measured Result for Run-3	141
Figure 5-33 Comparison of Z-Direction Response between ANACAP Analysis at Upper Slab Corner No.2 and Measured Result for Run-3	141
Figure 5-34 Comparison of Z-Direction Response between ANACAP Analysis at Upper Slab Corner No.3 and Measured Result for Run-3	142
Figure 5-35 Comparison of Z-Direction Response between ANACAP Analysis at Upper Slab Corner No.4 and Measured Result for Run-3	142
Figure 5-36 Comparison of Hysteresis Loops in X-Direction for Run-3	143
Figure 5-37 Comparison of Hysteresis Loops in Y-Direction for Run-3	143
Figure 5-38 ANACAP Calculated SRSS Base Shear vs. SRSS Shear Strain for Run-3	144
Figure 5-39 Comparison of X-Direction Response between ANACAP Analysis at Upper Corners of Shear Walls and Measured Data for Run-3'	144
Figure 5-40 Comparison of Y-Direction Response between ANACAP Analysis at Upper Corners of Shear Walls and Measured Data for Run-3'	145
Figure 5-41 Comparison of Z-Direction Response between ANACAP Analysis at Upper Slab Corner No.1 and Measured Result for Run-3'	145
Figure 5-42 Comparison of Z-Direction Response between ANACAP Analysis at Upper Slab Corner No.2 and Measured Result for Run-3'	146
Figure 5-43 Comparison of Z-Direction Response between ANACAP Analysis at Upper Slab Corner No.3 and Measured Result for Run-3'	146
Figure 5-44 Comparison of Z-Direction Response between ANACAP Analysis at Upper Slab Corner No.4 and Measured Result for Run-3'	147
Figure 5-45 Comparison of Hysteresis Loops in X-Direction for Run-3'	147
Figure 5-46 Comparison of Hysteresis Loops in Y-Direction for Run-3'	148
Figure 5-47 ANACAP Calculated SRSS Base Shear vs. SRSS Shear Strain for Run-3'	148
Figure 5-48 Comparison of X-Direction Response between ANACAP Analysis at Upper Corners of Shear Walls and Measured Data for Run-4.....	149
Figure 5-49 Comparison of Y-Direction Response between ANACAP Analysis at Upper Corners of Shear Walls and Measured Data for Run-4.....	150
Figure 5-50 Comparison of Z-Direction Response between ANACAP Analysis at Upper Slab Corner No.1 and Measured Result for Run-4	150
Figure 5-51 Comparison of Z-Direction Response between ANACAP Analysis at Upper Slab Corner No.2 and Measured Result for Run-4	151
Figure 5-52 Comparison of Z-Direction Response between ANACAP Analysis at Upper Slab Corner No.3 and Measured Result for Run-4	151
Figure 5-53 Comparison of Z-Direction Response between ANACAP Analysis at Upper Slab Corner No.4 and Measured Result for Run-4	152
Figure 5-54 Comparison of Hysteresis Loops in X-Direction for Run-4	152
Figure 5-55 Comparison of Hysteresis Loops in Y-Direction for Run-4	153
Figure 5-56 ANACAP Calculated SRSS Base Shear vs. SRSS Shear Strain for Run-4	153
Figure 5-57 Comparison of X-Direction Response between ANACAP Analysis at Upper Corners of Shear Walls and Measured Data for Run-5.....	154

Figure 5-58 Comparison of Y-Direction Response between ANACAP Analysis at Upper Corners of Shear Walls and Measured Data for Run-5.....	154
Figure 5-59 Comparison of Z-Direction Response between ANACAP Analysis at Upper Slab Corner No.1 and Measured Result for Run-5	155
Figure 5-60 Comparison of Z-Direction Response between ANACAP Analysis at Upper Slab Corner No.2 and Measured Result for Run-5	155
Figure 5-61 Comparison of Z-Direction Response between ANACAP Analysis at Upper Slab Corner No.3 and Measured Result for Run-5	156
Figure 5-62 Comparison of Z-Direction Response between ANACAP Analysis at Upper Slab Corner No.4 and Measured Result for Run-5	156
Figure 5-63 Comparison of Hysteresis Loops in X-Direction for Run-5	157
Figure 5-64 Comparison of Hysteresis Loops in Y-Direction for Run-5	157
Figure 5-65 ANACAP Calculated SRSS Base Shear vs. SRSS Shear Strain for Run-5	158
Figure 5-66 Comparison of X-Direction Response between ANACAP Analysis at Upper Corners of Shear Walls and Measured Data for Run-6.....	158
Figure 5-67 Comparison of Y-Direction Response between ANACAP Analysis at Upper Corners of Shear Walls and Measured Data for Run-6.....	159
Figure 5-68 Comparison of Z-Direction Response between ANACAP Analysis at Upper Slab Corner No.1 and Measured Result for Run-6	159
Figure 5-69 Comparison of Z-Direction Response between ANACAP Analysis at Upper Slab Corner No.2 and Measured Result for Run-6	160
Figure 5-70 Comparison of Z-Direction Response between ANACAP Analysis at Upper Slab Corner No.3 and Measured Result for Run-6	160
Figure 5-71 Comparison of Z-Direction Response between ANACAP Analysis at Upper Slab Corner No.4 and Measured Result for Run-6	161
Figure 5-72 Comparison of Hysteresis Loops in X-Direction for Run-6	161
Figure 5-73 Comparison of Hysteresis Loops in Y-Direction for Run-6	162
Figure 5-74 ANACAP Calculated SRSS Base Shear vs. SRSS Shear Strain for Run-6	162
Figure 5-75 Comparison of ANACAP Analysis without Considering Prior Damages for Run-6 in X-Direction at Upper Corners of Shear Walls and Measured Data	163
Figure 5-76 Comparison of ANACAP Analysis without Considering Prior Damages for Run-6 in Y-Direction at Upper Corners of Shear Walls and Measured Data	163
Figure 5-77 Comparison of ANACAP Analysis without Considering Prior Damages for Run-6 in Z-Direction at Upper Slab Corner No.1 and Measured Result	164
Figure 5-78 Comparison of ANACAP Analysis without Considering Prior Damages for Run-6 in Z-Direction at Upper Slab Corner No.2 and Measured Result	164
Figure 5-79 Comparison of ANACAP Analysis without Considering Prior Damages for Run-6 in Z-Direction at Upper Slab Corner No.3 and Measured Result	165
Figure 5-80 Comparison of ANACAP Analysis without Considering Prior Damages for Run-6 in Z-Direction at Upper Slab Corner No.4 and Measured Result	165
Figure 5-81 Comparison of ANACAP Hysteresis Loop without Considering Prior Damages for Run-6 in X-Direction and Test Result	166
Figure 5-82 Comparison of ANACAP Hysteresis Loop without Considering Prior Damages for Run-6 in Y-Direction and Test Result	166
Figure 5-83 ANACAP Calculated SRSS Base Shear vs. SRSS Shear Strain without Considering Prior Damages for Run-6	167
Figure 5-84 Comparison of X-Direction Response from ANACAP Analysis Considering Prior Damages but with X-Input Motion only and Test Result for Run-6.....	167
Figure 5-85 Comparison of X-Direction Response from ANACAP Analysis Considering No Prior Damages but with X-Input Motion only and Test Result for Run-6.....	168

Figure 5-86 Comparison of X-Direction Hysteresis from ANACAP Analysis Considering Prior Damages but with X-Input Motion only and Test Result for Run-6.....	168
Figure 5-87 Comparison of X-Direction Hysteresis from ANACAP Analysis Considering No Prior Damages but with X-Input Motion only and Test Result for Run-6.....	169
Figure 5-88 ANACAP Calculated SRSS Base Shear vs. SRSS Shear Strain Considering Prior Damages and X-Input Motion only for Run-6.....	169
Figure 5-89 ANACAP Calculated SRSS Base Shear vs. SRSS Shear Strain Considering No Prior Damages and X-Input Motion only for Run-6.....	170

LIST OF TABLES

Table 2-1 Material Properties and Configurations of Test Specimens	12
Table 2-2 Designations of Test specimens and Parameters	14
Table 2-3 Concrete Properties of Specimens at Times of Tests	14
Table 2-4 Rebar Material Properties at Times of Tests	15
Table 2-5 Material Properties of Test Specimens	17
Table 2-6 Maximum Deformation Amplitudes for Multi-Axis Tests.....	20
Table 2-7 Test Results for Specimens Subjected to Uni-Directional Loading	33
Table 2-8 Test Results of Initiation of Cracks for Multi-Axis Cyclic Test Specimens	34
Table 2-9 Frequencies of Specimens at Each Runs	34
Table 2-10 Peak Responses for Specimen DT-B-01.....	34
Table 2-11 Peak Responses for Specimen DT-B-02.....	35
Table 2-12 Peak Responses for Specimen DT-C-01.....	35
Table 3-1 Specimen Properties and Shear Strengths	75
Table 3-2 Summary of Results using ASCE (Barda et al.) Method	75
Table 3-3 Comparison of Prediction Equation to Test Results.....	75
Table 3-4 Values of F	76
Table 3-5 Interaction Effect in Eq. 3-19	76
Table 3-6 Interaction Effect in Eq. 3-24	76
Table 3-7 Summary of Results using ACI 349 Chapter 11 Method.....	76
Table 3-8 Summary of Results using ACI 349 Chapter 21 Method.....	77
Table 3-9 Parameters to be Used for Predicting F_{μ} for Run 6 on DT-B-02.....	77
Table 3-10 Comparison of Predicted Versus Estimated F_{μ} Factors for Run 6 Y-Direction, Structure DT-B-02 (Estimated F_{μ} =3.85 from JNES Test).....	77
Table 4.1 Concrete and Rebar Properties for Static Loading Specimens	88
Table 5-1 Maximum Base Responses from ANACAP Simulation for Run-1.....	170
Table 5-2 Maximum Base Responses from ANACAP Simulation for Run-2.....	170
Table 5-3 Maximum Base Responses from ANACAP Simulation for Run-2'	170
Table 5-4 Maximum Base Responses from ANACAP Simulation for Run-3.....	171
Table 5-5 Maximum Base Responses from ANACAP Simulation for Run-3'	171
Table 5-6 Maximum Base Responses from ANACAP Simulation for Run-4.....	171
Table 5-7 Maximum Base Responses from ANACAP Simulation for Run-5.....	171
Table 5-8 Maximum Base Responses from ANACAP Simulation for Run-6.....	171
Table 5-9 Maximum Base Responses from ANACAP Considering No Prior Damages for Run-6.....	171

EXECUTIVE SUMMARY

As part of collaborative efforts between the United States and Japan on seismic issues, the U.S. Nuclear Regulatory Commission (NRC) and Brookhaven National Laboratory (BNL) participated in the JNES/NUPEC shear wall test program. JNES/NUPEC provided their test results to NRC and BNL in the form of presentations and also provided selected test data for test runs analyzed by BNL in electronic format. NRC agreed to have BNL perform analyses for selected tests and provide the results in a series of presentations and reports. The objectives of this research activity were to (1) assess analysis methods for seismic shear wall capacity using the JNES/NUPEC multi-axis cyclic loading and shaking table test data, (2) determine the technical significance of the JNES/NUPEC data related to the effects of out of plane motions on the overall methodology used for assessing the seismic capacity of reinforced concrete shear walls, and (3) analyze the Japanese test results and provide insights that can be clearly understood and utilized by NRC staff and stakeholders.

There are six major elements contained in this report, which include: 1) the use of simplified methods to estimate the seismic failure capacities of the JNES/NUPEC shear wall specimens and to compare the analytical estimates with the seismic shear wall failure capacities inferred from the JNES/NUPEC test data for both the uni- and multi- axis cyclic tests, as well the shaking table test, 2) the development of an ANACAP static FE model for the JNES/NUPEC shear wall test specimens and the comparisons of the results from the shear wall cyclic analysis using the ANACAP static model with the JNES/NUPEC single and multi-axial cyclic test data, 3) the development of an ANACAP dynamic FE model which was used to perform a 3-D simulation analysis of the JNES shaking table test data, 4) an ANACAP analysis for Run-6 (high level motion) without considering prior damages to assess the effect of prior damage history on the FE analysis of the seismic response of shear wall structures, 5) an ANACAP analysis for Run-6 using uni-directional input to the shear wall model which has been damaged from previous test runs, and 6) same as case 5, except that the prior history of damage was not considered.

Based on the analyses performed on the shear wall test models and the comparisons made between the analysis results and the test data, the following observations and conclusions were reached:

Failure capacity estimates using simplified methods

Test results from eleven box-type RC shear wall specimens were used for assessing shear failure capacity estimated by simplified methods. These shear wall specimens, having aspect ratios in the range of 0.47 – 0.87, were tested by JNES/NUPEC by applying various uni-directional and multi-axis cyclic loads. These test data offer valuable insights into the interaction effect of out-of-plane shear and moment on the in-plane shear failure, which is not considered by consensus standards for shear wall design in the U.S., and therefore provide a unique opportunity for assessing the adequacy of methods based on consensus standards for shear wall capacity estimates. To this end, shear strength of the JNES/NUPEC cyclic test specimens was computed using Chapters 11 and 21 of ACI 349-01, and ASCE 43-05 which is based on the Barda et al. method. The computed shear strength was compared against the JNES/NUPEC test results and the interaction effect on the adequacy of these methods was assessed.

For the ACI methods, the computed shear strength was compared against the test results in terms of the maximum shear of the two directions and the resultant of the bi-axis shears. The comparison showed that shear strength computed by the ACI methods appear to be quite conservative as would be expected. The level of conservatism is large for smaller aspect ratios

and reduces as the aspect ratio increases. In addition, the interaction intensity which measures the bi-axis interaction effect also reduces the conservative margin; however, no significant un-conservative bias is introduced when the bi-axis shear components are probabilistically combined (which is the current industry practice for seismic analysis of RC shear walls).

An extensive evaluation of the ASCE 43-05 method for estimating the capacity of RC shear walls was performed. A regression equation involving the interaction intensity and an adjustment factor was established to closely correlate the ASCE 43-05 calculated shear strength to the test data. The adjustment factor, designated in this report as F , was established as a linear function of the aspect ratio. For shear walls with small or no interaction effect (interaction intensity is approximately equal to one), the ratio of the ASCE 43-05 calculated shear strength to test data becomes simply the adjustment factor F . In this case, the use of ASCE 43-05 is very close and for most cases conservative when compared to the JNES/NUPEC test results on walls having aspect ratios in the range of 0.47 to 0.87. For walls with more significant interaction effect, the shear strength calculated based on ASCE 43-05 when corrected with the adjustment factor compares very closely to the test results. However, due to the limited range of aspect ratios for the test specimens, application of the ASCE 43-05 method should be cautioned for shear walls having aspect ratios greater than 0.9.

It was further concluded that when two horizontal components of seismic input motions are treated as being statistically independent from one another, the interaction effect could be neglected. It was demonstrated that when the seismic loads in both horizontal directions are statistically uncorrelated and the shear forces are combined probabilistically in accordance with the 100-40-40 rule, the un-conservatism by neglecting the interaction effect is only 6.1% (It should be noted that the conservatism is attributed to both the interaction intensity and the adjustment factor F). Thus, no significant un-conservative bias is introduced by considering each direction independently so long as the bi-axis shear components are uncorrelated.

Assessment of methods for calculating inelastic energy absorption factors

Four methods for computing the inelastic energy absorption factor F_{μ} were selected to compare with the JNES/NUPEC shaking table test estimate of F_{μ} . These methods include: Riddell-Newmark, effective frequency/effective damping (EFED), Spectral Averaging and Secant Frequency methods. Among these methods, Riddell-Newmark conservatively bounds the test results (under predict F_{μ} by about 18 to 19% in the x and y directions) while EFED and Spectral Averaging generally over predict the test results. The reason for over-estimating F_{μ} by EFED or Spectral Averaging in this case was due to a local valley that existed in the response spectrum at the effective frequency which is higher than the secant frequency. Therefore, when a local valley exists in the response spectra at frequencies above the secant frequency, the calculation of F_{μ} should be limited to no more than that computed by the Secant Frequency Method. The calculation of F_{μ} using the Secant Frequency Method was shown to provide the best comparison to the test data (about 14% over prediction in the x direction and about 6% over prediction in the y direction). Therefore, for this specimen configuration and earthquake motion, the Secant Frequency Method provided the most accurate overall comparison to the test results.

ANACAP static cyclic analyses

To assess the performance of the ANACAP capability for modeling nonlinear cyclic characteristics of reinforced concrete shear wall structures, the ANACAP analysis results of the JNES/NUPEC cyclic test models were compared to the test data in terms of the base shear capacity, hysteresis loops of the shear force vs. displacement, and shear force orbits. The computed base shear capacities by ANACAP compare well with those of the tests with the

relative differences mostly around 10%, with one exception that results in a relative difference of 21%. These differences may be attributed to the simplifications introduced in the ANACAP models; nevertheless, the differences shown are well within the general acceptable range for reinforced concrete material.

Reasonable agreement between the analysis results and the test data were also achieved for the hysteresis loops and the shear force orbits, in terms of both the overall shape and the cycle-to-cycle comparisons. These correlations further exhibit the ANACAP capability in characterizing the reinforced concrete material behavior associated with concrete stiffening, softening, shear retention and shedding, load cycling, and rebar bond and anchorage effect. Although ANACAP does not define the final failure of the structure due to its intentional modeling strategy, the capability of the ANACAP analysis extending from the pre- to post-ultimate load bearing behaviors permits the determination of the failure capacity of the shear walls, based on a sound engineering practice.

ANACAP simulation of JNES/NUPEC shaking table tests

The ANACAP simulation analysis was performed for the JNES/NUPEC box-type shear wall shaking table test. The same ANACAP RC model as for the static cyclic analysis was used for the dynamic simulation analysis of the JNES/NUPEC shaking table tests. Eight runs with progressive increases of the shaking input motion to the RC shear wall were analyzed, and the analysis results were compared with the test data in terms of response spectra at the top of the shear wall, hysteresis loops and the base shears. The ANACAP simulation generally captured the progressive degrading behavior of the shear wall as indicated from the test data, which demonstrated the capability of the ANACAP concrete material model in characterizing the non-linear softening of RC structures. With the exception for Run-1, the simulation generally captured the frequency shifts in the response spectra comparisons with the test and the roof accelerations were reasonably matched to the test within about plus or minus 20%. The level of agreement for the in-structure response spectral peaks was about plus or minus 30% in the horizontal comparisons and about plus or minus 50% in the vertical comparisons. The largest discrepancy in the response spectra comparisons occurred in the simulation for Run-1, which has the smallest input level and the shear wall was expected to remain elastic. This discrepancy was believed to be possibly attributed to the prescribed damping for the ANACAP model. As the test runs progressed, the energy dissipation of the shear wall was gradually controlled by the hysteresis characteristics of the reinforced concrete material model; therefore, the prescribed damping became less important and the level of agreement between test and analysis results increased. Although the peaks of the calculated in-structure response spectra were not as closely matched to the test results as one might expect to achieve, the overall progressive failure behavior of the JNES/NUPEC shaking table test was reasonably captured by the simulation analysis of the ANACAP RC shear wall model.

The ANACAP capability for predicting the shaking table shear wall test was further demonstrated through the close comparisons of the hysteresis loops as presented in this report. The incipient failure of the shear wall is inferred from the calculated hysteresis loops for Run-6, which is very close to the actual failure declared for the test model.

With the exception of the vertical reaction for Run-6, base reactions were reasonably matched between test and analysis within about plus or minus 20%. The base shears predicted by ANACAP are mostly higher than test results, except for Runs 1, 4, and 5. For Runs 4 and 5, ANACAP under-predicted the base shears by approximately 3 – 8%, while ANACAP under-predicted the base shears for Run-1 by about 23%. The variability in the base shear calculations

was shown to be higher for the dynamic analysis than the static cyclic results, largely attributed to the introduced inertia effect in the dynamic analysis.

Effect of damage history and the use of uni-direction input motion

Based on comparisons between the shaking table test for Run-6 and the ANACAP analysis for the same run, but without the effect of the previous cumulative damage history, little effect of prior damage was shown for response spectra in the X-direction for the low frequency range (less than 30 Hz), but for frequencies greater than 30 Hz, substantially higher spectral amplitude than the test result was shown when prior damage is ignored. Similarly, higher computed spectra than the test spectra were also observed in the Y-direction when prior damage was not considered, especially near about 10 Hz. In terms of the base reactions, ignoring prior damage resulted in higher base shears than the test results, but little change in the vertical reaction calculation. The response differences between including and ignoring prior damage history demonstrated the importance of appropriately accounting for the correct boundary conditions in the seismic analysis of shear walls.

Finally, the out-of-plane effect was investigated by applying only the X-directional input motion to the ANACAP shear wall model for Run-6 and comparing the analysis results with the test data and analysis results with three directional input motions. The comparisons show that in terms of response spectra, good correlation was exhibited when prior damages are appropriately accounted for, while ignoring prior damage resulted in significantly higher spectral accelerations than the test results between 10 - 20 Hz. Furthermore, the out-of-plane effect appeared to have only increased the base shear by 9% if prior damage is appropriately included. However, when prior damage is ignored, the out-of-plane effect reduced the base shear estimate by 27%. The lesser out-of-plane effect is also an expected outcome of the fact that the seismic input motions applied to the shaking table in the three orthogonal directions are statistically independent.

In summary, the analyses presented in this report provide valuable insights into various scenarios in that important parameter considerations need to be appropriately included in the seismic response analysis of shear wall structures. The analysis methods utilized for performing the predictive analyses of the JNES/NUPEC cyclic and shaking table tests of shear walls performed well, which confirm the capability of the current technology for shear wall seismic response calculations. Based on the conclusions discussed above, it is recommended that the JNES/NUPEC cyclic and shaking table test data analyzed in this report be used as a benchmark for future validations or confirmations of the adequacy of other alternative analytical methods or computer programs for the seismic response analysis of NPP low-rise shear wall structures with comparable aspect ratios utilized for the JNES/NUPEC cyclic and shaking table tests.

ACKNOWLEDGMENTS

The Office of Nuclear Regulatory Research of the U.S. Nuclear Regulatory Commission (NRC) sponsored the research program described in this report. The authors would like to express their gratitude to Dr. Syed Ali and Dr. Andrew Murphy, NRC Project Managers, for the technical and administrative support they have provided in performing this study.

This research program was performed as part of the Implementing Agreement between the U.S. Nuclear Regulatory Commission and the Japan Nuclear Energy Safety Organization (JNES) in the Area of Seismic Engineering Research. This agreement is an item of the Implementing Arrangement between the United States Nuclear Regulatory Commission and the Nuclear and Industrial Safety Agency (NISA) of Japan for Cooperation in the Field of Nuclear Regulatory Matters and Nuclear Safety Research and Development.

Prior to the establishment of JNES, the Nuclear Power Engineering Corporation (NUPEC) of Japan performed the multi-axis loading tests of reinforced concrete (RC) shear walls discussed in this report. All of the test results and information about the test models included in this report were provided by JNES/NUPEC and are greatly appreciated. The authors especially thank Dr. Yoshio Kitada of JNES/NUPEC, for his support and technical guidance throughout this collaborative study. The authors also wish to acknowledge the helpfulness and cooperation provided by Mr. Hiroshi Abe and Mr. Yuichi Uchiyama of JNES/NUPEC, Mr. Kazuhiro Kusama and Mr. Atsushi Suzuki of Kajima Corporation, and Mr. K. Shintani of Taisei Corporation. Many others from these and other organizations participated in the meetings and laboratory visits during this study. Their hospitality and technical contributions to this work are greatly appreciated.

The authors would like to express their special thanks to Dr. Robert Kennedy of RPK Structural Mechanics Consulting for the technical guidance he provided in the course of this study and for his detailed review of this report. The valuable and insightful comments and recommendations he has provided were instrumental for the preparation of this report, especially in developing Section 3 of this report.

The authors acknowledge and thank Dr. Robert Dunham and Mr. Randy James of ANATECH Corporation for providing technical assistance in the application of the ANACAP computer code on this project.

The authors also express special thanks to Ms. Susan Monteleone for her secretarial help throughout this program and in the preparation of this report.

1 INTRODUCTION

1.1 Background

Prior to the establishment of the Japan Nuclear Energy Safety Organization (JNES), the Nuclear Power Engineering Corporation (NUPEC) of Japan performed multi-axis loading tests of reinforced concrete (RC) shear walls. This ten-year test program was completed in 2004 and included element tests, diagonal cyclic loading tests of box walls, multi-directional simultaneous cyclic loading tests of box and cylinder walls, and shaking table tests of box and cylinder walls.

As a result of the element tests, researchers in Japan developed a shear transfer constitutive model as a function of both shear and axial stresses. One of the major conclusions by JNES/NUPEC from all the box and cylinder wall tests was that for shear deformation angles smaller than 2×10^{-3} the effect of multi-axis loading is negligibly small and the methodology recommended in the Japanese guidelines for one directional loading can be applied. For shear deformation angles greater than 2×10^{-3} the seismic capacity of the specimen decreased explicitly due the effect of simultaneous multi-axis loading and JNES/NUPEC concluded that this effect should be considered in the analysis. JNES/NUPEC also concluded that the non-linear response of an RC structure and its hysteretic curve for the restoring force can be evaluated satisfactorily if FEM analysis is applied with a four-way crack model.

Many of the analytical methods used by the nuclear industry in the United States have been primarily correlated with the results of single-element shear wall tests in which the walls were subjected to one-directional loading in the plane of the wall. The JNES/NUPEC test results provide unique information in that they tested box and cylindrical walls under the effect of multi-axis loading.

1.2 Scope and Objectives

As part of collaborative efforts between the United States and Japan on seismic issues, the U.S. Nuclear Regulatory Commission (NRC) and Brookhaven National Laboratory (BNL) participated in the JNES/NUPEC shear wall test program. The collaboration program included a series of periodic technical meetings held in Japan and the U.S. to review and evaluate the test and analyses results. In accordance with the collaboration agreement, JNES/NUPEC provided their test results to NRC and BNL in the form of presentations and also provided selected test data for test runs analyzed by BNL in electronic format. NRC agreed to have BNL perform analyses for selected tests and provide the results in a series of presentations and reports. As part of the collaboration effort, NRC and BNL staff members were invited to witness the shaking table testing of two of the shear wall specimens, as well as to observe the post-test condition of the specimens for a number of the cyclic shear wall tests.

The specific objectives of this research activity were to (1) assess analysis methods for seismic shear wall capacity using the JNES/NUPEC multi-axis cyclic loading and shaking table test data, (2) determine the technical significance of the JNES/NUPEC data related to the effects of out of plane motions on the overall methodology used for assessing the seismic capacity of reinforced concrete shear walls, and (3) analyze the Japanese test results and provide insights that can be clearly understood and utilized by NRC staff and stakeholders.

1.3 Report Organization

The purpose of this report is to present a summary of the JNES/NUPEC test program, to describe the BNL analyses, and to discuss the insights gained from the program.

Section 2.0 provides a description and summary results of the JNES/NUPEC cyclic and shaking table tests. Information regarding the test specimens, procedures and instrumentation are described to a degree sufficient for independent analyses of the test data. Summaries of the test results are also provided, enabling comparisons between analysis results and the test measurements.

Section 3 describes a number of simplified methods used in the nuclear industry to estimate the ultimate capacity of low-rise reinforced concrete shear walls subjected to seismic loadings. These methods are also applied to the JNES/NUPEC test specimen configurations to predict the failure capacity of the box type structure containing shear walls. A comparison is then made between the predicted (calculated) values using the various simplified methods.

Section 4 describes the analytical prediction of the performance of a box type shear wall under one- or two-directional cyclic loadings, using the concrete finite element code ANACAP. The analytical predictions are compared to the test results and the findings are summarized in this section. Section 5 describes the ANACAP 3-D finite element simulation of one of the dynamic shaking table tests of a box-type shear wall. The analytical predictions are also compared to the test results. In addition, the results of additional analyses are discussed that considered three other scenarios: 1) an analysis using a high level test run without prior history of damage to the wall, 2) applying a uni-directional input to the shear wall model, which has been damaged from the previous test runs, and 3) same as case 2, except that the prior history of damage was not considered.

A summary of conclusions and recommendations for further research are presented in Section 6.0.

2 DESCRIPTION OF JNES CYCLIC AND SHAKING TABLE TESTS

This section describes both the cyclic and shaking table tests of reinforced concrete (RC) shear wall specimens performed by JNES and its predecessor – NUPEC. The shear wall specimens were made of box-type and cylinder capped by slabs on both ends. The cyclic tests include both one - and two – directional loading patterns for studying the restoring force characteristics of RC shear walls, while the shaking table tests were performed for the shear wall specimens subjected to the simultaneous applications of three orthogonal seismic input ground motions.

Information regarding the test specimens, procedures and instrumentations are described to a degree sufficient for independent analyses of the test data. A summary of the rest results are also provided, enabling comparisons between analysis results and the test measurements.

2.1 Test Specimens

2.1.1 Uni-Directional Cyclic Loading Test Specimens

For the uni-directional cyclic loading test, box type RC shear wall specimens with shear span ratios (M/Qd or h/d) of 0.6, 0.8 and 1.0 were constructed. The shear walls were intended to be part of a typical reactor building and were designed based on a survey of actual nuclear power plant (NPP) reactor building shear walls in Japan. The effect of the direction of the loading was investigated by selecting different angles of the loading axis with the walls. The details of the test description can be found in Reference [Habasaki, A., et al., 2000].

Figure 2-1 provides the layouts and the overall dimensions of the test specimens. The shear walls consist of a 1500 mm square box, capped with the reinforced concrete top loading slab and a base slab. The slabs have a plan dimension of 2700 mm x 2700 mm. The base slab has a thickness of 500 mm, while the top loading slab is 400 mm thick. Also shown in the figure are the three loading angles equal to 0° , 26.6° , and 45° , respectively; these loading angles were selected to investigate the effect of loading directions on the load resisting characteristics of the RC shear walls.

In all specimens, the reinforcing bars with yield strength equal to 345 kN/mm^2 were deployed for the shear walls in both the vertical and horizontal directions with double-fold in 70 mm pitch, which results in an equivalent 1.2% of reinforcement ratio for both directions. The vertical reinforcing bars were sufficiently extended into the loading slabs to ensure adequate load transfer to the shear walls.

The RC shear walls were poured with the concrete of pea gravel having design strength of 30 Mpa. Concrete strength of each specimen was measured during the test, which is shown in Table 2-1. Note that for shear span ratio equal to 1.0, the tests were performed for the loading angles equal to 0 and 45 degrees, respectively.

Furthermore, the shear span ratios of 0.6, 0.8 1.0 were selected to ensure predominant shear deformations for the specimens and the effect of bending deformation is relatively small, which are demonstrated in Figure 2-2, which shows the plots of different deformation components at the cyclic peak for SD-08 series shear walls.

2.1.2 Multi-Axis Cyclic Loading Test Specimens

The multi-axis cyclic loading tests were designed to investigate the restoring force characteristics of RC shear walls subjected to multi-axis loadings. Past analyses of seismic response of shear

walls subjected to three components seismic motion reveal that the shape of response acceleration orbit typically exhibits a pattern consistent with a combination of a circular or elliptical orbit and a radial orbit. In order to study the effect of these loading orbits on the shear wall restoring force characteristics, four loading patterns were developed for the multi-axis cyclic loading test. They are: a rectangular loading, a cross loading and a diagonal cross loading for three box type specimens and a rectangular loading for a fourth cylindrical specimen. This section provides the design and the layout of the test specimens. Information of other properties such as dimensions, material properties and the details of reinforcing bar layout is also provided, which are extracted from Reference [Hiroshi, T., et al., 2001]. The details of the loading patterns are described in Section 2.2.

Four shear wall test specimens were built for the multi-axis loading tests of different loading patterns. Of these, three were designed as box type walls and one was a cylindrical wall. The overall dimensions of these specimens are shown in Figure 2-3 and Figure 2-4. The box type walls were designated as: SB-B-01 for the rectangular loading test, SB-B-02 for the cross loading test, SB-B-03 for the diagonal cross loading test. The cylindrical type wall is designated as SB-C-01 for the rectangular loading test. Table 2-2 shows the specimen designations and their test parameters.

The overall dimensions of the box type shear wall specimens are the same as those for the one – directional cyclic loading test specimens. For the cylindrical type shear wall specimen, as shown in Figure 2-4, it has a wall diameter of 1910mm, which was determined to have about the same effective shear area (and nearly the same ultimate shear strength) as that of the box type specimens. The shear span ratios of the box type and cylindrical type specimens are: $M/(Qd) = 0.8$ (box type) and $M/(Qd) = 0.63$ (cylindrical type), respectively.

The reinforcement arrangements for the shear wall specimens are shown in Figure 2-5 and Figure 2-6. The reinforcing bars of D6 (6 millimeters in diameter) are deployed in both the vertical and transverse directions with double-fold in 70mm pitch except for the corner part of the box type wall. The anchorage length of the vertical reinforcing bar is 300mm (=50d) at the upper part (within the loading slab) and 500mm at the lower part (within the base slab). Horizontal reinforcing bars placed both inside and outside of each wall are lapped at the joint with length longer than 210mm (=35d). The wall-reinforcement ratio is approximately 1.2% for both types of specimen.

Pea gravel concrete with coarse aggregate (maximum dimension of 10mm) was used for the specimens. Table 2-3 shows the concrete material properties at the time of the tests. As indicated in this table, the concrete strength for the specimens: SB-B-01 and SB-B-02, were about 15% higher than the others, due to the fact that these were fabricated four months earlier than the other specimens. Table 2-4 provides the material properties of the reinforcing bar.

To ensure predominant shear deformations for the specimens, the shear wall deformations were separated into shear, flexural and rotational components, which were plotted in Figure 2-7 for the specimen SB-B-01. This plot confirms the suitability of the fabricated specimens for the purpose of the multi-axis cyclic loading shear wall tests.

2.1.3 Shaking Table Test Specimens

The shaking table tests were designed to study the dynamic response of RC shear walls subjected to repeated strong ground motions. Such tests would provide insights into the characteristics of the load-carrying capacity of RC shear walls in the elasto-plastic and ultimate failure states, and

also provide the necessary response data to validate analytical models for RC shear wall seismic response analyses.

Two box-type shear wall specimens, designated as: DT-B-01 and DT-B-02, and one cylindrical type specimen assigned as DT-C-01, were fabricated for the shaking table tests. The details of the tests can be found in Reference [Torita, H., et al., 2004].

Figure 2-8 shows the overall dimensions of the specimens. As compared to the specimens for the cyclic static tests, the specimens for the shaking table tests consist of four parts: shear walls, a base slab, an upper slab and an extra block weight on the top of the upper slab. Dimensions of the walls of box-type specimens are 1.5 m square x 1.0 m height x 75 mm thickness, while the cylindrical wall is of 1.91 m diameter (measured between the center lines of the wall) x 1.0 m height x 75 mm thickness. Rebar arrangements for the specimens are shown in Figure 2-9. The box-type walls have the rebar layout of two layers with D6@70 in both vertical and horizontal directions, leading to a reinforcement ratio equal to 1.2%. In the corners of the walls, the horizontal reinforcing bars placed both inside and outside of each wall are lapped at the joint as shown in Figure 2-10. In case of the cylindrical-type specimen, the rebar arrangement was made such that the resulting reinforcement ratio of the cylindrical wall is equal to those of box-type specimens.

In order to induce an axial stress of 1.47 Mpa at the bottom of the shear wall specimens, an extra block weight was placed on the top of the top slab. The block weight consists of four pieces of weights, each weighing 15.62 ton. The block weight is attached to the top slab using pre-stressing concrete (PC) rods. Combining the masses of the block weight, the upper slab and the upper half of the walls at a lumped mass point, the total weight is calculated to be 67 ton and the corresponding values of rotational inertia were determined to be: $I_x = I_y = 71.7 \text{ ton}\cdot\text{m}^2$ and $I_z = 112 \text{ ton}\cdot\text{m}^2$.

Pea gravel concrete with coarse aggregate was used for the specimens. The details of the concrete mixes were provided in Table 2-5, which also presents the resulting concrete and rebar material properties at the time of the tests.

2.2 Test Instrumentation and Procedures

Both the cyclic static and shaking table tests were performed at Public Works Research Institute of Japan. Multiple loading cycles were employed for the cyclic tests to gradually increase the load level on the shear wall specimens such that the restoring force characteristics of the RC shear walls can be studied progressively from the elastic to plastic and eventual failure states. With regard to the shaking table tests, three orthogonal seismic inputs were applied to the shear wall specimens on a shaking table. The level of the seismic inputs was increased gradually to study the progressive damage of RC shear wall structures. This section provides a brief description of the loading apparatus and the test procedures employed for these tests.

2.2.1 Cyclic static tests

Two types of cyclic static tests were performed: single axis tests and multi-axis tests. The single axis test specimens were described in Section 2.1.1 while the multi-axis test specimens were discussed in Section 2.1.2. For the single axis tests, the loading apparatus is shown in Figure 2-11. The horizontal loading is applied to the top slab through two loading actuators and a vertical actuator is placed on the top of the top slab to induce the axial load in the shear walls. The horizontal load on the shear walls is controlled by monitoring the force-displacement response of the shear walls to prevent the introduction of the torsional deformation. Multiple loading cycles

were prepared such that specific horizontal target deformation in terms of the shear strain of the wall was reached. Figure 2-12 provides the loading cycles. The dashed lines distinguish between the cycles where specific target deformations are achieved. As reported in Reference 1, six deformation targets in terms of horizontal deformation divided by the height of the wall were defined, which are: 0.5, 1.0, 2.0, 4.0, 6.0 and 8.0×10^3 radian, each repeating twice in both positive and negative directions within one cycle.

Conventional seismic response analysis of shear wall structures assumes that the maximum damage to the shear wall occurs when the horizontal force is applied parallel to the shear wall (corresponding to the zero degree in the horizontal loading angle). To investigate the effect of the horizontal loading angles on the damage of shear walls, tests for three different horizontal loading angles, namely, 0° , 26.6° , and 45° were performed.

With respect to the multi-axis cyclic tests performed using the loading apparatus as shown in Figure 2-13, three different loading patterns were designed to simulate the response orbit of shear wall structures as observed in actual earthquake response records. These loading patterns designated as: rectangular, cross and diagonal cross, are shown in Figure 2-14. A total of seven cycles of incremental loadings were defined as shown in Figure 2-15. The loading patterns are accomplished by controlling the total deformation angles (R_x and R_y) as shown in Figure 2-16. These angles are calculated from the lateral displacements D_x and D_y measured at the bottom of the loading slab by dividing by the height of the shear wall (1000 mm: clear height of wall). Table 2-6 summarizes maximum amplitudes of deformation angles at each loading cycle in both X and Y directions for the three loading patterns. At the peak of each loading cycle, a ratio of R_x/R_y for all loading patterns is maintained at 1/0.8 to control the effect of each directional loading on the damage and/or severe deformation of the specimen. As shown in Figure 2-17 for the shear force orbits between Q_x and Q_y , due to the rectangular loading pattern, the resulting shear orbits due to the deformation controlled rectangular loading procedure produce an approximate rectangular orbit, which would allow for studying the effect of the orthogonal loading not only on the shear wall damage but also on the orthogonal deformation. Similarly, the cross loading patterns produce closely a radial response pattern, allowing for examining the orthogonal loading effect on shear wall damages. The rectangular loading is believed to be one of the most severe two directional loading patterns for RC shear walls. Therefore, the test data generated using the rectangular loading pattern are effective in validating the adequacy of nonlinear RC material models for analyzing RC shear wall response subjected to multidirectional loadings. The diagonal cross loading pattern is considered to be a variation of cross loading. At the peak load point of each loading cycle, the difference of the loading path can be used to compare the test results of diagonal cross loading with those of the rectangular loading.

2.2.2 Shaking Table Tests

The shaking table at the Public Works Research Institute of Japan was used to perform the dynamic loading tests for the shear wall specimens. Three orthogonal uncorrelated artificial input motions were generated, which fit to a smooth target spectrum as shown in Figure 2-18. The generated acceleration time histories with the same intensity as depicted in Figure 2-19 were applied to the base of the shear wall simultaneously in the three orthogonal directions. The intensity level for the synthetic acceleration time histories of the input waves was increased gradually to induce the dynamic loads to the shear walls from the elastic region to various elasto-plastic states and the ultimate failure state of the walls.

Two box-type and one cylindrical-type specimens were tested, and for each, a number of runs were scheduled. Since each run had a specific target response level to be attained, and for this

reason, should the target response level was not achieved for a particular run, an additional excitation is added to the run, which is designated with the same run number primed.

Measurements of the dynamic responses of the shear walls were made in terms of accelerations and displacements at various wall locations, as well as rebar strains. The upper and base slabs are much stiffer than the walls and therefore were assumed to behave as rigid bodies. A sampling period of 400 Hz was used in the data acquisition for the specimen DT-B-01 and Runs #1 and #2 of the specimen DT-B-02, and a sampling period of 1000 Hz was used for the rest of runs. The acquired response data was filtered using a low-pass filter with the frequency characteristics of the filter shown in Figure 2-20. The schematics of the acceleration measurement locations are shown in Figure 2-21 and Figure 2-22. Vertical accelerometers were placed in four corners of both top and base slabs to determine possible rocking motions of the RC shear wall specimens. The locations of the displacement gauges are displayed in Figure 2-23 and Figure 2-24. Strain gauges were also deployed to measure the rebar strains as shown in Figure 2-25 through Figure 2-27.

2.3 Summary of JNES Test Results

This section presents a summary of the JNES cyclic and shaking test results as discussed in References [Habasaki, A., et al., 2000, Hiroshi, T., et al., 2001, Torita, H., et al., 2004]. The cyclic test results are described in terms of uni-directional and multi-directional loading tests and the shaking table tests are presented for box-type and cylindrical-type shear wall specimens subjected to simultaneous application of three orthogonal components of seismic inputs of various intensities.

2.3.1 Cyclic Static Test Results

The cyclic static tests were performed to investigate: 1) the effect of the applied uni-directional loading angles and shear span ratio on the shear strength of the box-type shear walls, and 2) the effect of multi-axis loading on the shear strength of both box-type and cylindrical-type shear walls.

For the uni-directional tests, Figure 2-28 shows the load-deformation hysteresis loops for the SD-08 series with the loading angles equal to 0° , 26.6° , and 45° . The results for all three test series are summarized in Table 2-7. The data presented in this table include the maximum shear and the corresponding deformation (divided by the height of the wall) at different deformation stages in a progressive manner. It also includes the initial stiffness for the specimens. As indicated in the table, shear cracks occur shortly before the bending cracks initiate, and continue until the yielding of rebars develop. The maximum shear strength is observed for the specimens with more slanted loading angles than the situation where the load is parallel to the walls; however, the differences in the shear strengths resulting from the loading angles appear insignificant from a practical standpoint.

Figure 2-29 shows a comparison of envelope curves of the load-deformation hysteresis for the tests. For the test cases with the loading angles equal to 26.6° and 45° , the maximum load and its overall deformation became larger than the cases with the 0° loading angle.

The patterns of cracks on the walls at the onset of failure for the SD-08 series specimens are exhibited in Figure 2-30. In case of loading angle $\theta = 0^\circ$, shear sliding failure occurred around the lower portion of faces C and A when the shear wall deformed in a range of the magnitude $\pm 8 \times 10^{-3}$ radian (divided by the height of the wall). Upon reaching that deformation, the shear strength decreased rapidly. Also, in case of $\theta = 26.6^\circ$, the similar failure can be observed near the

lower portion of face C. In case of $\theta = 45^\circ$, shear sliding failure occurred around the lower portions of faces A and D, and failure developed around the lower portions of faces B and C simultaneously. However, despite this damage, the shear strength of the walls reduced gradually. Similar crack patterns were also documented according to different loading angles for the test specimens having different shear span ratios.

In Reference [Habasaki, A., et al., 2000], comparisons were also made between the test data and the calculated shear wall response using the methodology of restoring force characteristics of RC seismic shear walls as established in the "Technical guidelines for aseismic design of nuclear power plants" by the Japan Electric Association (JEAG)" (hereinafter JEAG model) [JEAG, 1991]. Figure 2-31 shows a comparison of the calculated maximum shear forces using the JEAG recommendation and the test results. Both the test and calculated maximum shear forces are normalized by the maximum shear forces obtained from the tests corresponding to the loading angle: $\theta = 0^\circ$. As shown in the figure, the calculated results agree well with the test results and the maximum shear forces were not much affected by the angle of applied load and the shear span ratio. Both the test and calculated maximum shears are located slightly outside of the arc which represents the vector combination of two orthogonal horizontal loads. In addition, Figure 2-32 provides the comparison of test and calculated hysteresis loops for the shear and bending deformation components. For the shear deformation component, the calculated results agree well with the test results, while for the bending component, the calculated stiffness becomes greater than the test results. However, as depicted in the figure, the effect of bending components is relatively small; the response of the walls is predominantly the shear deformation. Consequently, the calculated and the test restoring force characteristics based on the overall deformations are compared well for the tested RC box-type seismic shear wall subjected to diagonal loading.

With respect to the multi-axis loading tests, Reference [Hiroshi, T., et al., 2001] provides the response results for the three different loading patterns and their effects on the shear strength of the tested shear walls, which are summarized as follows.

For the illustration convenience, the four faces of box-type shear wall specimens are designated as the shear walls A and C, which are parallel to the X-axis, and the other two shear walls are assigned to: B and D, which are parallel to the Y-axis. Similarly, each quarter portion of the cylindrical-type shear wall is also provided with the same designation as the box-type shear wall specimen. Furthermore, the shear forces in the X and Y directions are designated as Q_x and Q_y , respectively. In addition, a vector shear force of Q_v is defined as the square-root-sum-of-squares (SRSS) of the Q_x and Q_y in the X-Y loading plane. Table 2-8 provides the initial stiffness and the shear-deformation pairs at the initiations of bending and shear cracks for the tests. The shear-deformation hysteresis loops resulting from different loading patterns are shown in Figure 2-33 through Figure 2-36. The deformations R_x and R_y shown in the figures follow the notation as depicted in Figure 2-16.

As exhibited in these figures, for the specimen SB-B-01 (box-type wall with the rectangular loading), the maximum shear forces in the X and Y directions were observed to be $Q_x = 1376$ kN ($R_x = 4.01 \times 10^{-3}$) and $Q_y = 1381$ kN ($R_y = 3.19 \times 10^{-3}$), respectively. Upon reaching the maximum vector force of $Q_v = 1600$ kN, which occurred at the time of the maximum shear Q_x , the shear force gradually decreases with the increase of the applied load. During the loading cycle #7, shear slip failures was observed in the face C at $R_x = 11.1 \times 10^{-3}$ and in the face A at $R_x = 14.6 \times 10^{-3}$ together with the rapid reduction in the shear forces. For the specimen SB-B-02 (box-type wall with the cross loading), the maximum shear forces in the X and Y directions were observed to be $Q_x = 1596$ kN ($R_x = 5.76 \times 10^{-3}$) and $Q_y = -13251$ kN ($R_y = -3.23 \times 10^{-3}$), respectively. The maximum vector force Q_v is identical to Q_x due to the nature of the cross loading. This specimen failed also

during the loading cycle #7 in the face C at $R_x = -9.14 \times 10^{-3}$. After the Q_v was reached, rapid shear force decrement occurred.

For the specimen SB-B-03 (box-type wall with the diagonal cross loading), the maximum shear forces in the X and Y directions from the test were equal to $Q_x = 1261$ kN ($R_x = 4.00 \times 10^{-3}$) and $Q_y = -1034$ kN ($R_y = -4.64 \times 10^{-3}$), respectively. The maximum vector shear force was calculated to be $Q_v = 1588$ kN. During the loading cycle #7, the shear forces began to decrease at the total deformation $R_x = 10.89 \times 10^{-3}$ was reached, and the shear crack began to open widely in the face C. The shear forces decreased rapidly after the occurrence of the shear slip failure in the face B at $R_x = 16.36 \times 10^{-3}$ and $R_y = 13.14 \times 10^{-3}$.

For the cylindrical-type specimen SB-C-01 (cylinder-type wall for rectangular loading), the maximum shear forces in the X and Y directions were observed to be $Q_x = 1223$ kN ($R_x = 11.91 \times 10^{-3}$) and $Q_y = 1189$ kN ($R_y = 3.15 \times 10^{-3}$), respectively. During the loading cycle #7, the shear failure occurred in the face C at $R_x = 12.91 \times 10^{-3}$, and the shear slip failure occurred in the face A in the middle height of the wall at $R_x = 17.39 \times 10^{-3}$. Subsequent to the shear failure, rapid shear force decrease occurred.

When the envelope curves are superimposed on the hysteresis loops as shown in Figure 2-33 through Figure 2-36, the restoring force characteristics for different loading patterns are established. Figure 2-37 shows the resulting restoring force characteristics curves for different loading patterns in both X and Y directions. These force characteristics curves reflect the fact that there is a 15% difference in the concrete compression strength among the specimens. As indicated in this figure, the envelope curve for the diagonal cross loading is similar to that of rectangular loading, which implies that a loading path (process) of the multi-axis loads applied to shear walls does not affect the restoring force characteristics. Further, it is noted that the envelope curve for the cross loading case, which does not have an orthogonal loading component, became larger than the envelope curves for other loading patterns.

Figure 2-38 shows the final crack pattern of each specimen by unfolding all four faces A through D. As indicated in this figure, under multi-axis loadings, each wall alternatively acts either as web or flange depending on the changes of dominant loading axis. Therefore, the horizontal (bending) and shear cracks appeared together in all faces of specimens. For the test results of the box-type specimens, major differences in the crack patterns appear to be in horizontal cracks (bending crack). In the crack pattern for the specimen SB-B-02 of the cross loading, horizontal cracks distributed to all parts of wall faces B and D, while for the rectangular loading and the diagonal cross loading, web wall resists to the shear force and the flange wall resists the axial force in the wall. For the reason stated, the combined effect of the positive and negative diagonal shear cracks forms an edge of a saw. Therefore, the combined cracks became dominant instead of horizontal bending cracks under the rectangular and the diagonal cross loading patterns.

2.3.2 Shaking Table Test Results

The shaking table test results were presented in Reference [Torita, H., et al.], which is summarized in this subsection. Before commencing each run, the natural frequencies of the specimens were measured to establish the effect of progressive damages on the frequency characteristics of the shear walls. The measured natural frequencies for the test specimens are tabulated in Table 2-9. This table shows that, as the excitation level increases, the shear wall frequencies are reduced rapidly, indicating the effect of increasing ground shaking levels on the stiffness characteristics of shear wall structures.

The peak responses of the two box-type and one cylindrical-type shear wall specimens are summarized in Table 2-10 through Table 2-12. The notations used in these tables are provided in Figure 2-39. The specimen DT-B-01 failed at the end of Run #6. The recorded peak shears Q_x and Q_y are equal to 1309 kN in Run #5 and 1496 kN in Run #6, respectively. For the specimen DT-B-02, the pre-test analysis predicted that the specimen would fail during Run #6. However, the failure of the specimen actually occurred shortly after Run #7 commenced; the peak responses recorded for Run #7 may not reflect actual condition of the shear wall. Therefore, Run #6 is used for determining the peak responses of the Specimen DT-B-02. According to Table 2-11, the recorded peak shears Q_x and Q_y are equal to 1165 kN 1296 kN, both occurring in Run #6. For the cylindrical-type shear wall specimen, the recorded peak shears Q_x and Q_y are equal to 1235 kN 1296 kN, also occurring in Run #6.

The shear wall response time histories were also provided. Figure 2-40 presents the horizontal acceleration response of the upper slab of the box-type specimen DT-B-02 in the X-direction for Runs #1, #5 and #6. Figure 2-41 shows the acceleration responses of the upper slab of DT-B-02 in two horizontal directions and the vertical direction for Run #3. Similarly, for the cylindrical-type specimen DT-C-01, the horizontal acceleration responses of the upper slab in the x-direction are presented in Figure 2-42 for Runs #4, #5 and #6, while the acceleration responses of the upper slab in two horizontal directions and the vertical direction are depicted in Figure 2-43.

Figure 2-44 through Figure 2-50 present various hysteresis loops from the shaking table test results. These hysteresis loops are expressed in terms of the response orbits (accelerations and displacements) in the horizontal and vertical planes, and acceleration vs. displacement relationships for selected Runs. The response orbits from the shaking tests confirm the assumption used in the multi-axis tests that the response orbits can be approximately represented by a combination of a circular or elliptical orbit and a radial orbit.

As the shaking table base excitation level advanced, the progressive development of cracks in the shear wall specimen DT-B-02 was recorded and the developed crack patterns are shown in Figure 2-51. As shown in the figure, the bending cracks were observed at the foot of the walls after Run #1. The initial shear cracks were found at the mid portion of the wall after Run #2, which initiation of shear crack was predicted by the pretest analysis. The number of cracks in the wall gradually increases after Run #2. In the final run, the concrete at the foot of the walls was completely spalled. For the cylindrical-type shear wall specimen DT-C-01, Figure 2-52 shows the progressive development of crack patterns. Due to the four safety protection steel columns installed in close proximity to the cylindrical wall, observation of the crack development at 0° , 90° , $\pm 180^\circ$, and -90° was technically difficult. Nevertheless, the initial bending cracks were identified after Run #2' and the first shear cracks were found after Run #3. Although the crack patterns at the failure appear similar to those of DT-B-02, most of shear cracks at the mid-height of the cylindrical wall were initiated well before the failure of the specimen.

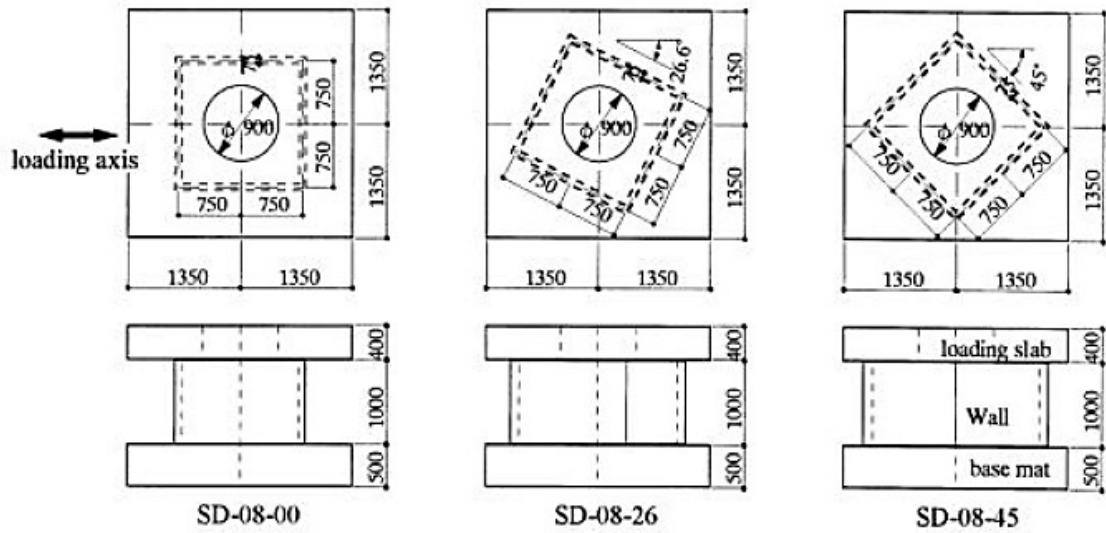


Figure 2-1 Uni-Directional Cyclic Test specimens (SD-08 Series)

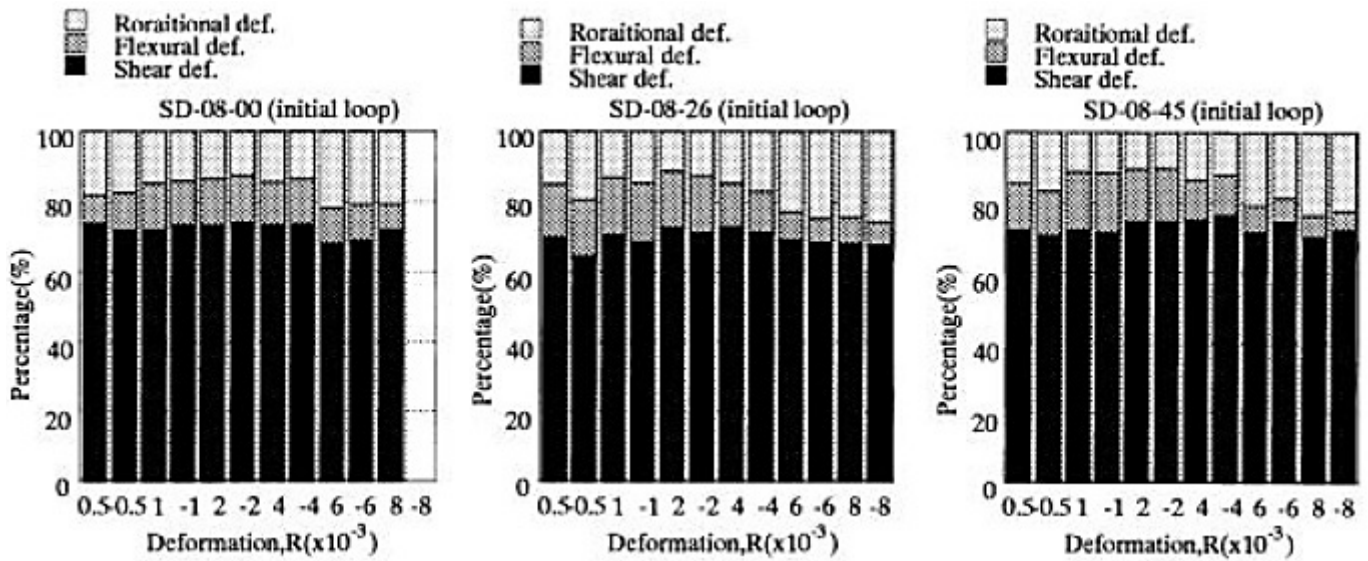


Figure 2-2 Proportions of Different Deformation Components at Cycle Peaks

Table 2-1 Material Properties and Configurations of Test Specimens

Specimens code	Shear span ratio M/QD	Loading angle $\theta (^{\circ})$	Concrete strength (MPa)
SD-06-00	0.6	0	30.7
SD-06-26		26.6	29.2
SD-06-45		45	33.2
SD-08-00	0.8	0	34.9
SD-08-26		26.6	34.8
SD-08-45		45	37.4
SD-10-00	1.0	0	37.8
SD-10-45		45	37.2

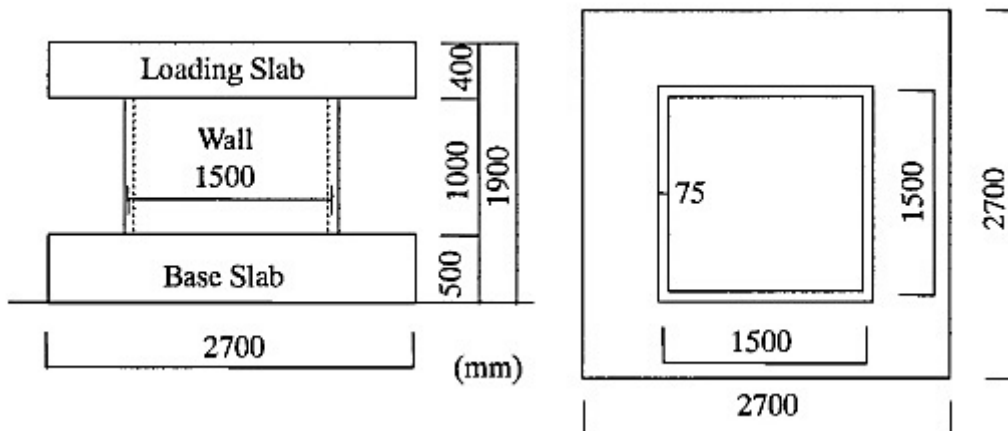


Figure 2-3 Box-Type Shear Wall Specimen for Multi-axis Cyclic Tests

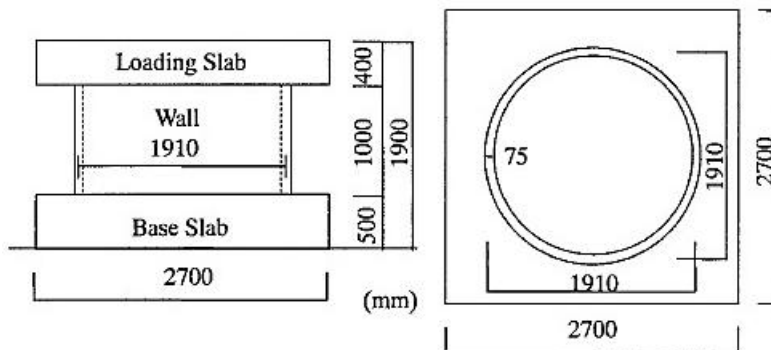


Figure 2-4 Cylindrical-Type Shear Wall Specimen for Multi-Axis Cyclic Tests

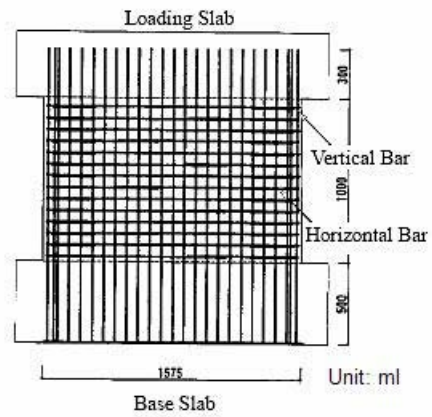


Figure 2-5 Reinforcement Arrangement for Box-Type Shear Wall Specimen

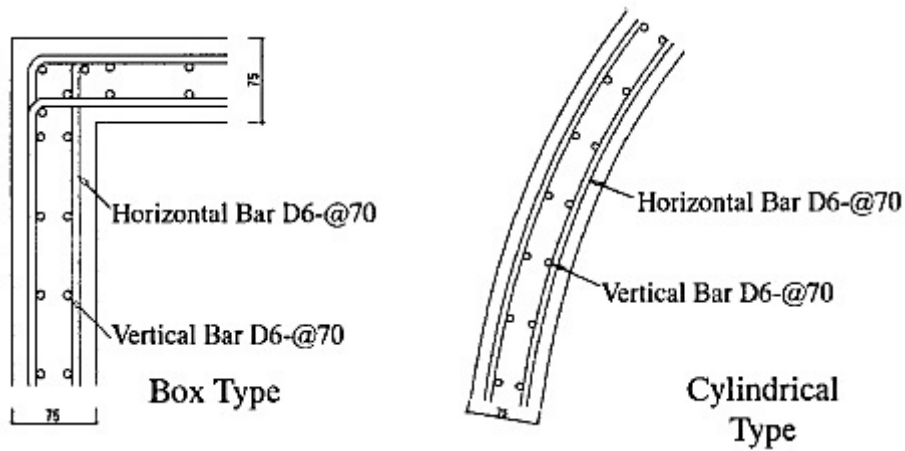


Figure 2-6 Reinforcement Details for both Box- and Cylindrical-type Walls

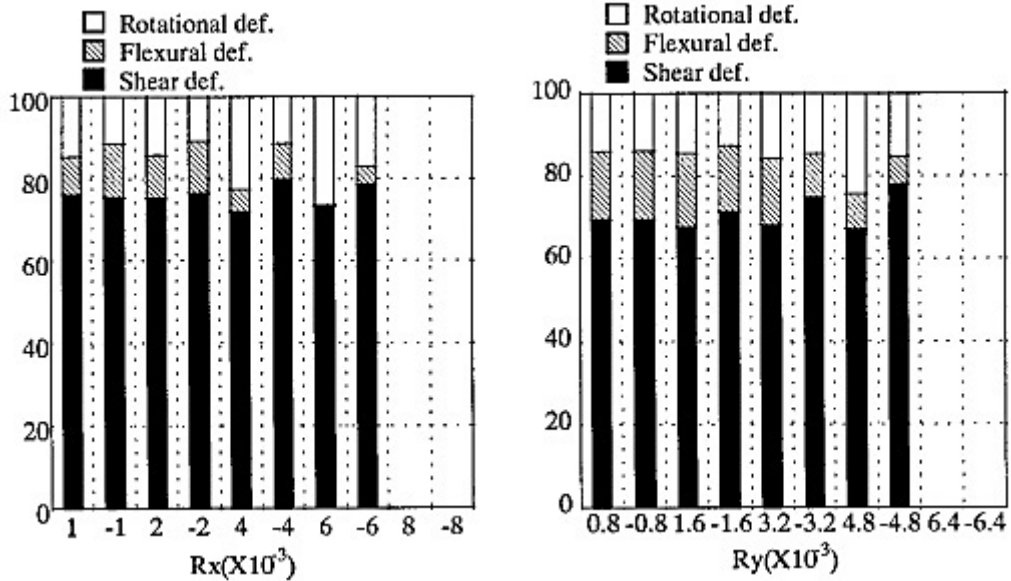


Figure 2-7 Proportions of Deformation Components for Specimen SB-B-01

Table 2-2 Designations of Test specimens and Parameters

Specimen	Wall Shape	M/Qd	Loading Pattern
SB-B-01	Box Type	0.80	Rectangular Loading
SB-B-02			Cross Loading
SB-B-03			Diagonal Cross Loading
SB-C-01	Cylindrical Type	0.63	Rectangular Loading

Table 2-3 Concrete Properties of Specimens at Times of Tests

Item	Unit	Specimen			
		SB-B-01	SB-B-02	SB-B-03	SB-C-01
Young's modulus : E_c	Gpa	30.7	30.7	32.0	31.9
Compressive strength : σ_b	Mpa	41.3	39.7	34.9	34.3
Peak Strain : ϵ_c	μ	2060	2022	1817	1896
Poisson's Ratio: ν		0.18	0.17	0.19	0.20
Tensile Strength ^{*1} : F_t	Mpa	1.74	1.70	1.56	1.54

*1: Calculated Using Eq. $F_t = 0.73 \cdot 0.20 \cdot \sigma_b^{2/3}$

Table 2-4 Rebar Material Properties at Times of Tests

Item	Unit	D6 (at Wall)
Yield Strength : σ_y	Mpa	375
Young's Modulus : E_s	Gpa	200
Tensile Strength : F_b	Mpa	493
Tensile Strain at Flucture	%	28

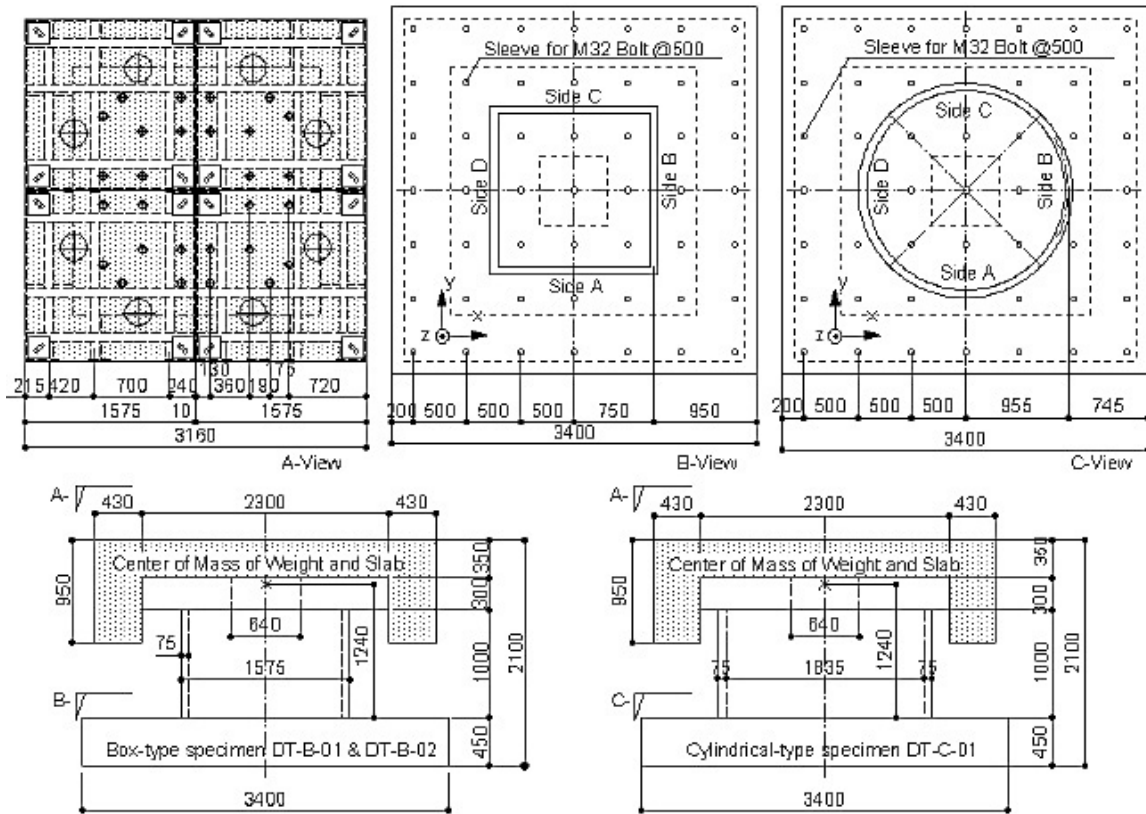
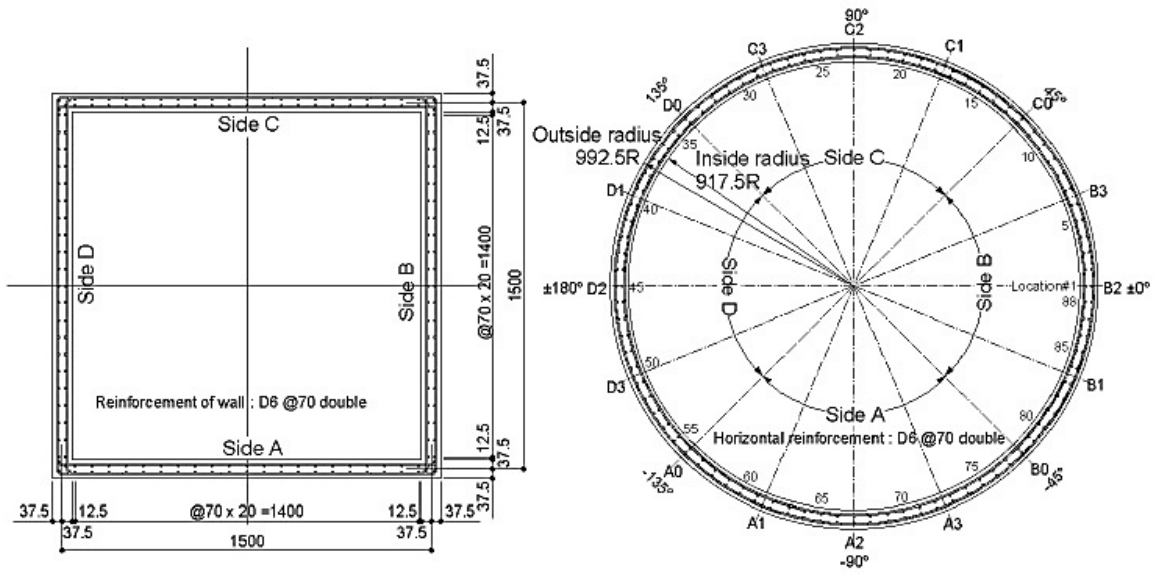


Figure 2-8 Dimensions of Shaking Table Test Specimens in mm unit



(a) Box-type DT-B-01 and DT-B-02 specimen (b) Cylindrical type DT-C-01 specimen

Figure 2-9 Rebar Arrangements and Details of Test Specimens

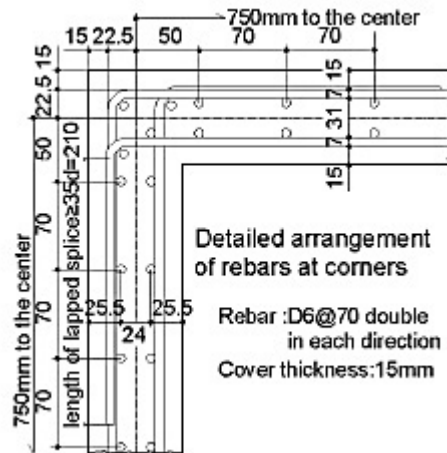


Figure 2-10 Rebar Details at Corners of Box-Type Specimens

Table 2-5 Material Properties of Test Specimens

Mix proportion of concrete	DT-B-01	DT-B-02	DT-C-01	Rebar(SD345, D6) property	DT-B-01	DT-B-02	DT-C-01
Water cement ratio (%)	65.0	67.0	62.0	Yield point f_y (MPa)	381	380	378
Sand aggregate ratio (%)	52.0	54.0	52.5	Tensile strength f_u (MPa)	499	502	501
Unit water content (kg/m ³)	178	180	172	Elongation (%)	29.1	27.4	29.8
Cement (kg/m ³)	274	269	277	Young's modulus E_s (GPa)	171	180	185
Sand (kg/m ³)	951	969	938				
Pea grabbel (kg/m ³)	840	822	848				
Pozolis#70 (kg/m ³)	0.685	0.673	2.77				

Concrete property	DT-B-01	DT-B-02	DT-C-01
Comp. strength σ_B (MPa)	38.6	34.4	37.5
Comp. strain ϵ_c at σ_B (μ)	-2033	-2207	-1928
Young's modulus E_c (GPa)	29.3	26.6	30.7
Poisson's ratio ν_c	0.20	0.19	0.16
Split tensile strength (MPa)	2.63	2.88	3.00
σ_B of upper slab (MPa)	46.8	40.5	46.7
σ_B of base slab (MPa)	39.7	43.6	48.3

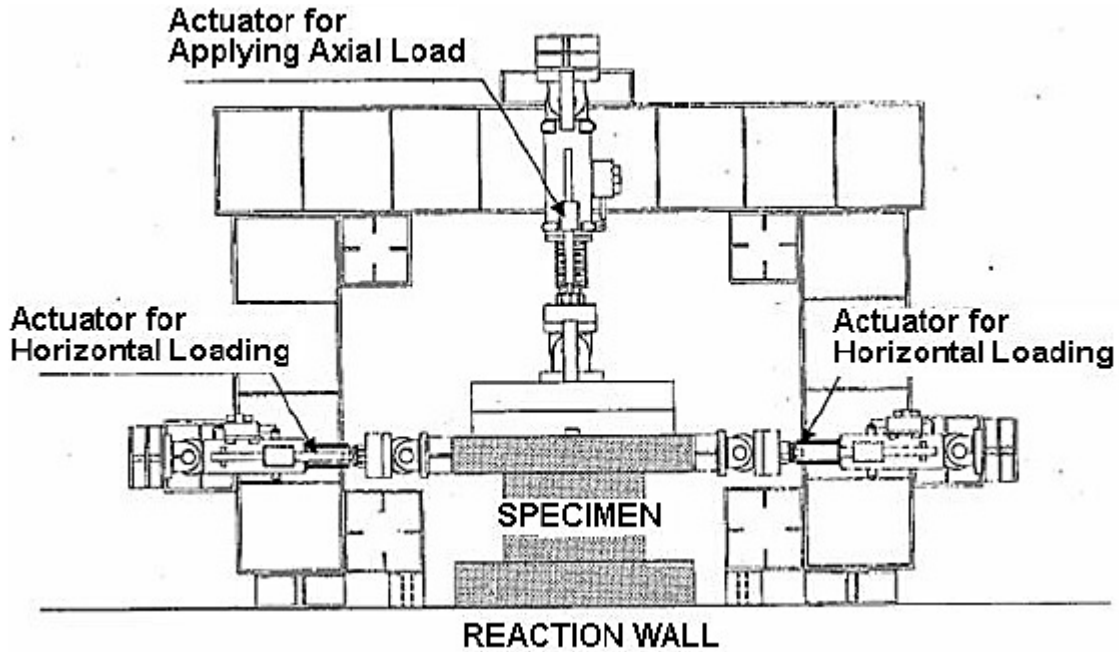


Figure 2-11 Loading Apparatus Schematics for Uni-Directional Cyclic Tests

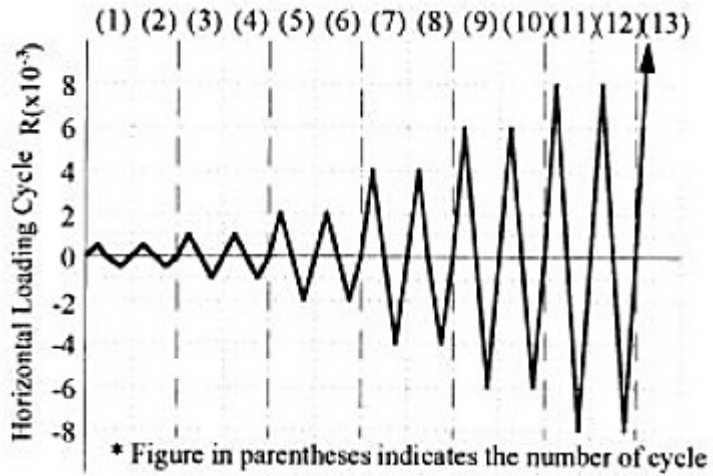


Figure 2-12 Loading Cycle Schematics for Uni-Directional Cyclic Tests

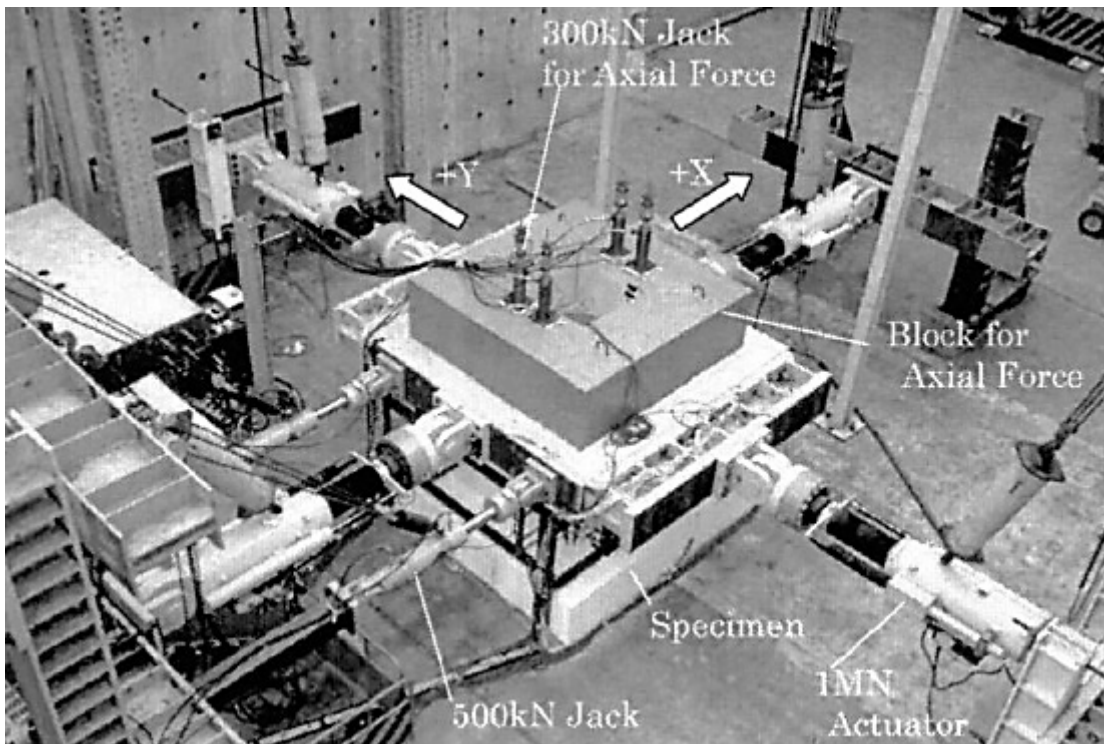


Figure 2-13 Loading Apparatus schematics for Multi-axis Cyclic Tests

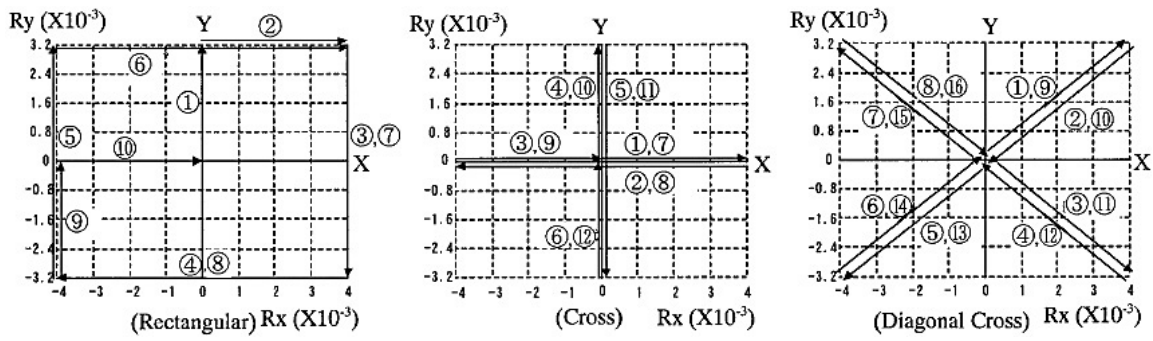


Figure 2-14 Loading Patterns for Multi-axis Cyclic Tests

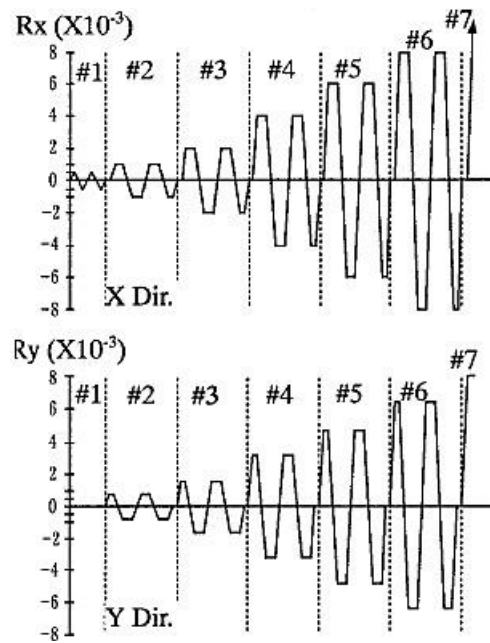


Figure 2-15 Loading Cycle Schematics for Multi-axis Cyclic Tests

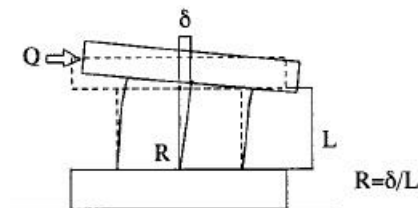


Figure 2-16 Shear Force and Deformation Schematics for Multi-axis Cyclic Tests

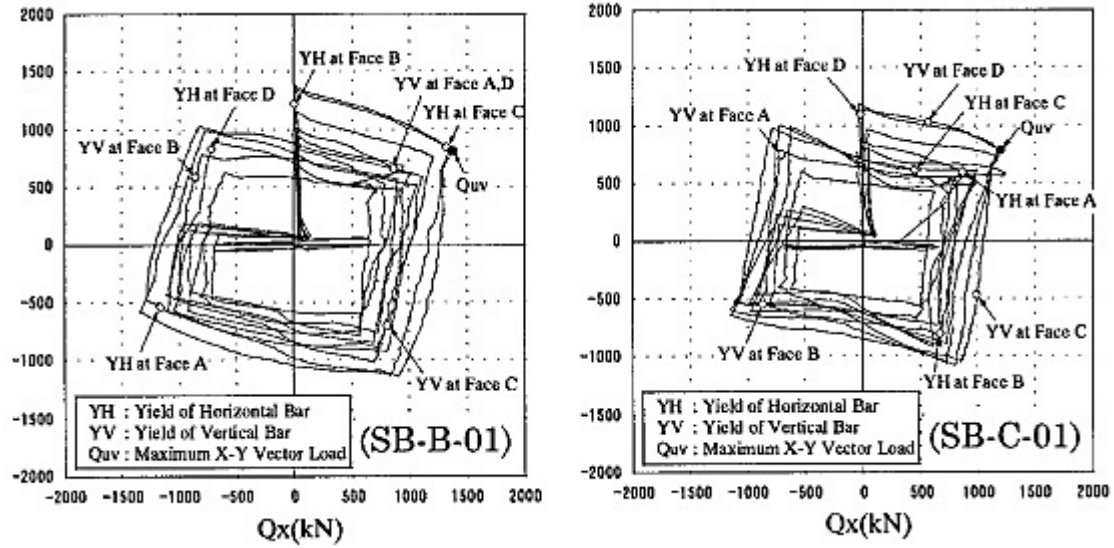


Figure 2-17 Computed Shear Force Orbits for Multi-Axis Tests

Table 2-6 Maximum Deformation Amplitudes for Multi-Axis Tests

Loading Pattern	Direction	Loading Cycle						
		#1	#2	#3	#4	#5	#6	#7
Rectangular Loading	Rx ($\times 10^{-3}$)	± 0.5	± 1.0	± 2.0	± 4.0	± 6.0	± 8.0	+Push Over
	Ry ($\times 10^{-3}$)	0.	± 0.8	± 1.6	± 3.2	± 4.2	± 6.4	+8.0
Cross Loading	Rx ($\times 10^{-3}$)	Ditto to Rectangular Loading						± 10.0
	Ry ($\times 10^{-3}$)	Ditto to Rectangular Loading						(+Push Over) ^{*1}
Diagonal Cross Loading	Rx ($\times 10^{-3}$)	Ditto to Rectangular Loading						+Push Over (1.0)
	Ry ($\times 10^{-3}$)	Ditto to Rectangular Loading						+Push Over (0.8)

*1:Not Executed

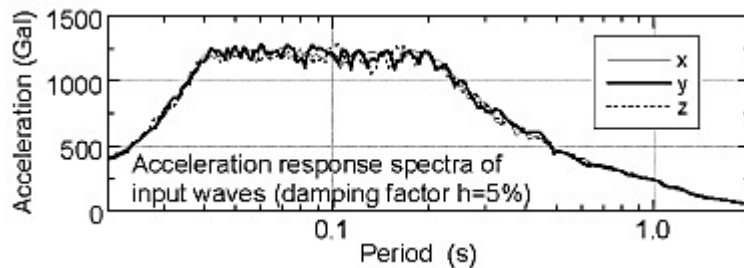


Figure 2-18 Response Spectra for Input Motions to Shaking Table

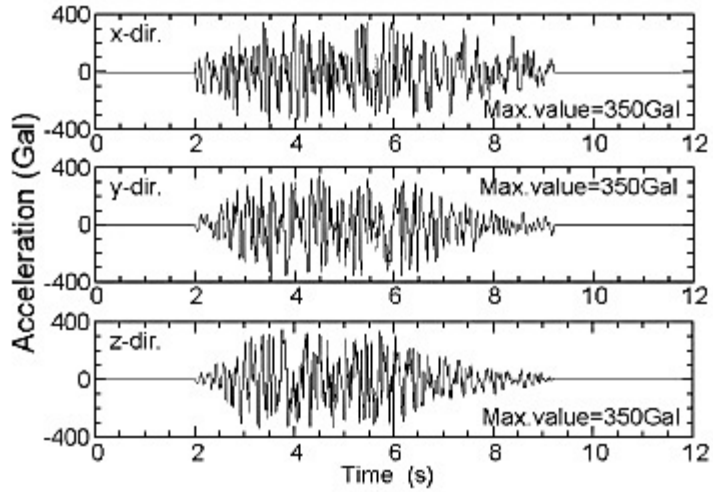


Figure 2-19 Input Motion Acceleration Time Histories to Shaking Table

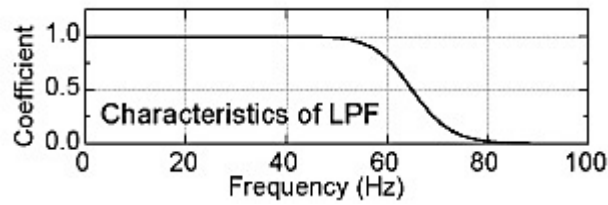
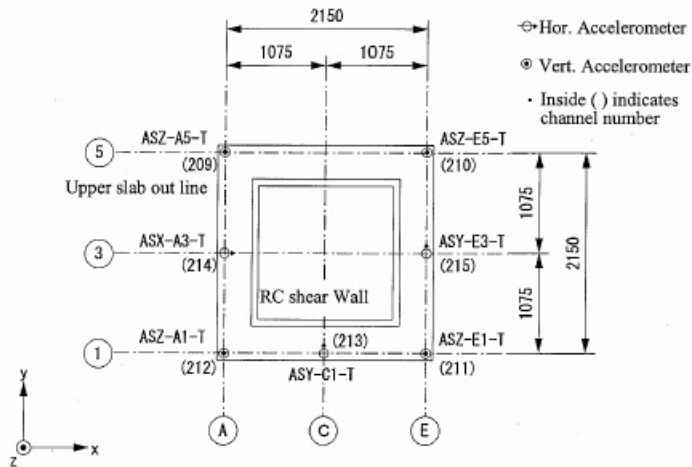
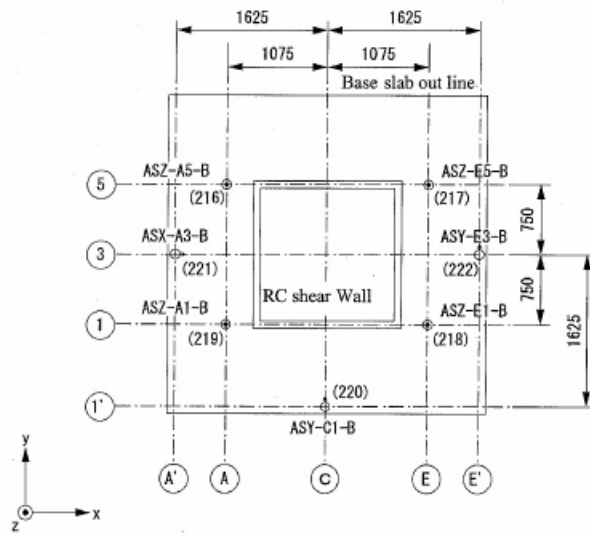


Figure 2-20 Low-Pass High Cut Filter Applied to Recorded Response Data



Positions of Acceleration Measurement at Upper Slab Top



Positions of Acceleration Measurement at Base Slab Top

Figure 2-21 Schematic Locations of Accelerometers on Top and Base Slabs

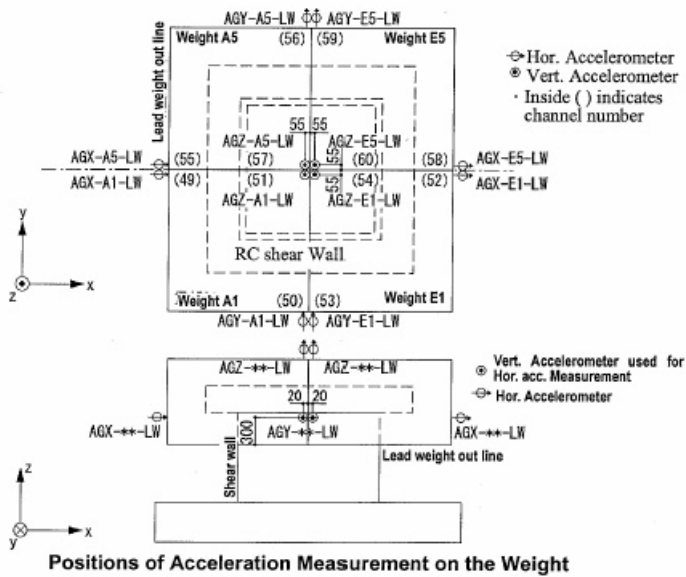
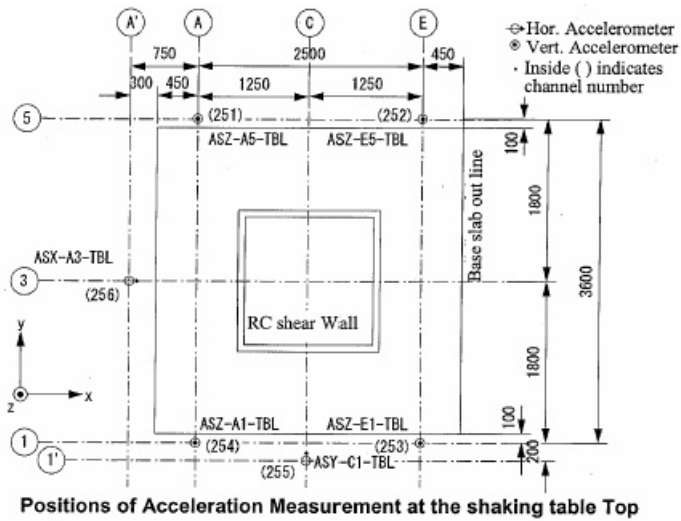
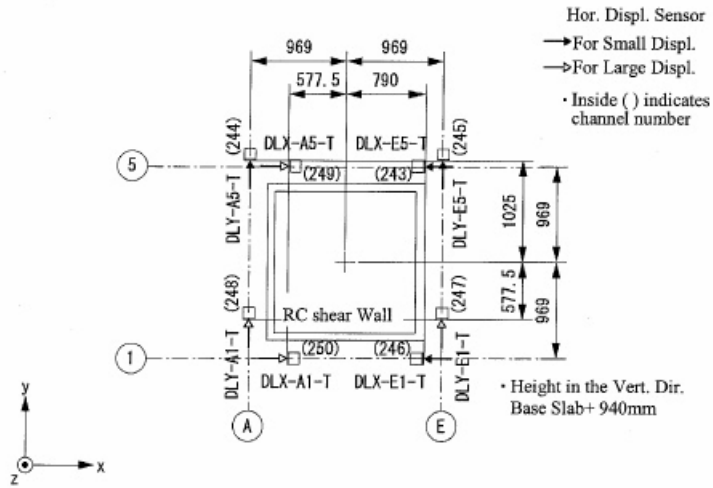
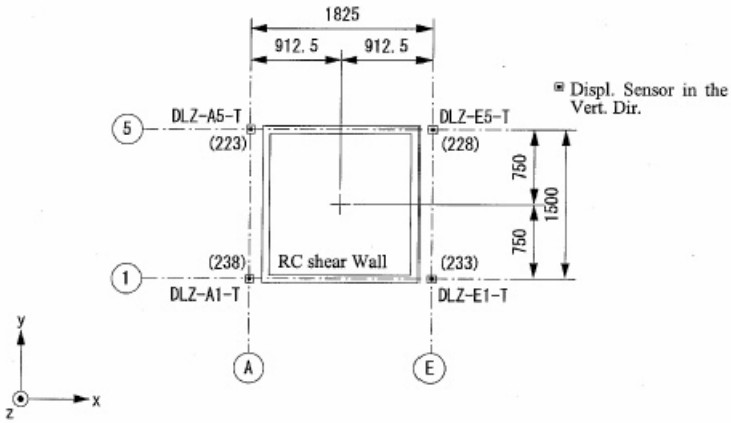


Figure 2-22 Schematic Locations of Accelerometers on Table Top and Top Weight

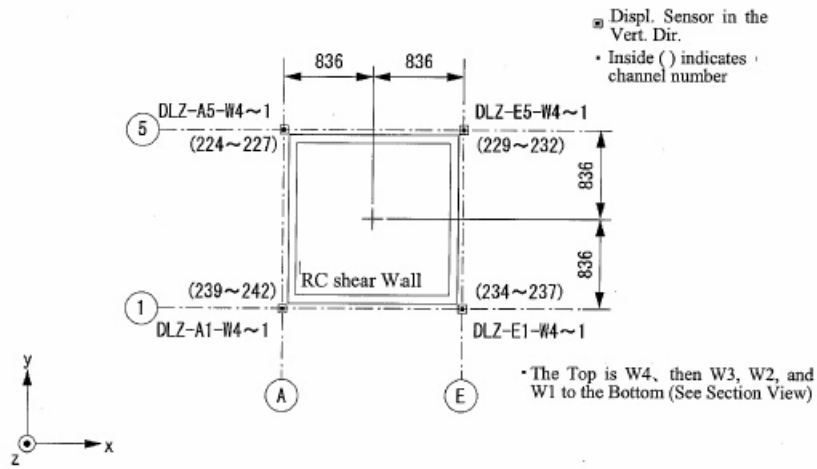


Positions of Hor. Displ. Measurement at the Shear Wall Top

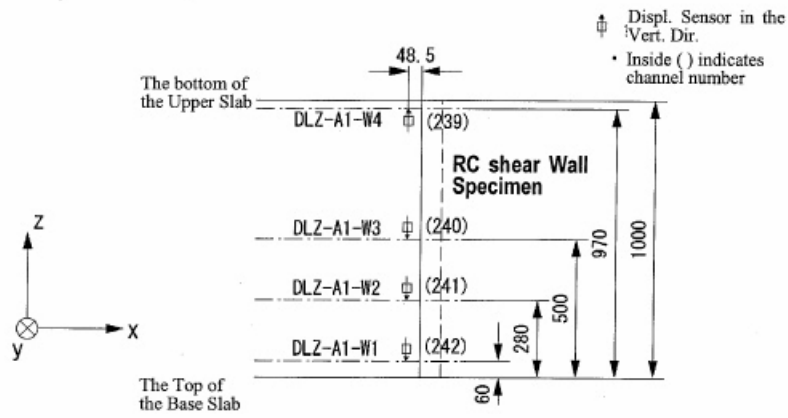


Positions of Vert. Displ. Measurement at the Shear Wall Top

Figure 2-23 Schematic Locations of Displacement Gauges on Top of Walls



Positions of Vert. Displ. Measurement at the Middle Part of the Shear Wall (Plan)



Positions of Vert. Displ. Measurement at the Middle Part of the Shear Wall (Plan, Example of A1 Part)

Figure 2-24 Schematic Locations of Displacement Gauges on Mid-Height of Walls

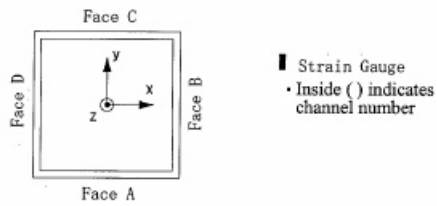
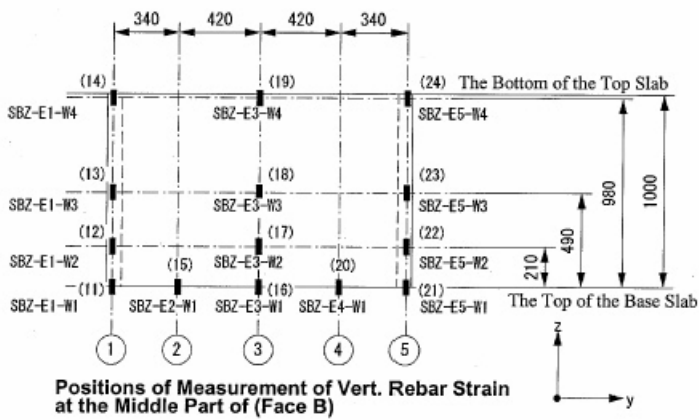
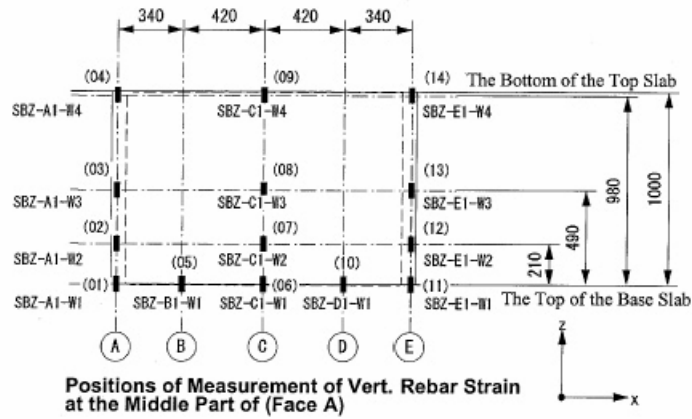


Figure 2-25 Schematic Locations of Strain Gauges of Vertical Rebars of Walls (A & B)

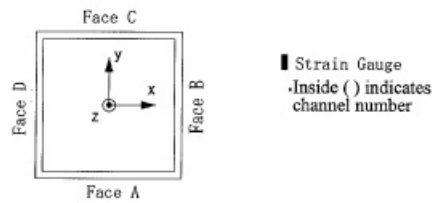
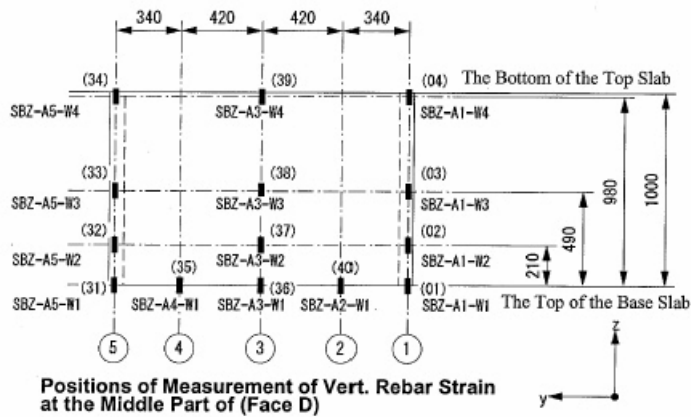
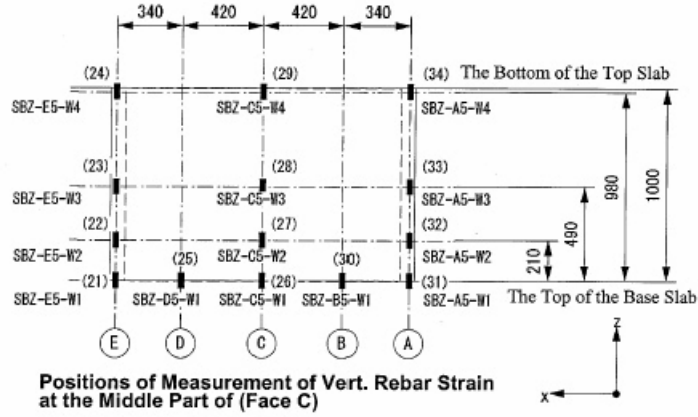


Figure 2-26 Schematic Locations of Strain Gauges of Vertical Rebars of Walls (C & D)

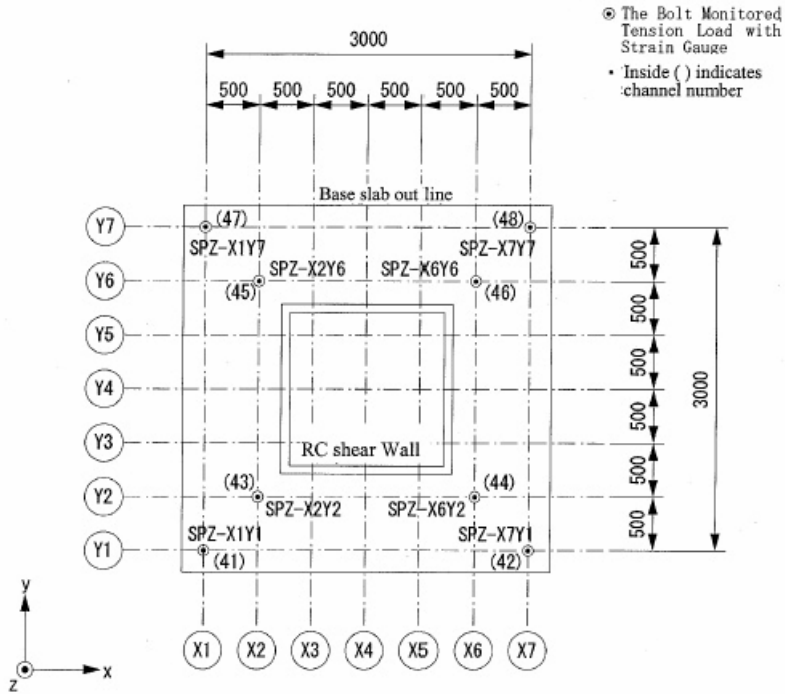


Figure 2-27 Schematic Locations of Strain Gauges of Bolts Fastening Slab to Table

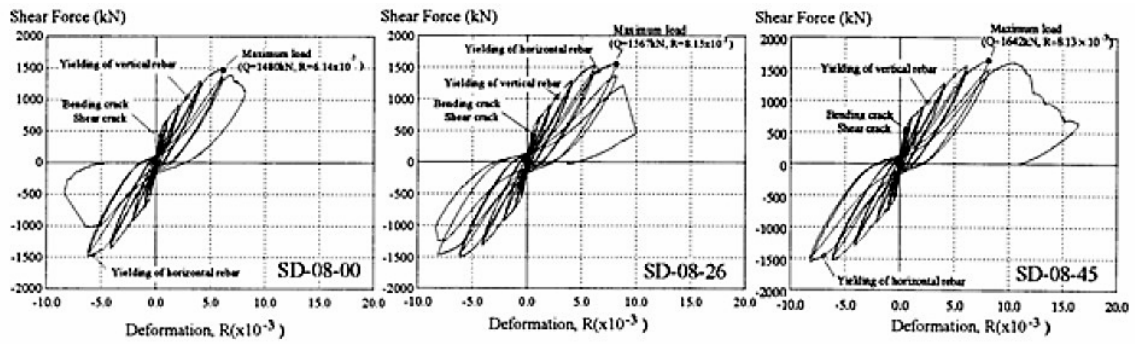


Figure 2-28 Hysteresis Loops for SD-08 Series Specimens Subjected to Uni-Directional Cyclic loading

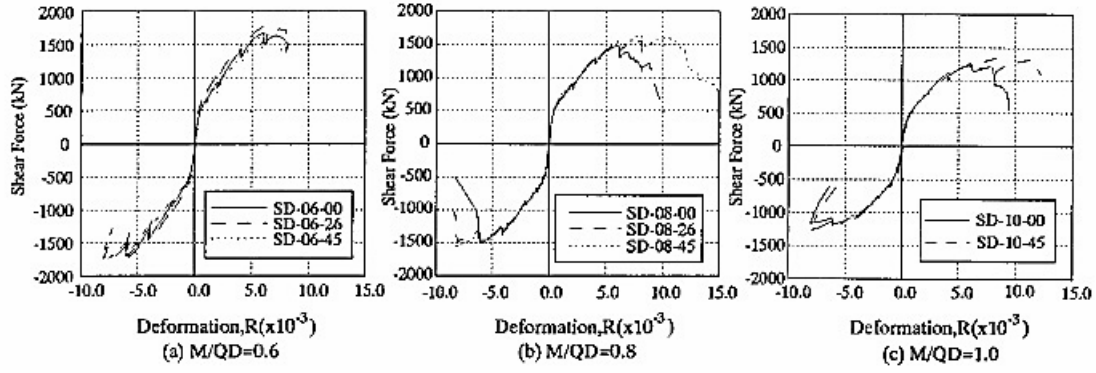


Figure 2-29 Envelopes of Hysteresis Loops for SD-08 Series Specimens Subjected to Uni-Directional Cyclic loading

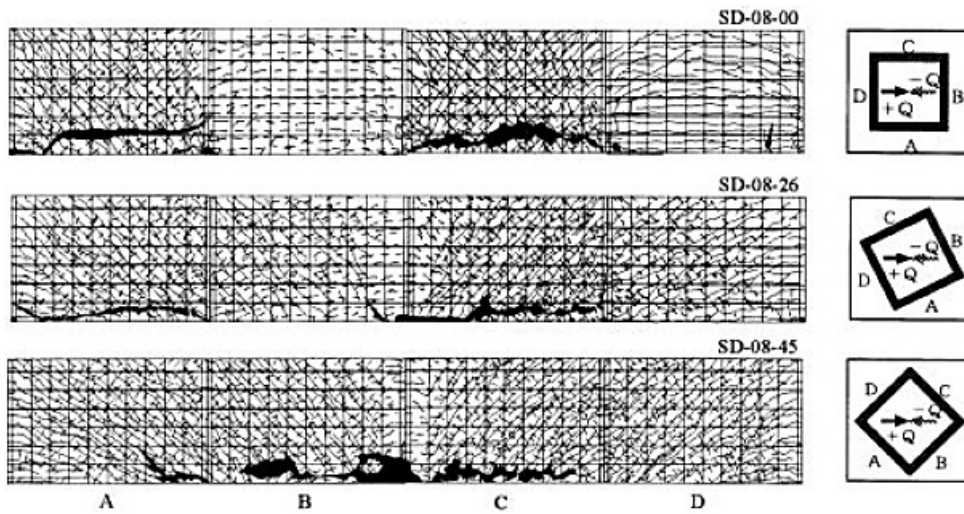


Figure 2-30 Crack Patterns of Shear Walls for SD-08 Series Specimens at Onset of Failure

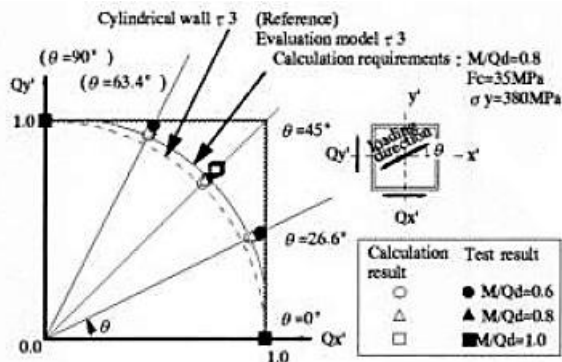


Figure 2-31 Comparison of JEAG Calculations of Shear Forces with Test Data

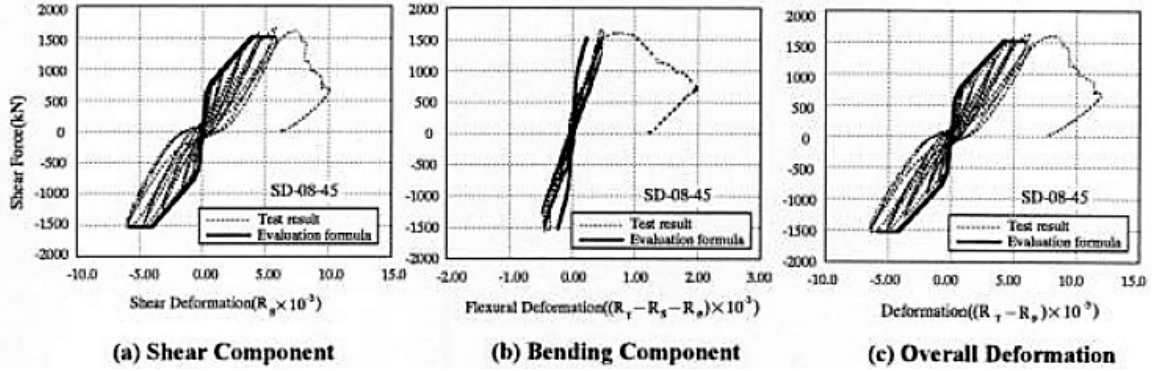


Figure 2-32 Comparison of JEAG Calculations of Hysteresis Loops with Test Data

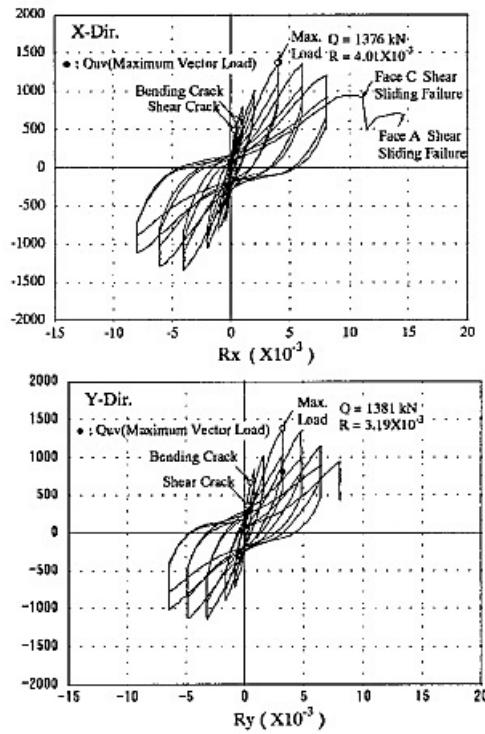


Figure 2-33 Shear-Deformation Hysteresis Loops for Specimen SB-B-01 (Rectangular Loading)

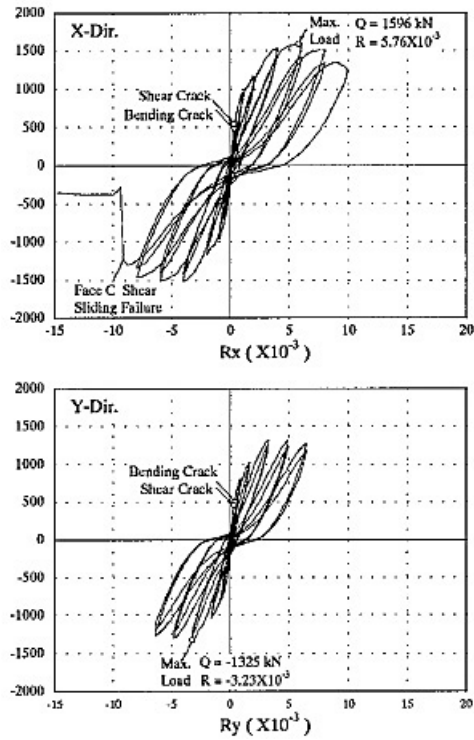


Figure 2-34 Shear-Deformation Hysteresis Loops for Specimen SB-B-02 (Cross Loading)

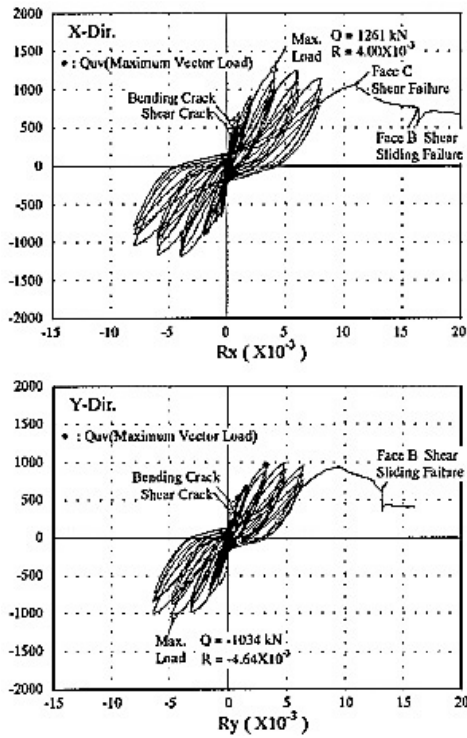


Figure 2-35 Shear-Deformation Hysteresis Loops for Specimen SB-B-03 (Diagonal Cross Loading)

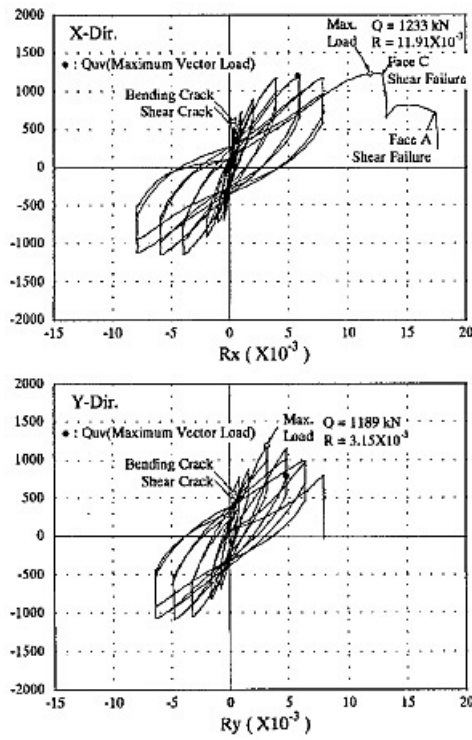


Figure 2-36 Shear-Deformation Hysteresis Loops for Specimen SB-C-01 (Rectangular Loading)

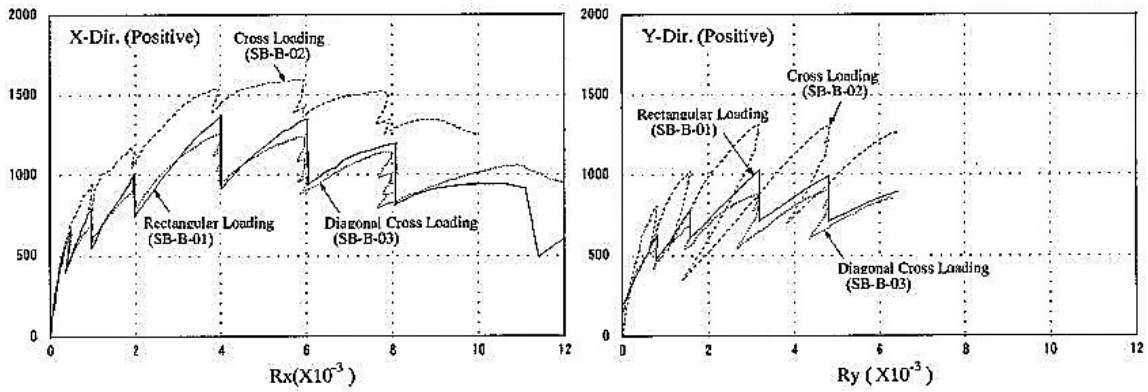


Figure 2-37 Comparisons of Shear-Deformation Envelope Curves for Different Loading Patterns

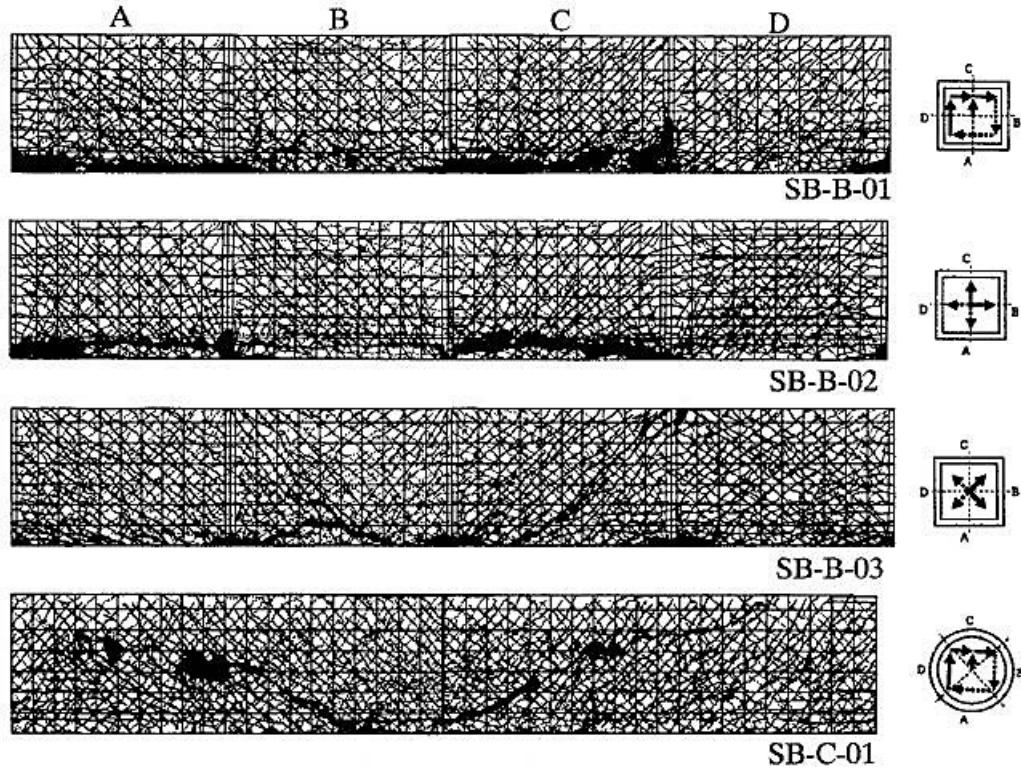


Figure 2-38 Crack Patterns of Shear Walls at Onset of Failure for Specimens Subjected to Different Loading Patterns

Table 2-7 Test Results for Specimens Subjected to Uni-Directional Loading

Specimens	Initial stiffness	Bending crack		Shear crack		Yield of vertical rebar		Yield of horizontal rebar		Maximum load	
	K0 (MN/mm)	Q (KN)	R ($\times 10^{-3}$)	Q (KN)	R ($\times 10^{-3}$)	Q (KN)	R ($\times 10^{-3}$)	Q (KN)	R ($\times 10^{-3}$)	Q (KN)	R ($\times 10^{-3}$)
SD-06-00	2.01	517	0.53	442	0.40	1376	3.81	1527	8.11	1686	6.11
SD-06-26	1.80	330	0.20	488	0.33	1206	2.68	1701	6.97	1794	6.31
SD-06-45	1.91	399	0.34	399	0.34	1213	3.48	1659	11.25	1835	10.81
SD-08-00	1.50	437	0.36	437	0.36	1044	2.84	-1461	-5.65	1480	6.14
SD-08-26	1.48	448	0.43	448	0.43	1036	2.72	1448	6.53	1567	8.15
SD-08-45	1.61	560	0.51	532	0.50	985	2.55	-1454	-6.90	1642	8.13
SD-10-00	0.95	389	0.44	299	0.30	932	2.82	1141	6.27	1231	6.00
SD-10-45	1.17	349	0.33	407	0.42	811	2.34	1305	7.41	1334	8.01

Table 2-8 Test Results of Initiation of Cracks for Multi-Axis Cyclic Test Specimens

Specimen			SB-B-01		SB-B-02		SB-B-03		SB-C-01		
			X	Y	X	Y	X	Y	X	Y	
Initial Stiffness			(MN/mm)	2.14	1.88	2.14	1.62	2.32	-	2.63	1.95
Bending Crack	X-Dir.	Qx	(kN)	631	-3	496	-40	563	26	603	-38
		Rx	($\times 10^{-3}$)	0.44	-0.01	0.27	-0.02	0.39	0.00	0.37	-0.01
	Y-Dir.	Qy	(kN)	31	672	20	504	480	445	-30	472
		Ry	($\times 10^{-3}$)	-0.01	0.51	0.00	0.36	0.48	0.39	-0.02	0.26
Shear Crack	X-Dir.	Qx	(kN)	497	-14	542	-38	463	31	546	-34
		Rx	($\times 10^{-3}$)	0.30	-0.01	0.31	-0.03	0.28	0.00	0.27	-0.01
	Y-Dir.	Qy	(kN)	28	367	20	461	333	360	-41	570
		Ry	($\times 10^{-3}$)	-0.02	0.22	0.00	0.31	0.29	0.23	-0.02	0.36

Table 2-9 Frequencies of Specimens at Each Runs

DT-B-01	x-dir.	y-dir.	z-dir.	DT-B-02	x-dir.	y-dir.	z-dir.	DT-C-01	x-dir.	y-dir.	z-dir.
Run-0	22.5	22.5	46.8	Run-1	20.6	20.4	42.8	Run-1	24.1	24.1	47.1
Run-1	15.2	14.4	36.4	Run-2	20.3	22.3	44.5	Run-2	23.7	23.6	45.5
Run-2	16.2	15.1	34.6	Run-2'	15.4	13.8	39.2	Run-2'	23.4	23.2	45.1
Run-3	13.1	14.2	33.4	Run-3	15.2	13.6	39.6	Run-3	22.9	21.9	44.4
Run-3'	11.5	13.1	33.0	Run-3'	14.8	13.4	39.5	Run-4	21.5	20.4	42.3
Run-4	12.0	12.5	30.6	Run-4	14.5	13.0	39.5	Run-5	21.0	20.2	42.5
Run-5	12.5	11.8	33.8	Run-5	14.3	12.2	38.1	Run-5'	18.7	18.1	39.7
Run-6	8.8	7.2	29.9	Run-6	13.0	11.5	37.9	Run-6	9.2	9.5	34.5
f ₁ before each Run (Hz)				Run-7	7.3	6.4	32.4	Run-7	7.6	7.5	33.0

Table 2-10 Peak Responses for Specimen DT-B-01

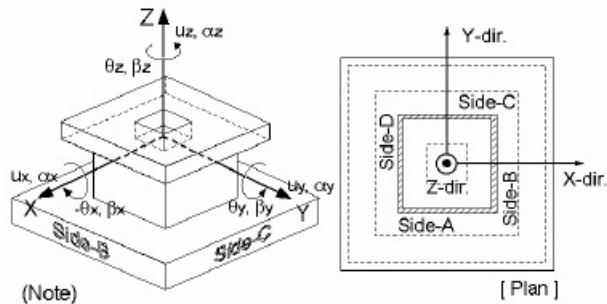
DT-B-01	Run-0	Run-1	Run-2	Run-3	Run-3'	Run-4	Run-5	Run-6
Oxbase [Gal]	-1512	-165	384	460	-735	-1162	-1617	-1678
Oybase [Gal]	-554	-148	-514	751	-910	-1186	-1570	-1754
Ozbase [Gal]	1537	-105	321	515	721	996	-985	635
Bxbase [rad/s ²]	-2.32	-0.55	1.82	2.29	-2.72	2.50	2.80	-1.89
Bybase [rad/s ²]	-10.76	-0.67	-2.18	2.46	-4.29	-5.84	7.14	-7.65
Bzbase [rad/s ²]	2.10	0.08	-0.25	-0.35	0.55	0.59	1.03	0.91
Oxtop [Gal]	-1231	268	-620	-846	989	-1489	-1955	1604
Oytop [Gal]	650	-259	-754	967	1450	-1707	2115	-2235
Oztop [Gal]	-2497	250	-669	969	1350	1726	1905	1490
Bxtop [rad/s ²]	-7.37	-1.82	8.86	10.41	14.30	14.53	16.77	-17.63
Bytop [rad/s ²]	-19.54	2.15	5.25	-6.55	-9.82	12.19	-16.04	13.98
Bztop [rad/s ²]	5.56	0.44	1.48	-1.93	-3.01	3.27	5.08	4.02
Ux [mm]	1.520	0.351	0.767	1.209	1.863	2.704	4.288	8.942
Uy [mm]	-0.443	-0.259	0.858	-1.383	-2.499	-2.765	-4.246	15.855
Uz [mm]	1.048	0.240	0.420	0.724	4.121	1.248	1.894	3.712
-θx [0.001 rad]	-0.435	0.122	0.749	0.929	3.502	1.540	1.964	4.131
θy [0.001 rad]	-1.544	0.225	0.488	0.677	-4.070	1.759	2.644	-2.140
θz [0.001 rad]	-0.071	-0.056	-0.171	0.327	-0.554	0.804	-1.156	4.003
γx [0.001 rad]	1.345	-0.218	0.472	0.712	-1.097	1.620	2.698	6.764
γy [0.001 rad]	1.056	-0.181	-0.501	-0.845	-1.815	-2.067	-3.118	12.054
Ubx [mm]	0.542	0.084	0.188	0.272	0.499	0.683	-0.646	-0.652
Uby [mm]	-0.737	0.059	0.290	0.368	0.557	0.655	0.713	0.749
Ox [kN]	824	-179	415	567	-662	997	1309	-1074
Oy [kN]	-436	174	505	-647	-971	1144	-1416	1496
Nz [kN]	2213	825	1052	1306	1561	1814	1933	1656
Tz [kN.m]	-622	-49	-166	216	338	-366	-570	-451

Table 2-11 Peak Responses for Specimen DT-B-02

DT-B-02	Run-1	Run-2	Run-2'	Run-3	Run-3'	Run-4	Run-5	Run-6	Run-7
Cxbase [Gal]	143	933	256	484	1063	1005	1499	-1950	-1551
Cybase [Gal]	-122	-826	-173	340	-731	982	-1231	-2131	-1893
Czbase [Gal]	85	839	181	375	777	712	1050	1385	941
Pxbase [rad/s ²]	-0.45	-2.60	-0.52	1.22	2.47	3.01	3.92	4.59	-2.75
Pybase [rad/s ²]	-0.50	3.25	-0.76	1.44	-4.22	3.69	6.47	8.04	1.87
Pzbase [rad/s ²]	-0.10	0.53	0.18	-0.22	0.52	0.57	0.77	-1.17	-0.79
Cxtop [Gal]	-472	-941	-359	-568	-1113	-1275	-1649	1739	-1780
Cytop [Gal]	433	-766	335	642	-1153	-1383	-1794	-1934	-2672
Cztop [Gal]	-182	1152	285	650	-1786	-1395	2105	2190	1435
Pxtop [rad/s ²]	-2.99	-7.97	-1.70	4.22	8.62	-11.75	12.71	18.78	16.80
Pytop [rad/s ²]	3.45	9.66	3.68	-5.64	-12.13	-12.15	-15.19	17.03	-14.76
Pztop [rad/s ²]	-0.30	1.79	0.55	1.50	-2.80	-2.63	4.07	-4.65	5.54
Ux [mm]	0.260	-0.938	-0.471	-0.733	-1.779	-2.160	-3.004	-4.901	18.941
Uy [mm]	-0.230	-1.011	-0.459	-0.893	1.419	2.097	3.005	5.135	-26.349
Uz [mm]	0.018	0.620	0.200	0.385	0.814	0.925	1.297	-	-
-θx [0.001 rad]	-0.109	-0.673	0.179	0.471	0.843	-1.036	-1.272	-	-
θy [0.001 rad]	-0.138	-0.909	-0.280	0.516	-1.087	1.126	1.805	-	-
θz [0.001 rad]	-0.024	0.187	0.084	0.150	0.370	-0.524	0.610	1.548	10.788
γx [0.001 rad]	0.156	-0.508	-0.312	-0.447	-1.155	-1.482	-2.114	-4.901	18.941
γy [0.001 rad]	-0.151	-0.571	-0.350	-0.603	0.975	1.473	2.120	5.135	-26.349
Ubx [mm]	-0.028	-0.432	-0.177	-0.297	-0.537	-0.554	-0.764	-	-
Uby [mm]	-0.022	0.295	-0.104	-0.200	-0.367	-0.482	-0.631	-	-
Ox [kN]	316	630	241	380	745	854	1104	-1185	1192
Oy [kN]	-290	513	-224	-430	772	926	1202	1296	1790
Nz [kN]	757	1429	848	1092	1836	1588	2067	2125	1619
Tz [kN.m]	34	-200	-62	-168	314	295	-456	521	-621

Table 2-12 Peak Responses for Specimen DT-C-01

DT-C-01	Run-1	Run-2	Run-2'	Run-3	Run-4	Run-5	Run-5'	Run-6	Run-7
Cxbase [Gal]	115	199	346	868	794	1311	1566	-1212	-1466
Cybase [Gal]	-126	-190	429	938	891	-1525	-1724	-1327	-1680
Czbase [Gal]	110	145	225	907	-699	847	-1071	-752	918
Pxbase [rad/s ²]	-0.57	-0.85	0.60	2.67	2.89	-4.55	4.33	1.63	2.11
Pybase [rad/s ²]	-0.63	-0.81	-0.82	-2.36	2.68	-4.07	5.59	-1.30	-2.23
Pzbase [rad/s ²]	0.12	-0.16	-0.25	0.55	-0.41	0.68	-0.80	-0.60	39.58
Cxtop [Gal]	516	595	-857	-974	-907	-1397	-1474	1844	-1631
Cytop [Gal]	523	678	-1140	-1013	-920	-1358	-1712	-1935	-1825
Cztop [Gal]	208	325	447	1251	1116	-1341	1905	1698	1415
Pxtop [rad/s ²]	-3.10	-4.61	-6.16	-7.56	7.56	-13.28	-13.10	12.57	-7.98
Pytop [rad/s ²]	-3.17	-3.83	-5.62	-7.23	-7.94	-13.97	-10.27	-10.12	-10.29
Pztop [rad/s ²]	-0.36	-0.51	-1.12	-3.05	-2.23	3.59	4.64	3.98	-3.22
Ux [mm]	-0.228	-0.304	0.485	1.030	-1.132	-1.716	-3.028	-6.388	8.296
Uy [mm]	-0.236	0.349	0.681	-1.205	-1.237	-2.157	-2.912	-6.845	8.863
Uz [mm]	0.022	0.036	0.123	0.600	0.593	0.868	1.244	1.868	-
-θx [0.001 rad]	0.122	0.187	0.291	0.571	-0.567	1.005	1.246	1.630	-
θy [0.001 rad]	-0.122	0.143	0.273	0.559	-0.636	0.983	-0.903	-1.709	-
θz [0.001 rad]	0.023	-0.025	0.072	0.246	0.244	-0.719	-1.000	-1.306	3.163
γx [0.001 rad]	-0.143	-0.189	-0.306	0.558	-0.734	1.112	-2.150	-4.966	8.328
γy [0.001 rad]	-0.149	0.220	0.421	0.764	-0.785	-1.571	2.236	-5.332	8.951
Ubx [mm]	0.005	-0.011	0.036	0.205	0.228	0.415	0.448	-1.084	-
Uby [mm]	-0.011	-0.021	-0.044	-0.210	-0.205	-0.388	-0.502	0.989	-
Ox [kN]	-346	-399	574	652	607	936	988	-1235	1093
Oy [kN]	-350	-454	763	678	616	910	1147	1296	1222
Nz [kN]	796	875	957	1495	1405	1497	1933	1794	1605
Tz [kN.m]	41	57	125	341	250	-402	-520	-446	361



(Note)

- α, β :sway and rotational acceleration,
- u, θ :sway and rotational displacement,
- γ :shear deformation angle,
- u_b :flexural component of horizontal displacement,
- Q, N, T :shear force, axial force, and torque around vertical axis,
- base, top :suffix to distinguish the base slab and the upper slab
- Max. values before failure are adopted for the last Runs.

Figure 2-39 Schematic Notations employed in Displays of Shaking Table Test Results

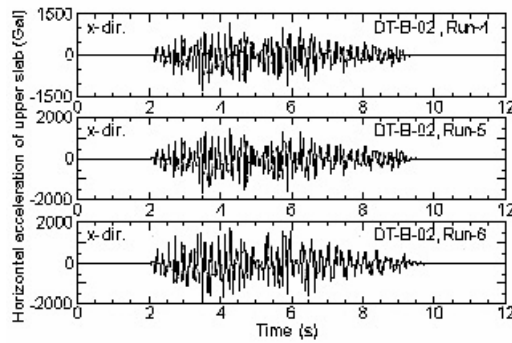


Figure 2-40 Horizontal Acceleration Response of Upper Slab for Specimen DT-B-02

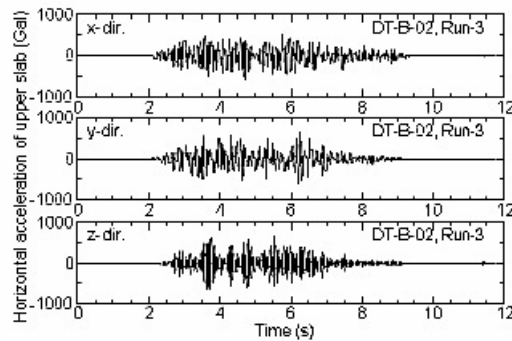


Figure 2-41 Three Orthogonal Components of Acceleration Response of Upper Slab for Specimen DT-B-02

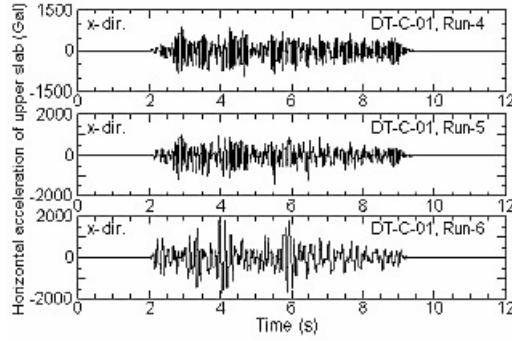


Figure 2-42 Horizontal Acceleration Response of Upper Slab for Specimen DT-C-01

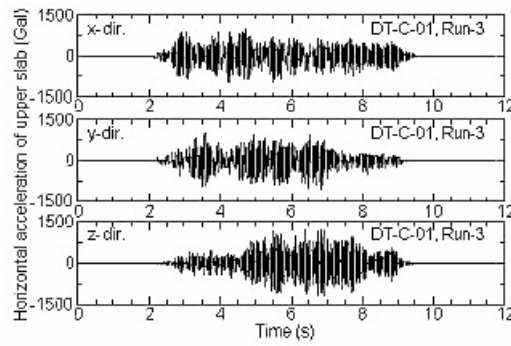


Figure 2-43 Three Orthogonal Components of Acceleration Response of Upper Slab for Specimen DT-C-01

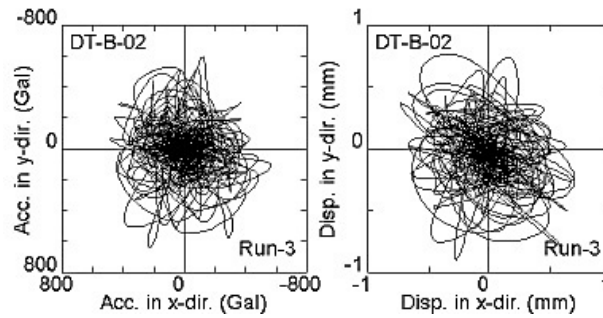


Figure 2-44 Horizontal Acceleration and Displacement Orbits from Run 3 for DT-B-02

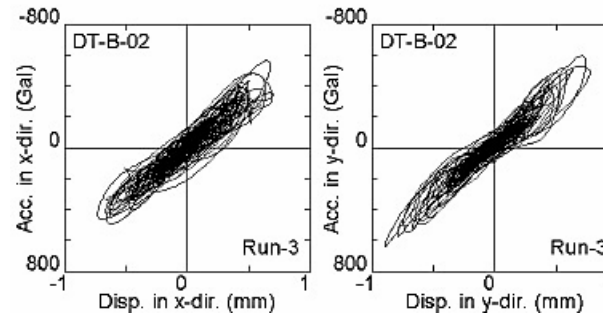


Figure 2-45 Horizontal Hysteresis Loops from Run 3 for DT-B-02

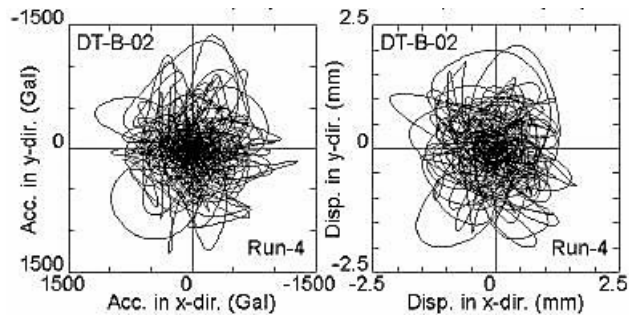


Figure 2-46 Horizontal Acceleration and Displacement Orbits from Run 4 for DT-B-02

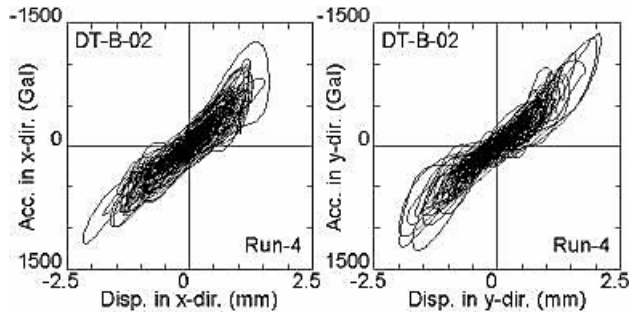


Figure 2-47 Horizontal Hysteresis Loops from Run 4 for DT-B-02

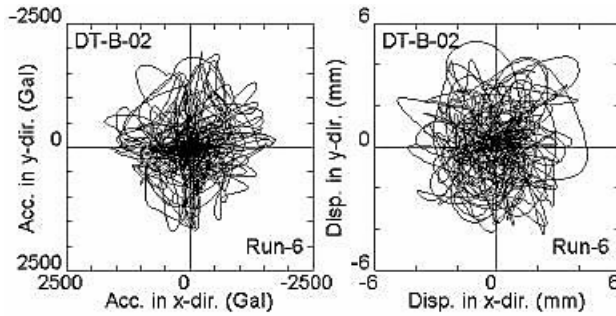


Figure 2-48 Horizontal Acceleration and Displacement Orbits from Run 6 for DT-B-02

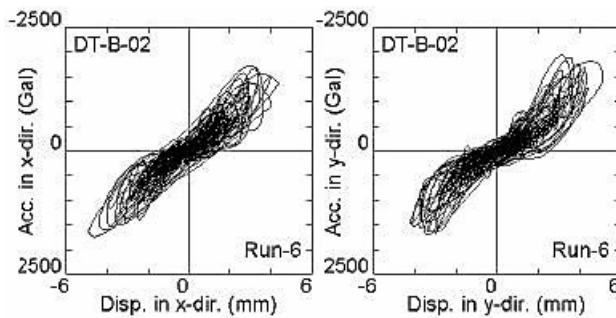


Figure 2-49 Horizontal Hysteresis Loops from Run 6 for DT-B-02

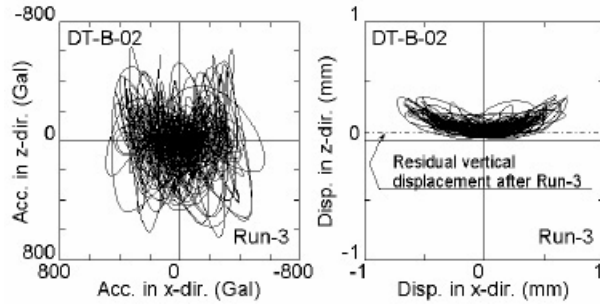


Figure 2-50 X-Z Plane Acceleration and Displacement Orbits from Run 36 for DT-B-02



Figure 2-51 Progressive Development of Shear Wall Cracks for DT-B-02

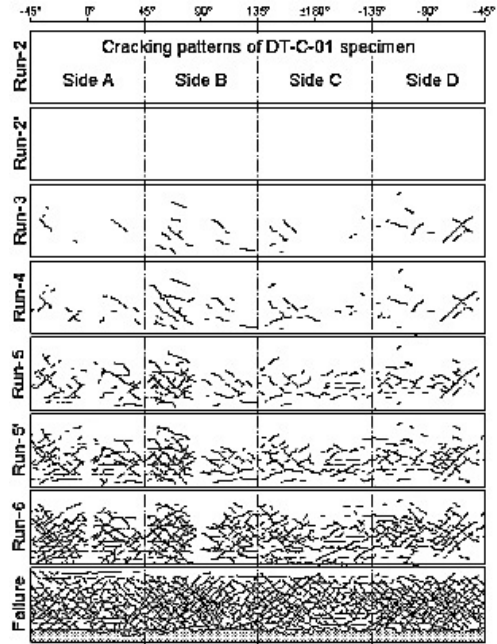


Figure 2-52 Progressive Development of Shear Wall Cracks for DT-C-01

3 ASSESSMENT OF SIMPLIFIED METHODS FOR ESTIMATING SHEAR WALL SEISMIC STRENGTH AGAINST TEST DATA

Many of the simplified methods used by the nuclear industry have been primarily correlated with the results of single-element shear wall tests in which the walls were subjected to one-directional loading in the plane of the wall. The JNES test results provide unique information in that they tested box and cylindrical walls under the effects of multi-axis loading.

This section of the report describes a number of simplified methods used in the nuclear industry to estimate the ultimate capacity of low rise reinforced concrete shear walls (defined in terms of aspect ratio of height to length of the wall) subjected to seismic loadings. These methods are also applied to the JNES test specimen configurations to predict the failure capacity of the box type test structures containing shear walls. A comparison is then made between the predicted (calculated) values using the various simplified methods and the test results to determine the accuracy of these methods, discuss why some differences may exist, and also examine what additional insights might be developed from the test results.

Section 3.1 below describes simplified methods for calculating the ultimate strength of shear walls and provides the comparisons made with the test data. Section 3.2 describes methods for determining the inelastic energy absorption factor (F_{μ}), which is used to account for nonlinear behavior before failure occurs under dynamic cyclic earthquake motions. Section 3.2 also provides the comparison of results with the test data.

3.1 Methods for Calculating Ultimate Capacity and Comparison to Test Results

3.1.1 ACI Design Code Method

Based on ACI 349-01, Chapter 11 - Shear and Torsion

For Concrete

According to ACI 349-01 (and ACI 318-02), Section 11.10 - Special Provisions for Walls, the nominal shear strength V_C (expressed as in-plane shear force at section) provided by the concrete shall be permitted to be computed by the smaller value obtained from Equations 3-1 and 3-2. The nominal strength values in accordance with the ACI Code are used herein without the strength reduction factor, ϕ , because the goal is to obtain an estimate of the ultimate capacity rather than develop a design for a shear wall.

$$V_C = 3.3\sqrt{f'_c}hd + \frac{N_u d}{4l_w} \quad (3-1)$$

$$V_C = \left[0.6\sqrt{f'_c} + \frac{l_w \left(1.25\sqrt{f'_c} + 0.2 \frac{N_u}{l_w h} \right)}{\frac{M_u}{V_u} - \frac{l_w}{2}} \right] hd \quad (3-2)$$

where,

f'_c = compressive strength of concrete

h = wall thickness

l_w = length of wall

$d = 0.8 \times l_w$ (per ACI 349-01, Section 11.10.4). A larger value, corresponding to the distance from the extreme compression fiber to the centroid of force of all reinforcement in tension when determined by a strain compatibility analysis is permitted.

N_u = factored axial load normal to cross section

M_u = factored moment at section

V_u = factored shear force at section

When the expression

$$\frac{M_u}{V_u} - \frac{l_w}{2} \quad (3-3)$$

in Eq. 3-3 is negative, then Eq. 3-2 shall not be used.

Eq. 3-1 determines the inclined cracking strength corresponding to a principal tensile stress of approximately $4\sqrt{f'_c}$. Eq. 3-2 calculates the shear strength corresponding to a flexural tensile stress of $6\sqrt{f'_c}$ at a section $l_w/2$ above the section being investigated. Also, in accordance with Section 11.10.7 of ACI 349-01, the critical section to design for shear is a distance equal to the smaller of one-half of the wall length or one-half of the wall height.

For Steel Reinforcement

Per ACI 349-01 (and ACI 318-02), Section 11.10.9, the nominal shear strength V_s provided by the steel reinforcement shall be computed by

$$V_s = \frac{A_v f_y d}{s_2} \quad (3-4)$$

where,

A_v = area of horizontal reinforcement within distance s_2

s_2 = spacing of horizontal reinforcement

f_y = yield strength of reinforcement

Total Nominal Shear Strength (V_n)

$$V_n = V_c + V_s \quad (3-5)$$

Also, per ACI 349-01, Section 11.10.3:

$$V_n < 10\sqrt{f'_c} h d \quad (3-6)$$

Based on ACI 349-01, Chapter 21 - Special Provisions for Seismic Design

ACI 349-01, Section 21.6 - Structural Walls, Diaphragms, and Trusses, provides requirements that apply to structural walls that are part of a seismic lateral load resisting system. Section 21.6.1 indicates that for shear walls with aspect ratio h_w/l_w of less than 2.0 (h_w is the height of the wall),

the provisions of 21.6.5 - Shear Strength, can be waived. However, for purposes of comparison with Chapter 11 of the Code, the nominal shear strength provided by Section 21.6.5 will be calculated. According to Section 21.6.5, the nominal shear strength V_n can be determined from Equation 3-7 for h_w/l_w ratios less than 2.0.

$$V_n = A_{cv} \left(\alpha_c \sqrt{f'_c} + \rho_n f_y \right) \quad (3-7)$$

where,

α_c varies linearly from 3.0 for $h_w/l_w = 1.5$ to 2.0 for $h_w/l_w = 2.0$

A_{cv} = the net cross-sectional area of the horizontal wall segment.

ρ_n = the ratio of shear reinforcement on a plane perpendicular to plane of A_{cv}

Also, per ACI 349-01, Section 21.6.5.7:

$$V_n < 10A_{cp} \sqrt{f'_c} \quad (3-8)$$

where,

A_{cp} = the cross-sectional area of a horizontal wall segment.

Note that for shear wall with solid cross section, A_{cp} equals $h \times l_w$.

Observations on Differences between Chapter 11 and 21 of the ACI Code

Reviewing the differences in the equations for the concrete shear strength of low rise shear walls for $h/l_w < 2.0$ leads to the following observations:

	<u>Chapter 11</u>	<u>Chapter 21</u>
1. Coefficient applied to the $\sqrt{f'_c}$ term	3.3	2.0 to 3.0
2. Length of wall for effective shear area	$d = 0.8 \times \text{length of wall}$	$d = 1.0 \times \text{length of wall (based on definition of } A_{cv} \text{)}$
3. Contribution from compressive load	$\frac{N_u d}{4l_w}$	None
4. Separate check on shear limit	$10\sqrt{f'_c} hd$	$10A_{cp} \sqrt{f'_c}$

Based on the above comparison, these differences are compensating to some extent; and the calculated wall capacities using Chapters 11 and 21 of the Code will depend on the h_w/l_w ratio, whether there is a preload in the wall, and the horizontal cross section of the wall.

Example – Application of ACI Methodology to Test Specimen SD-08-00

To demonstrate the application of the ACI methodology and show the comparison to actual test results for the box type reinforced concrete shear wall structures, the JNES uni-directional cyclic

loading test data were utilized. A description of the test program is provided in Section 2.0 which presents the configuration and material properties for the test specimen. Further details of the test description and design of the selected test specimen SD-08-00 is presented in Habasaki, A., et al., 2000. Test specimen SD-08-00 corresponds to the box type structure loaded at an angle of 0 degree (i.e., in-plane) with respect to the two side walls of the structure. This specimen has a height of 1000 mm, length of 1575 mm (outside dimension of the walls), and wall thickness of 75 mm. For calculation purposes, the length of the wall corresponding to the center of one wall to the center of the other parallel wall is used. This results in the length of the wall equal to 1500 mm, which leads to a height to width ratio of 0.667. This height to width ratio is typical of reinforced concrete shear walls found at most nuclear power plants.

In the following sections, US units (in, lbf, psi), converted from metric, are utilized in the calculation in order to facilitate the use of the ACI Code equations. Final results are then, also presented in SI metric units.

Based on ACI 349-01, Chapter 11 - Shear and Torsion

From Section 2.1 of this report and the test summary [Habasaki, A., et al., 2000], the material properties and design parameters for test specimen SD-08-00 are $f'_c = 34.9$ MPa (5,062 psi), $f_y = 345$ MPa (50,025 psi), h (wall thickness for two walls treated as one) = 150 mm (5.91 in), $l_w = 1,500$ mm (59.1 in), $d = 1200$ mm (47.2 in), and $N_u = 165$ kN (74,356 lbs) for two walls. These parameters were substituted into Eq. (3.1.1-1) which resulted in a concrete shear strength contribution of V_c equal to 358 kN (80,377 lb). Using Eq. (3.1.1-4), the shear strength contribution from the steel reinforcement, V_s , was calculated to be 745 kN (167,484 lb). The total nominal shear strength V_n , which is the sum of V_c and V_s is equal to 1103 kN (247,861 lb).

As required by the ACI 349-01 Code, the shear strength using Eq. (3.1.1-2) must also be calculated and the smaller of the two values for V_c shall be used. The critical section, h_c , for determining shear must be calculated based on Section 11.10.7 of the ACI 349-01 Code. This resulted in h_c equal to one-half the height of the wall or 500 mm (19.7 in). Using this location for the critical section for calculation of shear, the expression in Eq. (3.1.1-3) resulted in a negative value. Therefore, as noted in ACI 349-01, when this expression is negative, Eq. (3.1.1-2) shall not be used.

In accordance with Section 11.10.3 of ACI 349-01, the nominal shear strength must also be less than that given by Eq. (3.1.1-6) which was calculated to be 883 kN (198,502 lb). Therefore, based on the provisions in Chapter 11 of ACI 349-01, the nominal shear strength of test specimen SD-08-00 is limited to 883 kN (198,502 lb).

Based on ACI 349-01, Chapter 21 - Special Provisions for Seismic Design

Using the same test specimen properties and design parameters, Eq. (3.1.1-7) was utilized to determine the nominal shear strength. The net cross-sectional area of the horizontal wall segment $A_{cv} = 2,250$ cm² (348.8 in²). With a height to width ratio of 0.67, $\alpha_c = 3.0$. Substituting all of the parameters into Eq. (3.1.1-7) led to a shear strength of (1,262 kN) (283,793 lb). However, in accordance with Section 21.6.5.7 of ACI 349-01, the shear strength must be less than that given by Eq. (3.1.1-8), which was calculated to be 1104 kN (248,128 lb). Therefore, based on the provisions in Chapter 21 of ACI 349-01, the nominal shear strength of test specimen SD-08-00 is limited to 1104 kN (248,128 lb). This shear strength is somewhat higher than the 883 kN (198,502 lb) using the provisions of Chapter 11 of ACI 349-01.

Comparison of ACI Results to Test Data

The measured shear load capacity for specimen SD-08-00 from the test [Habasaki, A., et al., 2000] is 1480 kN. The test results show that the ACI predicted strength of 883 kN, using Chapter 11 of the Code, under predicts the strength from the test by 40%. For the provisions in Chapter 21 of the ACI Code, the test results show that the predicted strength of 1104 kN under predicts the strength from the test by 25%. These results indicate that the use of Chapter 11 of the Code provides a large margin while Chapter 21 of the Code still provides a sizeable level of conservatism. This confirms what is generally known that the ACI Code equations provide conservative estimates of the shear strength of low rise reinforced concrete shear walls for the set of equations following Chapter 11 and Chapter 21 of the Code.

It should also be noted that for design purposes, if the ACI Code required strength reduction factor, ϕ , was used then the design margin would be even larger for both results (i.e., based on Chapter 11 and Chapter 21).

3.1.2 ASCE 43-05 (Barda et al.) Method

Barda et al. Methodology and the Development of the ASCE 43-05 Method

Research performed by Barda, F., et al., 1976, developed an empirical method to determine the ultimate shear strength of low rise (height to length ratio $h_w/l_w < 1.0$) reinforced concrete shear walls. The ultimate capacity, v_u , of the reinforced concrete shear wall is given by

$$v_u = v_{cu} + v_{su} \quad (3-9)$$

where,

v_{cu} = shear capacity contribution from concrete (expressed as stress)

v_{su} = shear capacity contribution from steel reinforcement (expressed as stress)

For steel reinforcement, the contribution to shear stress capacity remains the same as the ACI Code requirement.

$$v_{su} = \rho_v f_y \quad (3-10)$$

For concrete, the contribution to the shear capacity is given by

$$v_{cu} = 8.3\sqrt{f'_c} - 3.4\sqrt{f'_c} \left(\frac{h_w}{l_w} - \frac{1}{2} \right) + \frac{N}{4l_w t} \quad (3-11)$$

where,

f'_c = concrete compressive strength

h_w = wall height

l_w = wall length

N = normal (bearing) load

f_y = yield strength of reinforcing steel

t = wall thickness

ρ_v = vertical steel reinforcement ratio

A plot of the concrete strength versus aspect ratio for shear walls using the Barda equation is presented in Figure 3-1. Results from various tests are also shown on this plot for comparison.

The test data points correspond to the contribution of concrete (i.e., without the contribution from steel).

As indicated in Cover, L. E., et al., 1985, the expressions given above for calculating the contribution of the steel reinforcement were modified to reflect the data of Shiga T., et al., 1973; Cardenas, A. E., et al., 1973; and Oesterle, R. G., et al., 1979. The contribution of the horizontal and vertical steel reinforcement to the shear strength of a wall was determined to be given by Eq. 3-12 shown below. The combination of the Barda equation for concrete (Eq. 3-11) and the expression for steel (Eq. 3-12) is referred to in this report as the "Barda et al. Method."

$$v_{su} = (A\rho_v + B\rho_h)f_y \quad (3-12)$$

where,

f_y = yield strength of reinforcing steel

ρ_v = vertical steel reinforcement ratio

ρ_h = horizontal steel reinforcement ratio

$A = 1$ and $B = 0$, for $h_w/l_w \leq 0.5$

$A = 2(1 - h_w/l_w)$ and $B = 2(h_w/l_w) - 1$, for $0.5 < h_w/l_w \leq 1.0$

$A = 0$ and $B = 1$, for $h_w/l_w > 1.0$

It should be noted that when the horizontal and vertical reinforcement ratios are the same, the expression for the contribution of the steel to shear capacity can be shown to be the same as the ACI Code requirement given in Eq. 3-4 and the Barda method given by Eq. 3-10.

In 2005, a new standard, ASCE/SEI 43-05, was issued that provides performance-based and risk-consistent seismic design criteria for structures, systems, and components (SSC) in nuclear facilities. This Standard provides an alternate method that could be used in place of the ACI 349 approach for calculating the strength of low rise reinforced concrete shear walls. From ASCE 43-05, Section 4.2.3 "Capacity of Low Rise Concrete Shear Walls," the equation for calculating the shear strength of low rise shear walls ($h_w/l_w \leq 2.0$) is given by Eq. 3-13 shown below. This equation is almost identical to the Barda et al. method formulation presented above.

$$v_u = \phi \left[8.3\sqrt{f'_c} - 3.4\sqrt{f'_c} \left(\frac{h_w}{l_w} - 0.5 \right) + \frac{N_A}{4l_w t_n} + \rho_{se} f_y \right] \quad (3-13)$$

The effective steel ratio, ρ_{se} , is given by the following expression:

$$\rho_{se} = A\rho_v + B\rho_u \quad (3-14)$$

where,

ϕ = Capacity reduction factor = 0.8

v_u = ultimate shear strength

f'_c = concrete compressive strength

h_w = wall height

l_w = wall length

N_A = axial load

t_n = wall thickness

f_y = steel yield strength

ρ_v = vertical steel reinforcement ratio

ρ_u = horizontal steel reinforcement ratio

A, B constants given as follows:

$h_w/l_w \leq 0.5$	$A = 1$	$B = 0$
$0.5 \leq h_w/l_w \leq 1.5$	$A = -h_w/l_w + 1.5$	$B = h_w/l_w - 0.5$
$h_w/l_w \geq 1.5$	$A = 0$	$B = 1$

According to ASCE 43-05, Eq. 3-13 is applicable to shear wall aspect ratios less than or equal to 2.0 and for ρ_v and ρ_u less than or equal to 0.01. If ρ_v or ρ_u is greater than 0.01, then ρ_{se} shall be limited to 0.01. Also, v_u shall be less than $20\phi\sqrt{f'_c}$.

According to ASCE 43-05, the total shear capacity is given by:

$$V_U = v_u d t_n \quad (3-15)$$

where d is the distance from the extreme compression fiber to the center of force of all reinforcement in tension which may be determined from a strain compatibility analysis. In lieu of an analysis, d equal to $0.6 \times l_w$ is used.

The ASCE 43-05 methodology is very similar to the Barda et al. formulations described earlier. The differences primarily relate to the definition of low rise shear walls (h_w/l_w less than or equal to 2.0), calculation of the A and B constants, limitation on ρ_v and ρ_u , and reduced distance " d " to be used to calculate total shear strength from the unit shear stress v_u .

All of the test specimens described in this report have equal steel reinforcement in the horizontal and vertical directions. Therefore, it can be seen from Eq. 3-14 that the steel ratio ρ_{se} will equate to the same value as $\rho_v = \rho_u = 0.012$ for all of the test specimens. Therefore, the differences in calculating the A and B constants will not have any effect on the JNES test specimens. The limitation on ρ_{se} , when ρ_v or ρ_u is greater than 0.01, still remains a difference from the prior description of the Barda et al. method. Regarding the reduced value of $d = 0.6 \times l_w$ (rather than $0.8 \times l_w$), a conservative factor of 0.6 was selected in ASCE 43-05 to account for walls that may have a low ratio of vertical reinforcement, no integral perpendicular end walls, and only a small compressive load. All of the JNES test specimens utilized in this report have a high ratio of vertical reinforcement with integral perpendicular end walls, and significant compressive loads. Therefore, for comparison with the JNES test data, it would be unreasonable to use the 0.6 factor. For these walls the factor of 0.8 will be utilized instead. Based on the above, for the JNES test specimens the only difference remaining lies in the limitation on the steel ratio ρ_{se} , which for the ASCE 43-05 method, reduces the value from 0.012 to 0.01.

In this report, the capacity reduction factor, ϕ , is not used in Eq. (3.1.2-5) since it is desired to obtain a best estimate and not a design value for the ultimate capacity.

Example – Application of the ASCE 43-05 (Barda et al.) Methodology to Test Specimen SD-08-00

To demonstrate the application of the ASCE 43-05 (Barda et al.) methodology and show the comparison to actual test results for the box type reinforced concrete shear wall structures, test specimen SD-08-00 from the JNES uni-directional cyclic loading test was utilized. This is the same test specimen selected previously to demonstrate the application of the ACI methodology to the test data. As indicated before, the description of the test program is provided in Section 2.0 which presents the configuration and material properties for the test specimen. Further details of the test description and design of the selected test specimen SD-08-00 is presented in Habasaki,

A., et al., 2000. Test specimen SD-08-00 corresponds to the box type structure loaded at an angle of 0 degree (i.e., in-plane) with respect to the two side walls of the structure. Specific design parameters needed for calculation of the shear capacity are summarized in Section 1.1.1 under the heading “Example – Application of ACI Methodology to Test Specimen SD-08-00.”

Using Eq. 3-13, the contribution to shear capacity from concrete and steel can be calculated separately and then summed. The contribution from concrete is equal to the equation in the square bracket without the last term $\rho_{se} f_y$. Substituting the wall design parameters into this formulation results in a unit concrete shear strength contribution of $v_{cu} = 4.16$ MPa (604 psi). To calculate the shear strength contribution from the steel reinforcement, the h_w/l_w ratio of the walls was used to determine coefficients A and B . With the h_w/l_w ratio equal to 0.667, coefficients A and B are equal to 0.833 and 0.167, respectively. The steel ratios, ρ_v and ρ_h , are equal to 0.012 and f_y is equal to 345 MPa (50,025 psi). Substituting these parameters into Eq. 3-14, the effective steel ratio $\rho_{se} = 0.012$, which is the same as the horizontal and vertical reinforcement ratio. This was expected since the horizontal and vertical reinforcement ratios are equal. Since the effective steel ratio exceeds 0.01, the ASCE 43-05 method limits the effective steel ratio to 0.01. The contribution of the steel reinforcement is calculated using the last term in the squared bracket in Eq. 3-13, which results in a unit shear strength contribution from the steel reinforcement, v_{su} , equal to 3.45 MPa (500 psi). Using Eq. 3-13, the total nominal unit shear strength, v_u , is equal to the summation of the contribution from concrete and steel, which leads to a total unit shear strength of 7.61 MPa (1104 psi). The total shear strength across the section, using $d = 0.8 \times l_w$ and without the capacity reduction factor of 0.8, is equal to 1370 kN (307,945 lb).

Comparison to Test Data

The measured shear load capacity from the test [Habasaki, A., et al., 2000] is 1480 kN. The test results show that using the ASCE 43-05 (Barda et al.) method, the predicted strength of 1370 kN under predicts the strength from the test by 7.4%. The prediction using the ASCE 43-05 (Barda et al.) method is considered to be very close to the test results. The application and comparison of the ASCE 43-05 method for all of the test specimens is provided in the following two subsections.

3.1.3 Relevant Information of the JNES/NUPEC Specimens

As described in Section 2, JNES/NUPEC conducted tests of 11 box type shear walls that were subjected to uni- and multi-directional cyclic loadings [Habasaki, A., et al., 2000, Hiroshi, T., et al., 2001]. Among the 11 specimens, 8 box type shear walls were tested using uni-directional loadings at angles 0° , 26.6° , and 45° , and 3 walls were tested using multi-directional loadings that include rectangular, cross, and diagonal cross loading scenarios. Details of these loading conditions are described in Section 2. As shown in the first column of Table 3-1, the specimen ID “SD-NS-ND” series represent the specimens subjected to the uni-directional loading with NS as the shear span ratio (M/Qd) and ND as the loading angle, while specimen “SB-B-NN” series are the ones subjected to multi-directional loading with NN equal to 1, 2 and 3 as the indicator for rectangular loading, cross loading, and diagonal cross loading respectively. The shear span ratio for the “SB-B-NN” series is 0.8.

The information for these tests that is pertinent to the use of the simplified methods is presented in Table 3-1, in which the specimens are ordered based on their shear span ratio. The specimens presented in the first 3 rows have a shear span ratio of 0.6, the ones in the shaded 6 rows in the middle have a shear span ratio of 0.8, and the ones in the last 2 rows have a shear span ratio of 1.0.

All specimens have the same dimension in plan view, which is a square with each side having a length of 1.5 m (center to center distance between two flange walls). The shear walls in both directions for all 11 specimens have a thickness of 75 mm. The heights of the walls for the 3 shear span ratios are 0.7 m, 1 m, 1.3 m respectively, which results in aspect ratios of 0.47, 0.67, and 0.87 respectively. The loading slab on the top of the shear walls has a thickness of 400 mm for all 11 specimens, and the displacement loading is applied at the mid height of the loading slab. The specimens are fixed to the base slab in the tests.

Also listed in Table 3-1 are the uniaxial compressive strength f'_c of the concrete and the yield strength f_y of the rebars. The maximum shear strength of the walls in either horizontal direction obtained from the tests is designated as V_{MT} (strength of 2 walls in parallel) and is tabulated in this table, as well as the maximum vector shear strength V_{VT} (resultant) of the box type walls. The starred V_{MT} values in Table 3-1 are calculated by BNL using the maximum vector shear strength and the loading angle. It is important to observe that both V_{MT} and V_{VT} represent the same maximum loading that the test specimen can take.

The walls for all 11 specimens have double layer reinforcement with rebar designation D6 (6 mm diameter) at 70 mm spacing in both horizontal and vertical directions, which result in a reinforcement ratio of 1.2% for both directions. All walls in consideration have a vertical compressive load that is equivalent to a constant axial stress of 1.47 MPa, a typical value for the lower story of NPP structures in Japan.

The subsections that follow utilize the above test specimen properties to calculate the shear wall capacities of the box type structures using the ASCE 43-05 method followed by the ACI method. For all of the analyses, the length of 1.5 m (center to center dimension) is used for all walls. Also, the two walls in parallel are considered as one wall with double the thickness of a single wall.

3.1.4 Application of ASCE 43-05 Method to All Test Specimens

3.1.4.1 Strength Capacities Using the ASCE 43-05 Method

Following the same order of specimens listed in Table 3-1, Table 3-2 shows the results for all 11 cases using the ASCE 43-05 (Barda et al.) method. V_U is the capacity calculated using the ASCE 43-05 method. The data listed in columns labeled V_U/V_{VT} and V_U/V_{MT} are the ratios of the predicted (calculated) capacity to the resultant test result and predicted capacity to the maximum test result of the two horizontal directions. The magnitude of V_{VT}/V_{MT} indicates the significance of the (concurrent) bi-axis shear force effect at the time of failure of the specimens. For example, $V_{VT}/V_{MT} = 1$ for specimen SD-06-00 indicates that there are no concurrent bi-axis shear forces acting, while $V_{VT}/V_{MT} = 1.414$ for specimen SD-06-45 shows that the bi-axis shear forces achieve their maximum at the same time. The ratio of V_{VT}/V_{MT} is therefore referred to as the interaction intensity in this report. The aspect ratio of the walls, an important factor used later in this subsection, is also listed in this table.

Several observations can be made based on the ratios in Table 3-2. By examining V_U/V_{MT} in Table 3-2, where a value greater 1 means over-prediction by the ASCE method, there appears to be two factors that may affect the accuracy of this method. The first factor is the aspect ratio. V_U/V_{MT} is between 0.82 and 1.09 for an aspect ratio of 0.47, between 0.92 and 1.20 for an aspect ratio of 0.67, and between 1.09 and 1.41 for an aspect ratio of 0.87. In particular, when there is no bi-axis shear force effect, i.e., $V_{VT}/V_{MT} = 1$, V_U/V_{MT} increases from 0.82 to 1.09 as the aspect ratio increases. The data suggests that as the aspect ratio increases, the ASCE 43-05 method tends to

over predict the shear strength to some extent. This observation is also consistent with the trend shown in Figure 3-2. The second factor is the bi-axis shear force effect (interaction intensity). For any given aspect ratio, as the interaction intensity (V_{VT}/V_{MT}) grows, the ASCE method tends to over predict the shear strength.

V_U/V_{VT} in Table 3-2 provides the ratio of the calculated shear capacity of a specimen to the maximum vector shear capacity of the specimen from the test. The ratios of V_U/V_{VT} are smaller than 1 except for the case of specimen SD-10-00 where no bi-axis shear force effect is present. V_U/V_{VT} generally increases as the aspect ratio increases: between 0.76 and 0.82 for an aspect ratio of 0.47, between 0.85 and 0.93 for an aspect ratio of 0.67, and between 1.0 and 1.09 for an aspect ratio of 0.87. For any given aspect ratio, V_U/V_{VT} appears to decrease slightly as the bi-axis effect increases.

These observations will be investigated analytically in the next two subsections, to assess how one could adjust the ASCE 43-05 (Barda et al.) method in order to more accurately predict the strengths in these tests. The discussion will be categorized into two approaches: one considers the strength adjustment based on a single wall and the other considers the strength adjustment based on treating the specimen (four walls) as an overall-box structure.

3.1.4.2 Strength Adjustment Based on a Single-Wall Approach

The ASCE 43-05 method, as well as the Barda et al. method which it is based on, have been developed to calculate the shear strength of a single wall. Therefore, comparing V_U to V_{MT} for accuracy assessment appears to be a reasonable approach. However, the ratios of V_U/V_{MT} for all 11 cases as shown in Table 3-2 are scattered above and below 1.0, and if taken literally, do not suggest any conclusive conservative or unconservative observation. The ASCE 43-05 method considers only the vertical load effect, leaving out moments and the out-of-plane shear force that can coexist in the wall. When a single wall fails in these tests, the in-plane and out-of-plane shears and moments coexist and interact with each other and can lead to a lower shear capacity in the tests. For the ASCE 43-05 method to be applicable to situations where multiple internal forces exist, it is important to take these interaction effects into account.

The consideration of interaction effect is simplified herein by utilizing the ratio of V_{VT}/V_{MT} , which measures the intensity of the interaction in an overall sense. Figure 3-2 shows four regression analyses that fit the various permutations of the test data into power type equations. The thick fitted curve is for all 11 cases, while the 3 thin fitted curves correspond to the 3 different aspect ratios. It is clear that the fit is not good if all 11 cases are considered at the same time, as indicated by the R^2 value that represents the variance reduction by the regression. However, if the influence of the aspect ratio is considered, by using the three separate curves, the regression equations achieve a very tight fit to the data. This finding from Figure 3-2 agrees with those observations discussed previously.

The 6 specimens with an aspect ratio of 0.67 not only represent the maximum number of available data with respect to aspect ratio but also include all loading scenarios among the tests. The regression equation using these 6 cases should be more reliable than the cases with the other aspect ratios. The regression equation so developed is summarized as,

$$\frac{V_U}{V_{MT}} = 0.924 \left(\frac{V_{VT}}{V_{MT}} \right)^{0.797} \quad (3-16)$$

This equation is also very close to the one using all 11 cases, which is

$$\frac{V_U}{V_{MT}} = 0.912 \left(\frac{V_{VT}}{V_{MT}} \right)^{0.828} \quad (3-17)$$

The close comparison between the two equations is clearly evident in Figure 3-2.

By assuming a general form of the regression equation

$$\frac{V_U}{V_{MT}} = F \left(\frac{V_{VT}}{V_{MT}} \right)^e, \quad (3-18)$$

where F is a linear function of the aspect ratio h_w/l_w , a least-square minimization of $\frac{V_U}{V_{MT}}$ yields the following optimum regression equation

$$\frac{V_U}{V_{MT}} = F \left(\frac{V_{VT}}{V_{MT}} \right)^{0.8} \quad (3-19)$$

$$F = 0.5 + 0.65 \frac{h_w}{l_w}$$

Table 3-3 compares V_U/V_{MT} predicted by Eq. 3-19 with V_U/V_{MT} obtained using ASCE 43-05 for all 11 tests. The median ratio of Eq. 3-19 over ASCE 43-05 for computing V_U/V_{MT} is 1.002. The logarithmic standard deviation β_{EQN} of the ASCE 43-05 V_U/V_{MT} with respect to the regression equation is only 0.024. This shows that Eq. 3-19 closely represents V_U/V_{MT} calculated using ASCE 43-05 for all 11 test cases.

Eq. 3-19 can be explained further by examining two contributing factors: the bias of the ASCE 43-05 method for V_U for these 11 cases and the interaction effect. First, considering a scenario where the interaction does not exist, i.e. $V_{VT}/V_{MT} = 1$, Eq. 3-19 is then simplified to

$$\frac{V_U}{V_{MT}} = F \quad (3-20)$$

In this expression, F , which is a function of h_w/l_w , indicates the degree of bias of the ASCE 43-05 method. Table 3-4 presents the calculated values of F over the range of aspect ratios that can be used with the ASCE 43-05 method. The shaded rows represent the range of the aspect ratios in the tests, and the non-shaded rows correspond to extrapolated values. F greater 1 indicates that the ASCE 43-05 method produces an unconservative shear strength. As indicated in Table 3-4, for any aspect ratio greater than 0.77, the ASCE 43-05 equation becomes unconservative. In addition, the ASCE 43-05 method might become significantly unconservative when h_w/l_w exceeds 1.0 and might be significantly conservative when h_w/l_w is less than 0.5. Since the aspect ratio of 0.9 results in less than a 10% unconservative bias, caution should be used when applying the ASCE 43-05 method for h_w/l_w ratios that exceed 0.9.

The second contributing factor in Eq. 3-19, is the interaction effect from bi-axis shear forces, which is given by $(V_{VT}/V_{MT})^{0.8}$. This term was calculated for the possible range of V_{VT}/V_{MT} , and is tabulated in Table 3-5. The interaction effect always introduces an unconservative bias to the

shear strength estimated by the ASCE 43-05 equation. However, if the $V_{VT}/V_{MT} < 1.12$, i.e., the interaction intensity is not significant, this bias is less than about 10% and for practical purposes could be neglected. For the purpose of simplifying the application, $(V_{VT}/V_{MT})^{0.8}$ can be approximated as a linear function,

$$\left(\frac{V_{VT}}{V_{MT}}\right)^{0.8} \approx 0.2 + 0.8 \frac{V_{VT}}{V_{MT}}, \quad (3-21)$$

and the error introduced is less than 1% for all possible values of V_{VT}/V_{MT} .

Although the interaction effect is unconservative, its combination with the F factor may lead to a larger range of applicable scenarios, especially for shear walls in nuclear power plants that typically have an aspect ratio less than 1.0. Figure 3-3 shows a series of V_U/V_{MT} contour curves on the $V_{VT}/V_{MT} - h_w/l_w$ plane, where any point below the curve “ $V_U/V_{MT}=1$ ” indicates a conservative case for the ASCE 43-05 method. For example, when the aspect ratio is 0.5, the ASCE 43-05 method can still predict a conservative capacity for any interaction intensity $V_{VT}/V_{MT} < 1.27$, rather than the criteria $V_{VT}/V_{MT} < 1.12$ discussed above. It also confirms that for any aspect ratio greater than 0.77, the ASCE 43-05 equation may become unconservative in spite of the interaction effect. Figure 3-4 shows the same contour curves in terms of the loading angle, which is defined as the angle between the wall and the vector shear force, and has a maximum value of 45° . For the same wall, having an aspect ratio of 0.5, the loading angle can be as high as 38° for the ASCE 43-05 method to still predict conservative results. These figures also show that for walls with an aspect ratio less than 0.4, the interaction effect can be neglected (presuming that Eq. 3-19 is correct beyond the aspect ratio range of [0.47, 0.87]).

3.1.4.3 Strength Adjustment Based on an Overall-Box Structure Approach

In assessing the effect of bi-axis shear loading, Hiroshi [2001] normalized the maximum vector shear forces by the one directional shear strength calculated using a Japanese concrete design standard, and plotted the normalized maximum vector shear forces on the X-Y plane. This plot included the data for 6 box type specimens which have an aspect ratio of 0.67 and one cylindrical type specimen. This plot shows that the maximum vector forces for these 6 box type specimens fall outside a unit circle. This trend has also been observed previously in this report using Table 3-2. A similar approach, with the shear strength calculated using the ASCE 43-05 method, is developed below in order to examine the interaction effect considering the overall-box structure.

Let V_X and V_Y denote the shear forces at failure in the X and Y directions from the tests, respectively, and V_U be the shear strength of two parallel walls calculated using the ASCE 43-05 method. Then, the unit circle, defined in Hiroshi [2001], can be expressed as

$$\left(\frac{V_X}{V_U}\right)^2 + \left(\frac{V_Y}{V_U}\right)^2 = 1 \quad (3-22)$$

or,

$$\frac{V_{VT}}{V_U} = 1 \quad (3-23)$$

Figure 3-5 shows the normalized shear forces in the X-Y plot, where all of the data conservatively fall outside the unit circle defined by Eq. 1-7, with one exception corresponding to the SD-10-00 specimen. In another words, the ASCE 43-05 method conservatively predicts the

resultant vector for all specimens except for one case if the design had been done in terms of the overall structure.

Eq. 3-19 can be transformed into the following equation,

$$\left(\frac{V_U}{V_{VT}} \right) = F \left(\frac{V_{VT}}{V_{MT}} \right)^{-0.20} \quad (3-24)$$

This equation can lead to the same ratio of predicted to test results as achieved by Eq. 3-19. Eq. 3-24 can be rewritten in a form similar to Eq. 3-23 as,

$$\left(\frac{V_{VT}}{V_U / F} \right) = \left(\frac{V_{VT}}{V_{MT}} \right)^{0.20}, \quad (3-25)$$

where the right hand side represents any bias that the interaction intensity V_{VT}/V_{MT} may introduce to Eq. 3-23, and V_U/F is the adjusted shear strength by the ASCE 43-05 method, with the aspect ratio accounted for. The bias term $(V_{VT}/V_{MT})^{0.2}$ and its approximate linear form have been tabulated in Table 3-6. It is obvious then that the conservative bias introduced by the interaction is only 7.2% as a maximum value. Figure 3-6 shows the maximum vector shear forces that are normalized by V_U/F , and also demonstrates that a bias (deviation from the unit circle) grows slightly in the conservative direction as the interaction intensity V_{VT}/V_{MT} increases. Figure 3-6 also exhibits much smaller variation in the normalized vector shear forces than those in Figure 3-5.

In this approach, the bi-axis shear force effect is directly accounted for by Eq. 3-23. Therefore, after the bias introduced by the ASCE 43-05 method (factor F) has been removed, the test results are very close to the unit circle with just a small additional bias.

3.1.4.4 Discussions

For shear walls with small or no interaction effects in the loading, the use of the ASCE 43-05 (Barda et al.) method has been shown to be very close and in most cases conservative when compared to the JNES/NUPEC test results based on walls having aspect ratios in the range of 0.47 to 0.87. For walls with more significant interaction effects, and to improve the accuracy of predicting shear wall strengths for walls with small and no interaction effects, an adjustment should be applied to the ASCE 43-05 method.

In both assessment approaches considering the single-wall and overall-box structure, the bi-axis effect is considered in a simplified fashion, in which the interaction intensity V_{VT}/V_{MT} is a global measure to the overall structure. For general nuclear power plant structures that usually do not resemble the test specimens in terms of equal shear strengths in the two horizontal directions, symmetric wall configurations, and other aspects, these simplified approaches may not necessarily be applicable. Further investigations are recommended to assess walls of aspect ratios smaller than 0.47 or greater than 0.87, and more detailed studies of the interaction effect in individual walls may also be needed for confirmation of the findings described above. Given the scope of this study however, the following remarks can be made.

To enhance the accuracy of the ASCE 43-05 method, an adjustment factor should be applied. This adjustment factor can be represented very well by a linear function of the aspect ratio. In addition, application of the ASCE 43-05 method should be cautioned for shear walls having an aspect ratio greater than 0.9.

With the adjustment to the ASCE 43-05 method, both approaches can accurately account for the bi-axis effect. The apparent high level of conservatism in V_U/V_{VT} can be removed by taking out the bias from the ASCE 43-05 method. The conservative bias introduced by the interaction effect is considered small.

Generally, the interaction should be dealt with in an analytical way, rather than simply addressing it in terms of the level of conservatism or unconservatism. However, for certain range of shear walls (in terms of aspect ratio) and certain loading conditions, the interaction effect may be negligible. For very small aspect ratios, the interaction effect can even be totally neglected no matter how severe it is.

In the case of nuclear power plant design, the common practice is to demonstrate that the three seismic input motions are statistically independent from one another. When the seismic loads in both horizontal directions are statistically uncorrelated, the shear forces V_X and V_Y can be combined probabilistically in accordance with the 100-40-40 rule:

$$V_{VT} = \sqrt{(V_1)^2 + (0.4V_2)^2}, \quad (3-26)$$

where V_1 (also V_{MT}) is the larger of V_X or V_Y , and V_2 is the lesser value. The maximum interaction intensity V_{VT}/V_{MT} is only:

$$\frac{V_{VT}}{V_{MT}} = \sqrt{1^2 + 0.4^2} = 1.077, \quad (3-27)$$

which corresponds to a loading angle of 21.8° . The unconservatism from the interaction effect is only 6.1% ($(1.077)^{0.8} = 1.061$ from Eq. 3-21). Thus, no significant unconservative bias is introduced by considering each direction independently so long as the bi-axis shear components are uncorrelated.

3.1.5 Application of ACI Methods to All Test Specimens

This section discusses the application of the ACI methods as described in Section 3.1.1 to the 11 test specimens. Shear strength capacities were calculated using ACI methods and compared against the test results in which the shear was calculated using: (1) the maximum shear of the two test directions and (2) the resultant of the bi-axis shears. Note that a regression analysis was not performed for the ACI methods because it is understood that ACI methods were developed with inherent conservatism for design purposes and a regression analysis would not yield much useful insights.

ACI 349 Chapter 11 Method

Table 3-7 presents the predicted (calculated) shear wall strengths, V_U , for the 11 specimens using the ACI 349 Chapter 11 method (described in Section 3.1.1 of this report). The calculation of the shear strength for all 11 cases is governed by the upper bound limit of $10hd\sqrt{f'_c}$, which is explained in Section 3.1.1. The tabulated data in the columns labeled V_U/V_{VT} and V_U/V_{MT} , in Table 3-7, are the ratios of the predicted capacity to the resultant test result and predicted capacity to the maximum test result of the two horizontal directions. Reviewing the ratios V_U/V_{VT} and V_U/V_{MT} indicates that the ACI 349 Chapter 11 method is conservative for all cases. The level of conservatism is very large for smaller aspect ratios and diminishes as the aspect ratio increases to 0.87.

ACI 349 Chapter 21 Method

Table 3-8 presents the predicted shear wall strengths for the 11 specimens using the ACI 349 Chapter 21 method (described in Section 3.1.1 of this report). The calculation of the shear strength for all 11 cases is also governed by the upper bound limit of $10A_{cp}\sqrt{f'_c}$, which is higher than the $10hd\sqrt{f'_c}$ used in the Chapter 11 method. The ratios of V_U/V_{VT} and V_U/V_{MT} show that this method is also conservative for all cases except for SD-10-45. The level of conservatism is large for smaller aspect ratios and diminishes as the aspect ratio increases. In the case of SD-10-00, which corresponds to the loading in the plane of the wall, the approach is still somewhat conservative. However, when the interaction effect is present in the test (i.e., specimen SD-10-45 acting at a 45 degree angle), the ratio of V_U/V_{MT} is greater than 1 indicating that the predicted strength is unconservative. If the interaction effect is directly considered as in the V_U/V_{VT} term, it results in a conservatively predicted value. The interaction intensity V_{VT}/V_{MT} for specimen SD-10-45 is at its maximum value of 1.414, which is however unlikely to be practical in a typical seismic design setting. As discussed in Section 3.1.4.4, if the seismic loads are combined probabilistically in accordance with the 100-40-40 rule, as in the common practices, the interaction intensity is limited to 1.077. This level of interaction would not be likely to introduce a significant unconservative bias to the predicted shear strength for this specimen.

Both ACI 349 methods appear to be quite conservative for walls with low aspect ratios (i.e., less than about 0.9, which is consistent with the data shown in Figure 3-1).

It should be noted that the above results using the ACI 349 Chapter 11 and 21 methods are based on the JNES/NUPEC test specimens and so caution should be exercised in extrapolating the conclusions to other configurations/designs.

3.2 Methods for Calculating Inelastic Energy Absorption Factor and Comparison to Test Results

This section of the report compares various methods used to account for the energy absorption behavior present when structures are subjected to cyclic earthquake motions. These methods calculate an inelastic energy absorption factor, F_μ , which accounts for the nonlinear behavior before failure occurs. The factor is a measure of the structure's capacity to absorb energy inelastically and thereby withstand earthquake motions stronger than would be predicted from a linear analysis. It is typically applied to reduce the linearly calculated response spectra (demand) or, alternatively, to increase the capacity of a structure. In the following subsections, the inelastic energy absorption factor F_μ from the JNES shaker table test (Torita, H., et al., 2004) will be determined and then the inelastic energy absorption factor calculated from several different methods will be described and compared to the results from the JNES tests.

3.2.1 Estimation of Inelastic Energy Absorption Factor for JNES Shaker Table Test

Parameters to be Used for Predicting the Inelastic Energy Absorption Factor

In order to utilize the various methods for calculating the inelastic energy absorption factor, some initial parameters such as the natural frequency, ductility factor and damping are needed. Since the JNES dynamic shaker table test utilized a series of increasing test motions to reach failure, the parameters needed for these methods must be based on the initial parameters for the last run preceding failure of the test specimen. Therefore, the next subsection will first determine the

initial parameters from the JNES test data needed for predicting the inelastic energy absorption factor, F_μ .

A summary of the JNES dynamic test and results is presented in Section 2 of this report with a more detailed description contained in Torita, H., et al., 2004. The specimen DT-B-02, used for the dynamic test, was subjected to a total of 8 complete excitations identified as Run 1, 2, 2', 3, 3', 4, 5, and 6. These were applied at increasing levels of acceleration and then failure occurred in Run 7. The test motion for Run 7 was short due to the failure of the box structure and it's not clear at what point in the motion the walls failed. Thus the test motion for Run 7 would not be appropriate for use in this evaluation. Therefore, for the evaluation of the various simplified analytical methods, the specimen properties prior to Run 6 will be used because failure occurred some time during the Run 7 motion.

Based on the test results at the start of Run 1, the elastic (initial) structural frequency, f , was 20.6 Hz and 20.4 Hz in the X and Y directions, respectively. At the start of Run 6, the initial frequency dropped to 13.0 Hz and 11.5 Hz in the X and Y directions, respectively. This demonstrates that significant degradation has occurred in the runs prior to Run 6. Table 3-9 shows the natural frequency for use in predicting F_μ for Run 6. Table 3-9 also shows the secant frequency f_s after Run 6 has been performed. All of the above values were taken from Torita et al., 2004. Next, the ductility factor μ associated with Run 6 is computed from

$$\mu = (f / f_s)^2 \quad (3-28)$$

and is also shown in Table 3-9. Lastly, Figures 22 through 24 of Reference [Torita et al., 2004], indicate that the effective viscous plus hysteretic damping β_e during the strong shaking portion of Run 5 was about 7%. From this information, an estimate of the viscous damping β at the start of Run 6 would be about 5%, which is also shown in Table 3-9.

Estimation of F_μ Associated with Run 6 Results for DT-B-02

The actual F_μ effect which occurred during Run 6 for DT-B-02 can be estimated from:

$$F_\mu = \frac{W(SA_{f,\beta})}{V_T g} \quad (3-29)$$

where,

- $SA_{f,\beta}$ = input spectral acceleration at frequency f and damping β
- V_T = maximum shear which occurred during Run 6 (g is gravity units)
- W = structure weight

Equation (3.2.1-1) can be solved for both X and Y-direction input.

For the X direction – compute F_μ

In the X direction for frequency $f = 13.0$ Hz, and $\beta = 5\%$

$$SA_{f,\beta} = 6.74 \text{ g}$$

$$W = 147,600 \text{ lbs}$$

$$V_{XT} = 1165 \text{ kN (From Torita et al.)}$$

$$F_{\mu} = \frac{147,600 \text{ lbs}(6.74)}{1165 \text{ kN}(224.8 \frac{\text{lbs}}{\text{kN}})} = 3.80 \quad (3-30)$$

For the Y direction – compute F_{μ}

In the y direction for frequency $f = 11.5$ Hz, and $\beta = 5\%$

$$SA_{f,\beta} = 7.60 \text{ g}$$

$$W = 147,600 \text{ lbs}$$

$$V_{YT} = 1296 \text{ kN (From Torita et al.)}$$

$$F_{\mu} = \frac{147,600 \text{ lbs}(7.60)}{1296 \text{ kN}(224.8 \frac{\text{lbs}}{\text{kN}})} = 3.85 \quad (3-31)$$

Such large F_{μ} factors are calculated for both X and Y directions because SA reduces very rapidly as the frequency is reduced from the initial frequencies f equal to 13 Hz and 11.5 Hz to the secant frequencies f_s equal to 7.3 and 6.4 Hz, as can be seen in Figure 3-7 and Figure 3-8.

3.2.2 Ridell-Newmark Method

Description of Methodology

The Riddell-Newmark Method (Riddell, R., and Newmark, N. M., 1979) is an approach to develop factors for constructing inelastic spectra from elastic spectra using the inelastic energy absorption factor F_{μ} . This enables users to perform an elastic response analysis which considers the nonlinear effects in elasto-plastic, bilinear, and stiffness degrading systems. Further guidance on the use of the Riddell-Newmark Method is presented in Kennedy, R. P., et al., 1988, Cover L. E., et al., 1985, and Kennedy R. P., et al., 2001.

At 33 Hz, the approximate expression (mean level)

For damping $\beta = 2\%$ and 5% :

$$F_{\mu} = \mu^{0.10} \quad (3-32)$$

For damping $\beta = 10\%$:

$$F_{\mu} = \mu^{0.13} \quad (3-33)$$

In the amplified spectral acceleration region

For damping β between 2% and 10% :

$$F_{\mu\alpha} = (\rho\mu - q)^r \quad (3-34)$$

where,

$\mu =$ ductility ratio (factor)

$$\rho = q + 1$$

$$q = 3.0\beta^{-0.30}$$

$$r = 0.48\beta^{-0.08}$$

The Riddell-Newmark method places a limitation on F_μ in the acceleration region if the spectral acceleration for the resulting inelastic spectrum (using F_μ from above) is less than the ZPA of the elastic spectrum.

In the amplified spectral velocity frequency region

For damping β between 2% and 10%:

$$F_{\mu v} = (\rho\mu - q)^r \quad (3-35)$$

$$F_\mu = F_{\mu v} C_f$$

where,

$$q = 2.7\beta^{-0.40}$$

$$r = 0.66\beta^{-0.04}$$

with μ and ρ as defined above.

$$\text{When } \left(\frac{f_k}{f} \right) < 1.0 \text{ then } C_f = \left(\frac{f_k}{f} \right)$$

$$\left(\frac{f_k}{f} \right) \geq 1.0 \text{ then } C_f = 1.0$$

Where f_k is the knuckle frequency (i.e., frequency at transition from acceleration to velocity region in the spectra) and f is the elastic natural frequency. This knuckle frequency can be approximated by:

$$f_k = \frac{SA_{\max}}{(SA/f)_{\max}} \quad (3-36)$$

where SA_{\max} is the maximum spectral acceleration and $(SA/f)_{\max}$ is the maximum spectral velocity divided by 2π .

Application of Ridell-Newmark Method to JNES Test

The Riddell-Newmark method was utilized to determine the inelastic energy absorption factor F_μ for Run 6 in the JNES Shaker table test (Torita, H., et al., 2004). This was done separately for the X and Y directions as shown below:

For the X direction:

Amplified Spectral Acceleration Region –

Using 5% damping ($\beta = 5$) and $\mu = 3.17$ (from Table 3-9), the parameters for use in Eq. 3-34 are:

$$q_a = 1.851 \qquad r_a = 0.422 \qquad \rho = 2.851$$

Substituting these values into Eq. 3-34 results in

$$F_{\mu a} = [(2.851)(3.17) - 1.851]^{0.422} = 2.30$$

Amplified Spectral Velocity Region –

$$q_v = 1.418 \qquad r_v = 0.619 \qquad \rho = 2.418$$

$$F_{\mu v} = [(2.418)(3.17) - 1.418]^{0.619} = 3.11$$

For the 5% damped response spectrum for Run 6 X-direction;

$$SA_{\max} = 9.74 \text{ g at } 16.6 \text{ Hz}$$

$$(SA/F)_{\max} = 0.669 \text{ g - sec at } 2.88 \text{ Hz}$$

$$f_k = \frac{9.74}{.669} = 14.56 \text{ Hz}$$

Since f_k is greater than f (= 13.0 Hz from Table 3-9),

$$C_f = 1.0$$

and F_{μ} equals:

$$F_{\mu} = F_{\mu v}(C_f) = 3.11 (1.0) = 3.11$$

At frequencies below f_k (velocity region), $F_{\mu} = 3.11$.

For the Y direction:

Amplified Spectral Acceleration Region –

Using 5% damping ($\beta = 5$) and $\mu = 3.23$ (from Table 3-9), the parameters for use in Eq. (3.2.2-3) are:

$$q_a = 1.851 \qquad r_a = 0.422 \qquad \rho = 2.851$$

Substituting these values into Eq. 3-34 results in

$$F_{\mu a} = [(2.851)(3.23) - 1.851]^{0.422} = 2.32$$

Amplified Spectral Velocity Region –

$$q_v = 1.418 \qquad r_v = 0.619 \qquad \rho = 2.418$$

$$F_{\mu v} = [(2.418)(3.23) - 1.418]^{0.619} = 3.15$$

For the 5% damped response spectrum for Run 6 Y-direction;

$$SA_{\max} = 7.60 \text{ g at } 11.48 \text{ Hz}$$

$$(SA/F)_{\max} = 0.662 \text{ g-sec at } 11.48 \text{ Hz}$$

$$f_k = \frac{7.60}{.662} = 11.48 \text{ Hz}$$

In this case, the response spectrum is so narrow peaked that SA_{\max} and $(SA/f)_{\max}$ both occur at the same frequency and therefore, the knuckle frequency is clearly 11.48 Hz.

For $f = 11.5$ Hz from Table 3-9:

$$C_f = \frac{f_k}{f} = \frac{11.48}{11.5} = 0.998$$

and F_{μ} equals:

$$F_{\mu} = F_{\mu v}(C_f) = 3.15 (0.998) = 3.14$$

At frequencies below f_k (velocity region), $F_{\mu} = 3.14$.

Comparison to Test Data

Table 3-10 compares F_{μ} predicted by the Riddell-Newmark Method in the X and Y directions with the estimated F_{μ} given by Eq. 3-31 for Run 6. This comparison shows that the Riddell-Newmark method under predicts F_{μ} by 19.2% and 18.4% in the X and Y directions, respectively. A closer comparison was not achieved because the Riddell-Newmark Method was intended for use with broad frequency design-type response spectra. As shown in Figure 3-7 and Figure 3-8, the input motions are narrow frequency spectra.

3.2.3 Effective Frequency/Effective Damping Methods (EFED)

Other methods have been developed based on the effective frequency/effective damping of the structure. Two approaches that fall into this category are called the Point Estimate Method and the Spectral Averaging Method. Both of these methods are described below with more detailed information presented in Kennedy, R. P., et al., 1984.

Point Estimate Method

In this method, the ratio of secant frequency to elastic frequency is determined from

$$\frac{f_s}{f} = \sqrt{\frac{1}{\mu}} \quad (3-37)$$

The effective frequency can be calculated from

$$\frac{f_e}{f} = (1 - A) + A \left(\frac{f_s}{f} \right) \quad (3-38)$$

where

$$A = C_F \left[1 - \frac{f_s}{f} \right] \quad (3-39)$$

which is to be taken less than or equal to 0.85.

C_F can be obtained from Table 4-2 of Reference [Kennedy, R. P., et al., 1984].

The effective damping can be estimated from

$$\beta_e = \left(\frac{f_s}{f_e} \right)^2 (\beta + \beta_H) \quad (3-40)$$

where β is the elastic damping and β_H is the pinched hysteretic damping which is approximated by

$$\beta_H = C_N \left(1 - \frac{f_s}{f} \right) \quad (3-41)$$

for strong durations greater than one second.

C_N can also be obtained from Table 4-2 of Reference [Kennedy, R. P., et al., 1984].

Then, the effective frequency and effective damping are used to obtain the spectral acceleration from the response spectrum curve, whose value is denoted by SA_{f_e, β_e} .

The inelastic energy absorption value F_μ is given by

$$F_\mu = \left(\frac{f_e}{f_s} \right)^2 \left[\frac{SA_{f, \beta}}{SA_{f_e, \beta_e}} \right] \quad (3-42)$$

Application of Methodology to Run 6 Test

For the X direction:

$$\frac{f_s}{f} = \frac{7.3}{13.0} = 0.562$$

From Table 4-2 of Kennedy, R. P., et al., 1984, $C_F = 2.3$. Therefore,

$$A = 2.3[1 - 0.562] = 1.007$$

which exceeds the upper limit on A of 0.85. Therefore,

$$\frac{f_e}{f} = (1 - 0.85) + 0.85(0.562) = 0.628$$

$$f_e = (0.628)(13.0) = 8.16 \text{ Hz}$$

Next, β_H is calculated using $C_N = 0.11$ (from Table 4-2 of Reference [Kennedy, R. P., et al., 1984]):

$$\beta_H = 0.11(1 - 0.562) = 0.0482$$

For an elastic damping $\beta = 5\%$, the effective damping is:

$$\beta_e = \left(\frac{7.3}{8.16} \right)^2 (5 + 4.82) = 7.86\%$$

From interpolation of the X-direction response spectra, the spectral acceleration at the effective frequency f_e and effective damping β_e is estimated to be:

$$SA_{f_e, \beta_e} = 1.79g$$

and for $f = 13.0$ Hz, and $\beta = 5\%$

$$SA_{f, \beta} = 6.74g$$

Thus:

$$F_\mu = \left(\frac{f_e}{f_s} \right)^2 \left[\frac{SA_{f, \beta}}{SA_{f_e, \beta_e}} \right] = \left(\frac{8.16}{7.3} \right)^2 \left[\frac{6.74}{1.79} \right] = 4.70$$

Comparison to Test Data

Table 3-10 compares F_μ predicted by the EFED Point Estimate Method in the X direction with the estimated F_μ given by Eq. (3.2.1-4) for Run 6. This comparison shows that the EFED Point

Estimate Method over predicts F_μ by 22.1% in the X direction. The problem is that a local valley exists in the X-direction response spectrum between 5.5 Hz and 10 Hz. Therefore, the spectral accelerations between 7.3 Hz and about 9.5 Hz are actually less than they are at 7.3 Hz. Experience using the EFED Method suggests that when a local valley exists in the response spectra at frequencies above the secant frequency, one should limit F_μ to no more than the F_μ computed by the Secant Frequency Method described below.

Secant Frequency Method:

In this method, f_e is replaced by f_s . Thus,

$$f_e = f_s = 7.3 \text{ Hz}$$

$$\beta_e = (\beta + \beta_H) = (5\% + 4.82\%) = 9.82\%$$

from which:

$$SA_{f_e, \beta_e} = 2.03g$$

$$F_\mu = \frac{SA_{f, \beta}}{SA_{f_e, \beta_e}} = \frac{6.74}{2.03} = 3.32$$

which agrees closely with the estimated $F_\mu=3.85$ for Run 6.

It is recommended that F_μ computed by either the EFED Point Estimate Method or the EFED Spectral Averaging Method (discussed later) should be limited to no more than F_μ computed by the Secant Frequency Method described above.

For the Y direction:

$$\frac{f_s}{f} = \frac{6.4}{11.5} = 0.557$$

From Table 4-2 of Kennedy, R. P., et al., 1984, $C_F = 2.3$. Therefore,

$$A = 2.3[1 - 0.557] = 1.02$$

which exceeds the upper limit on A of 0.85. Therefore,

$$\frac{f_e}{f} = (1 - 0.85) + 0.85(0.557) = 0.623$$

$$f_e = (0.623)(11.5) = 7.17 \text{ Hz}$$

Next, β_H is calculated using $C_N = 0.11$ (from Table 4-2 of Reference [Kennedy, R. P., et al., 1984]):

$$\beta_H = 0.11(1 - 0.557) = 0.0488$$

For an elastic damping $\beta = 5\%$, the effective damping is:

$$\beta_e = \left(\frac{6.4}{7.17} \right)^2 (5 + 4.88) = 7.87\%$$

From interpolation of the y-direction response spectra, the spectral acceleration at the effective frequency f_e and effective damping β_e is estimated to be:

$$SA_{f_e, \beta_e} = 1.93g$$

and for $f = 11.5$ Hz, and $\beta = 5\%$

$$SA_{f, \beta} = 7.6g$$

Thus:

$$F_\mu = \left(\frac{f_e}{f_s} \right)^2 \left[\frac{SA_{f, \beta}}{SA_{f_e, \beta_e}} \right] = \left(\frac{7.17}{6.4} \right)^2 \left[\frac{7.6}{1.93} \right] = 4.94$$

Comparison to Test Data

Table 3-10 compares F_μ predicted by the EFED Point Estimate Method in the Y direction with the estimated F_μ given by Eq. (3.2.1-4) for Run 6. This comparison shows that the EFED Point Estimate Method over predicts F_μ by 28.3% in the Y direction. As before for the X direction, the problem is that a local valley exists in the Y-direction response spectrum between 5.5 Hz and 8.5 Hz. Therefore, the spectral accelerations between 6.4 Hz and about 8.3 Hz are actually less than they are at 6.4 Hz. When a local valley exists in the response spectra at frequencies above the secant frequency, one should limit F_μ to no more than the F_μ computed by the Secant Frequency Method.

Secant Frequency Method

f_e is replaced by f_s . Thus,

$$f_e = f_s = 6.4 \text{ Hz}$$

$$\beta_e = (\beta + \beta_H) = (5\% + 4.88\%) = 9.88\%$$

from which:

$$SA_{f_e, \beta_e} = 1.86g$$

$$F_{\mu} = \frac{SA_{f,\beta}}{SA_{f_e,\beta_e}} = \frac{7.59}{1.86} = 4.08$$

which agrees closely with the estimated $F_{\mu}=3.85$ for Run 6.

As stated earlier, it is recommended that F_{μ} computed by either the EFED Point Estimate Method or the EFED Spectral Averaging Method (discussed later) should be limited to no more than F_{μ} computed by the Secant Frequency Method described above.

Spectral Averaging Method

In this method, the ratio of secant frequency to elastic frequency is determined from

$$\frac{f_s}{f} = \sqrt{\frac{K_s}{K}}$$

where K is the initial (elastic) stiffness and K_s is the effective stiffness during nonlinear response corresponding to different resistance functions. The secant stiffness is defined by:

$$k_s = \frac{V_U}{\delta_U}$$

where V_U is the ultimate strength reached, and δ_U is the ultimate deformation associated with reaching V_U .

An upper frequency is also calculated using the expression:

$$\frac{f_u}{f} = (1 - B) + B \frac{f_s}{f}$$

where

$$B = 2C_F \left(1 - \frac{f_s}{f} \right) - 1 \quad \text{except that } B \text{ must be } \geq 0 \text{ and } \leq 0.7.$$

C_F was defined previously under the Point Estimate Method.

The effective frequency is given by:

$$f_{ea} = \frac{(f_u + f_s)}{2} \quad \text{which is the average of the upper frequency and the secant frequency.}$$

The effective hysteretic damping is:

$$\beta_H = C_N \left(1 - \frac{f_s}{f} \right)$$

C_N was defined previously under the Point Estimate Method.

The effective damping is given by:

$$\beta_{ea} = \left(\frac{f_s}{f_{ea}} \right)^2 (\beta + \beta_H)$$

Finally, the inelastic energy absorption factor can be calculated from the expression:

$$F_\mu = \mu \left(\frac{f_{ea}}{f} \right)^2 \frac{SA_{f,\beta}}{\overline{SA}_{(f_u-f_s),\beta_{ea}}}$$

where $SA_{f,\beta}$ is the spectral acceleration at the frequency f and damping β , while $\overline{SA}_{(f_u-f_s),\beta_{ea}}$ is the average spectral acceleration between the secant frequency and the upper frequency at the effective damping β_{ea} .

Application of Methodology to Run 6 Test

For the X direction:

$$\frac{f_s}{f} = \frac{7.3}{13.0} = 0.562$$

$$B = 2(2.3)(1 - 0.562) - 1 = 1.01$$

which exceeds the upper limit of B equal to 0.70. Therefore, the upper frequency can be calculated from:

$$\frac{f_u}{f} = (1 - 0.70) + (0.70)(0.562) = 0.693$$

$$f_u = 0.693(13.0) = 9.01 \text{ Hz}$$

$$f_{ea} = \frac{(9.01 + 7.3)}{2} = 8.16 \text{ Hz}$$

Next, the effective hysteretic damping is:

$$\beta_H = 0.11(1 - 0.562) = 0.0482$$

For an elastic damping $\beta = 5\%$, the effective damping is:

$$\beta_{ea} = \left(\frac{7.3}{8.16} \right)^2 (5 + 4.82) = 7.86\%$$

Thus, the average spectral acceleration between the secant frequency f_s and the upper frequency f_u at $\beta_{ea} = 7.86\%$ was obtained using the 8% spectrum curve:

$$\overline{SA}_{(f_u-f_s),\beta_{ea}} = 1.93g$$

For $f = 13.0$ Hz, and $\beta = 5\%$:

$$SA_{f,\beta} = 6.74g$$

and from Table 3-3, $\mu = 3.17$. Thus:

$$F_\mu = \mu \left(\frac{f_{ea}}{f} \right)^2 \frac{SA_{f,\beta}}{\overline{SA}_{(f_u-f_s),\beta_{ea}}} = 3.17 \left(\frac{8.16}{13.0} \right)^2 \left[\frac{6.74}{1.93} \right] = 4.36$$

For the Y direction:

$$\frac{f_s}{f} = \frac{6.4}{11.5} = 0.557$$

$$B = 2(2.3)(1 - 0.557) - 1 = 1.04$$

which exceeds the upper limit of B equal to 0.70. Therefore, the upper frequency can be calculated from:

$$\frac{f_u}{f} = (1 - 0.70) + (0.70)(0.557) = 0.690$$

$$f_u = 0.690(11.5) = 7.93 \text{ Hz}$$

$$f_{ea} = \frac{(7.93 + 6.4)}{2} = 7.17 \text{ Hz}$$

Next, the effective hysteretic damping is:

$$\beta_H = 0.11(1 - 0.557) = 0.0487$$

For an elastic damping $\beta = 5\%$, the effective damping is:

$$\beta_{ea} = \left(\frac{6.4}{7.17} \right)^2 (5 + 4.87) = 7.86\%$$

Thus, the average spectral acceleration between the secant frequency f_s and the upper frequency f_u at $\beta_{ea} = 7.87\%$ was obtained using the 8% spectrum curve:

$$\overline{SA}_{(f_u-f_s),\beta_{ea}} = 1.87 g$$

For $f = 11.5$ Hz, and $\beta = 5\%$:

$$SA_{f,\beta} = 7.6 g$$

and from Table 3-3, $\mu = 3.23$. Thus:

$$F_\mu = \mu \left(\frac{f_{ea}}{f} \right)^2 \frac{SA_{f,\beta}}{\overline{SA}_{(f_u-f_s),\beta_{ea}}} = 3.23 \left(\frac{7.17}{11.5} \right)^2 \left[\frac{7.6}{1.87} \right] = 5.10$$

Comparison to Test Data

Table 3-10 compares F_μ predicted by the EFED Spectral Averaging Method in the X and Y directions with the estimated F_μ given by Eq. 3-31 for Run 6. This comparison shows that the EFED Spectral Averaging Method over predicts F_μ by 13.2% in the X direction and 32.5% in the Y direction. The EFED Spectral Averaging Method over predicts the estimated F_μ for Run 6 for the same reasons as previously discussed for the EFED Point Estimate Method. Again, F_μ should be limited to no more than F_μ computed by the Secant Frequency Method.

Overall Observations on Methods for Calculating Inelastic Energy Absorption Factors

Table 3-10 compares the inelastic energy absorption factor F_μ predicted by four different methods against the estimated F_μ derived from the JNES shaker table test. The first method called the Riddell-Newmark Method under predicted F_μ by about 18 to 19% in the X and Y directions, respectively. While this is still considered to be a reasonable comparison, the Riddell-Newmark Method was intended for use with broad frequency design-type response spectra. As shown in Figure 3-7 and Figure 3-8, the input motions for the test specimens were narrow frequency spectra.

Other methods have been developed based on the effective frequency/effective damping (EFED) of the structure. Two approaches that fall into this category are called the Point Estimate Method and the Spectral Averaging Method. For the EFED Point Estimate Method, Table 3-10 shows that this approach over predicted the F_μ values by about 22 to 28% in the X and Y directions, respectively. This occurred because there is a local valley in the response spectra at frequencies above the secant frequency. When this occurs, one should limit F_μ to no more than the F_μ computed by the Secant Frequency Method.

Using the Spectral Averaging Method, Table 3-10 shows that this approach also over predicted the F_μ values, in this case by about 13 to 33% in the X and Y directions, respectively. The EFED Spectral Averaging Method over predicted the estimated F_μ value for the same reason as previously discussed for the EFED Point Estimate Method. Again, F_μ should be limited to no more than F_μ computed by the Secant Frequency Method.

The calculation for the Secant Frequency Method provided the best comparison to the test data. Table 3-10 shows that this approach under predicted the F_μ value in the X direction by about 14%

and over predicted the F_{μ} value by about 6% in the Y direction. Therefore, for this specimen configuration and earthquake motion, the Secant Frequency Method provided the most accurate overall comparison to the test results. Because the comparison for the Secant Frequency Method was quite good, the results also suggest that the effect of the multi-direction excitation of the box-type reinforced concrete specimen did not significantly affect the calculation of the inelastic energy absorption factor.

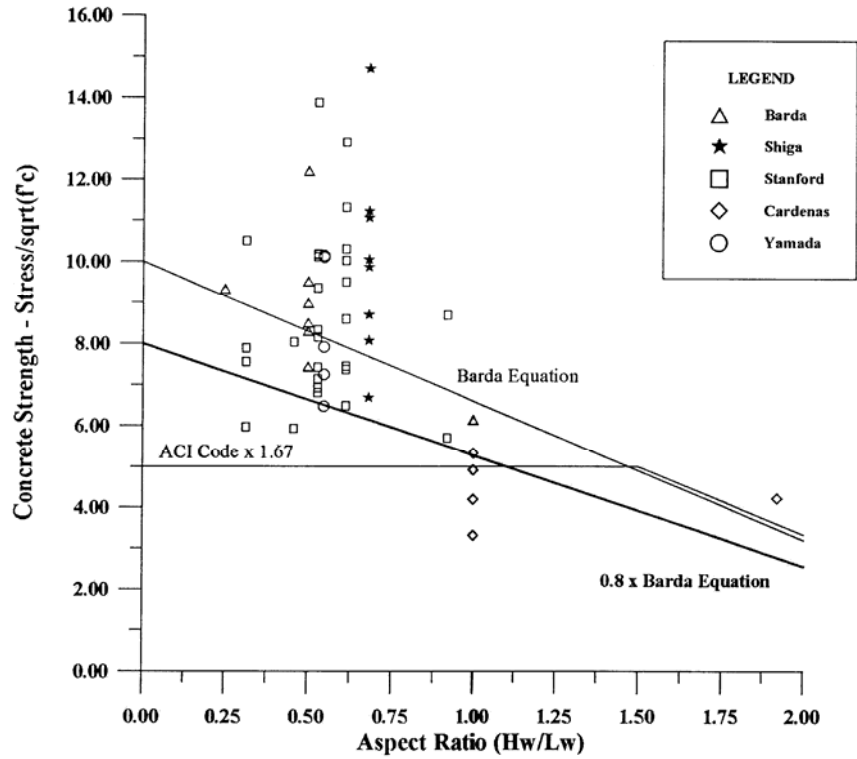


Figure 3-1 Concrete Shear Wall Strength as a Function of Aspect Ratio
 [from ASCE 43-05, 2004, With permission from ASCE]

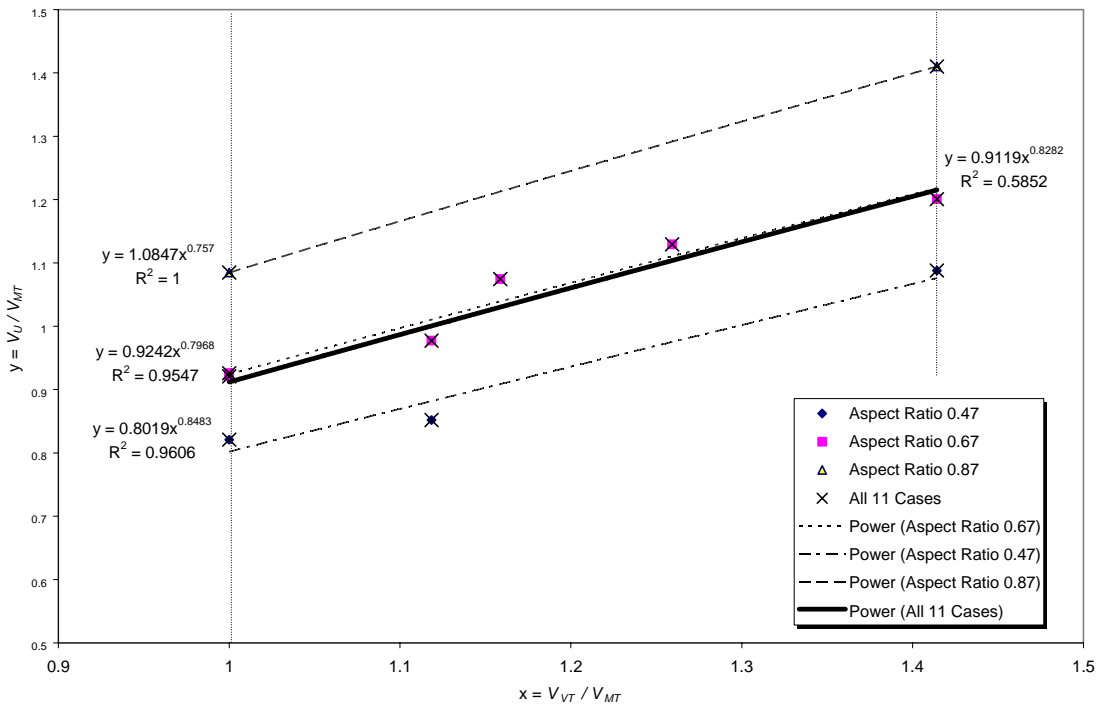


Figure 3-2 Regression Analysis of V_U/V_{MT} vs. V_{VT}/V_{MT}

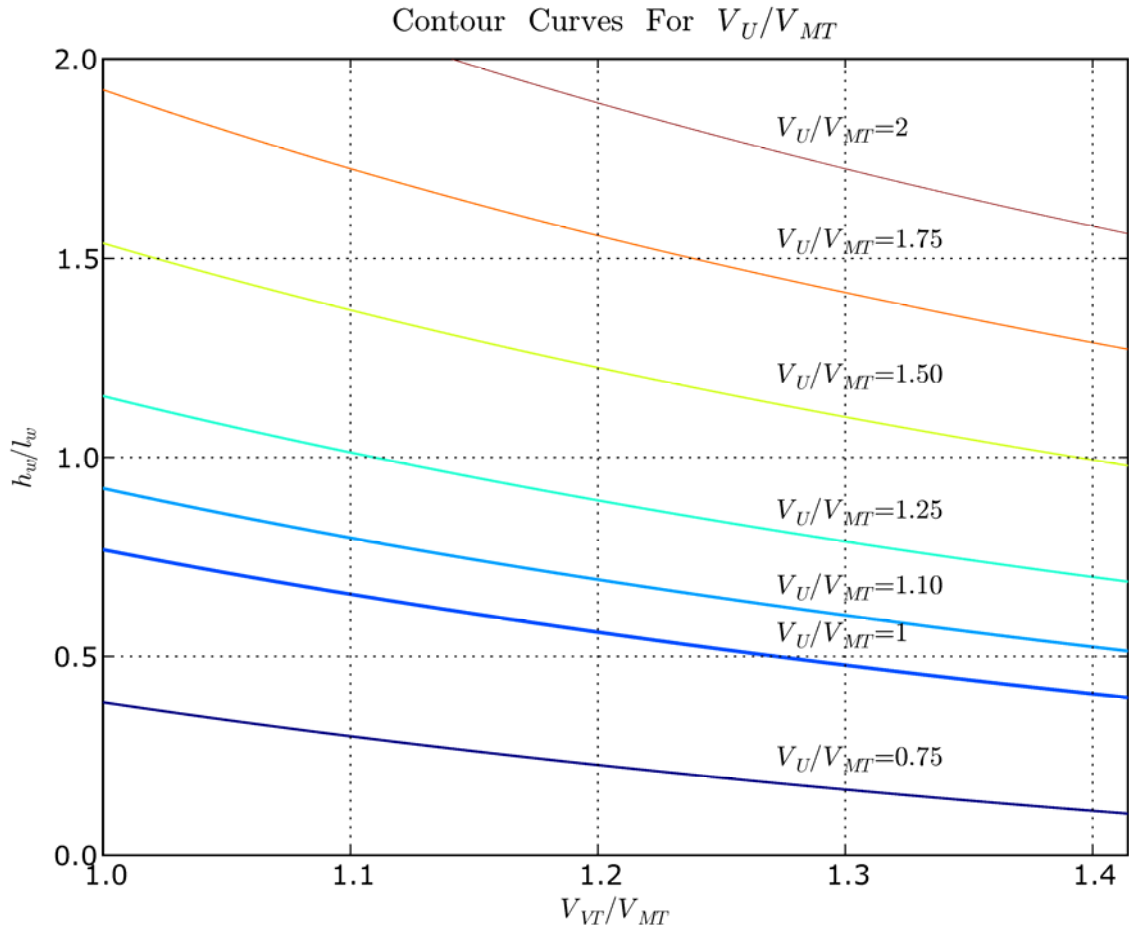


Figure 3-3 Contour Plot of Eq. 3-19

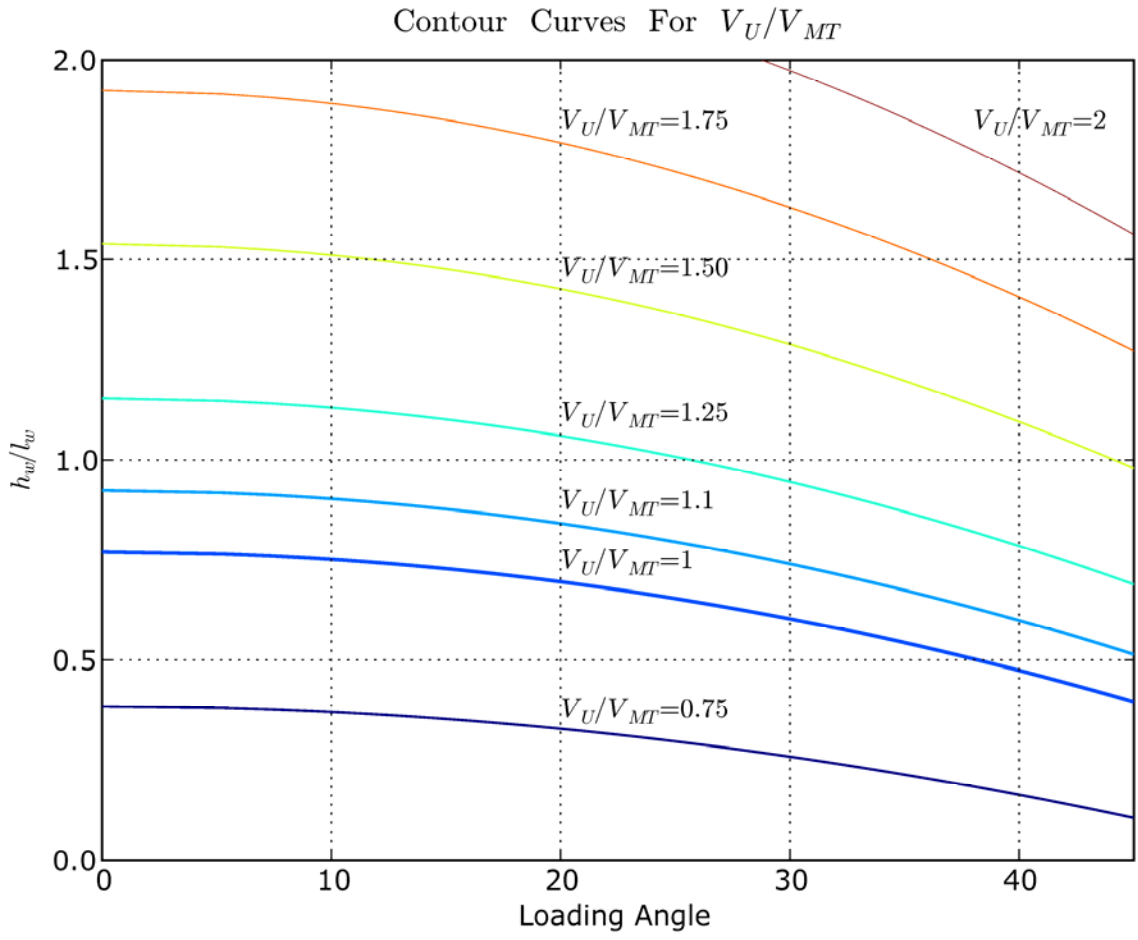


Figure 3-4 Contour Plot of Eq. 3-19 in Terms of Loading Angle

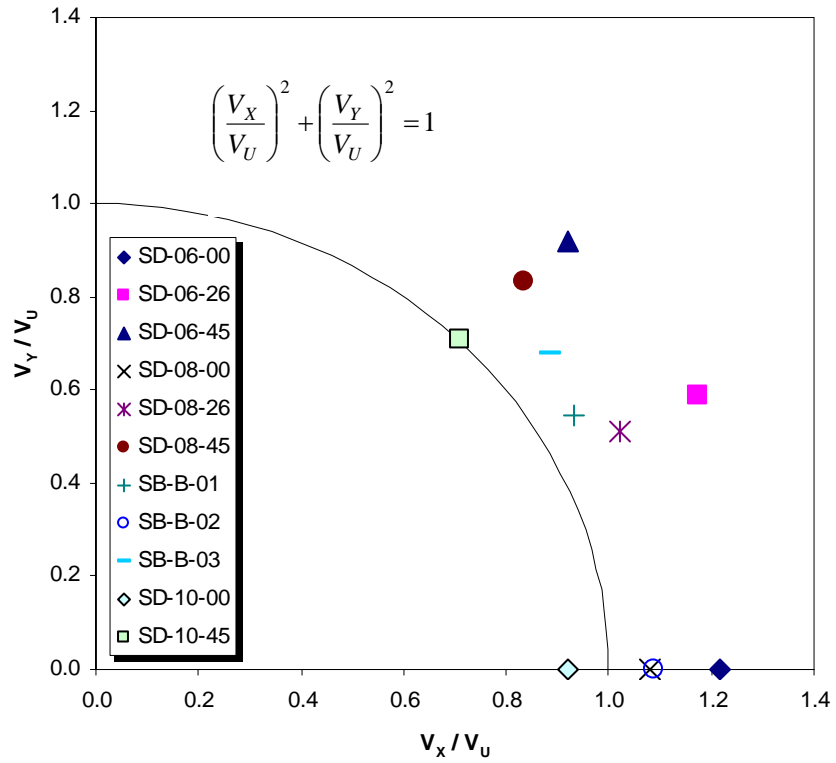


Figure 3-5 Maximum Vector Shear Forces Normalized by V_U

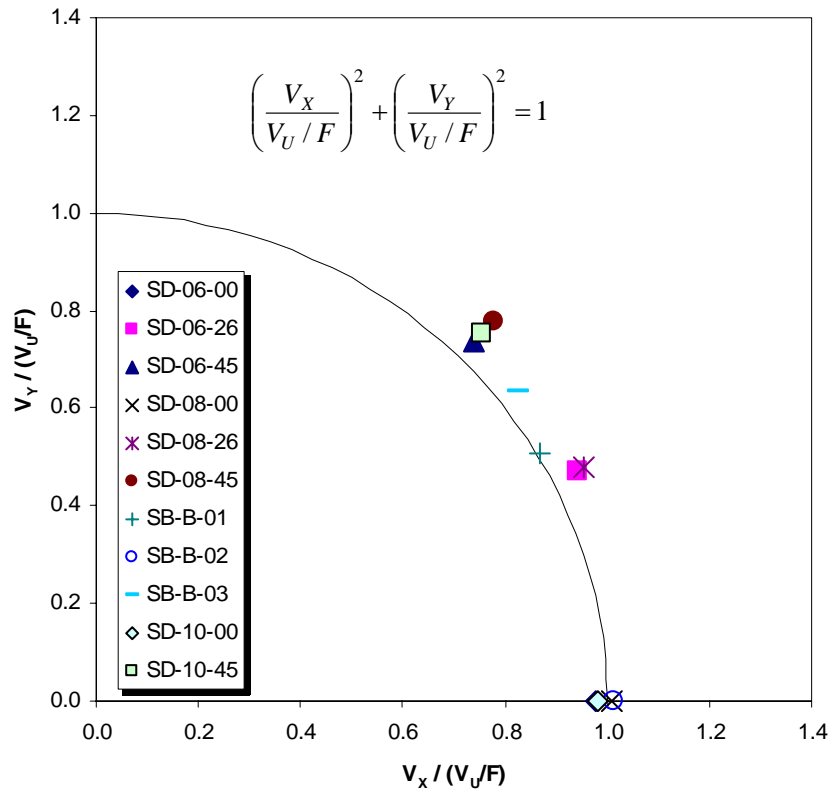


Figure 3-6 Maximum Vector Shear Forces Normalized by V_U/F

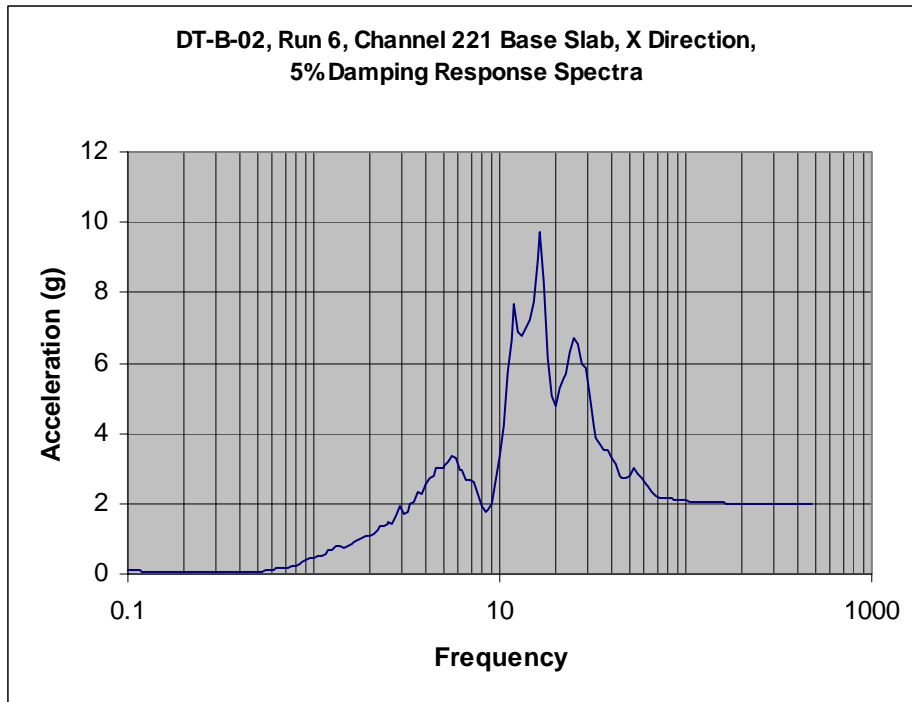


Figure 3-7 JNES Shaker Table Input Spectra X Direction, 5% Damping

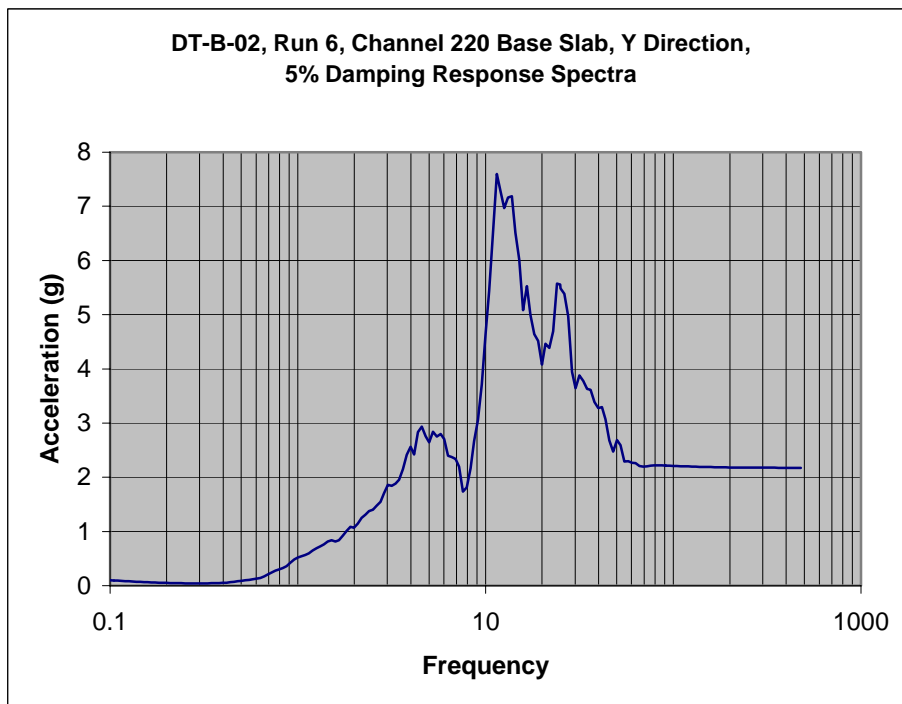


Figure 3-8 JNES Shaker Table Input Spectra Y Direction, 5% Damping

Table 3-1 Specimen Properties and Shear Strengths

Specimen	f'_c (MPa)	f_y (MPa)	h_w (m)	h_w/l_w	V_{MT} (kN)	V_{VT} (kN)
SD-06-00	30.7	345	0.7	0.47	1686	1686
SD-06-26	29.2	345	0.7	0.47	*1604.11	1794
SD-06-45	33.2	345	0.7	0.47	*1297.54	1835
SD-08-00	34.9	345	1	0.67	1480	1480
SD-08-26	34.8	345	1	0.67	*1401.14	1567
SD-08-45	37.4	345	1	0.67	*1161.07	1642
SB-B-01	41.3	375	1	0.67	1381	1600
SB-B-02	39.7	375	1	0.67	1596	1596
SB-B-03	34.9	375	1	0.67	1261	1588
SD-10-00	37.8	345	1.3	0.87	1231	1231
SD-10-45	37.2	345	1.3	0.87	*943.28	1334

* calculated value by BNL.

Table 3-2 Summary of Results using ASCE (Barda et al.) Method

Specimen	h_w/l_w	V_U (kN)	V_U/V_{VT}	V_U/V_{MT}	V_{VT}/V_{MT}
SD-06-00	0.47	1383.89	0.821	0.821	1
SD-06-26	0.47	1366.65	0.762	0.852	1.118
SD-06-45	0.47	1411.70	0.769	1.088	1.414
SD-08-00	0.67	1369.98	0.926	0.926	1
SD-08-26	0.67	1369.00	0.874	0.977	1.118
SD-08-45	0.67	1394.01	0.849	1.201	1.414
SB-B-01	0.67	1483.95	0.928	1.075	1.159
SB-B-02	0.67	1469.42	0.921	0.921	1
SB-B-03	0.67	1423.98	0.897	1.129	1.259
SD-10-00	0.87	1335.30	1.085	1.085	1
SD-10-45	0.87	1330.13	0.997	1.410	1.414

Table 3-3 Comparison of Prediction Equation to Test Results

Specimen	ASCE 43-05 V_U/V_{MT}	Eq. 3-19 V_U/V_{MT}	Ratio Eq. 3-19 / ASCE 43-05
SD-06-00	0.821	0.804	0.979
SD-06-26	0.852	0.879	1.031
SD-06-45	1.088	1.060	0.975
SD-08-00	0.926	0.934	1.008
SD-08-26	0.977	1.021	1.045
SD-08-45	1.201	1.232	1.026
SB-B-01	1.075	1.050	0.977
SB-B-02	0.921	0.934	1.014
SB-B-03	1.129	1.123	0.994
SD-10-00	1.085	1.064	0.981
SD-10-45	1.410	1.403	0.995

Median Ratio = 1.002 , $\beta_{EQN}=0.024$

Table 3-4 Values of F

h_w/l_w	F
0.35	0.728
0.47	0.806
0.50	0.825
0.67	0.936
0.77	1.001
0.87	1.066
0.90	1.085
1.00	1.150
1.50	1.475
2.00	1.800

Table 3-5 Interaction Effect in Eq. 3-19

V_{VT}/V_{MT}	$(V_{VT}/V_{MT})^{0.8}$	$0.2+0.8 V_{VT}/V_{MT}$
1.000	1.000	1.000
1.077	1.061	1.062
1.120	1.095	1.096
1.159	1.125	1.127
1.259	1.202	1.207
1.414	1.319	1.331

Table 3-6 Interaction Effect in Eq. 3-24

V_{VT}/V_{MT}	$(V_{VT}/V_{MT})^{0.2}$	$0.8+0.2 V_{VT}/V_{MT}$
1.000	1.000	1.000
1.077	1.015	1.015
1.120	1.023	1.024
1.159	1.030	1.032
1.259	1.047	1.052
1.414	1.072	1.083

Table 3-7 Summary of Results using ACI 349 Chapter 11 Method

Specimen	h_w/l_w	V_U (kN)	V_U/V_{VT}	V_U/V_{MT}
SD-06-00	0.47	828.14	0.491	0.491
SD-06-26	0.47	807.65	0.450	0.504
SD-06-45	0.47	861.19	0.469	0.664
SD-08-00	0.67	882.97	0.597	0.597
SD-08-26	0.67	881.70	0.563	0.629
SD-08-45	0.67	914.05	0.557	0.787
SB-B-01	0.67	960.52	0.600	0.696
SB-B-02	0.67	941.73	0.590	0.590
SB-B-03	0.67	882.97	0.556	0.700
SD-10-00	0.87	918.92	0.747	0.747
SD-10-45	0.87	911.60	0.683	0.966

Table 3-8 Summary of Results using ACI 349 Chapter 21 Method

Specimen	h_w/l_w	V_U (kN)	V_U/V_{VT}	V_U/V_{MT}
SD-06-00	0.47	1035.17	0.614	0.614
SD-06-26	0.47	1009.56	0.563	0.629
SD-06-45	0.47	1076.49	0.587	0.830
SD-08-00	0.67	1103.71	0.746	0.746
SD-08-26	0.67	1102.13	0.703	0.787
SD-08-45	0.67	1142.56	0.696	0.984
SB-B-01	0.67	1200.65	0.750	0.869
SB-B-02	0.67	1177.16	0.738	0.738
SB-B-03	0.67	1103.71	0.695	0.875
SD-10-00	0.87	1148.65	0.933	0.933
SD-10-45	0.87	1139.50	0.854	1.208

Table 3-9 Parameters to be Used for Predicting F_μ for Run 6 on DT-B-02

Parameter	Direction	
	X	Y
Frequency f (Hz)	13.0	11.5
Secant Freq. f_s (Hz)	7.3	6.4
Ductility Factor μ	3.17	3.23
Viscous Damping β (%)	5.0	5.0

Table 3-10 Comparison of Predicted Versus Estimated F_μ Factors for Run 6 Y-Direction, Structure DT-B-02 (Estimated $F_\mu = 3.85$ from JNES Test)

Method	Predicted F_μ		% Deviation From Estimated	
	X	Y	X	Y
<u>Riddell-Newmark Method</u>	3.11	3.14	-19.2%	-18.2%
<u>Eff. Freq/Eff Damping Methods</u>				
Point Estimate	4.70	4.94	+22.1%	+28.3%
Spectral Averaging	4.36	5.10	+12.5%	+33.2%
Secant Freq. Limit	3.32	4.08	-13.8%	+6.0%

4 ANACAP 3-D FINITE ELEMENT ANALYSIS OF STATIC CYCLIC TESTS

This section describes the analytical prediction of the performance of a box-shaped shear wall under one- or two-directional cyclic loading, using the concrete analysis code ANACAP, Version 3. In Subsection 4.1, the specimen used in both the NUPEC test and the BNL analysis will be briefly overviewed and the associated cyclic loading scenarios will be described. The ANACAP concrete model, the finite element model of the shear wall, and the static analysis procedure are introduced in Subsection 4.2. The analytical results and their comparisons to the test results are given in Subsection 4.3, and the findings learnt from the static analyses are summarized in the last subsection.

4.1 Specimens and Loadings

This subsection provides briefly the background information of the NUPEC tests and identifies a common specimen configuration to be used in all static cyclic loading analyses in this study. The loading scenarios, each of which corresponds to a specific specimen, will also be discussed in the following.

4.1.1 The NUPEC Specimens

As described in Section 2, NUPEC conducted several box-shaped and circular-shaped shear wall model tests subjected to multi-directional loading simultaneously. These tests were an effort to validate the design methodologies used in Japan, which obtains the design loads independently for different directions and does not reflect the reality that an earthquake strikes a structure in all directions at the same time. The base shear capacity of the shear walls was the major parameter used in the tests to evaluate the effect of the simultaneous multi-directional loadings. Each specimen, which was actuated by a particular cyclic loading sequence, experienced linear and significant nonlinear deformations and finally deformed to failure at the last loading cycle. These tests provide valuable insights on the shear force capacity and the force-deformation relation of the shear walls subjected to multi-directional cyclic loadings, and put forward a valuable benchmark for the analytical predictions using the ANACAP software.

Among the various configurations of the shear wall used in the NUPEC tests, one box-shaped shear wall with a shear span ratio 0.8 is selected as a common model for the analytical study in this report. This configuration will be used for all the cyclic loading scenarios described in this section, and also for the analyses of the multi-directional shaking table tests to be described in the next section. Figure 4-1 illustrates the elevation and plan views of this model. The shear wall has four faces of identical dimensions that form a square in plan; each face is 1000 mm tall, 1500 mm wide (center to center), and 75 mm thick. The loading slab on the top of the shear wall is 400 mm thick and 2700 mm in both sides in plan. The base slab has the same dimensions as the loading slab except that it has a thickness of 500 mm.

The rebars have a diameter of 6 mm and are arranged in a double layer bi-directional configuration as shown in Figure 4-2. For each layer, the rebars are placed in a grid that has a spacing of 70 mm x 70 mm on average, which approximately results in a reinforcement ratio of 1.2%. The anchorage length of the vertical rebars is 300 mm into the loading slab and 500 mm into the base slab, and had been shown in the tests adequate in preventing any anchorage loss. The maximum size of the aggregate used in the concrete wall is about 10 mm.

Although only one model configuration has been identified, it corresponds to 4 specimens in the NUPEC tests. Each of these 4 specimens was subjected to a unique cyclic loading pattern, which will be described in the next subsection, and has its own material properties for the concrete and

the rebars. The material properties for the 4 specimens are summarized in Table 4.1, in which the four specimens, using the same terms as in the NUPEC tests, are designated as SD-08-00, SB-B-01, SB-B-02, and SB-B-03. No material properties have been given in Table 4.1 to the loading slab and the base slab because they had higher strengths than the shear wall in the tests and will be assumed rigid in the analysis.

4.1.2 Cyclic Loading Scenarios

In the NUPEC tests, the various loadings were applied as horizontal forces at the center of the loading slab, at an elevation of 1200 mm above the top of the base slab. However, because the loadings were controlled in the experiments by matching the measured displacements at the top of the shear wall to predefined displacement demand sequences, the loadings in the ANACAP analyses will be specified as displacement sequences that are applied at the center of the bottom face of the loading slab. In addition to the horizontal loadings, all specimens were subjected to a vertical load that results in an axial stress of 1.47 MPa at the top of the shear wall. This axial stress level was selected to represent the stress level in the lowest story of typical reactor buildings [Habasaki, 2000, Hiroshi, 2001]. Rotation around the vertical axis was prevented in the tests by applying a torsion couple, and therefore will not be included in the analysis.

Four loading patterns, associated respectively with the four specimens described above and also shown in Table 4.1, will be described in the following. The 1-D cyclic loading pattern that is applied to model SD-08-00 has only one displacement sequence in the X direction, while the rest patterns, namely rectangular loading pattern for SB-B-01, cross loading pattern for SB-B-02, and diagonal cross loading pattern for SB-B-03, have two displacement sequences in both horizontal directions.

1-D Cyclic Loading Pattern

The 1-D diagonal loading tests in the NUPEC experiment include three horizontal loading angles at 0°, 26.6°, and 45°; the case of angle 0° will be used in this study and is designated as 1-D cyclic loading pattern. As shown in Figure 4-3, the displacement sequence consists of 12 full cycles of piece-wise linear segments and a monotonically increasing displacement segment in the last non-cyclic cycle. The number cycles utilized for this test is chosen to be consistent with the rectangular loading test. The cyclic cycles have peaks of 0.5 mm, 1 mm, 2 mm, 4 mm, 6 mm, and 8 mm for every two cycles, while the last cycle increases the displacement demand until the shear wall fails (in the test). This displacement sequence is applied in the X direction in the analysis. In static analysis, the horizontal axis in the displacement sequence is only an indicator of the loading sequence for the computer program to march forward and has no physical meaning. However, it is still often termed as time for convenience.

Rectangular Loading Pattern

In Figure 4-4 showing the rectangular loading pattern, the thick solid line represents the displacement sequence pattern for X direction, while the thin dotted line represents that for Y direction. The two displacement sequences are defined as 12 full cycles of piece-wise linear segments and a cycle of increasing displacement demand at the end. Note that two cycles are required to complete the predefined rectangular loading pattern as shown in Figure 4-5. Except for the first two cycles that only involve small X direction displacement, other cycles include displacement segments in both X and Y directions. The concerted application of the two displacement sequences in both directions creates a rectangular movement in the loading slab, i.e. a displacement orbit in the X-Y plane, which is demonstrated in Figure 4-5 [Horishi, 2001]. For

each typical cycle, the loading slab starts to move in the Y direction till the peak, and then orbits almost twice along the edges of a rectangle that is formed with the positive and negative displacement peaks, and finally returns back to its rest position. The displacement peaks for the cyclic loading in the X direction are the same as those for the 1-D cyclic loading, while the peaks in Y direction are 80 % of those in X direction. The last cycle consists of a ramp to a displacement of 8 mm in the Y direction and a constantly increasing displacement demand in the X direction until the shear wall fails.

Cross Loading Pattern

Figure 4-6 shows the cross loading pattern that consists of 12 full cycles of piece-wise linear displacement segments for the two horizontal directions and an increasing displacement in the X direction at the end. The number cycles utilized for this test is chosen to be consistent with the rectangular loading test. The thick solid line represents the displacement pattern for the X direction, while the thin dotted line represents that for the Y direction. Similar to rectangular loading, the first two cycles only involve small displacement in the X direction, while other cycles involves displacements concertedly applied in both directions. Figure 4-7 shows a typical displacement orbit in the X-Y plane [Horishi, 2001], in which the loading slab oscillates first in the X direction and then in the Y direction, and repeats once. The peaks of the displacement sequence in the X direction are the same as those for the 1-D cyclic loading, while the peaks in the Y direction are 80 % of those in the X direction. In the last loading cycle, the loading slab moves in the positive X direction till 10 mm and then reverses with a continuously increasing displacement demand until the shear wall fails. No Y directional movement is involved in the last cycle.

Diagonal Cross Loading Pattern

With the same line styles as for previous loading patterns, Figure 4-8 and Figure 4-9 show the diagonal cross loading pattern and its typical displacement orbit in the X-Y plane respectively. The two displacements sequences for both directions are defined as 12 full cycles of piece-wise linear segments and a proportionally increasing displacement demands in both directions. The number cycles utilized for this test is chosen to be consistent with the rectangular loading test. In a typical cycle except for the first two that involve only small X displacement, the loading slab moves in quadrant I proportionally to the peaks at the same time, and then returns back along the same loading path to rest position; this movement then repeats for the other quadrants in the order of I, IV, III, and II. The peaks are the same as those of the patterns introduced previously. In the last loading cycle, the loading slab moves proportionally in the positive X and Y directions until the shear wall fails. Please note that the last cycle of the diagonal cross loading pattern in the analysis (see Figure 4-8) assumes a 1:1 ratio for the X and Y displacements, which is different from the 1:0.8 ratio used in the test (see Figure 4-12). This difference only affect the analytical result at the last cycle when the shear wall is about to fail and therefore does not change any conclusions to be made.

All four loading patterns described above are for the ANACAP analysis. Figure 4-10 to Figure 4-12 show the displacement histories measured at the top of the shear wall for the SB-B-01, SB-B-02, and SB-B-03 specimens, in which some segments in the displacement history are not straight lines. The shapes of the loading patterns used in the analyses differ apparently from those measured in the tests. However, the difference in the shapes of the displacement sequences do not represent any difference in static analysis, as long as the two loading sequences in the X and Y directions are fully concerted, i.e., remains the same proportion at all time (e.g. X:Y = 1:0.8 for most cycles).

4.2 Finite Element Model

ANACAP is a finite element software package that specializes in static and dynamic nonlinear analysis of reinforced concrete structures, with the capability to predict the performance of concrete structures before and after significant cracks are developed. It has been reportedly successful in a number of applications involving nuclear containments, bridge components, and other standard structural components [Dunham R.S. and Rashid Y.R., 2003]. This subsection provides descriptions of the ANACAP material models, the finite element model for the shear wall, and the ANACAP static analytical procedure for all analyses to follow.

4.2.1 ANACAP Constitutive Models

The ANACAP concrete constitutive model is a smeared-crack finite element model that was initially developed by Rashid Y.R. (1968) and becomes a unique approach fostered by ANATECH, the company who develops the ANACAP software. Among the four concrete material models provided in ANACAP, model 3 is the only ANACAP model suitable for this study because it allows full plasticity with strain softening capability in compression. The hysteresis behavior and the degradation of stiffness and strength under large cyclic loadings or strong earthquake motions can be predicted well. This model does not pursue any particular theory, but integrates various concrete models that have been reported in the literature. Although the units of various quantities are metric system unit in this report, ANACAP uses the US customary units for its input parameters, i.e., the basic units are lb, in, and sec.

As shown in Figure 4-13, this model considers the strain hardening and softening behavior of unconfined concrete under uniaxial compression, and models the confined concrete appropriately as well [Dunham R.S. and Rashid Y.R., 2003]. In ANACAP concrete model 3, the smeared cracking model is implemented at the integration points of each element, and therefore the cracking state can vary within an element. Multiple cracks can be formed orthogonally at any integration point. ANACAP uses its cracking mechanism to redistribute load and particularly to transfer load to reinforcement. A crack is initiated according to the criteria curve in Figure 4-14, and the normal stress across the crack is governed by the tension stiffening model as shown in Figure 4-15. Shear force along a crack can be resisted by the friction between the crack surfaces according to the shear retention model as shown in Figure 4-16. The unrealistic buildup of shear stress across an open crack is limited by the so-called shear shedding model in ANACAP if the crack continues to open.

Rebars are modeled as sub-elements embedded within concrete elements, which superimpose their strength and stiffness to the associated concrete elements. The constitutive model of rebars in ANACAP considers the rebar plasticity, bond slip, and anchorage losses, and has been validated with empirical data.

4.2.2 Shear Wall Model

To reduce the computational effort and to maintain a reasonable aspect ratio for the elements, the concrete shear wall is modeled using a single brick element through the thickness of the wall. The element B203D provided in ANACAP is a 20-node brick element and is used for the shear wall modeling, because it allows large element size. This modeling strategy should not affect the overall horizontal stiffness of the shear wall because the out-of-plane flexural stiffness of the walls is negligible for the box-shaped shear wall. In addition, a 3x3x3 Gauss integration scheme, which is used for these brick elements to prevent possible rigid body mode, can provide better out-of-plane bending capability than the standard 2x2x2 Gauss integration scheme. Figure 4-18 shows the finite element mesh of the shear wall. There are 12 elements along the width of each face including the two small corner elements, 6 elements along the height, and 1 element through

the wall thickness as described above. The entire boxed-shaped shear wall model consists of 408 brick elements in total.

The concrete material properties required by ANACAP are Young's modulus E_{ke} , Poisson's ratio ν_c , concrete density ρ_c , unconfined concrete crush strength σ_c , and the fracture strain ε_f . Most of these properties for the four specimens can be found in Table 4.1, except for the fracture strain ε_f . The fracture strain ε_f is related to the tensile strength σ_y and the Young's modulus E_{ke} by the following equation [ANATECH, 2004],

$$\varepsilon_f = \sigma_y / E_c. \quad (4-1)$$

The tensile strength σ_y of concrete material carries a great deal of uncertainties, and is often approximated according to empirical formulas using the unconfined crush strength σ_c . There are quite a number of such formulas in the literature. The following equation is implicitly used in the ACI code [Wang C.K. and Salmon C.G., 1979] and is used in this study,

$$\sigma_y = 6.7\sqrt{\sigma_c}, \quad \text{where } \sigma_c \text{ in psi.} \quad (4-2)$$

Using a typical value of $\sigma_c = 41.3$ MPa and $E_{ke} = 30.7$ GPa in Equations 4-1 and 4-2, ε_f can be calculated as 0.00012. It is not difficult to determine the fracture strain using the above equations; nevertheless, the fracture strain was set equal to 0.0001 for all four models, with the consideration of the uncertainties in the tensile strength and the different values yielded by different formulas.

Figure 4-17 shows the ANACAP finite element model with the shear wall and the loading slab distinguished by colors. As shown in Figure 4-18, the loading slab is modeled with one element through its thickness and has 144 elements in total. The displacement sequences are applied at the center of the bottom face of the loading slab, at which a single node resides. Because the loading slab is very thick (400 mm) comparing to the thickness of the shear wall (75 mm), it can be idealized as a rigid slab. In the analyses, the material model of the loading slab is an elastic isotropic steel material that ensures its rigidity with respect to the concrete shear wall. Moreover, since the rebars in the shear wall have an anchorage of 300 mm in the loading slab, the bonding between the shear wall and the loading slab is assumed perfect for all the models by sharing interface nodes between these two parts. Similarly, the base slab is also assumed rigid and is represented by a fixed boundary condition applied at all nodes at the bottom of the shear wall.

Figure 4-19 shows the rebar configuration of the model. Rebars are modeled as sub-elements in ANACAP, and can be generated using the preprocessor program ANAGEN that is bundled within the ANACAP package. All rebars have a diameter of 6 mm, and are modeled using a bilinear elastic-plastic material using the rebar properties in Table 4.1. The bond between a rebar and the concrete is assumed perfect (FULL in ANACAP terms), while the rebar confinement condition is assumed poor because the shear wall is thin.

4.2.3 Static Analysis

The static stress solution is performed in ANACAP for all four models subjected to the corresponding cyclic loading pattern in this study. Each of the four analyses needs two steps: (1) A pressure boundary of 1.47 MPa is applied at the top of the shear wall. The weight of the shear wall is not considered because it is negligible comparing to the pressure boundary condition. (2) The relevant displacement loading pattern is specified as the displacement boundary condition at the center of the bottom face of the loading slab. ANACAP is capable of simultaneously applying displacement boundary conditions in multiple directions. Using the *FUNCTION command in ANACAP, a displacement loading pattern is defined as a sequence of time-displacement pairs. It should be noted that "time" in the static cyclic analysis does not bear the

same sense of time as in dynamic analysis, and only works for convenience as an indicator for the finite element solver to march along the displacement sequence. The time increment Δt is set equal to 0.015625 for the models SD-08-00 and SB-B-01, and 0.03125 for the models SB-B-02 and SB-B-03. Referring back to the loading patterns introduced in Subsection 4.1.2, these small time increments ensures that any turning point on the loading curves are preserved in the solution process and that there are enough points on the hysteresis loops during post processing, in addition to the accuracy and convergence requirement by ANACAP.

The base shears are obtained by extracting the reaction forces from the ANACAP output file. The displacement histories at the top of the shear wall are obtained at the loading node for the two horizontal directions using the *POST and *PLOT commands in ANACAP.

4.3 Results and Comparisons

This subsection presents the results from the four ANACAP analyses and their comparisons to the tests for each of the loading scenarios. The comparisons will be made using the relation of shear force vs. displacement, the shear force orbit curve, the cycle-by-cycle shear force – displacement relation, and the base shear force capacity.

Result for 1-D Cyclic Loading Pattern

Figure 4-20 shows the relationship between the base shear force and the displacement at the top of the shear wall for the 1-D cyclic loading pattern, which is applied in the X direction. The dotted line is for the test, while the solid line is for the analysis. The overall shape of the hysteresis loops from the analytical prediction agrees well with that of the test, except that an unusual excursion exists on the test hysteresis curve. The ANACAP concrete model captures the stiffening and softening characteristics of specimen SD-08-00. As for the ultimate base shear capacity, the analysis predicts ultimate strengths of 1601 kN and -1534 kN in the positive and negative X directions, which are larger than the test values of 1480 kN and -1484 kN respectively. The relative error in these predicted base shear capacities are 8% and 3%.

The hysteresis loops shown in Figure 4-20 are severely overlapped so that the loading and unloading behavior of the model under the cyclic loading cannot be traced. To compare the analytical result and the test result in more detail and to examine the excursion of the test curve mentioned above, the shear force - displacement relationship is presented in a cycle-by-cycle manner in Figure 4-21. In general, the analytical hysteresis loops are thinner than those from the test, but the overall stiffness of the model is close to that of the specimen. The stiffness of both analytical model and the test specimen clearly degrades in a similar pace as the cyclic displacement sequence evolves to take larger values. For any two consecutive loading cycles of the same peak displacement, the first hysteresis loop is wider than the second, being true for both the analysis and the test. The explanation of this phenomenon is straightforward because the second loading cycle repeats the first cycle and therefore the shear wall does not develop any more cracks significantly in the second cycle.

For the first 4 cycles that the maximum displacement demand is 1 mm, both the stiffness and the peak base shear force of the analytical result are very close to those of the test. Starting from the 5th cycle and until the 9th cycle, which represent a peak displacement demand ranging from 2 mm to 6 mm, the analytical model is slightly stiffer and has a higher shear strength than the test specimen. At the 10th cycle, the second cycle that has a peak displacement of 6 mm, the behavior of the analytical model resembles very well that of the test specimen. The excursion on the test hysteresis curve is because the specimen failed prematurely in the 11th cycle. In contrast, the

ANACAP analysis continues to the last cycle and completes all the displacement sequence. The shear wall model deforms in the last cycle following a curve which is similar to the unconfined concrete compression behavior (see Figure 4-13). The ANACAP reinforced concrete model does not explicitly define a failure criterion to stop the analysis; rather, it continues the analysis with the model properties being degraded appropriately, and substantially after “failure”. This is in deed the essential technique for ANACAP to capture the post-ultimate performance of the reinforced concrete material.

Result for Rectangular Loading Pattern

Figure 4-22 and Figure 4-23 show the hysteresis loops of shear force vs. displacement for the X and Y directions respectively for the rectangular cyclic loading pattern. The dotted line is for the test result, while the solid line is for the analytical result from ANACAP. The overall shapes of the analytical hysteresis loops for both directions are narrower around the region where the base shear is small. For the X direction, the analytical loops follow the test result closely on loading and reaches the peaks closely as well. However, the response of the analytical model seems stiffer in the Y direction than the test specimen SB-B-01, and generally overestimates the base shear force peaks. The maximum base shear capacities for the X and Y directions are estimated as 1390 kN and 1571 kN, which compare to the test values of 1376 kN and 1381 kN respectively. The corresponding relative error in the estimate is 1% for the X direction and 14% for the Y direction.

Similarly to the 1-D cyclic loading case, comparisons are also made in detailed cycle-to-cycle views as shown in Figure 4-24 and Figure 4-25 for the X and Y directions respectively. The observations for the rectangular loading case are similar to those for the 1-D cyclic loading case as far as these cycle-to-cycle comparisons are concerned. The hysteresis loops for the analysis bear a reasonable resemblance of the loading and unloading stiffness to the test for both directions. This resemblance also takes into account the stiffness degradation of the shear wall as the displacement demand increases, and proves NAACP’s capability in predicting the performance of reinforced concrete that has a large amount of cracks developed. The test specimen failed in the last cycle, while the ANACAP analysis continues until the end of the displacement sequence because ANACAP does not have a failure criterion.

Without exception, the analytical hysteresis loops are all narrower than those of the test, which suggest that a partial bond assumption in rebar modeling may be more reasonable in this aspect. However, ANACAP provides only two options for rebar bond modeling, either FULL or SLIP. Moreover, preliminary analyses of this model using the SLIP bond rebar model significantly underestimated the overall stiffness and the base shear peaks, although did produce much wider hysteresis loops than the FULL rebar bond model. Therefore, the FULL rebar bond model has been used for all four analyses.

Figure 4-26 shows the relation of the shear forces for the two horizontal directions, so termed shear force orbits hereafter. The shapes of the orbits for both the model and the test are brutally similar to the displacement orbits as shown in Figure 4-5, but tilt clock-wise. The shape and orientation of the shear force orbits of the model are reasonably close to the test result, as demonstrated more clearly in the cycle-to-cycle comparison in Figure 4-27.

Result for Cross Loading Pattern

The hysteresis loops of shear force vs. displacement for the cross cyclic loading pattern are shown in Figure 4-28 and Figure 4-29 for the X and Y directions respectively, where the dotted line

represents the test result and the solid line represents the analytical result from ANACAP. The comparison between the overall shape of the analytical hysteresis loops and that of the test is greatly better than that in the rectangular loading case, however is very similar to that in the 1-D cyclic loading case. The predicted stiffening and softening behavior of the envelop curve, peak shear forces, and hysteresis loops are all very close to those of the test result. The similarity between the cross loading case and the 1-D cyclic loading case becomes obvious when the cross loading pattern is visualized as an alternating application of the 1-D cyclic loading to the X direction and the Y direction. The ANACAP analysis did not capture the sudden failure in the X direction as expected. The maximum base shear capacities for the X and Y directions are estimated as 1756 kN and 1600 kN respectively, both of which are larger than the corresponding test values of 1596 kN and 1325 kN. The errors in the predicted base shear capacities are 10% for the X direction and 21% for the Y direction.

Figure 4-30 and Figure 4-31 present detailed cycle-to-cycle comparisons of the hysteresis loops for the X and Y directions respectively. For both directions, the stiffness of the ANACAP model slightly varies from cycle to cycle with respect to that of the test, but only to a small extent that does not affect the conclusion of a good agreement between the model analysis and the test. A remarkable agreement can be observed at the 12th cycle for both direction, where the highly curved hysteresis loop of the test is predicted very well by the analysis, though wider than that of the analysis.

Figure 4-32 shows the shear force orbits for the two horizontal directions. The shapes of the orbits for both the model and the test reveal roughly the displacement orbits as shown in Figure 4-7. Because of the cross shape of the orbits, a detailed cycle-to-cycle comparison of the shear force orbits between the analysis and the test do not show more details than in Figure 4-32, and therefore is not present in this report.

Result for Diagonal Cross Loading Pattern

Figure 4-33 and Figure 4-34 demonstrate the hysteresis loops of shear force vs. displacement for the X and Y directions respectively for the diagonal cross cyclic loading pattern. The dotted line and the solid line correspond to the test result and the analytical result respectively. Except for the last cycle, the overall shape of the analytical hysteresis loops are especially close to that of the test. The maximum base shear capacity for the X direction is estimated as 1428 kN, which is 13% higher than the test value of 1261 kN; the maximum base shear capacity for the Y direction, excluding the last cycle, is 1126 kN, which is larger than test value of 1034 kN by a margin of 9%. The ANACAP analysis was unable to capture the failure as expected, and yielded unusually in the last cycle a higher base shear force in the Y direction than all the peaks for other cycles. The reason for this unusual behavior is that the displacement demand for the last cycle was prescribed as 1:1 between the X and Y directions in the analysis rather than 1:0.8 as in the test (see Figure 4-8 and Figure 4-12 for comparison).

As shown in Figure 4-35 and Figure 4-36 for the X and Y directions respectively, detailed cycle-to-cycle comparisons of the hysteresis loops further prove that ANACAP analysis predicts well the stiffness and the strength of the shear wall and especially the post-ultimate performance, which can be evidenced remarkably by the hysteresis loops of high curvature for the last 3 cycles.

Figure 4-37 shows the shear force orbits for the diagonal cross loading case. The shapes of the orbits for both the model and the test reveal roughly the displacement orbits as shown in Figure 4-9. Detailed cycle-to-cycle comparisons of the shear force orbits are also presented in Figure 4-38. Both figures show that the shear force orbits from the analysis agree well to that of the test,

except for the apparent drift in the last cycle because the displacement sequence specified in the analysis is different from the test.

4.4 Summary of the Static Cyclic Analyses

The correlation study in this section using the analytical results by ANACAP and the NUPEC tests results provided an important opportunity to assess the capability of the commercial code in predicting the performance of the box-shaped shear wall model structures, which are the major lateral force resistant component in the Nuclear Power Plant structures, subjected to various multi-directional cyclic loadings. This subsection summarizes the findings in terms of the modeling assessment and the result of comparisons.

In terms of modeling capability, ANACAP is a general purpose code for the nonlinear static and dynamic analyses of reinforced concrete structures. It has been widely used to predict the response of concrete structures that experience significant cracking and exhibit highly nonlinear post-ultimate-strength degradation under various loading conditions, such as cyclic static loading, seismic time history, and temperature gradient environment. It is very user friendly in modeling of the concrete and rebar materials, as it requires just a few parameters, such as the Young's modulus, Poisson's ratio, concrete density, unconfined concrete crush strength, and the fracture strain, which are normally available in most application scenarios. By using higher order elements, ANACAP allows a coarse mesh in the finite element model. Because of rebars being modeled as sub-elements in the concrete elements, the only apparently feasible way to generate a reasonably realistic model is to use the preprocessor ANAGEN, which however does require a good deal of effort in preparing its input. The post processor ANAPLOT can produce many types of plots and save the pertinent data to files, the later function of which has been found more useful. The base shear force, a summation of the horizontal nodal forces at the fixed boundary, cannot be plotted using ANAPLOT and therefore must resort programming to retrieve the information from the output file.

Comparisons between the ANACAP analytical results and the NUPEC test results have been made in terms of the base shear capacity, hysteresis loops of the shear force vs. displacement, and shear force orbits. All predicted base shear capacity are higher than those of the tests; the relative errors are mostly around 10%, with one exception that results in a relative error of 21%. These errors are well within the general acceptable range for reinforced concrete material. The good agreement in the hysteresis loops and the shear force orbits, in terms of both the overall shape and the cycle-to-cycle comparisons, proves that ANACAP is capable in properly predicting the reinforced concrete behavior in stiffening and softening, loading and unloading, and rebar bond and anchorage. ANACAP cannot predict the final failure of the shear wall models due to its intentional modeling strategy that elements can degrade greatly in stiffness and strength but never fail in order to appropriately capture the post ultimate behavior.

The good correlation between the analytical result and the test rest for the static cyclic loading cases provides a foundation for this model to be used in the nonlinear dynamic time history analyses, which is the topic of the next section. With concrete and rebar material properties updated to values specific to the shaking table test, the same shear wall model will be used for the dynamic analyses.

Table 4.1 Concrete and Rebar Properties for Static Loading Specimens

Description	SD-08-00 1-D Cyclic Loading	SB-B-01 2-D Rectangular Loading	SB-B-02 2-D Cross Loading	SB-B-03 2-D Diagonal Cross Loading
Concrete:				
Young's Modulus (GPa)	26.3	30.7	30.7	32.0
Compression Strength (MPa)	34.9	41.3	39.7	34.9
Poisson Ratio	0.21	0.18	0.17	0.19
Rebars:				
Young's Modulus (GPa)	175	200	200	200
Yield Strength (MPa)	345	375	375	375
Tensile Strength (MPa)	490	493	493	493
Tensile Strain At Fracture (%)	29.1	28.0	28.0	28.0

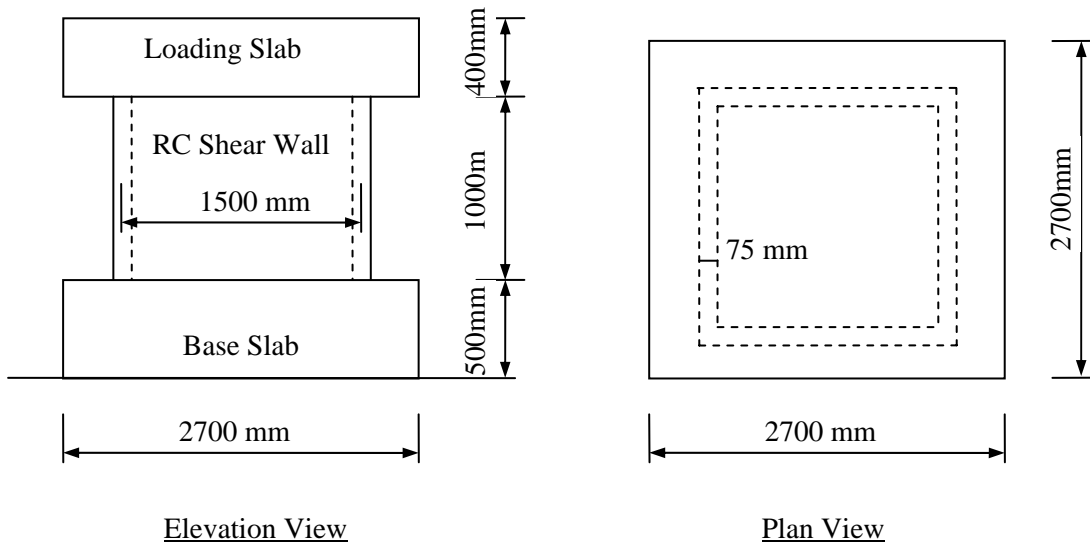


Figure 4-1 Box-shaped Shear Wall Dimension

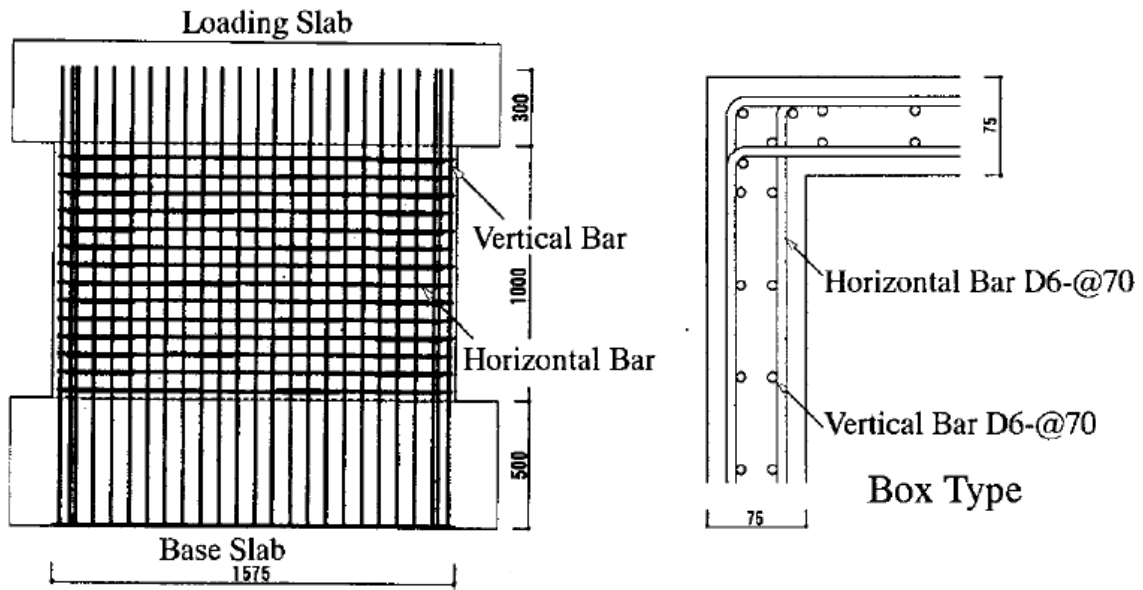


Figure 4-2 Rebar Configuration (Unit mm) [after Hiroshi, 2001]

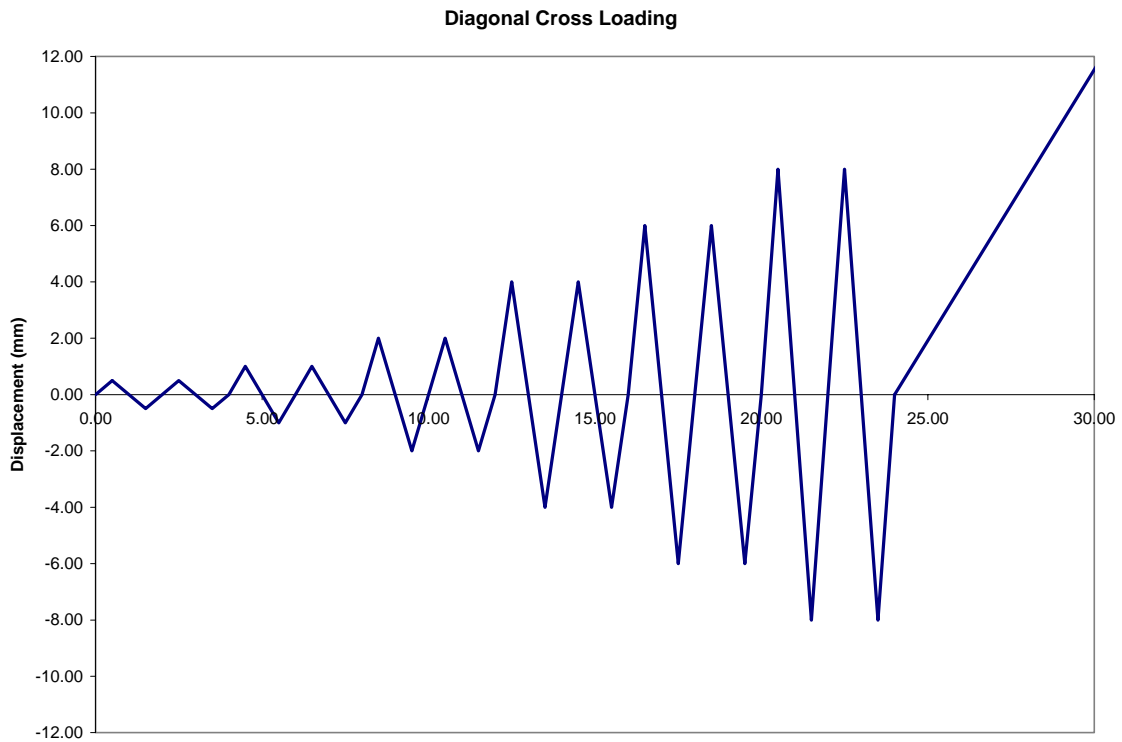


Figure 4-3 1-D Displacement Loading Pattern

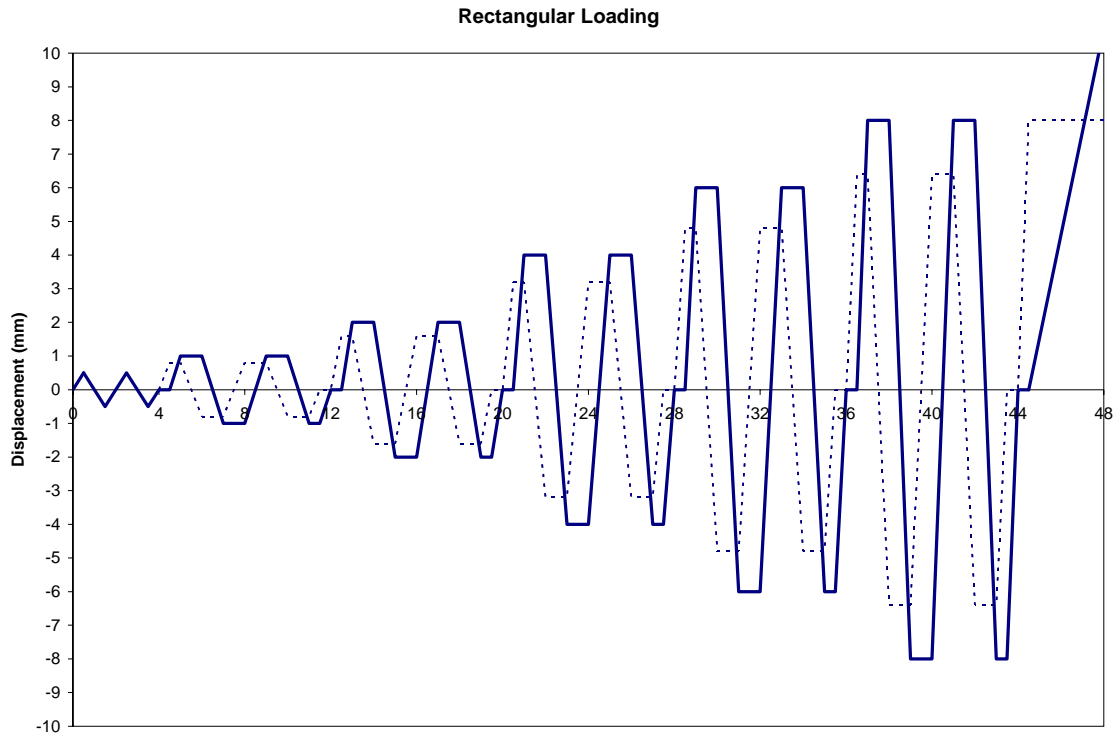


Figure 4-4 Rectangular Displacement Loading Pattern

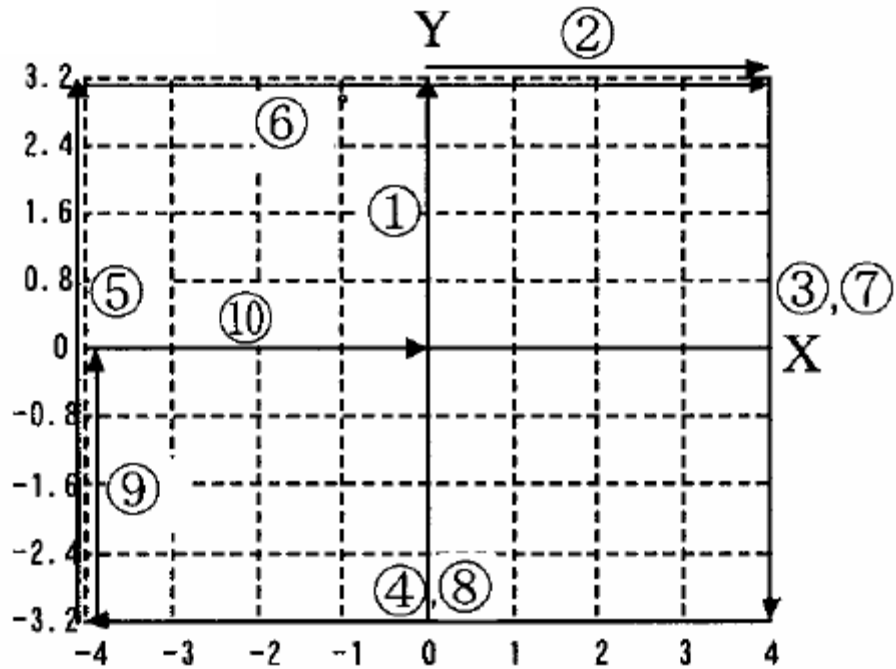


Figure 4-5 A Typical X-Y Displacement Orbit for Rectangular Loading [after Hiroshi, 2001]

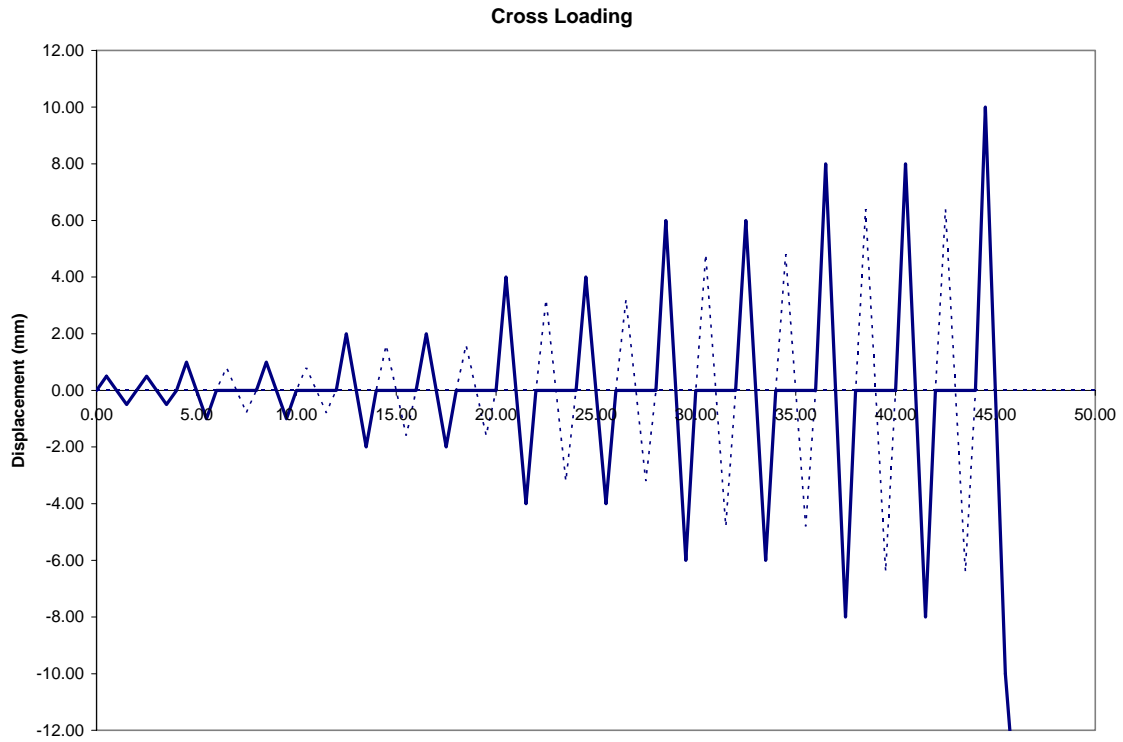


Figure 4-6 Cross Displacement Loading Pattern

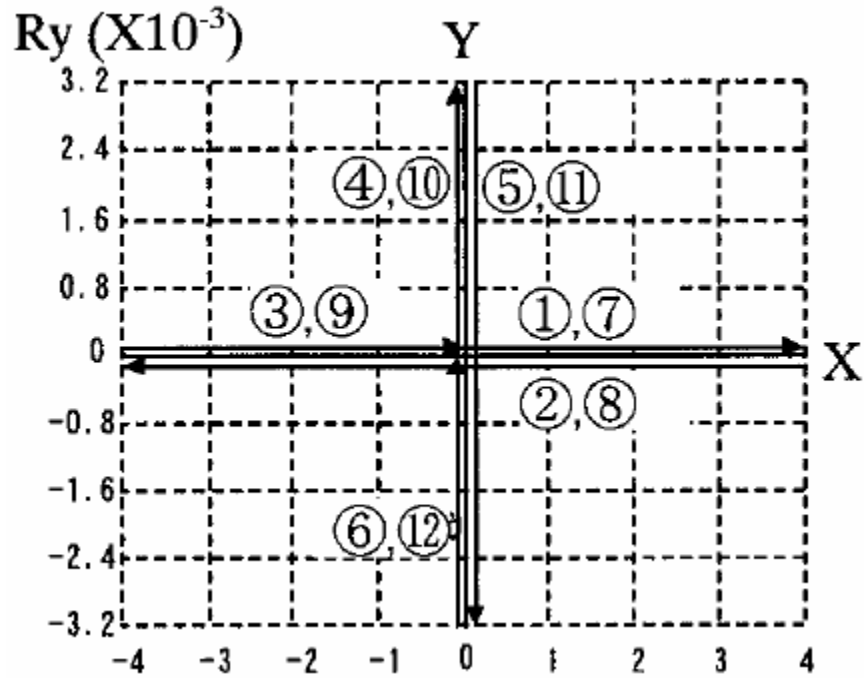


Figure 4-7 A Typical X-Y Displacement Orbit for Cross Loading [after Hiroshi, 2001]

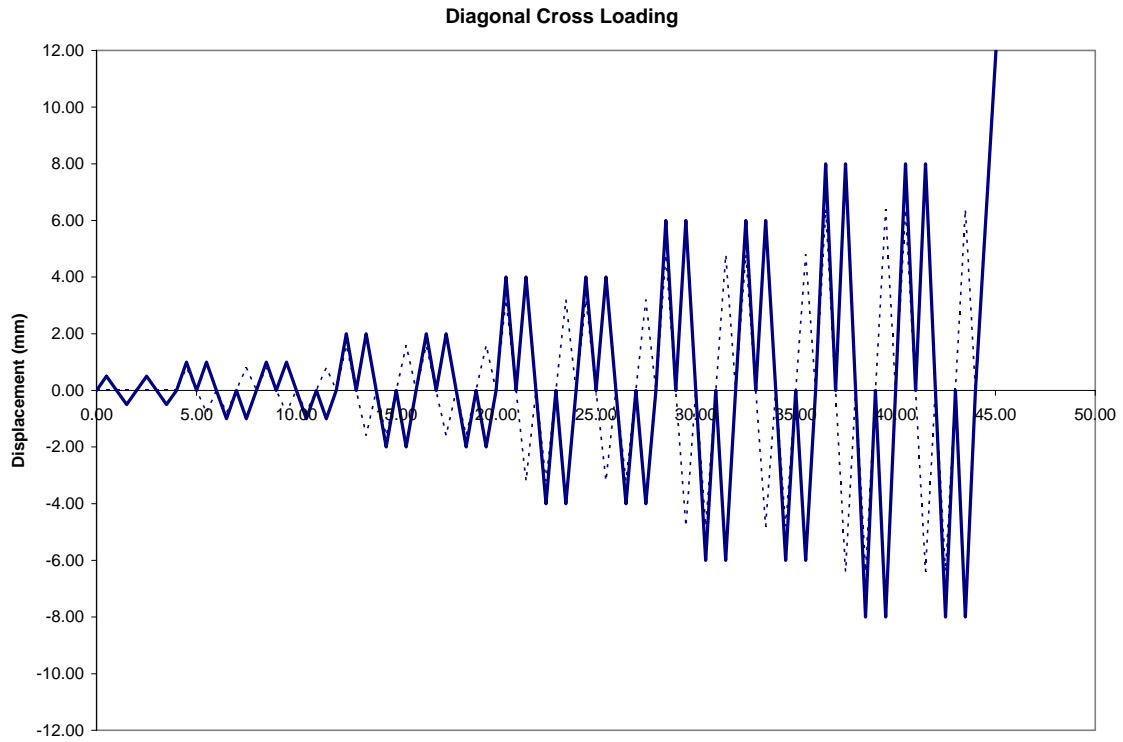


Figure 4-8 Diagonal Cross Displacement Loading Pattern

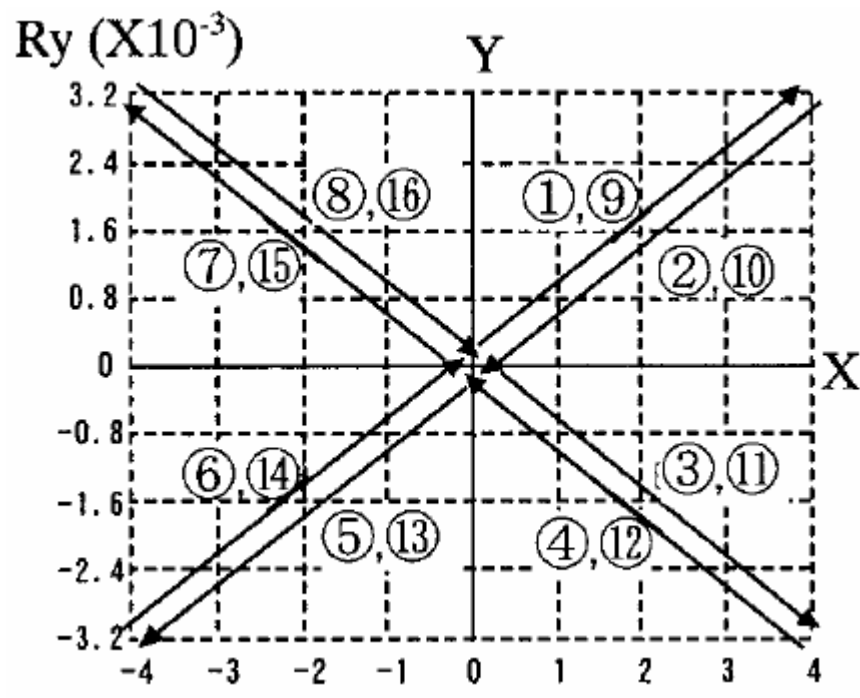


Figure 4-9 A Typical X-Y Displacement Orbit for Diagonal Cross Loading [after Hiroshi, 2001]

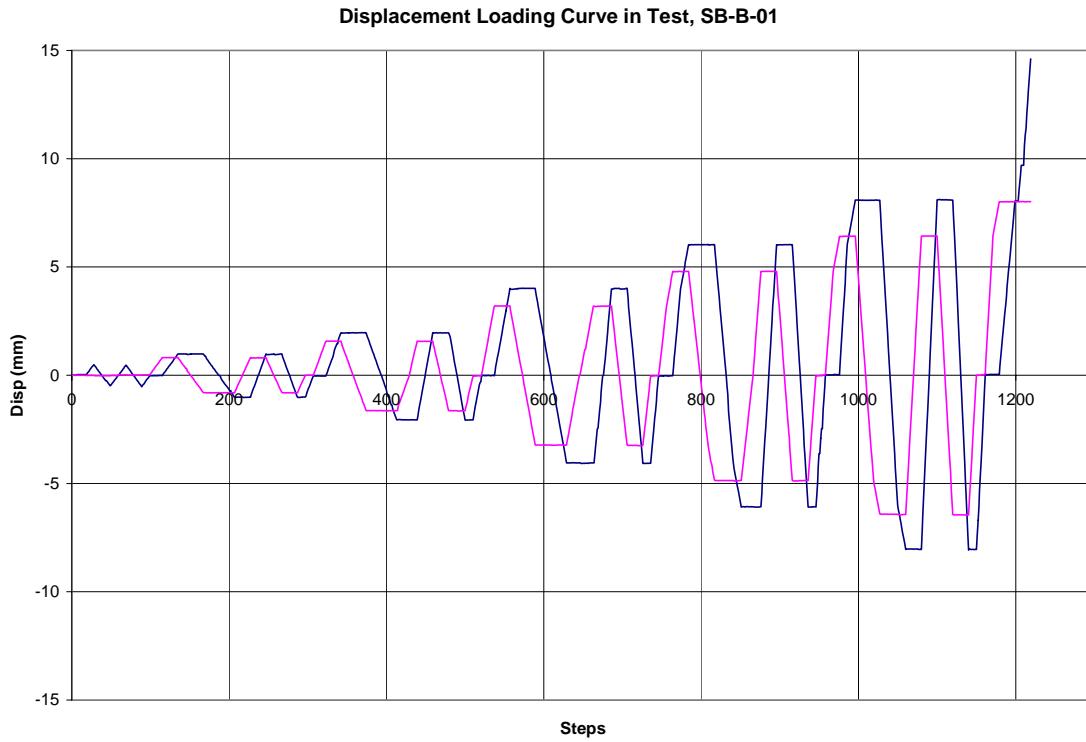


Figure 4-10 Displacement History at the Top of Shear Wall for SB-B-01



Figure 4-11 Displacement History at the Top of Shear Wall for SB-B-02

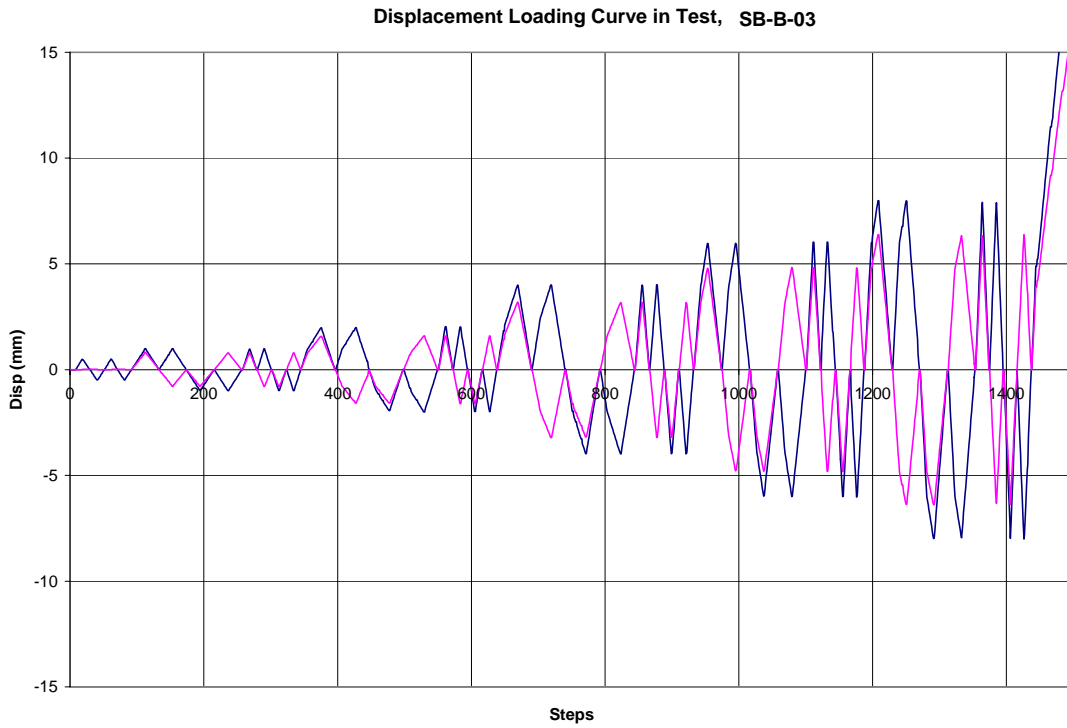


Figure 4-12 Displacement History at the Top of Shear Wall for SB-B-03

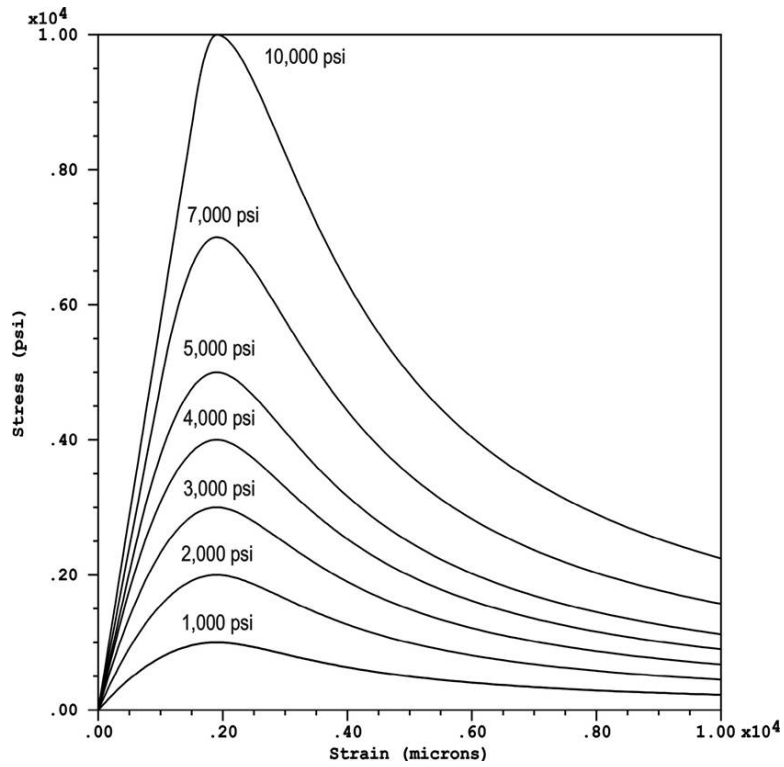


Figure 4-13 ANACAP Unconfined Concrete Compression Model
[from Dunham R.S. and Rashid Y.R., 2003, Courtesy of ANATECH]

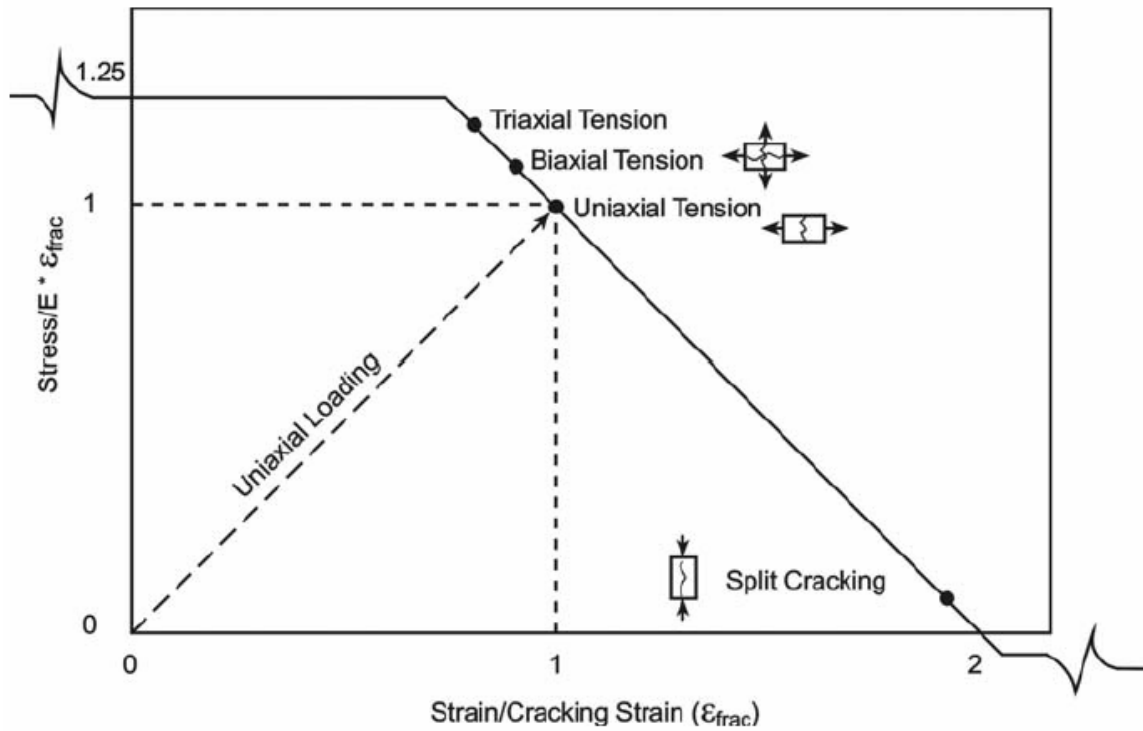


Figure 4-14 Criteria Curve for ANACAP Crack Initiation
 [from ANATECH 2004, Courtesy of ANATECH]

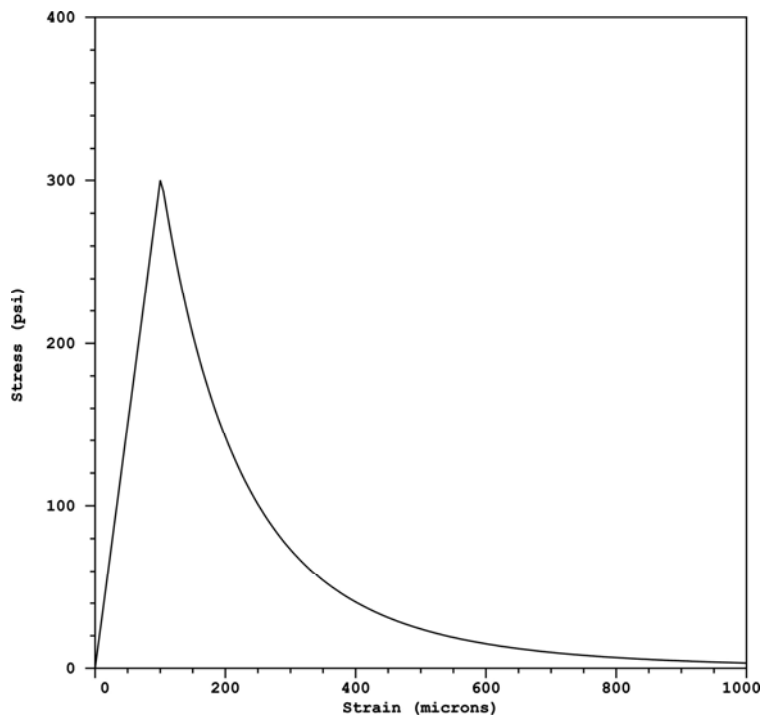


Figure 4-15 ANACAP Concrete Tension Stiffening Model
 [from Dunham R.S. and Rashid Y.R., 2003, Courtesy of ANATECH]

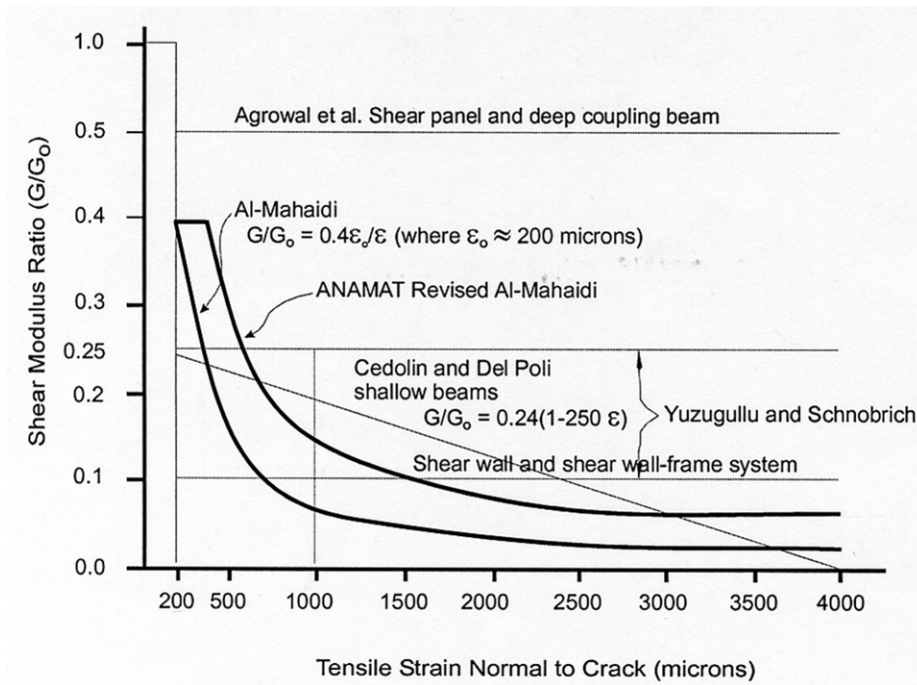


Figure 4-16 ANACAP Shear Retention Model
 [from Dunham R.S. and Rashid Y.R., 2003, Courtesy of ANATECH]

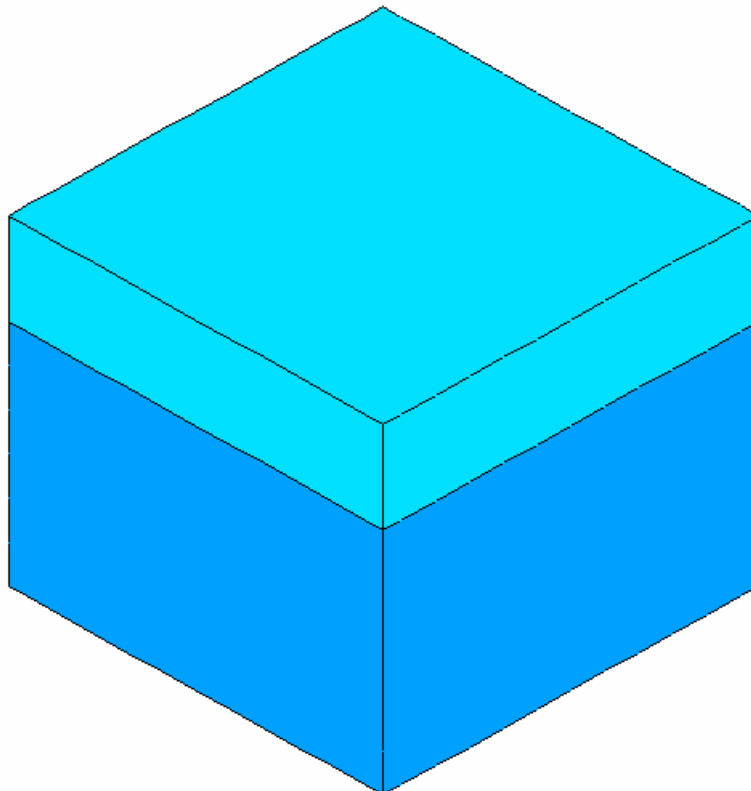


Figure 4-17 ANACAP Shear Wall Model

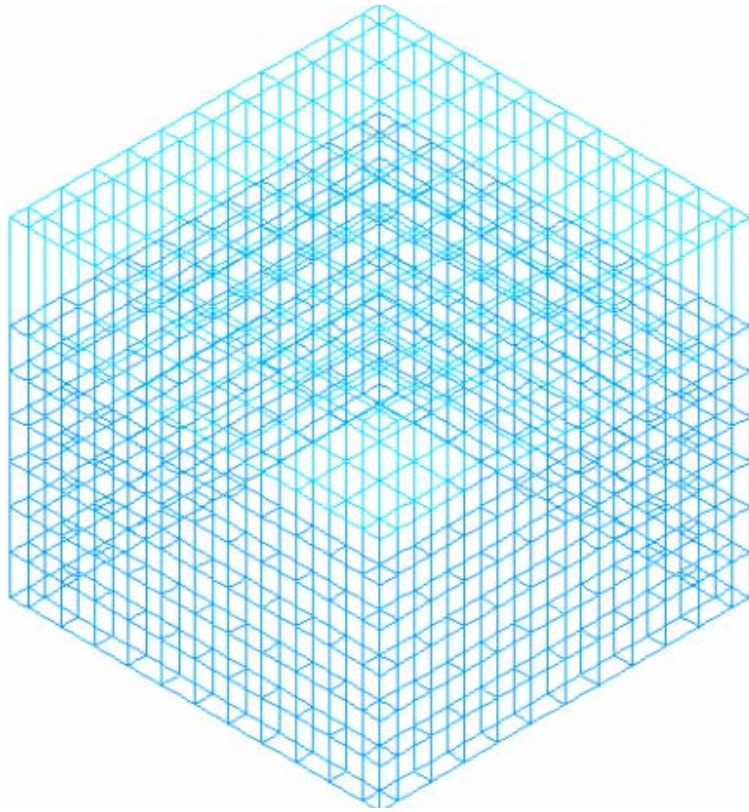


Figure 4-18 ANACAP Shear Wall Mesh

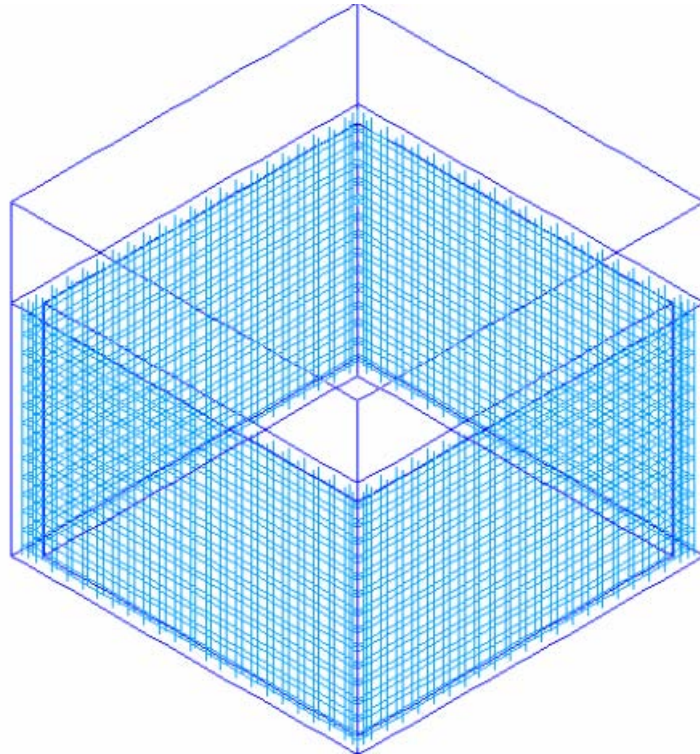


Figure 4-19 ANACAP Rebars Model for the Shear Wall

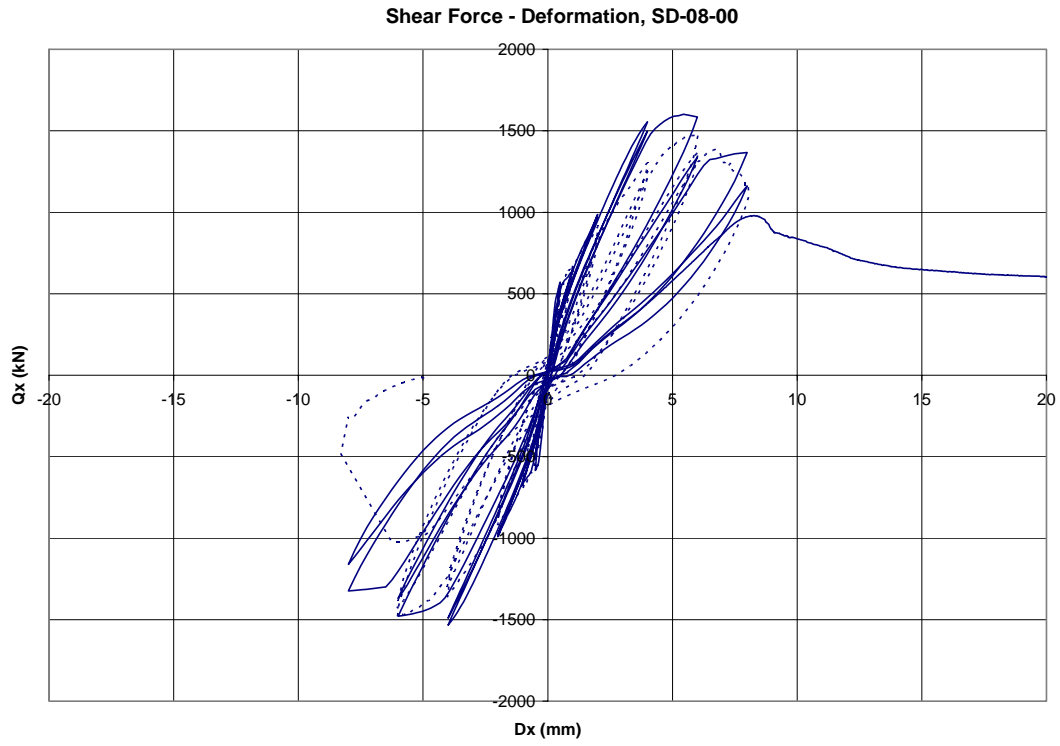


Figure 4-20 Shear Force – Displacement Relation For 1-D Cyclic Loading

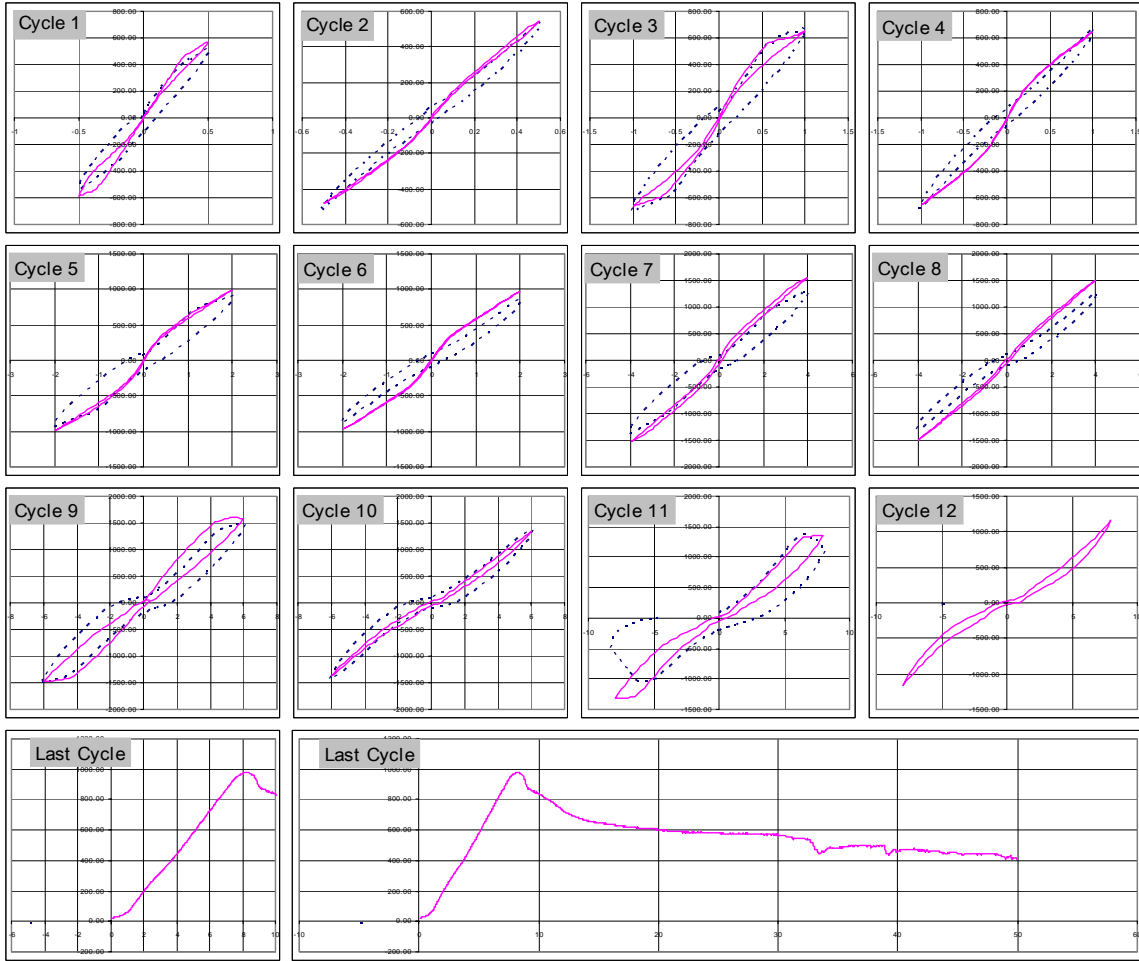


Figure 4-21 Cycle-By-Cycle Shear Force – Displacement Relation For 1-D Cyclic Loading

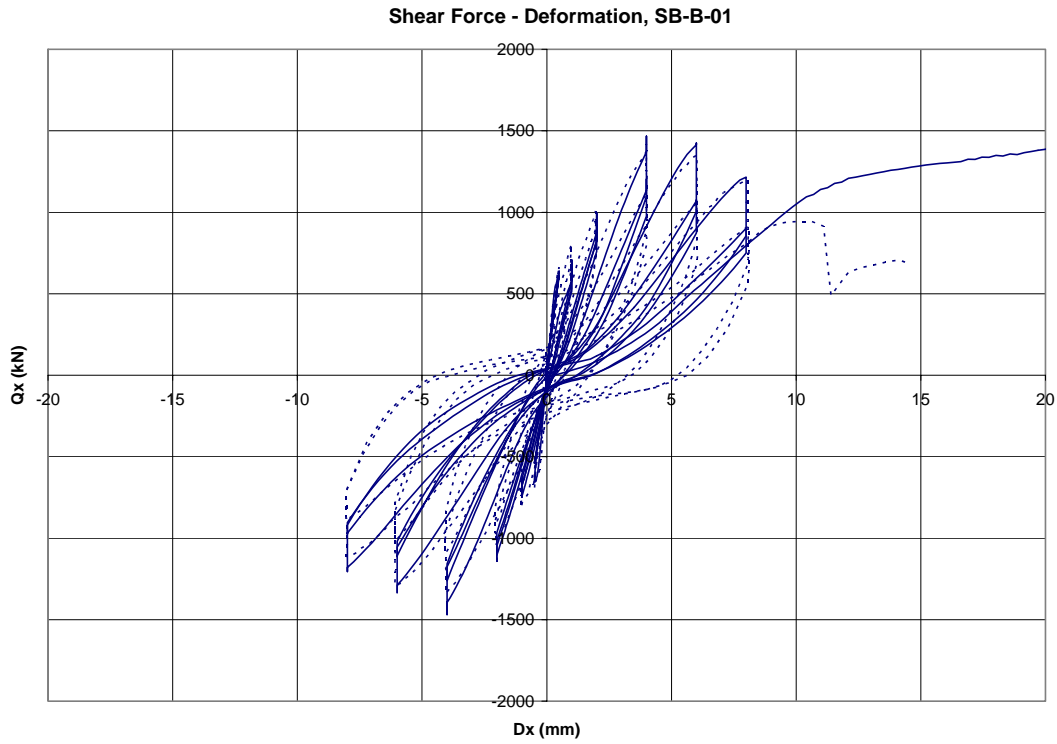


Figure 4-22 Q_x – D_x Relation for Rectangular Loading

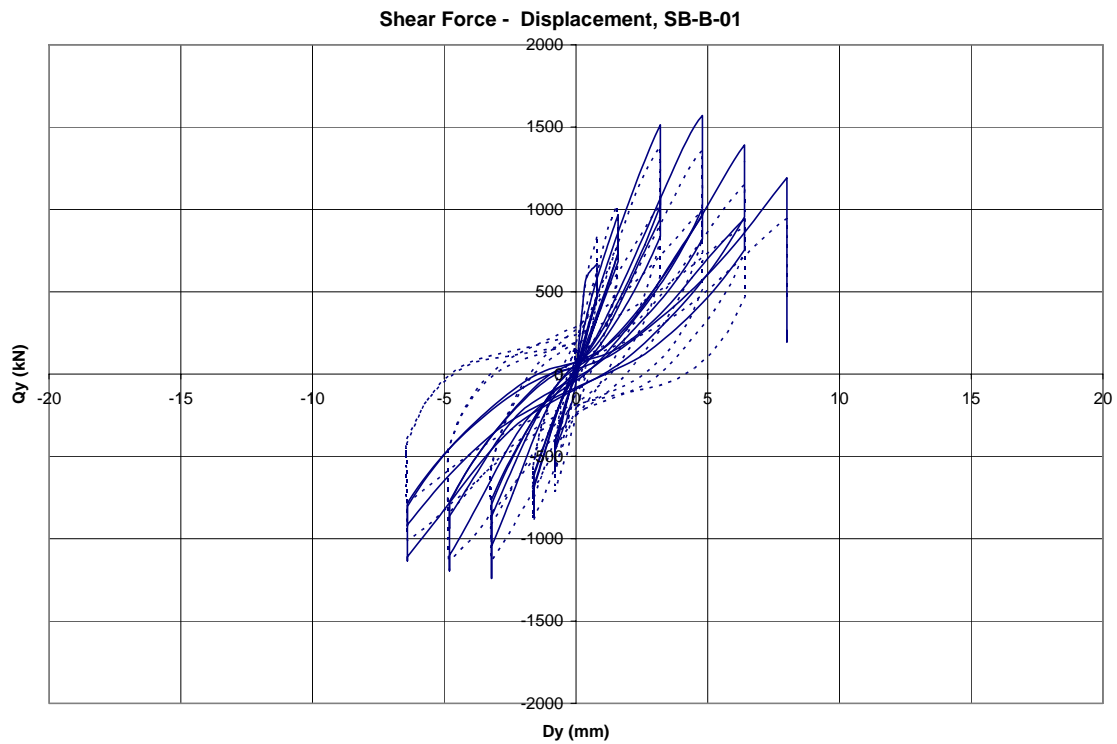


Figure 4-23 Q_y – D_y Relation for Rectangular Loading

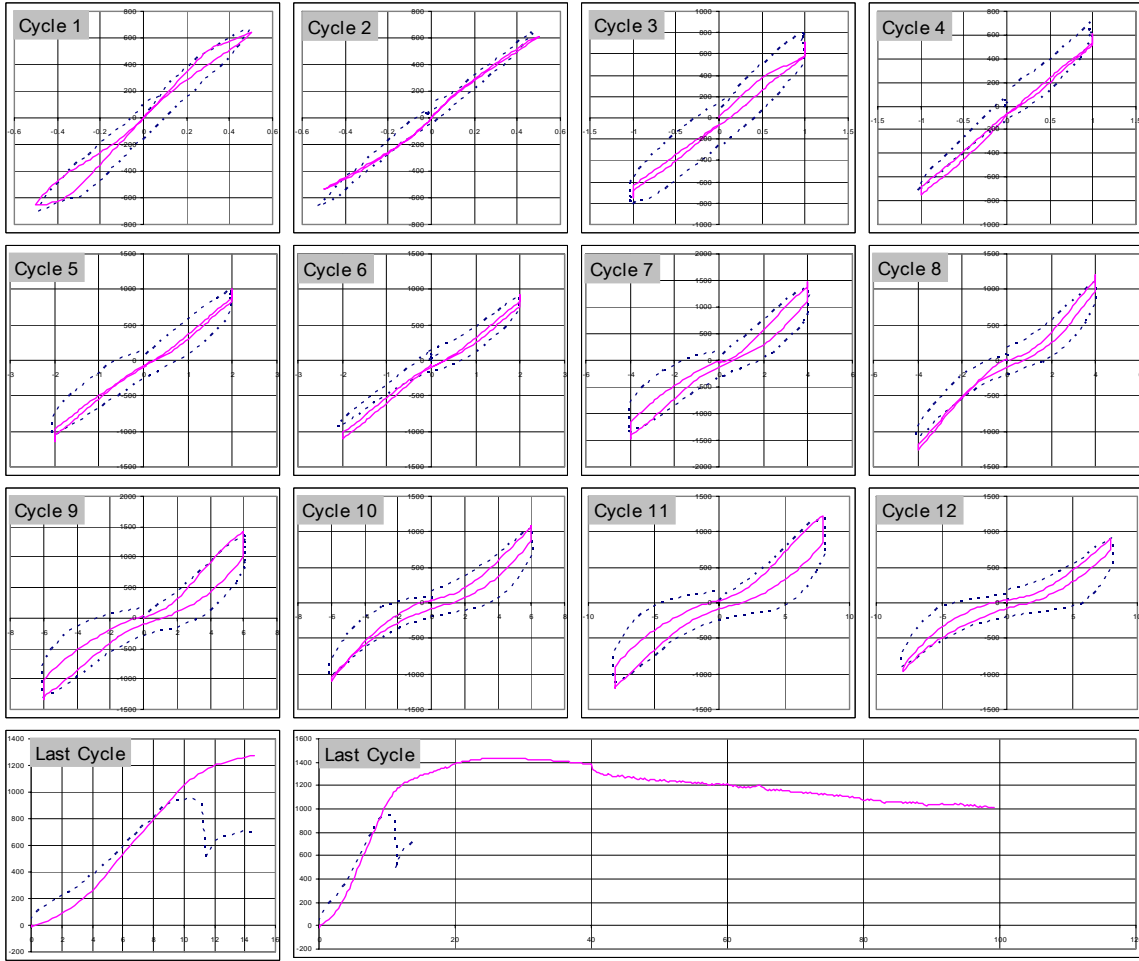


Figure 4-24 Cycle-By-Cycle $Q_x - D_x$ Relation For Rectangular Loading



Figure 4-25 Cycle-By-Cycle $Q_y - D_y$ Relation For Rectangular Loading

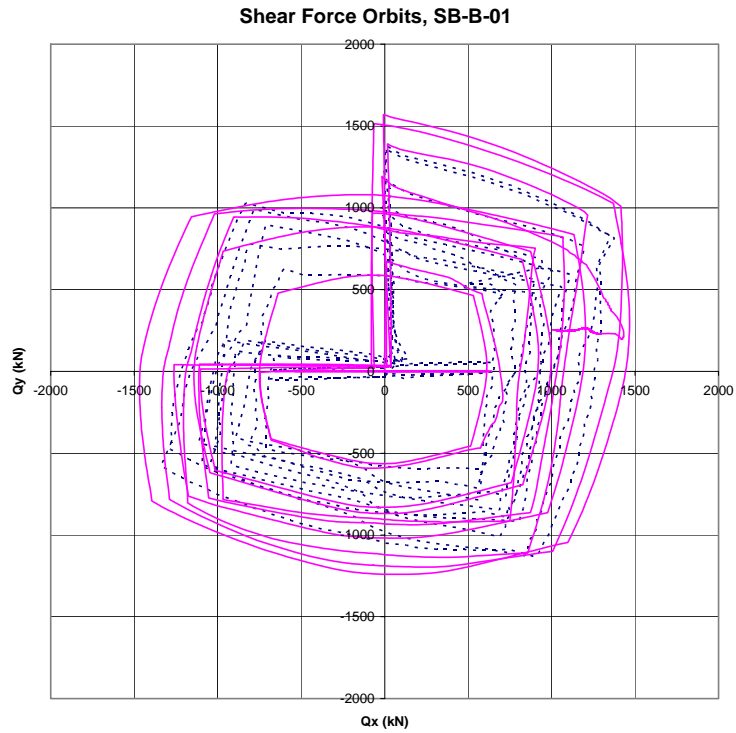


Figure 4-26 Shear Force Orbits for Rectangular Loading

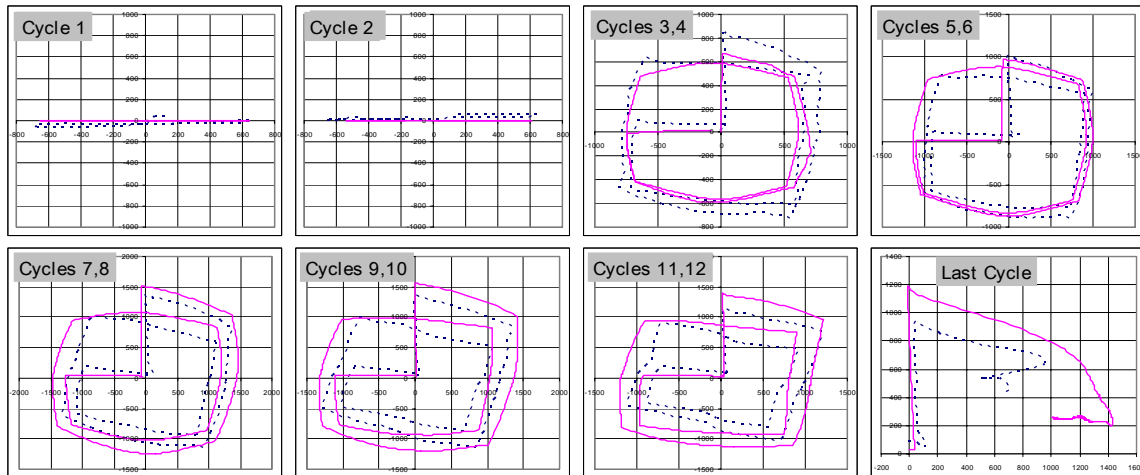


Figure 4-27 Cycle-By-Cycle Shear Force Orbits For Rectangular Loading

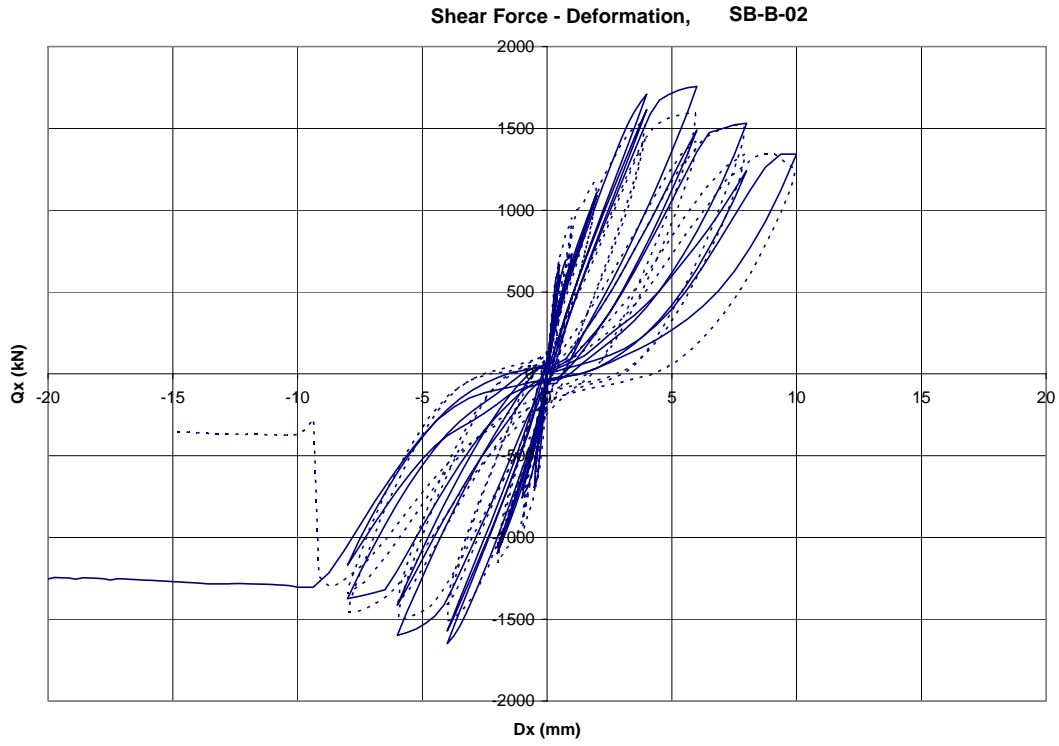


Figure 4-28 Qx – Dx Relation for Cross Loading



Figure 4-29 Qy – Dy Relation for Cross Loading



Figure 4-30 Cycle-By-Cycle $Q_x - D_x$ Relation For Cross Loading

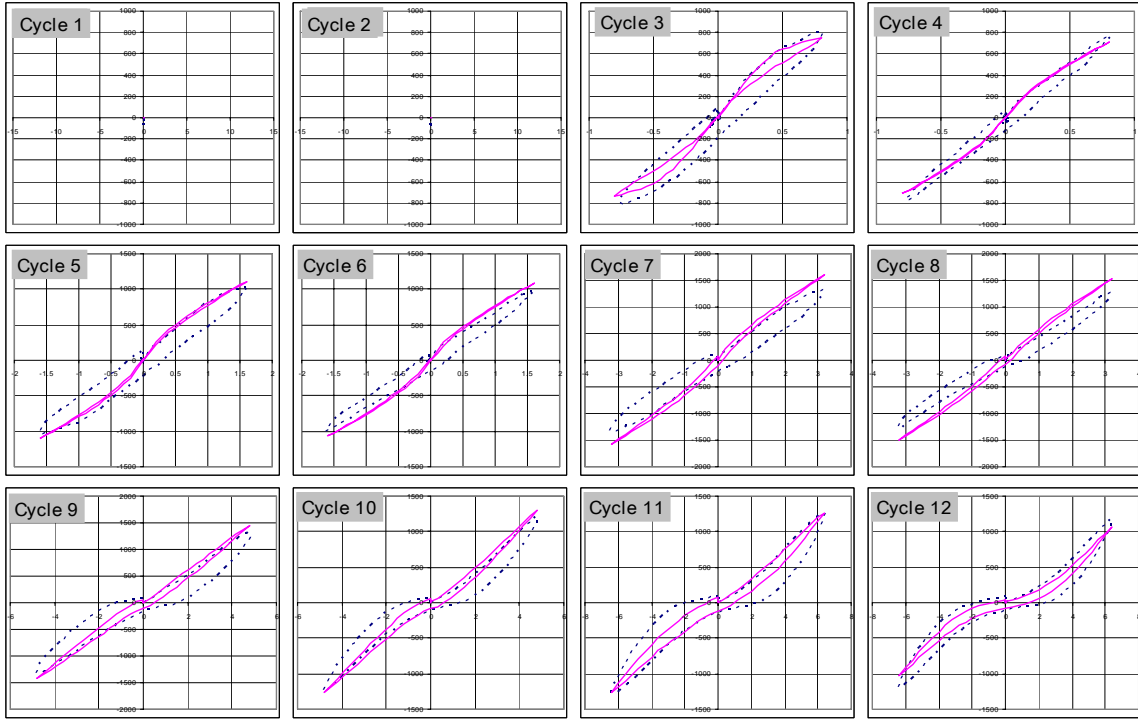


Figure 4-31 Cycle-By-Cycle $Q_y - D_y$ Relation For Cross Loading

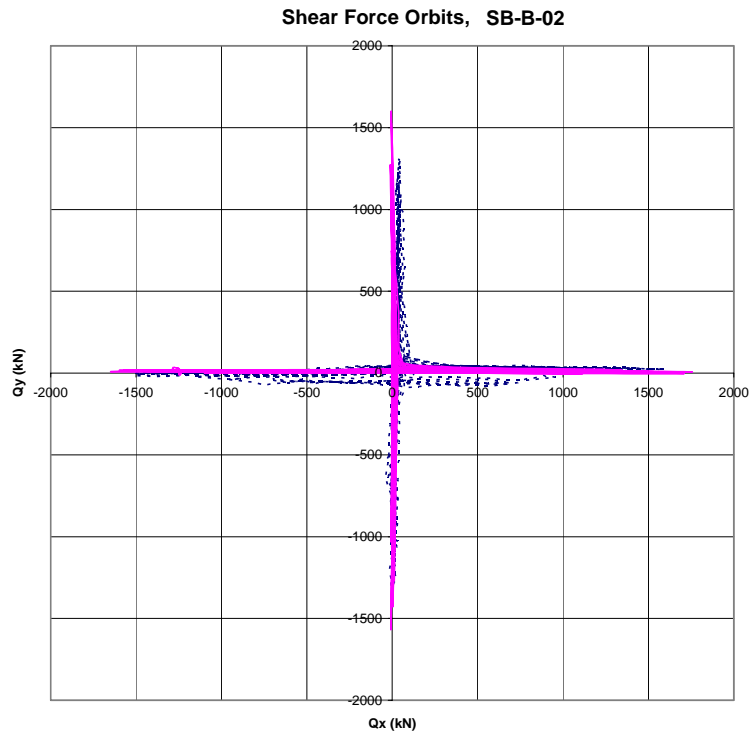


Figure 4-32 Shear Force Orbits for Cross Loading

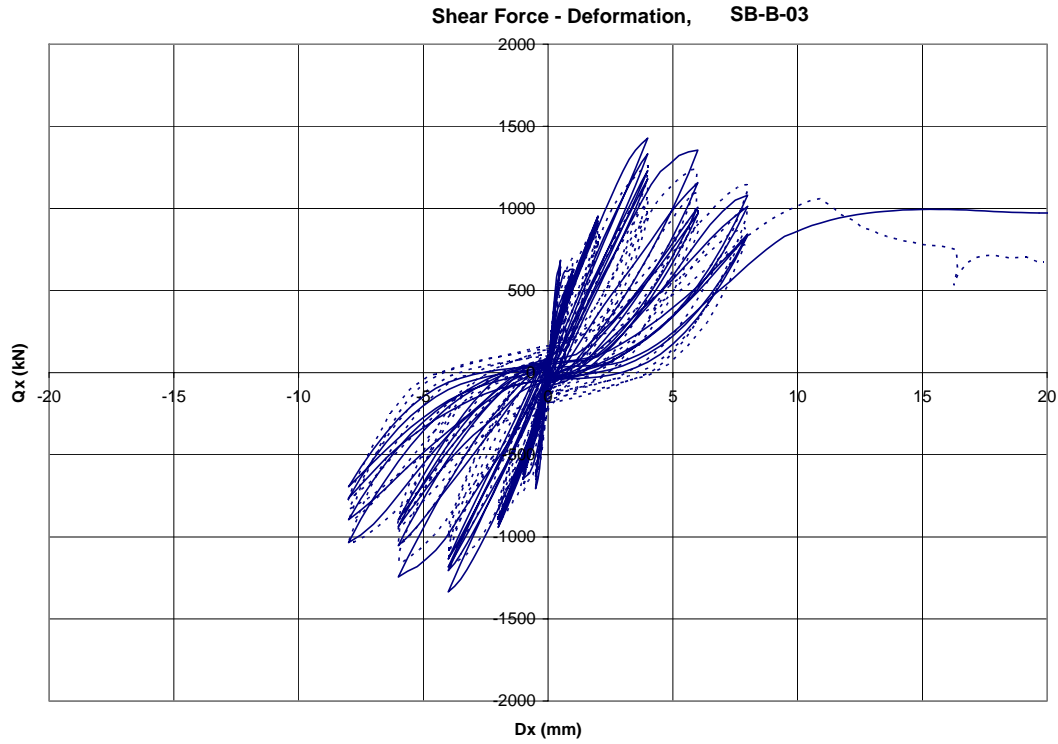


Figure 4-33 Qx – Dx Relation for Diagonal Cross Loading

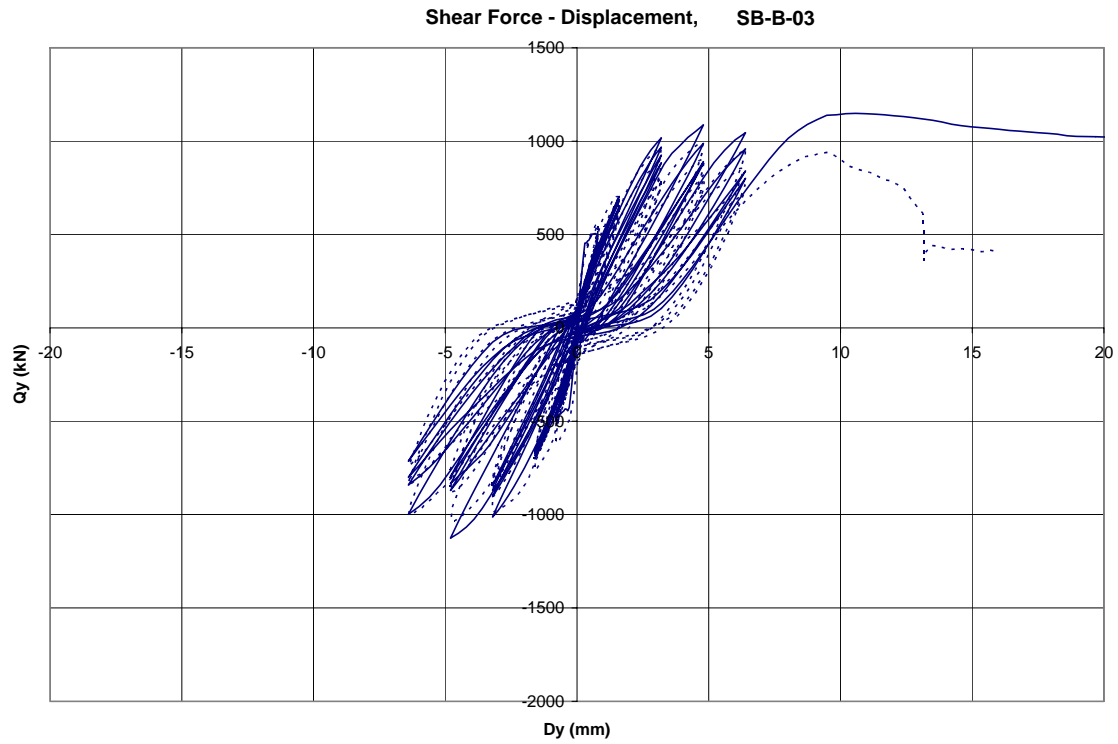


Figure 4-34 Qy – Dy Relation for Diagonal Cross Loading



Figure 4-35 Cycle-By-Cycle Qx – Dx Relation For Diagonal Cross Loading

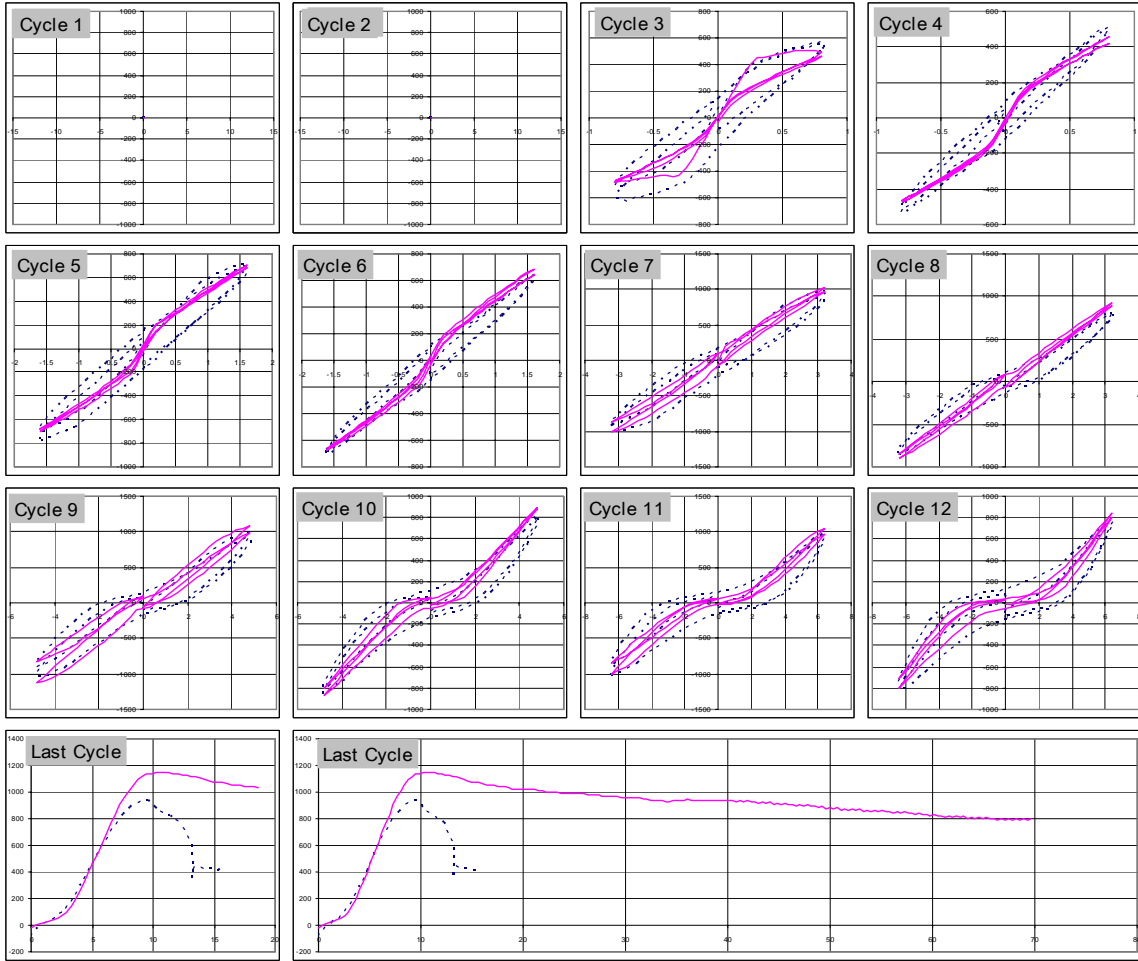


Figure 4-36 Cycle-By-Cycle $Q_y - D_y$ Relation For Diagonal Cross Loading

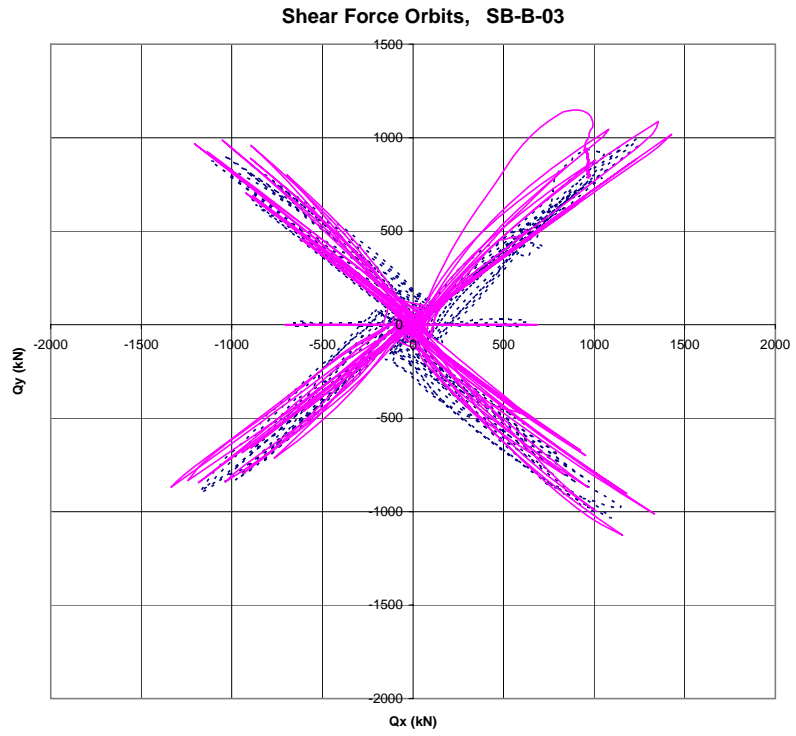


Figure 4-37 Shear Force Orbits for Diagonal Cross Loading

5 ANACAP 3-D FINITE ELEMENT SIMULATION OF DYNAMIC SHAKING TABLE TESTS

5.1 Description of ANACAP Dynamic Shear Wall Model

There were three specimens used in the JNES shaking table tests, in which the one designated as DT-B-02 in the test has been selected for the ANACAP simulation analysis. As shown in Figure 5-1, the shear wall of this specimen shares the same geometry and rebar configuration as those in the static cyclic loading tests described in the previous section. The constitutive models for the concrete and the rebars, the finite element mesh, and the rebar models are also the same as those in the static analyses (see Figure 5-3 through Figure 5-5). Therefore, this section will only describe those modeling features that are relevant in a dynamic loading situation.

The most noticeable difference between the specimen DT-B-02 and the specimens for static tests (Figure 5-1) is that the vertical load was applied by adding extra weight above the loading slab rather than applying vertical force as in the static tests. The weight, the loading slab, and the upper half of the shear wall constitutes a mass compound that weights 67 metric ton, and the resultant rotational inertia are $I_x = I_y = 71.7 \text{ ton}\times\text{m}^2$ and $I_z = 112 \text{ ton}\times\text{m}^2$. The center of gravity is at an elevation of 1240 mm above the top of the base slab. This added weight results in a vertical stress level of 1.47 MPa at the bottom of the shear wall, which is the same as in the static tests. The loading slab and the base slab have slightly different dimensions than those for the static tests, which however can still be considered rigid in the dynamic simulation and thus do not represent a significant difference in modeling.

Figure 5-2 shows a schematic representation of the analytical model that consists of four parts, namely the rigid weight ring, rigid connection ring, the shear wall, and the base slab. The weight and the loading slab are modeled together as the combination of the rigid weight ring and the rigid connection ring. Because ANACAP does not have the capability to model any part of a model as rigid, the loading slab and the base slab have to be assigned a large Young's modulus to simulate their rigidity. In addition, since higher order brick elements must be used for all parts due to the limitations in ANAGEN and consequently entails a high computational demand, a great deal of effort has been undertaken to minimize the number of the elements used in the model. As shown in Figure 5-3, the rigid weight ring, the rigid connection ring, and the shear wall are modeled using one brick element through their thickness (in plan), while the base slab is modeled using two brick elements in plan. The middle parts of the weight, loading slab, and the base slab are omitted from the model, by which the model size is reduced considerably. Approximation of the loading slab and the base slab by rings in the model is still valid because they have a very large stiffness because of the intentional high Young's modulus. All rigid parts have only one element along the vertical direction as shown in Figure 5-4. The model has 448 20-node brick elements (B203D). Figure 5-5 shows the double-layered bi-directional rebar model embedded in the outline of the model, which is basically the same as in the static models.

The material properties of the shear wall as reported in Torita H., et. al. [2004] are used in the analyses. The concrete material has a Young's modulus of 26.6 GPa, a compressive strength of 34.4 MPa, and a Poisson's ratio of 0.19. The fracture strain takes a fixed value of 0.0001 as in the static analyses. The rebar material has a Young's modulus of 180 GPa, a tensile strain at fracture of 27.4%, yield strength of 376 MPa, and a tensile strength of 479 MPa. The yield strength and the tensile strength of the rebars are taken from Mabuchi, K., et al. [2004], which are different than those reported in Torita H., et al. [2004] but are the same as in the data table provided by JNES. The mass density of the concrete is assumed 2400 kg/m^3 , while that of the rebars is assumed 7850 kg/m^3 .

The connect ring and the base slab are mass less in the model, while the rigid weight ring has a density of 155.6 ton/m^3 . As shown in Figure 5-4, the weight ring has an outer edge of 2866 mm long and an inner edge of 2150 mm long, and is 120 mm high. It is connected to the top of the shear wall by the connection ring that is 180 mm high. This configuration arrangement and the particular density of the weight ring make the model have the same mass properties as the specimen, except for the rotational inertia I_z . Because the model does not experience significant rotation deformation around the vertical axis, the value of I_z does not affect the calculation.

ANACAP uses a modified Raleigh damping implementation that is compatible with the damage state of the concrete. The damping values for all parts are assumed as $u_s=1\%$, $d_c=6\%$, and $m_c=1\%$ in the ANACAP input file, where u_s is the damping coefficient for the stiffness term for undamaged concrete, d_c is that for damaged concrete, and m_c is the damping coefficient for the mass term. ANACAP internally uses a damage index d to reflect the cracking level, and the resultant damping for each element is $[(1-d) \times u_s + d \times d_c] + m_c$. The effective damping in the shear wall model is 2% for the initial undamaged state and 7% for the totally damaged state. Because there will be no damage at all for all rigid parts, the effective damping coefficient is about 2% in the analysis.

The shear wall specimen DT-B-02 was subjected to 3-D motions simultaneously in the shaking table test. Examination of the vertical motion recordings at the 4 locations on the top of the base slab has shown that the shear wall was subjected to both vertical translational motion and rolling and rocking motions. This precludes the simple application of three motions, namely two horizontal motions and a vertical motion, to the bottom of the shear wall in the analysis. Therefore, an explicit modeling of the base slab was made with four nodes, shown in Figure 5-3 and Figure 5-4 as black dots and a circle, that correspond to the recording locations in the test. Because the exact rigidity of the base slab was not known and the base slab is modeled with very high rigidity, the application of all 4 motions at the four locations at the same time creates extremely large internal stress states in the base slab and consequently creates severe numerical problems in the reaction forces. More specifically, although the base slab, together with the shaking table, was very stiff, the locations of the 4 recordings do not maintain a perfect plane in reality during the 3-D shaking table test and therefore resulted in slight variation of the perfect plane. This variation in the 4 vertical recordings contradicts to the perfect plane assumed by the rigid base slab model and therefore cannot be applied at the same time. To resolve this problem, only three vertical motions are applied at the locations indicated by the solid dots in Figure 5-3, while the motion at the location indicated by the circle in this figure becomes a derivative quantity. The two horizontal motions are applied at all four indicated locations.

There were totally 9 runs in the test. The solution of the dynamic simulation is performed in ANACAP as follows. The gravity is first applied by the BODYFORCE option in the *STEP command, and then the 5 accelerograms are applied to simulate the shaking table test. Because ANACAP can only handle 2000 data points per *FUNCTION command, the acceleration recordings of each run have to be split into multiple segments and then multiple *STEP commands are used to execute a run. Multiple runs are carried out by restarting a previous run to preserve the damage state, and are organized in separate directories.

5.2 ANACAP Simulation of Shaking Table Shear Wall Tests

The BNL simulation analysis is performed for the specimen DT-B-02 using the ANACAP model. The ANACAP model is described in Section 5.1. There are a total of nine runs performed for the test, which are designated for convenience in this report as: Run Nos. 1, 2, 2', 3, 3', 4, 5, 6, 7. The input motions were calibrated to induce only a small tremor for Run-1 (shear wall remains elastic), and to increase the shaking intensity in an incremental manner for each run thereafter until eventual failure of the specimen. The pre-test analysis estimated that the shear wall specimen could reach failure at the end of Run-6. However, the actual failure of the specimen was declared during the extra test run (Run-7). Therefore, the quality of the data collected from Run-7 is questionable. For this reason, the BNL simulation analysis described in this section does not include the data for Run-7.

As described in Section 5.1, the shear walls from the shaking table tests are bolted to the base slab, which is stiff concrete slab anchored to the shaking table. The shaking table is subjected to the application of three components of seismic input motions of variable levels. Although additional hydraulic jacks were used to balance the table during tests, the shear wall specimen still experienced torsional and rocking modes of vibration during the tests. Therefore, the input motions to the ANACAP shear wall model are selected from the recorded base slab acceleration responses, which include two horizontal orthogonal components and three vertical components. The three vertical component motions are taken from three corner accelerometers of the base slab. Since the base slab remains rigid during the shaking, the motion of the slab can be uniquely defined by the motions of three non-coincidental points on the slab, which is the reason why three corner accelerometers of the slab were utilized to define the input vertical motion for ANACAP shear wall model.

Figure 5-6 through Figure 5-8 show the input motions, each having three components that are simultaneously applied to the ANACAP shear wall simulation analysis for each test run. As depicted in these figures, the input motion for Run-1 is rather small, which was intended for the elastic response of the shear wall specimen. The intensity of the input motion for Run-2, however, was dramatically increased. Subsequent to Run-2, the input motion intensity was reduced for Run-2' to the level slightly above Run-1. The input motions applied to subsequent test runs were then gradually but consistently ramped upward from Run-2' to Run-6, intended for investigating the progressive failures of shear walls as function of the ground motion intensity. All input motions used in the ANACAP analyses were baseline corrected using PCARES [Nie, et al., 2006] and quiet zones were added to each motion for the ANACAP simulation analysis.

The following subsections discuss the simulation analysis results and their comparisons with the test data.

5.2.1 ANACAP Analysis for Run-1

As described in the previous section, the input motion level for Run-1 was very small, which was intended for generating elastic response of the shear wall specimen. The ANACAP analysis was performed and Figure 5-9 through Figure 5-14 present the ANACAP analysis results and their comparisons with the test data for Run-1. In these figures, the solid lines represent the analysis results and the dashed lines show the corresponding response spectra computed from the recorded accelerometers. The analysis results are shown in terms of response spectra at 5% damping, computed on the top of the shear walls. Since the shear wall experienced rocking and torsion in addition to the translational motions, the response spectra in the horizontal directions were computed at the four upper corners of the shear walls, while in the vertical direction, the response spectra were compared at the four corners of the upper slab. The positions of the accelerometers

on the upper slab are shown in Figure 2-21 of Section 2 in this report. The test results discussed in this section also follow the notations depicted in Figure 2-21, in which the designations of the corners 1, 2, 3, and 4 as utilized in this and subsequent sections are relative to the positions defined by the lines A-1, E-1, E-5, and A-5, respectively.

The horizontal response spectra from the test results show a primary peak at 19 Hz, and the ANACAP analysis captures the frequency for this peak with a reasonable precision; however, the primary peak amplification estimate by the ANACAP analysis is off by nearly 50 percent, implying greater energy dissipation inherent in the ANACAP model for this run. In addition, the computed second peak of the horizontal response spectra is shifted toward a lower frequency with higher amplification than the respective spectral peak from the test result.

With respect to the vertical response spectra, the ANACAP model slightly under estimates the peak amplifications of test results.

The maximum shear forces at the base of the shear walls in both X and Y directions, as well as the maximum total vertical force (Z-direction) at the shear wall base are also computed from the ANACAP analysis. These computed base response forces are compared with the corresponding maximum forces recorded from the test run, which were provided by JNES. Table 5-1 provides the comparison of the estimate of maximum base responses by ANACAP analysis with the test results. As shown in this table, the maximum computed shears were less than the respective test results by 18 – 22%, while the computed maximum vertical force has an excellent agreement with the test result (about 1% difference).

5.2.2 ANACAP Analysis for Run-2

The input motion level for Run-2 was increased to above 1.0g, which is significantly higher than the input intensity for Run-1. It was estimated that the cracks were initiated in the shear wall specimen during Run-2. For the Run-2 phase, the ANACAP analysis is initialized at the end of the Run-1 analysis such that the state of stress-strain in the shear walls at the end of Run-1 is applied as the initial condition to the Run-2 analysis. Therefore, prior damage history is accounted for in the subsequent analysis.

The ANACAP analysis results and their comparisons with the test data for Run-2 are presented in Figure 5-15 through Figure 5-20. Similar to the Run-1 analysis, the analysis results are shown in terms of response spectra at 5% damping, computed on the top of the shear walls. Further, the response spectra are computed at the four upper corners of the shear walls for the horizontal directions and for the vertical spectra, the comparisons were made at the four corners of the upper slab.

As illustrated in Figure 5-15, the computed horizontal response spectrum in the X-direction captures with a good accuracy the frequency content but under estimates primary peak response amplification by about 30% of the respective response spectrum from the test result. However, for the response spectrum in the Y-direction as shown in Figure 5-16, the ANACAP analysis result envelops very closely to the respective test result in both the frequency content and the peak amplifications.

With regard to the vertical response spectra, the ANACAP model predicts well the frequency content of the test results. There were two prominent peaks in the test response spectra. The ANACAP calculation of the vertical response spectra slightly under estimates the low frequency peak but matches well to the second peak.

The maximum shear forces at the base of the shear walls in both X and Y directions, as well as the maximum total vertical force (Z-direction) at the shear wall base are compared between the ANACAP analysis and the test results. These computed base response forces and the corresponding maximum forces recorded during the test are tabulated in Table 5-2. As shown in this table, the maximum computed shear in the X-direction is slightly less than the test result while the Y-direction shear was estimated slightly higher than the test result. All in all, the differences between the analysis and the test results were about 18%. In addition, the computed maximum vertical force is about 11% higher than the test result.

5.2.3 ANACAP Analysis for Run-2'

After the strong input motion applied for Run-2, the test was returned to a much lower shaking intensity for Run-2'. Prior to Run-2', the prominent oscillation in the table shaking may be due to the calibration of the test itself. As shown in Figure 5-6 through Figure 5-8, from Run-2' thereafter, the intensity of the input motion is increased consistently in an incremental fashion. Again, the Run-2' analysis is performed as a continuation of Run-2, meaning that the end state of stress-strain field of Run-2 serves as the initial condition for Run-2'.

Figure 5-21 through Figure 5-26 present the ANACAP analysis results in terms of response spectra and their comparisons with the test data for Run-2'. The horizontal responses are computed at the four upper corners of the shear walls and the vertical responses are calculated at the four corners of the upper slab.

The computed horizontal response spectra generally envelop the respective test results, especially for the response in the Y-direction, where an excellent agreement between the computed and the test result is illustrated in Figure 5-22. Also shown in these figures are the remarkable agreement in the frequency contents between the ANACAP analysis and the test results.

With regard to the vertical response spectra, the ANACAP analysis generally captures well the frequency contents of the test results, as shown in Figure 5-23 through Figure 5-26. However, the ANACAP model under estimates the peak responses of the test results.

The maximum shear forces at the base of the shear walls in both X and Y directions, as well as the maximum total vertical force (Z-direction) at the shear wall base are tabulated in Table 5-3. As shown in this table, the maximum computed shear in the X-direction is larger than the test result by about 19%, while the Y-direction shear is estimated very closely to the test result by about 6%. Furthermore, an excellent agreement between the computed maximum vertical force and the test result is obtained within 2.5%.

In addition, the hysteresis loops are examined for Run-2'. Figure 5-27 and Figure 5-28 show the acceleration vs. relative displacement hysteresis loops comparisons between the ANACAP analysis and the test results. The accelerations in hysteresis loops are taken at the top of the shear walls and the relative displacements are computed from the displacements between the top and the base of the shear walls. The solid lines in the figures represent the analysis results and the dashed lines depict the test data. These figures illustrate that similar slope characteristics are exhibited between the analysis and the test results. Further, the test hysteresis loops show narrow banded behavior while the analysis indicates broader band hysteresis, implying that the analysis model dissipates more energy than the actual test run. Lastly, the square-root-of-sum-of-square (SRSS) base shear and SRSS shear strain are computed and plotted in Figure 5-29, which shows that the maximum strain in the shear wall is reached at 0.1% for Run-2'.

5.2.4 ANACAP Analysis for Run-3

This subsection describes the ANACAP simulation analysis for Run-3. The intensity of the input motion for Run-3 was increased to about twice the input motion intensity for Run-2'. The ANACAP analysis for Run-3 is initiated using the end state of the stress and strain in the shear walls for Run-2' as the initial conditions, thereby incorporating the prior cumulative damages in the current analysis.

Figure 5-30 through Figure 5-35 present the computed response spectra from the ANACAP analysis and their comparisons with the test data for Run-3. The comparisons are made at the four upper corners of the shear walls for the horizontal spectra, while for the vertical spectra the comparisons are made at the four corners of the upper slab.

The comparisons for the horizontal response spectra as shown in Figure 5-30 and Figure 5-31 indicate that the computed X-direction spectra generally match or exceed the respective test results and the computed Y-direction spectra envelop closely the test results. Therefore, the ANACAP model captures well the characteristics of the test results in the horizontal response spectra for Run-3.

For the vertical response spectra, the test results depict three prominent peaks. The computed vertical response spectra from the ANACAP analysis as shown in Figure 5-32 through Figure 5-35 generally compare well with the test results in the frequency content. With respect to the spectral peak amplifications, the comparisons between the computed and the test results are fair, although at the some corners, the computed spectral peaks are lower than the test results. The under estimate of the calculated spectral peak responses indicates that the ANACAP model dissipates more energy in the vertical direction than the actual energy dissipation from the test results.

The maximum shear forces at the base of the shear walls in both X and Y directions, as well as the maximum total vertical force (Z-direction) at the shear wall base are tabulated in Table 5-4. As shown in this table, the maximum computed shears in both X and Y directions exceed the test result by about 20%. Similar to the previous runs, an excellent agreement is demonstrated between the computed maximum vertical force and the test result with less than 4% difference.

The comparisons of the hysteresis loops are made between the ANACAP analysis and the test results for Run-3, as shown in Figure 5-36 and Figure 5-37. The hysteresis loops are computed in terms of the acceleration at the top of the shear walls vs. relative displacement between the top and the base of the shear walls. The solid lines in the figures represent the analysis results and the dashed lines depict the test data. These figures show similar slope characteristics between the analysis and the test results. However, the analysis hysteresis loop in the X-direction is broader than the test result, indicating higher energy dissipation from the analysis model than the actual test results. Lastly, the square-root-of-sum-of-square (SRSS) base shear and SRSS shear strain are computed and plotted in Figure 5-38, which shows that the maximum strain in the shear wall is reached at 0.17% for Run-3.

5.2.5 ANACAP Analysis for Run-3'

For Run-3', the input motion intensity was increased to twice the level of the input motion for Run-3. The ANACAP analysis for Run-3' continues using the state of the stress and strain in the shear walls at the end of Run-3 as the initial conditions.

Figure 5-39 through Figure 5-44 present the comparisons of the computed vs. test response spectra for Run-3'. The comparisons of the horizontal spectra are made at the four upper corners of the shear walls and the comparisons of the vertical spectra are rendered at the four corners of the upper slab.

For the horizontal response spectra, the comparisons are shown in Figure 5-39 and Figure 5-40. As depicted in these figures, the computed response spectra in both X and Y directions compare very well with the test results. The computed spectra generally match or envelop the respective test results and the frequency contents of the test results are captured well by the ANACAP analysis.

For the comparisons of vertical response spectra as shown in Figure 5-41 through Figure 5-44, the test results show three prominent peaks. The computed vertical response spectra from the ANACAP analysis compares fairly well to the test response spectra in the frequency content, although the low frequency peak amplifications from the analysis tend to be lower than the test results. By and large, the ANACAP shear wall model predicts well the overall characteristics of the test results for the vertical response.

The comparisons of the maximum shear forces at the base of the shear walls in both X and Y directions, as well as the maximum total vertical force (Z-direction) at the shear wall base are tabulated in Table 5-5. As indicated in this table, the maximum computed shear in the X direction matches the test result with less than 8% difference, and the maximum computed shear in the Y direction matches the test result with less than 1% difference. In addition, the computed maximum vertical force matches the test result with less than 2% difference.

The comparisons of the hysteresis loops for Run-3' are presented in Figure 5-45 and Figure 5-46. The hysteresis loops are computed in terms of the acceleration at the top of the shear walls vs. relative displacement between the top and the base of the shear walls. The solid lines in the figures represent the analysis results and the dashed lines depict the test data. As shown in these figures, the computed hysteresis loop in the X-direction has similar slope characteristics with the test results, while in the Y-direction the computed hysteresis loop appears slightly steeper than the test result, implying more degradation than predicted by the analysis in the Y-direction of the shear wall. Lastly, the square-root-of-sum-of-square (SRSS) base shear and SRSS shear strain are computed and plotted in Figure 5-47. This figure shows the state of the maximum strain level reached at the end of Run-3' as predicted by the ANACAP analysis, which is approximately 0.26%.

5.2.6 ANACAP Analysis for Run-4

For Run-4, the input motion was maintained at about the same level as the input motion for Run-3', and the ANACAP analysis for Run-4 continues using the state of the stress and strain in the shear walls at the end of Run-3' as the initial conditions.

Figure 5-48 through Figure 5-53 present the comparisons of the computed vs. test shear wall response spectra for Run-4. These comparisons are made at the four top corners of the shear walls for the horizontal spectral and the spectra calculated at the four corners of the upper slab are used for the comparisons of the vertical responses.

For the horizontal response spectra, the comparisons, as shown in Figure 5-48 and Figure 5-49, indicate that the ANACAP analysis closely predicts the test results for the horizontal responses. As depicted in these figures, the computed spectra either match or envelop the respective test

results and the frequency contents are matched very well between the test results and the ANACAP analysis.

For the comparisons of vertical response spectra shown in Figure 5-50 through Figure 5-53, the test results show multiple prominent peaks, which also vary depending on the measurement location. The computed vertical response spectra from the ANACAP analysis for Run-4 show much better comparisons to the test results than the previous runs. The analysis generally captures the frequency content of the test response spectra. Especially for the corner 4, the computed response spectrum traces very closely to the test result.

The comparisons of the maximum shear forces at the base of the shear walls in both X and Y directions, as well as the maximum total vertical force (Z-direction) at the shear wall base are tabulated in Table 5-6. As exhibited in this table, the maximum computed shear in the X direction matches the test result with about 8% difference, and the maximum computed shear in the Y direction matches the test result with about 4.5% difference. In addition, the computed maximum vertical force matches the test result with about 10.8% difference.

The comparisons of the hysteresis loops for Run-4 are shown in Figure 5-54 and Figure 5-55. The hysteresis loops in terms of the acceleration at the top of the shear walls vs. relative displacement between the top and the base of the shear walls are computed. The solid lines in the figures show the analysis results and the dashed lines represent the test data. As shown in these figures, the computed hysteresis loop in the X-direction has similar slope characteristics with the test results, while in the Y-direction the computed hysteresis loop appears slightly steeper than the test result, implying more cumulative damage in the actual test than predicted by the analysis in the Y-direction of the shear wall. This observation about the hysteresis loop for Run-4 is similar to the previous observation made for the Run-4 analysis. Again, the square-root-of-sum-of-square (SRSS) base shear and SRSS shear strain are computed and plotted for Run-4 in Figure 5-56. This figure shows the state of the maximum strain level reached at the end of Run-4 as predicted by the ANACAP analysis, which is approximately 0.35%.

5.2.7 ANACAP Analysis for Run-5

In the ANACAP simulation analysis for Run-5, the input motion was increased to the level about 30% higher than the input motion for Run-4, and the ANACAP analysis for Run-5 continues using the state of the stress and strain in the shear walls at the end of Run-4 as the initial conditions.

Figure 5-57 through Figure 5-62 present the comparisons of the computed vs. test shear wall response spectra for Run-5. The comparisons are rendered at the four top corners of the shear walls for the horizontal spectra, and at the four corners of the upper slab for the vertical spectra.

For the horizontal response spectra, the comparisons are illustrated in Figure 5-57 and Figure 5-58, which exhibit close matches between the calculated response spectra and the test results. As shown in these figures, the computed response spectra trace very well to the test results, especially in the Y direction where the computed spectrum envelops the spectral peaks from the test result. These comparisons indicate that the ANACAP model adequately captures the horizontal response characteristics of the test results.

For the comparisons of vertical response spectra for Run-5 shown in Figure 5-59 through Figure 5-62, the test results show one prominent spectral peak. The computed vertical response spectra from the ANACAP analysis show close comparisons to the test results, but under-estimate the spectral peak shown in the test result. This observation is consistent with the previous runs,

indicating that the ANACAP model has more energy dissipation than the test results in the vertical direction.

The comparisons of the maximum shear forces at the base of the shear walls in both X and Y directions, as well as the maximum total vertical force (Z-direction) at the shear wall base from Run-5 are tabulated in Table 5-7. As exhibited in this table, the maximum computed shear in the X direction matches the test result with about 8% difference, and the maximum computed shear in the Y direction matches the test result with less than 4% difference. In addition, the computed maximum vertical force matches the test result with about 14% difference.

The comparisons of the hysteresis loops for Run-5 are shown in Figure 5-63 and Figure 5-64. The hysteresis loops in terms of the acceleration at the top of the shear walls vs. relative displacement between the top and the base of the shear walls are computed. The solid lines in the figures show the analysis results and the dashed lines represent the test data. As shown in these figures, the computed hysteresis loop in the X-direction has similar slope characteristics with the test results, while in the Y-direction the computed hysteresis loop appears slightly steeper than the test result, which is consistent with the observation made for the previous run. Finally, the square-root-of-sum-of-square (SRSS) base shear and SRSS shear strain are computed and plotted for Run-5 in Figure 5-65. This figure shows the state of the maximum strain level reached at the end of Run-5 as predicted by the ANACAP analysis, which is approximately 0.42%.

5.2.8 ANACAP Analysis for Run-6

For Run-6, which is the last run in the ANACAP simulation analysis, the input motion intensity was increased to the level about 25% higher than the input motion for Run-5, and the ANACAP analysis for Run-6 continues using the state of the stress and strain in the shear walls at the end of Run-5 as the initial conditions. Although the actual “collapse” of the shear wall specimen was pronounced during Run-7, it is judged that the incipient failure of the shear wall occurred at the end of Run-6.

Figure 5-66 through Figure 5-71 present the comparisons of the computed vs. test shear wall response spectra for Run-6. The comparisons of the horizontal spectra are made at the four top corners of the shear walls, and the comparisons of the vertical spectra are presented at the four corners of the upper slab.

The comparisons for the horizontal response spectra between the test results and the ANACAP analysis are shown in Figure 5-66 and Figure 5-67. As shown in these figures, the computed response spectra match very well to the test results in the X-direction. In the Y-direction, the computed spectra under estimate the second spectral peak by about 30% from the test results. In both directions, the computed spectra appear to capture well the frequency contents of the test results.

For the comparisons of vertical response spectra for Run-6 shown in Figure 5-68 through Figure 5-71, the computed response spectra from the ANACAP analysis generally match or exceed the test results, reversing the under-predicted trend in the previous runs. In addition, the ANACAP model also captures well the frequency contents of the test results in the vertical direction.

The comparisons of the maximum shear forces at the base of the shear walls in both X and Y directions, as well as the maximum total vertical force (Z-direction) at the shear wall base from Run-6 are tabulated in Table 5-8. As indicated in this table, the maximum computed shear in the X direction matches the test result with less than 2% difference, while the maximum computed

shear in the Y direction is lower than the test result by 21%. The computed maximum vertical force appears to grossly exceed the test result by about 55%.

The comparisons of the hysteresis loops for Run-6 are shown in Figure 5-72 and Figure 5-73. The hysteresis loops in terms of the acceleration at the top of the shear walls vs. relative displacement between the top and the base of the shear walls are computed. The solid lines in the figures show the analysis results and the dashed lines represent the test data. As shown in these figures, the computed hysteresis loop in the X-direction initially has similar slope characteristics with the test results and gradually becomes more shallower the test result, indicating rapid reduction of loading bearing capability. Similar observation is also made for the hysteresis hoop comparison in the Y-direction. Finally, the square-root-of-sum-of-square (SRSS) base shear and SRSS shear strain are computed and plotted for Run-6 in Figure 5-74. This figure shows the state of the maximum strain level reached at the end of Run-6 as predicted by the ANACAP analysis, which is approximately 2.2%, about five times higher than the previous run. Therefore, the shear wall specimen is deemed to have reached failure at the end of Run-6 as predicted by the ANACAP analysis.

5.3 ANACAP Analysis of Test Run 6 without Considering Prior Damages

In the ANACAP simulation analysis, cumulative prior damage history is considered at each stage of the simulation analysis. In this subsection, another scenario of analysis is investigated, which does not consider prior damages. The purpose of this analysis is to examine the impact of prior damage history on the response analysis of shear walls performed on a single event basis. For this purpose, the same three orthogonal input motions from the Run-6 test used in the simulation analysis are applied, except that the shear wall specimen is assumed having no previous damage history. The shear wall responses in terms of response spectra and hysteresis loops, as well as the total base shears are compared with the test results that have the prior damage effects.

Figure 5-75 through Figure 5-80 present the comparisons of the computed shear wall response spectra including no prior damage history to the actual test results for Run-6. The comparisons are made at the four top corners of the shear walls for the horizontal spectra, and the four top corners of the upper slab for the vertical spectra.

The comparisons for the horizontal response spectra between the ANACAP analysis, which includes no prior damage history, and the test results from Run-6 are shown in Figure 5-75 and Figure 5-76. As shown in these figures, the computed response spectra match very well to the test results in the X-direction up to about 20 Hz and exhibit much higher spectral amplifications than the test results above 30Hz. In the Y-direction, the computed spectra trace very closely to the test results, and have demonstrated better matches to the test results than the ANACAP simulation analysis for Run-6 as shown in Figure 5-67.

For the vertical response spectra, the comparisons of the ANACAP analysis results without considering previous damage history and the test results for Run-6 are shown in Figure 5-77 through Figure 5-80. As depicted in these figures, the computed response spectra from the ANACAP analysis generally match or exceed the test results in a similar fashion to the ANACAP simulation analysis. Therefore, prior damage history does not appear to affect the estimate of the failure response in terms of response spectra.

To examine the effect of not including the prior damage history on the maximum base shears, the comparisons of the maximum shear forces at the base of the shear walls in both X and Y directions, as well as the maximum total vertical force (Z-direction) at the shear wall base between the ANACAP analysis and the test results from Run-6 are tabulated in Table 5-9. As

shown in this table, the maximum computed shear in the X direction without including the prior damages over estimates the test result by more than 50% in the X-direction, while in the Y direction almost a perfect match is obtained between the ANACAP analysis and the test result (just 0.7% difference). The computed maximum vertical force appears to grossly exceed the test result by about 50%. Therefore, the maximum base loads on the shear walls are mostly over estimated when the prior damage history is not included in the analysis.

The comparisons of the hysteresis loops for Run-6 between the ANACAP analysis with no prior damage history and the test results are shown in Figure 5-81 and Figure 5-82. The hysteresis loops in terms of the acceleration at the top of the shear walls vs. relative displacement between the top and the base of the shear walls are computed. The solid lines in the figures show the analysis results and the dashed lines represent the test data. As shown in these figures, the computed hysteresis loop in the X-direction initially has similar slope characteristics with the test results and gradually becomes more shallower the test result, indicating rapid reduction of loading bearing capability. Similar observation is also made for the hysteresis hoop comparison in the Y-direction. These observations are similar to the comparison for Run-6 between the ANACAP simulation and the test results. Therefore, no significant changes are identified due to the effect of the prior damage history. Finally, the square-root-of-sum-of-square (SRSS) base shear and SRSS shear strain are computed from the ANACAP analysis results and plotted in Figure 5-83. This figure shows the state of the maximum strain level reached at the end of the standalone Run-6 analysis, which is approximately 1.7%, much smaller than the 2.2% observed from the simulation analysis for Run-6.

5.4 ANACAP Analysis of Test Run 6 using Only X-Input Motion

In the previous subsection, an ANACAP analysis was presented for the three directional input motions from Run-6, when cumulative prior damage history is ignored. In the conventional seismic design analysis, the shear wall structures are often analyzed for only one input motion in an in-plane direction of the shear wall and the out-of-plane effect is ignored. In this subsection, to investigate the out-of-plane effect, two analyses are performed by applying the input motion in the X-direction only, and one analysis considers prior damage history and the other ignores the prior damage history. The input motion in X-direction for Run-6 is used for the analyses. The analysis results and their comparisons with the test results are provided as below.

Figure 5-84 and Figure 5-85 present the comparisons of the computed shear wall response spectra in the X-direction to the test results for Run-6. As shown in these figures, the analysis results computed using only the X-direction input and with prior damage history compares very well with the test results from the three orthogonal input motions for Run-6. However, when prior damage is ignored, the computed response spectra using only the X-direction input show grossly exaggerated spectral amplifications results in the frequencies between 10 – 20 Hz, compared to the test data.

The out-of-plane effect is also demonstrated by the comparisons of the maximum base shears. The maximum base shear from the test Run-6 is equal to 1165 kN, and the calculated maximum base shears resulting from the analyses using only the X-direction input motion, with and without prior damage history, are 1288 kN and 1292 kN, respectively. The resulting base shear calculations ignoring out-of-plane effect is about 10% higher than the test result. However, when the comparison is made in the context of ignoring prior damage, neglecting the out-of-plane effect in fact resulted in a decrease in the base shear by about 27% (the estimate of the base shear with three directional input motions equals to 1777 kN when prior damage is not considered).

The comparisons of the hysteresis loops between the ANACAP analyses using a single input motion and the test results for Run-6 are shown in Figure 5-86 and Figure 5-87. The hysteresis loops in terms of the acceleration at the top of the shear walls vs. relative displacement between the top and the base of the shear walls are computed. The solid lines in the figures show the analysis results and the dashed lines represent the test data. As shown in these figures, the computed hysteresis loops with and without prior damage history exhibit similar characteristics, although slightly larger displacement is noted for the analysis with prior damage history. With regard to the scenario of single input motion vs. three input motions, no noticeable differences were identified due principally to the symmetry of the test specimen. Finally, the square-root-of-sum-of-square (SRSS) base shear and SRSS shear strain are computed from the ANACAP analysis results and plotted in Figure 5-88 and Figure 5-89. These figures show the difference in the maximum cumulative strain levels computed with and without prior damage history are 2.2% vs. 1.7%.

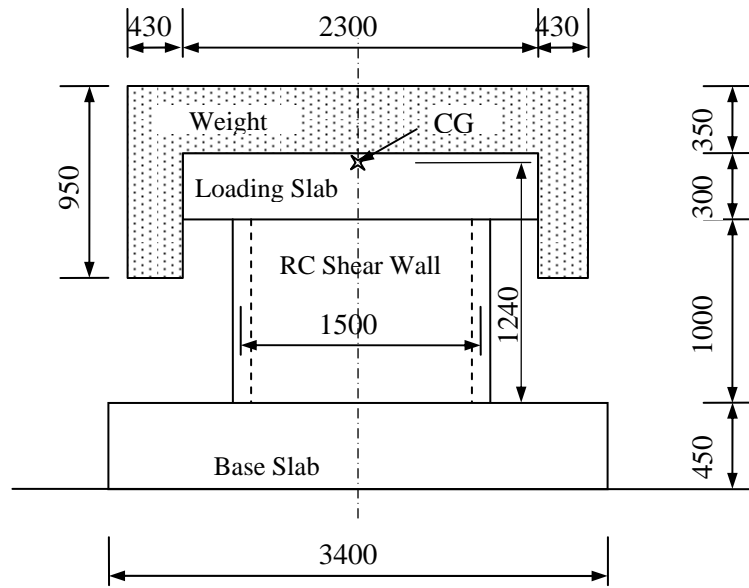


Figure 5-1 Elevation of DT-B-02 Model (Unit: mm)

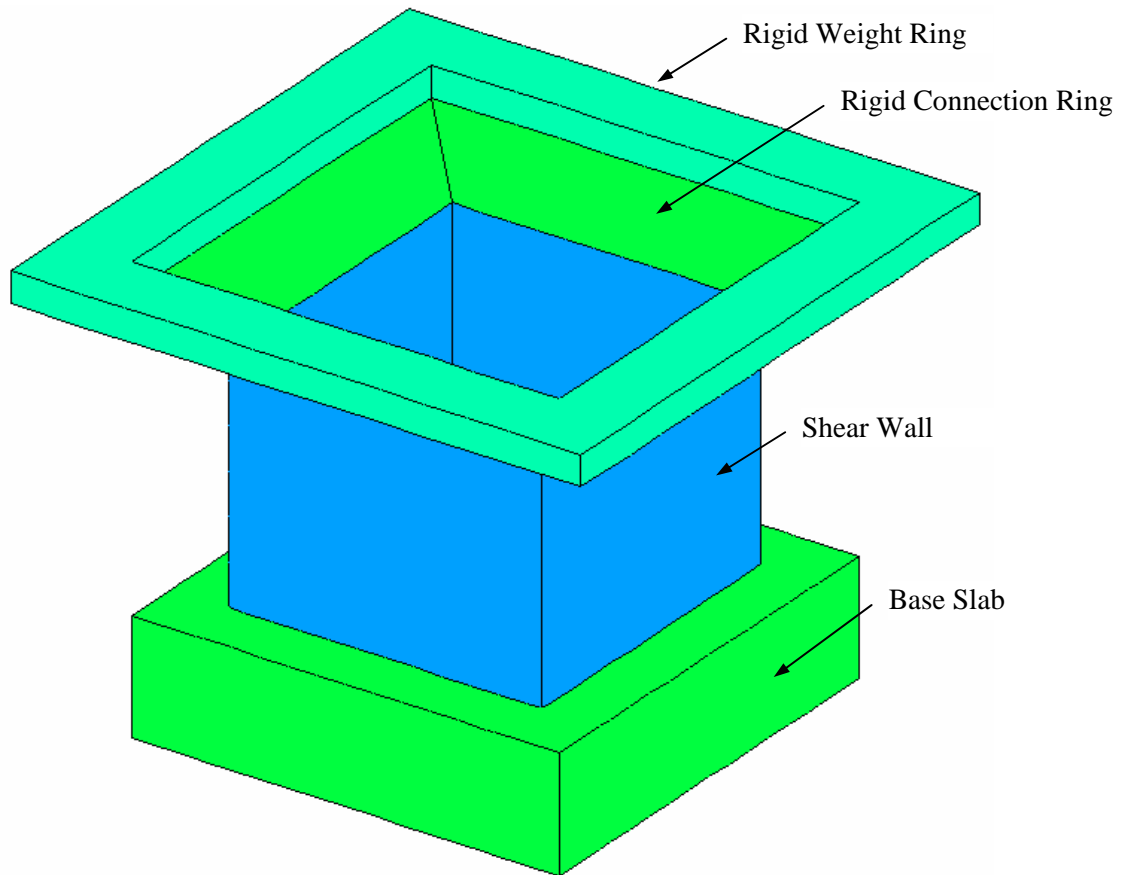


Figure 5-2 Shear Wall Model for Dynamic Simulation

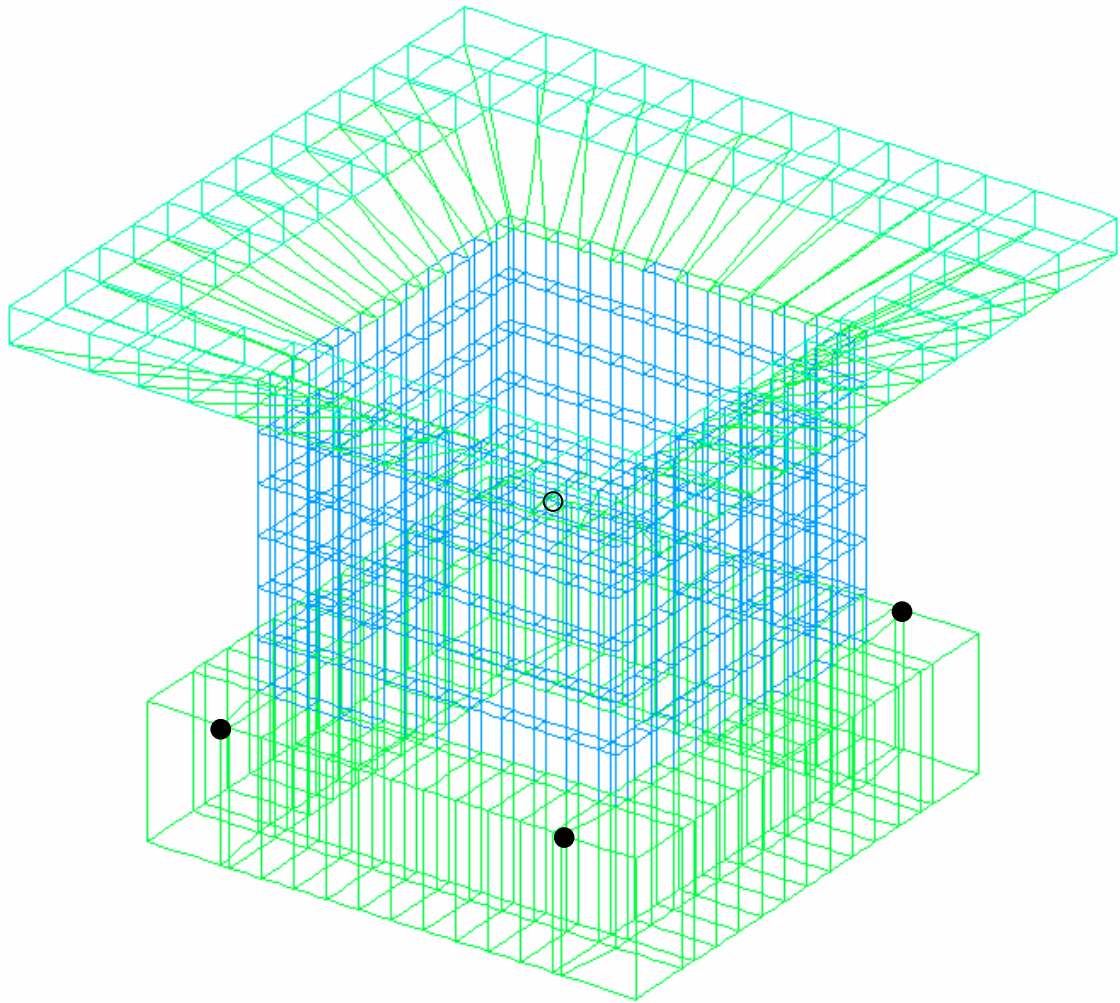


Figure 5-3 Shear Wall Mesh for Dynamic Simulation

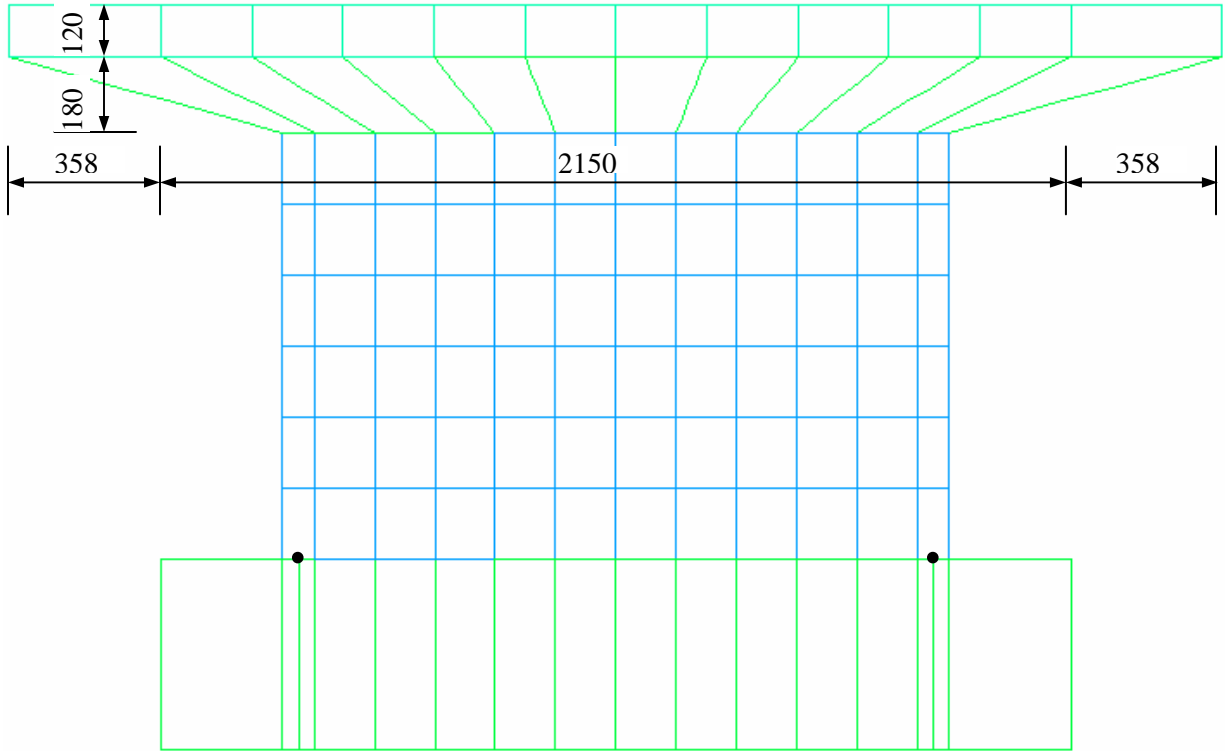


Figure 5-4 Shear Wall Mesh for Dynamic Simulation (Elevation, Unit mm)

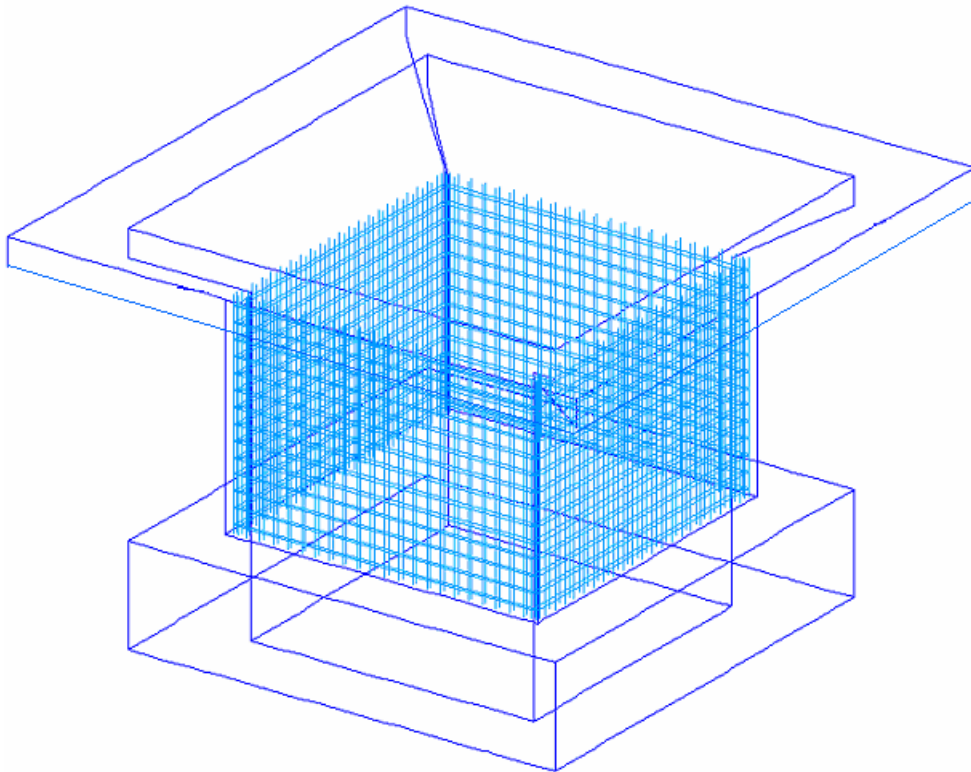


Figure 5-5 Shear Wall Rebars for Dynamic Simulation

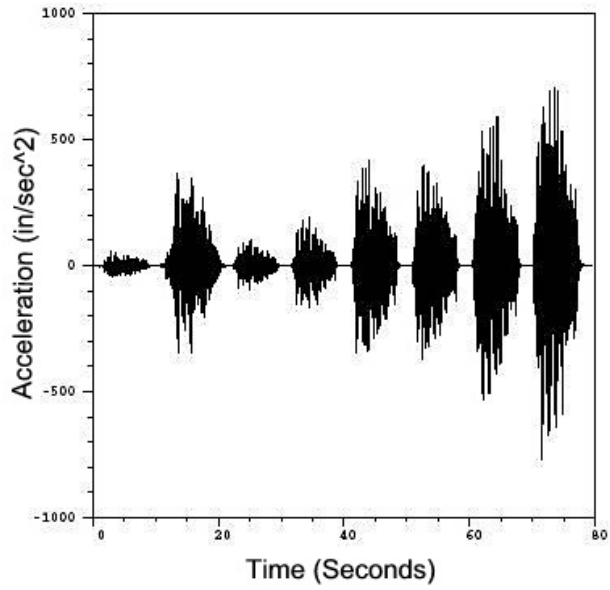


Figure 5-6 X-Input Motions for ANACAP Simulation Analysis

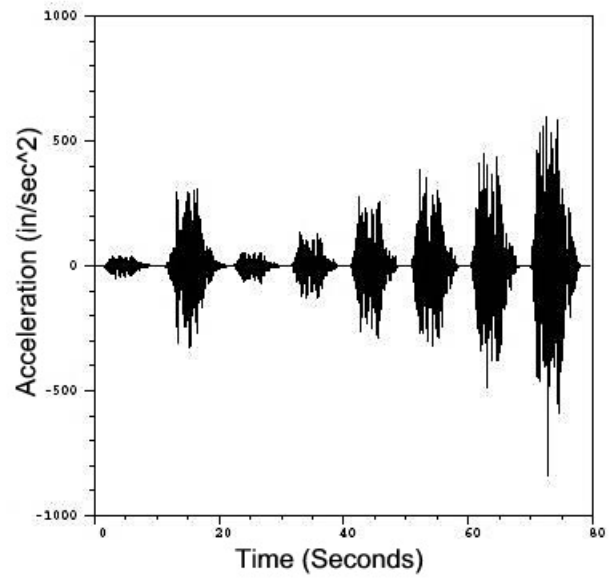


Figure 5-7 Y-Input Motions for ANACAP Simulation Analysis

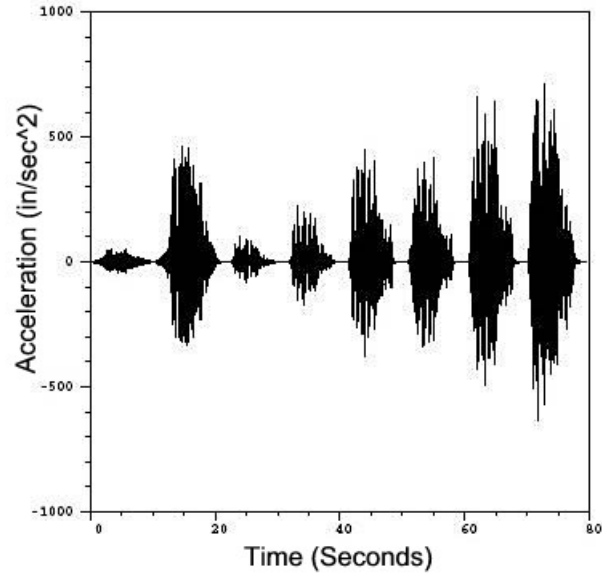


Figure 5-8 Z-Input Motions for ANACAP Simulation Analysis

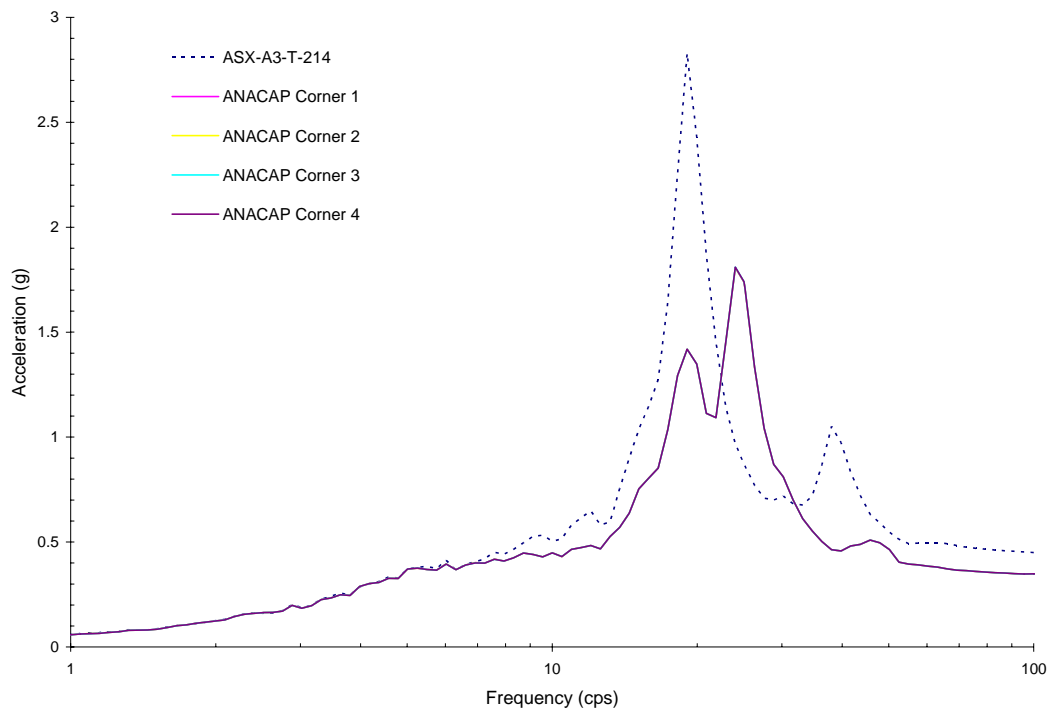


Figure 5-9 Comparison of X-Direction Response between ANACAP Analysis at Upper Corners of Shear Walls and Measured Data for Run-1

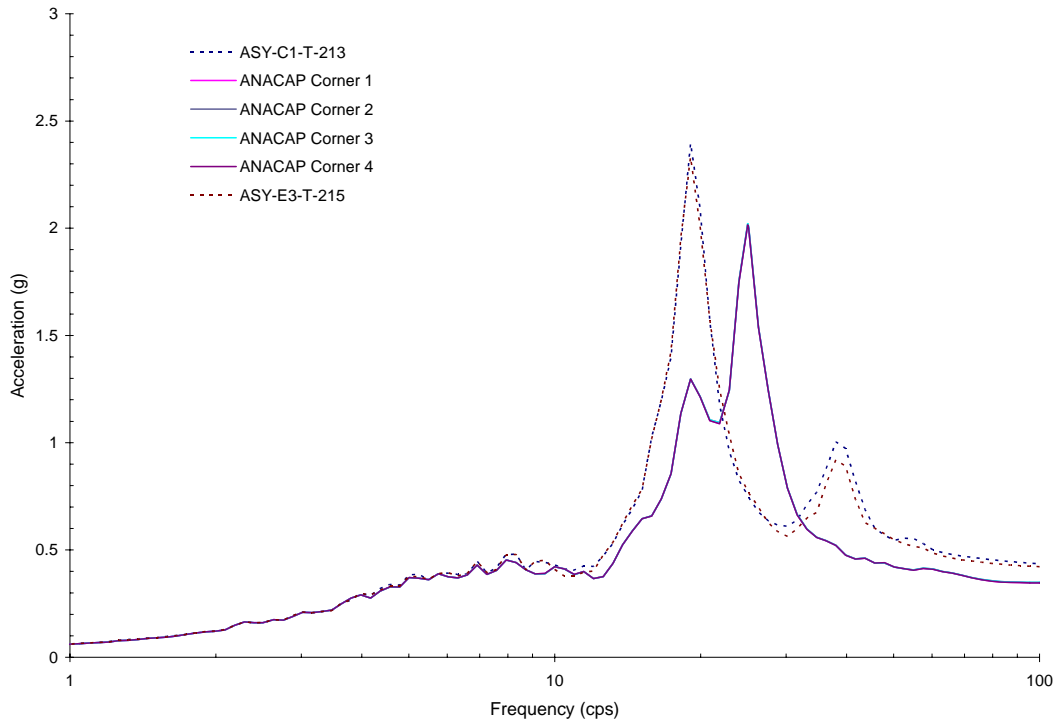


Figure 5-10 Comparison of Y-Direction Response between ANACAP Analysis at Upper Corners of Shear Walls and Measured Data for Run-1

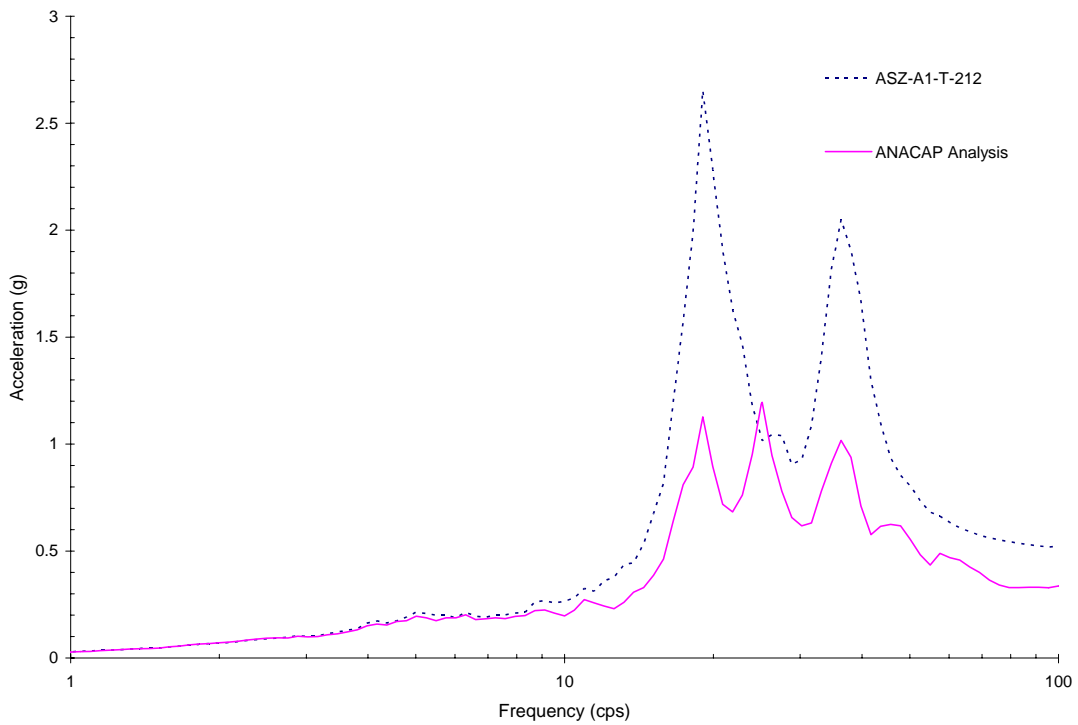


Figure 5-11 Comparison of Z-Direction Response between ANACAP Analysis at Upper Slab Corner No. 1 and Measured Result for Run-1

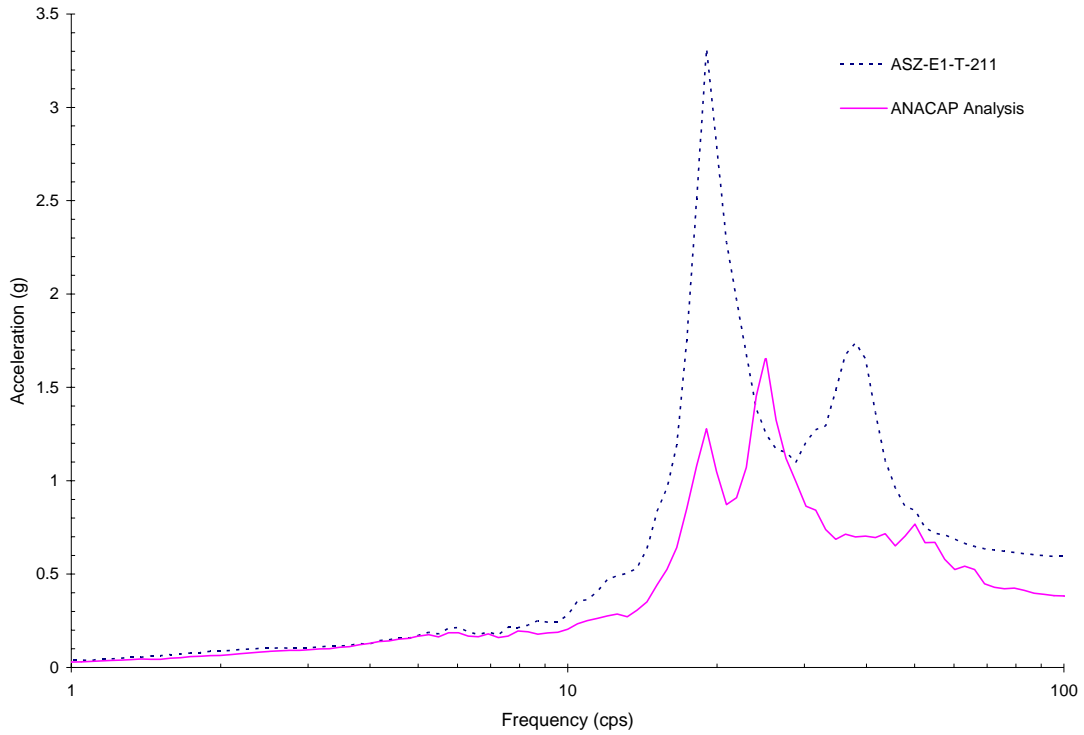


Figure 5-12 Comparison of Z-Direction Response between ANACAP Analysis at Upper Slab Corner No. 2 and Measured Result for Run-1

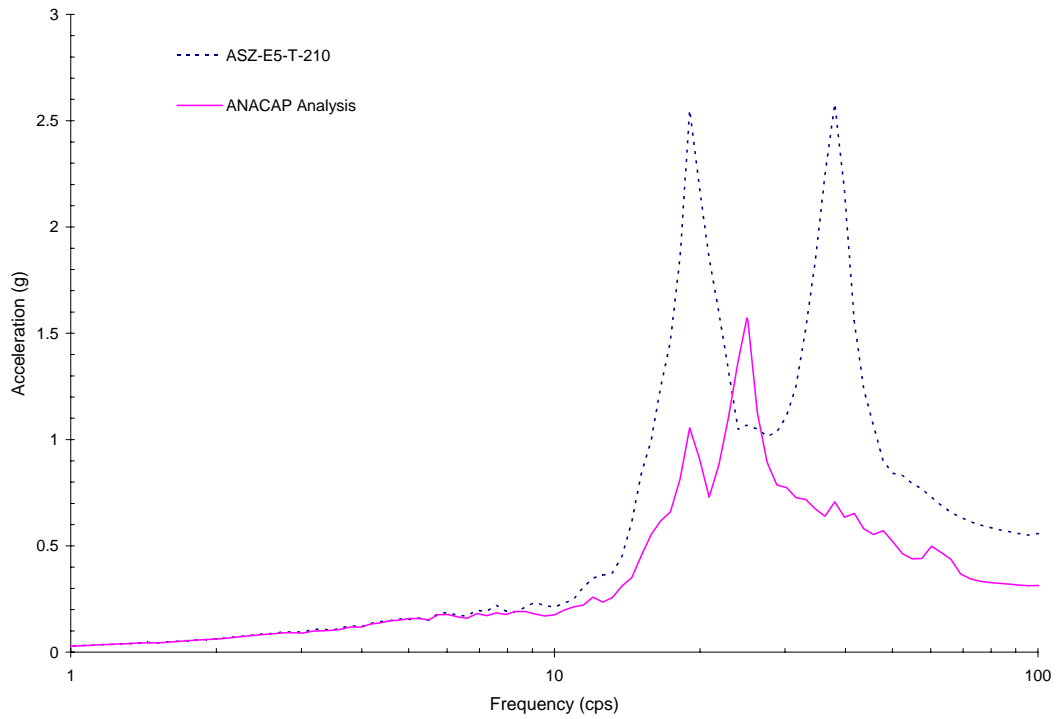


Figure 5-13 Comparison of Z-Direction Response between ANACAP Analysis at Upper Slab Corner No. 3 and Measured Result for Run-1

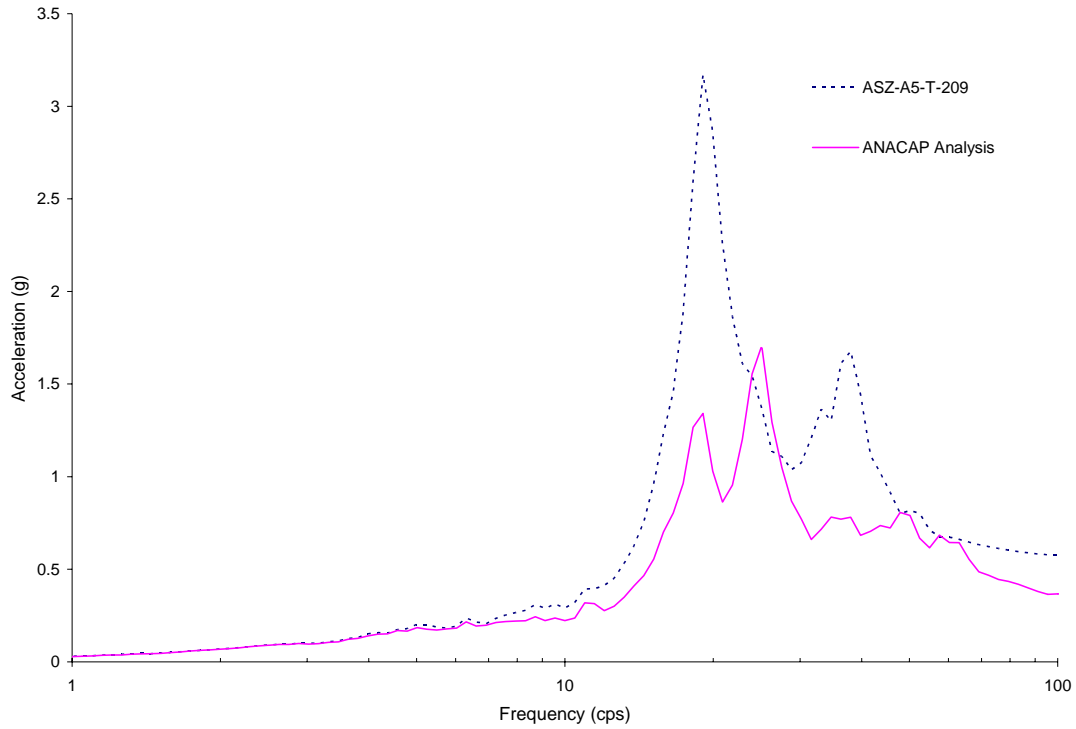


Figure 5-14 Comparison of Z-Direction Response between ANACAP Analysis at Upper Slab Corner No.4 and Measured Result for Run-1

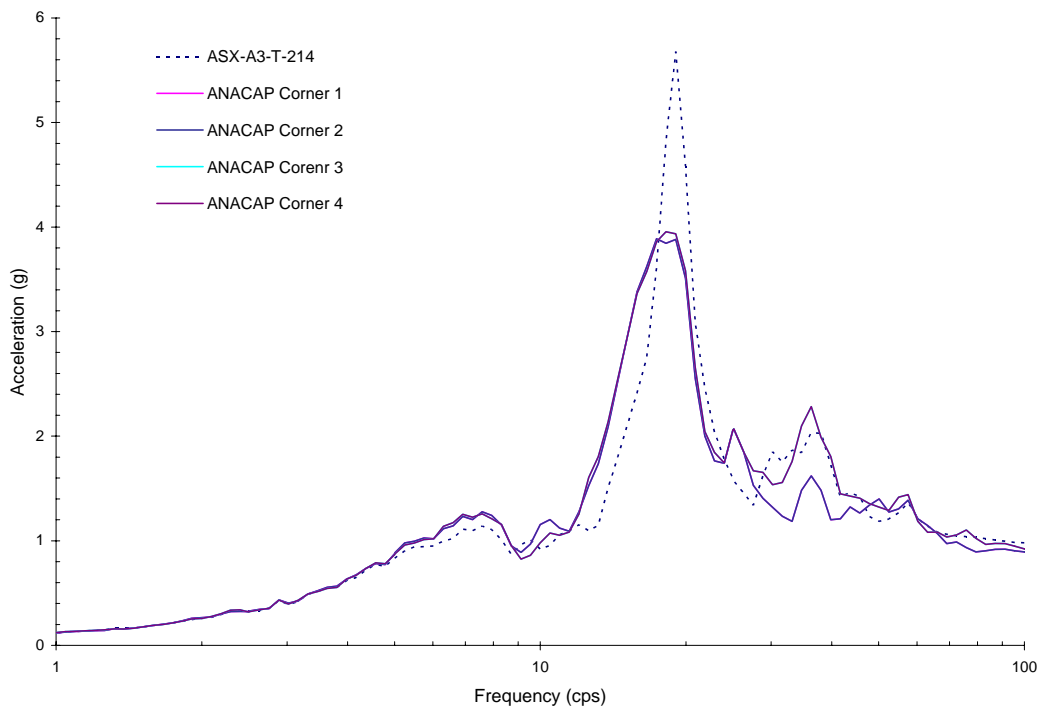


Figure 5-15 Comparison of X-Direction Response between ANACAP Analysis at Upper Corners of Shear Walls and Measured Data for Run-2

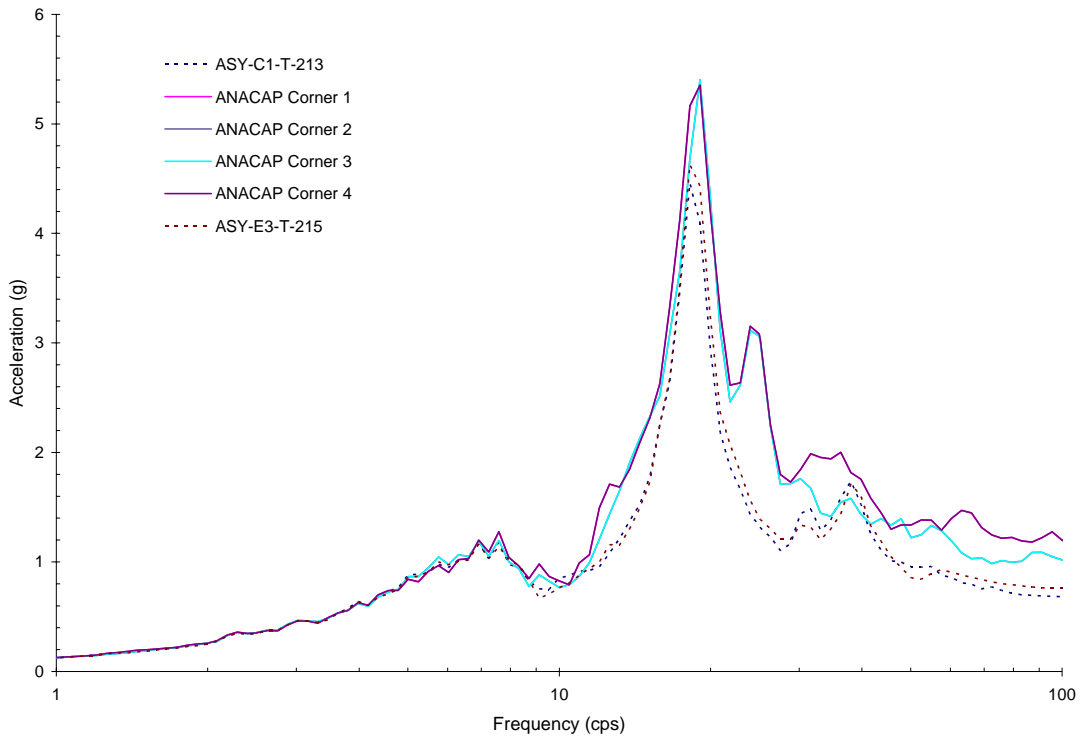


Figure 5-16 Comparison of Y-Direction Response between ANACAP Analysis at Upper Corners of Shear Walls and Measured Data for Run-2

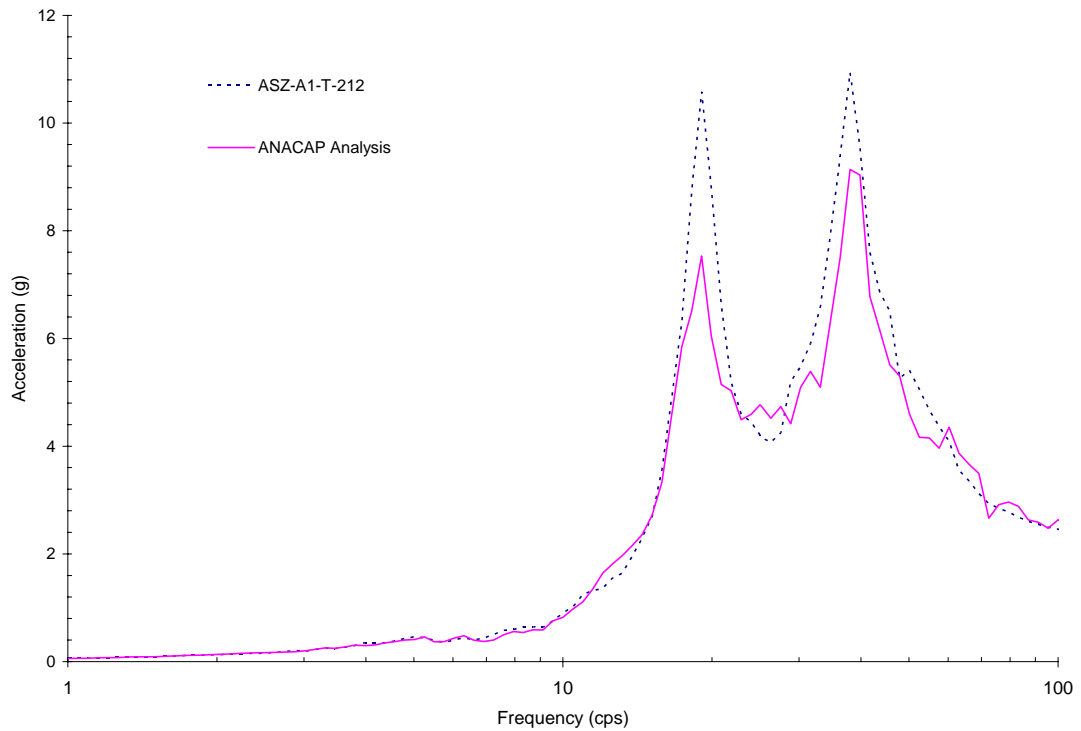


Figure 5-17 Comparison of Z-Direction Response between ANACAP Analysis at Upper Slab Corner No.1 and Measured Result for Run-2

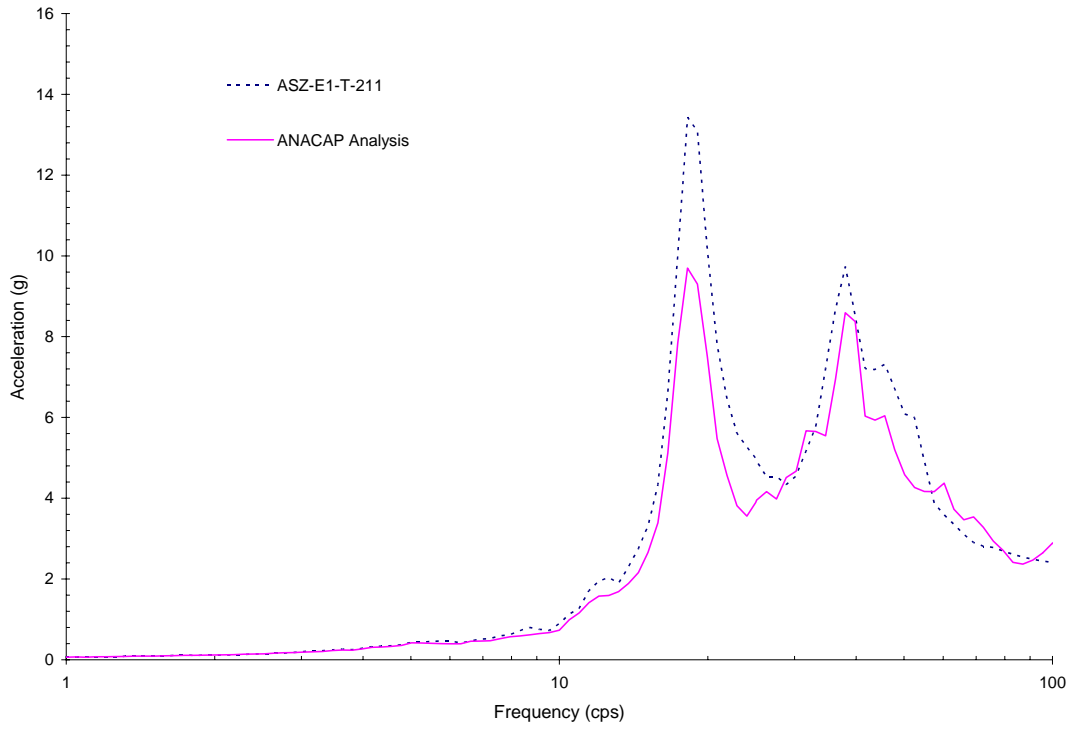


Figure 5-18 Comparison of Z-Direction Response between ANACAP Analysis at Upper Slab Corner No.2 and Measured Result for Run-2

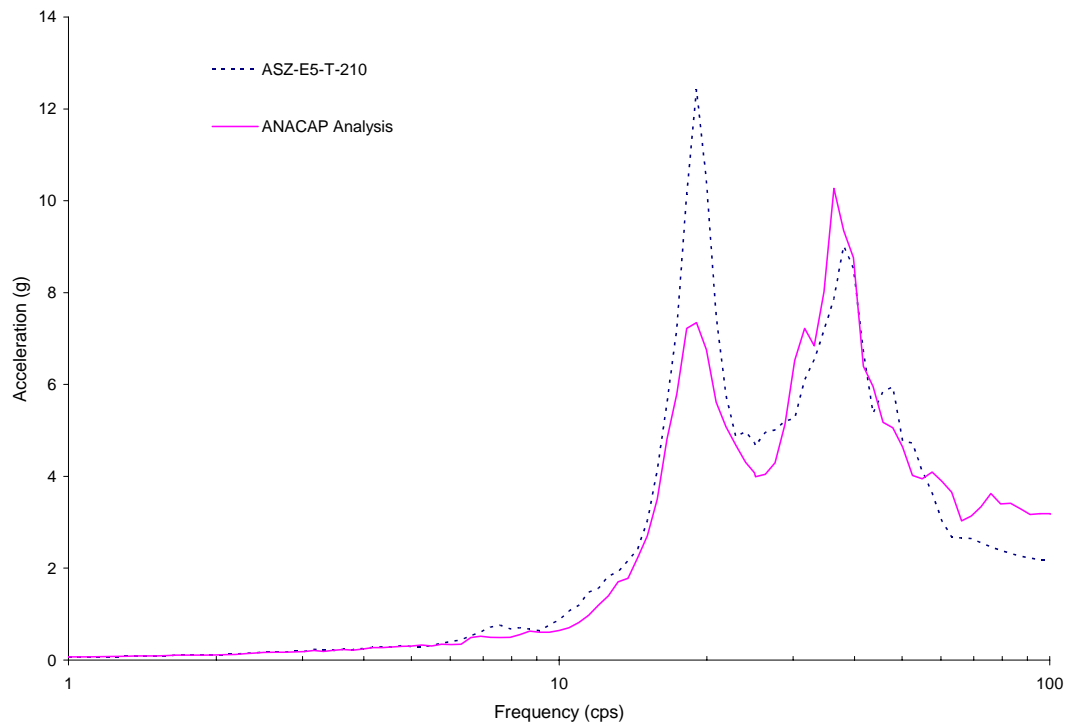


Figure 5-19 Comparison of Z-Direction Response between ANACAP Analysis at Upper Slab Corner No.3 and Measured Result for Run-2

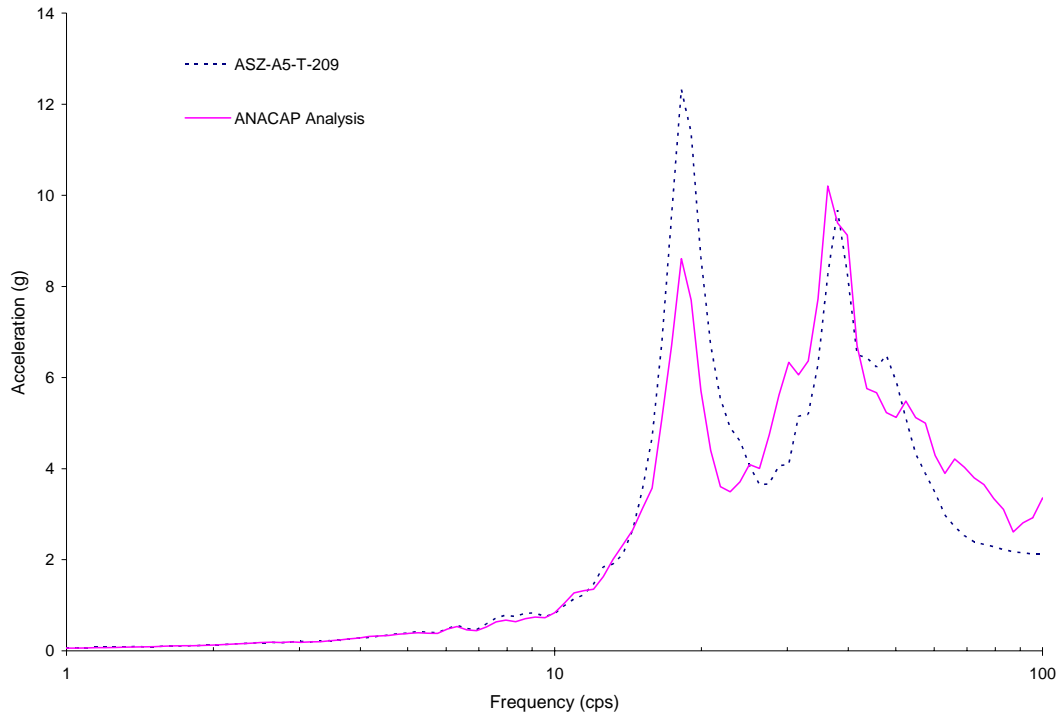


Figure 5-20 Comparison of Z-Direction Response between ANACAP Analysis at Upper Slab Corner No.4 and Measured Result for Run-2

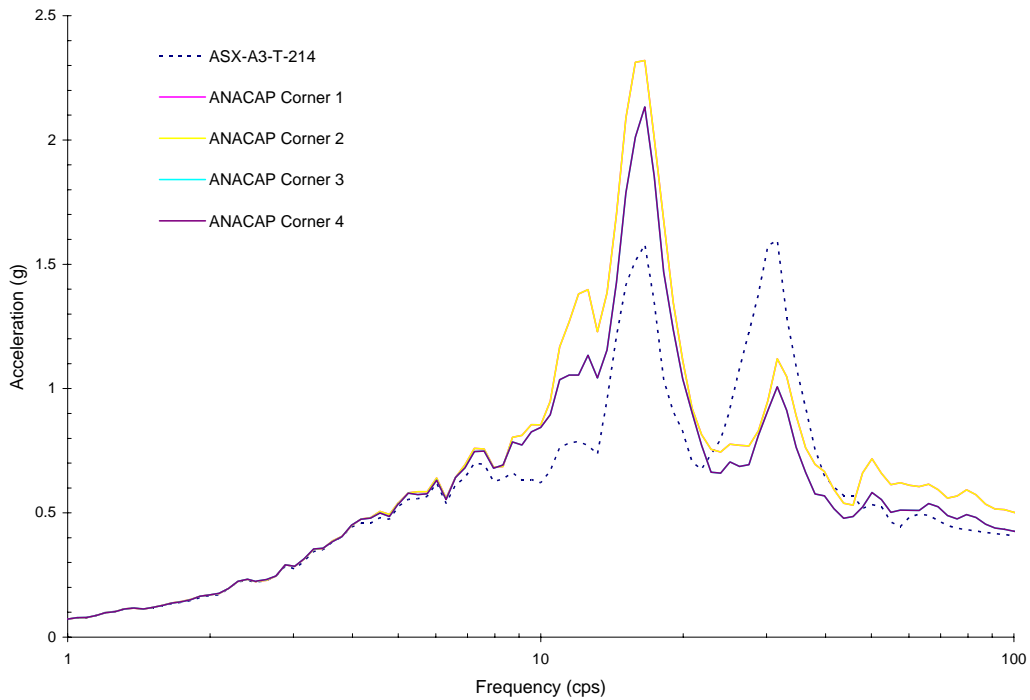


Figure 5-21 Comparison of X-Direction Response between ANACAP Analysis at Upper Corners of Shear Walls and Measured Data for Run-2'

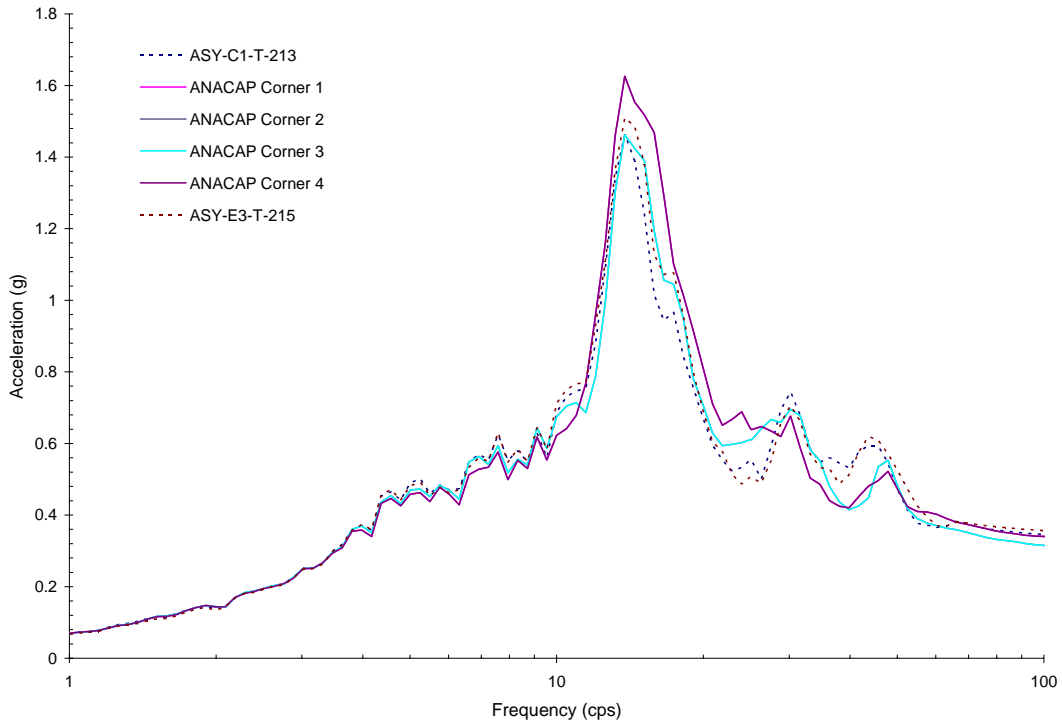


Figure 5-22 Comparison of Y-Direction Response between ANACAP Analysis at Upper Corners of Shear Walls and Measured Data for Run-2'

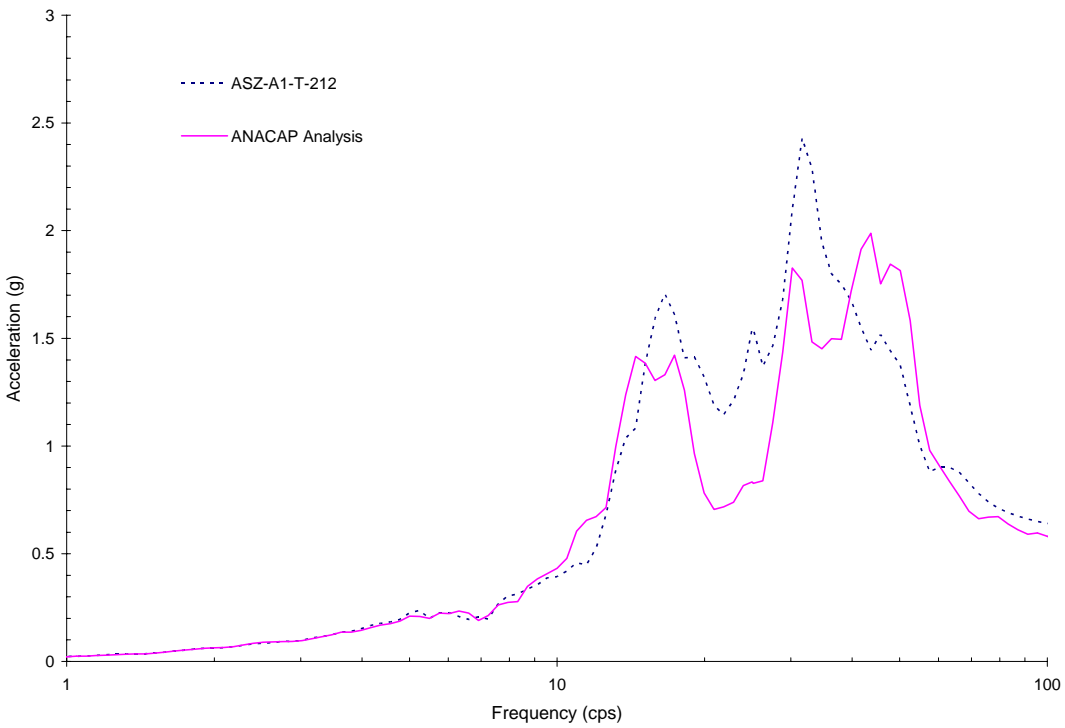


Figure 5-23 Comparison of Z-Direction Response between ANACAP Analysis at Upper Slab Corner No.1 and Measured Result for Run-2'

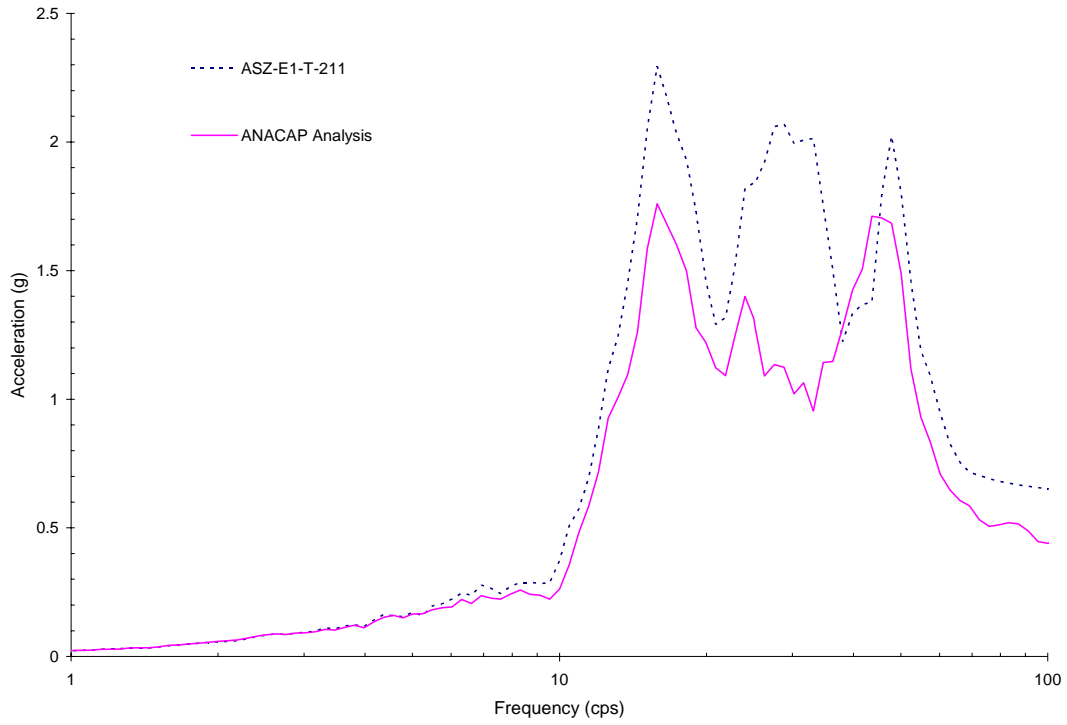


Figure 5-24 Comparison of Z-Direction Response between ANACAP Analysis at Upper Slab Corner No.2 and Measured Result for Run-2'

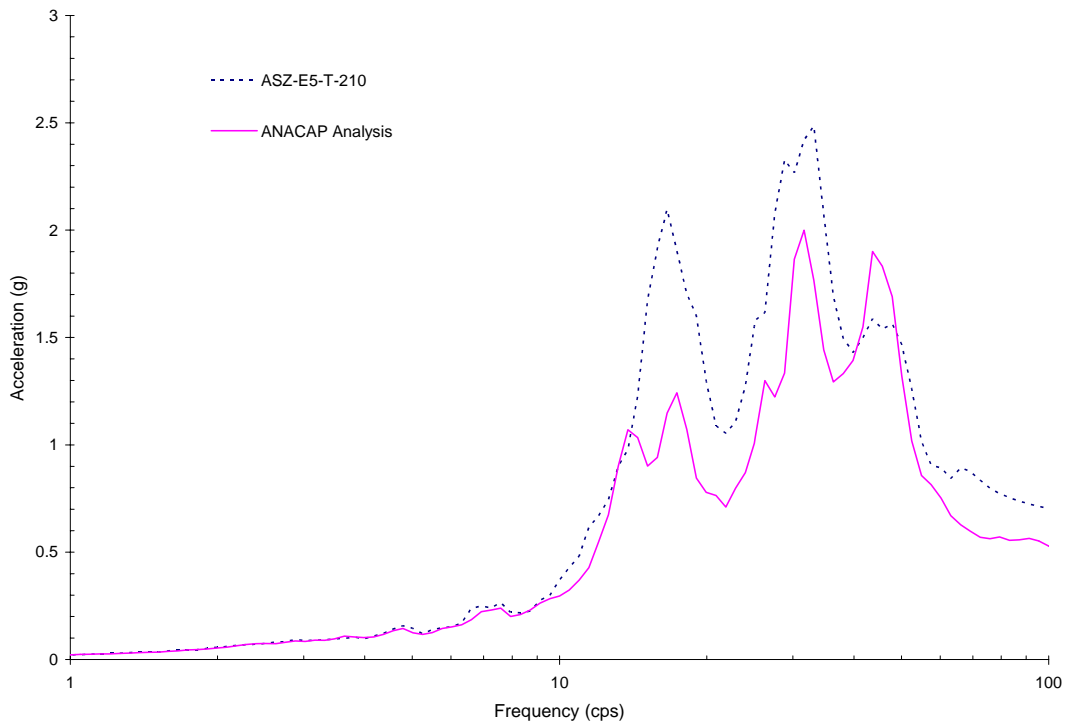


Figure 5-25 Comparison of Z-Direction Response between ANACAP Analysis at Upper Slab Corner No.3 and Measured Result for Run-2'

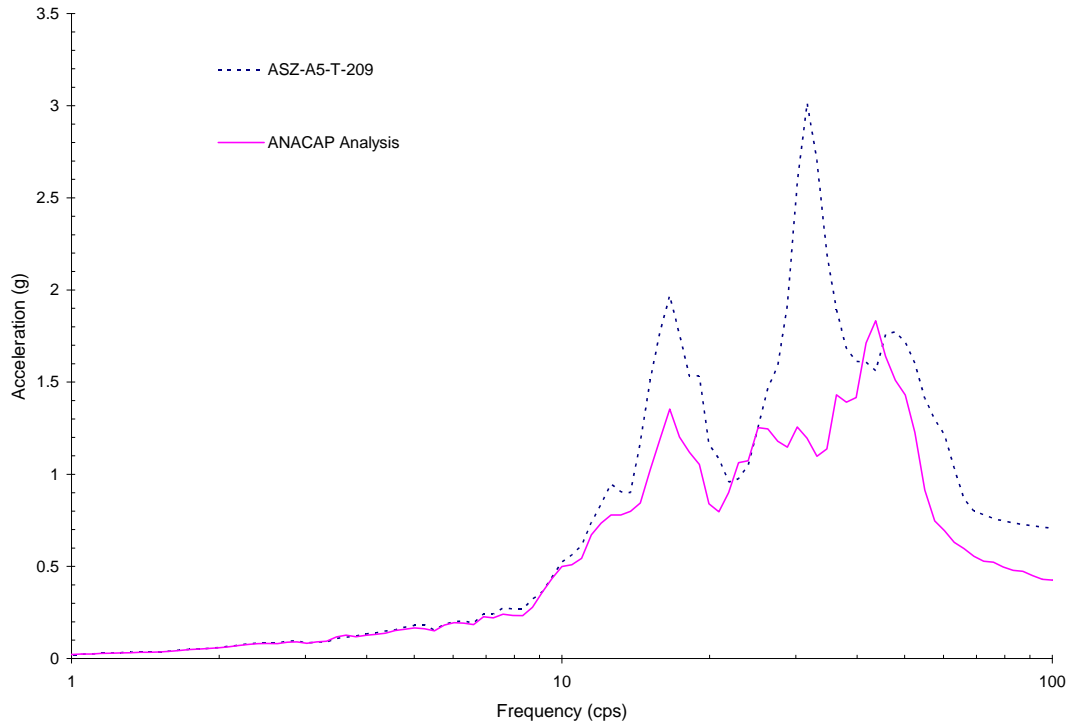


Figure 5-26 Comparison of Z-Direction Response between ANACAP Analysis at Upper Slab Corner No.4 and Measured Result for Run-2'

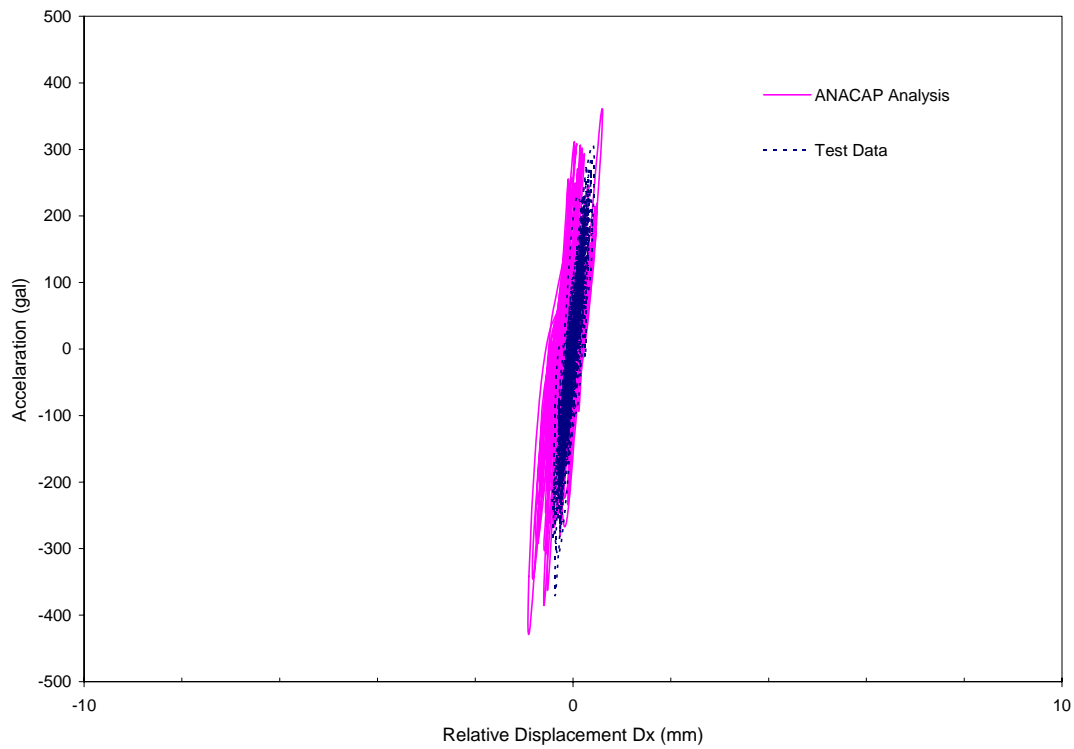


Figure 5-27 Comparison of Hysteresis Loops in X-Direction for Run-2'

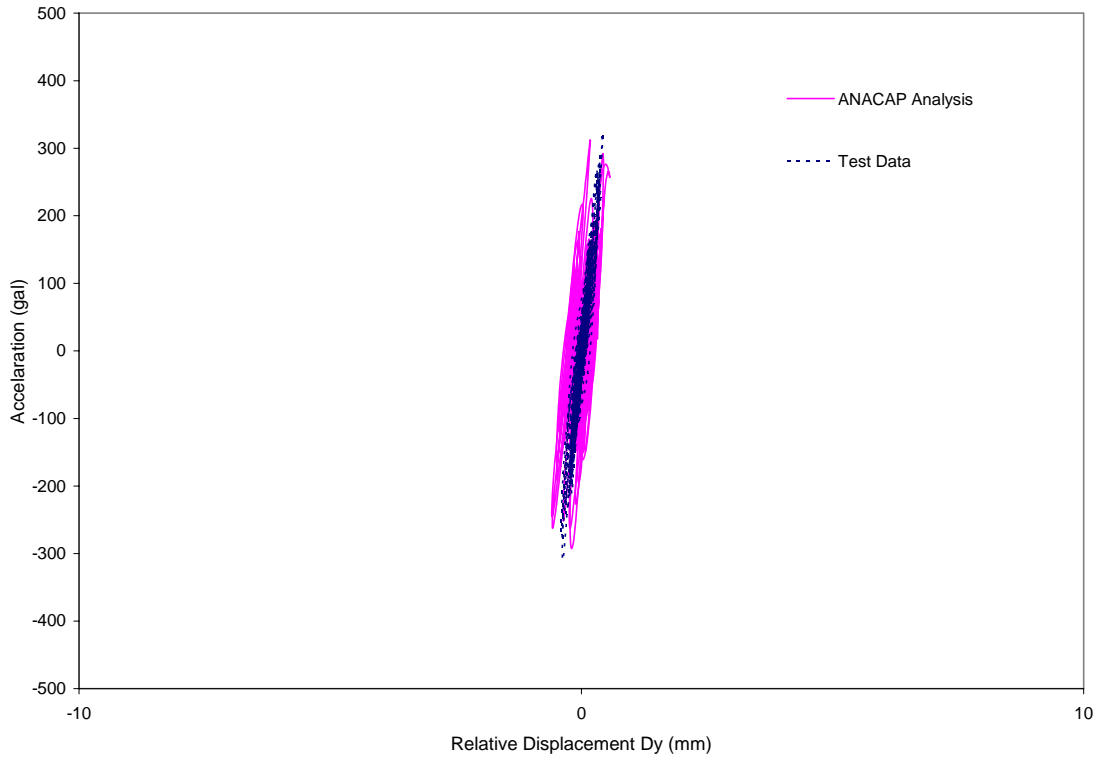


Figure 5-28 Comparison of Hysteresis Loops in Y-Direction for Run-2'

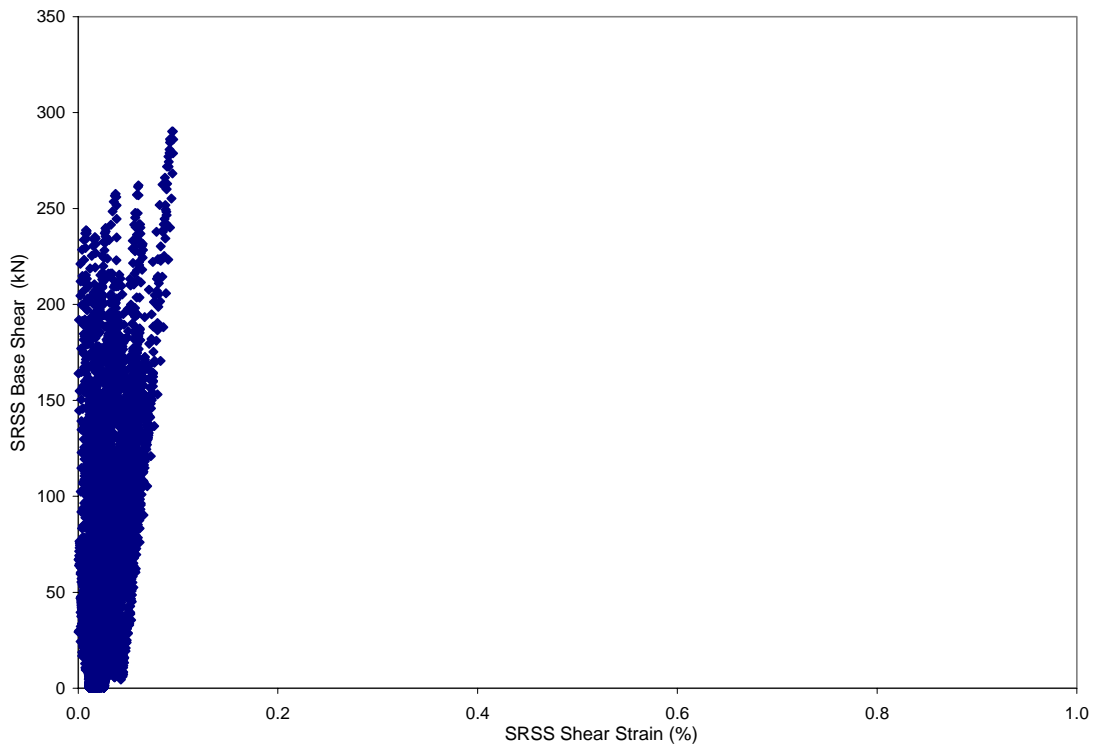


Figure 5-29 ANACAP Calculated SRSS Base Shear vs. SRSS Shear Strain for Run-2'

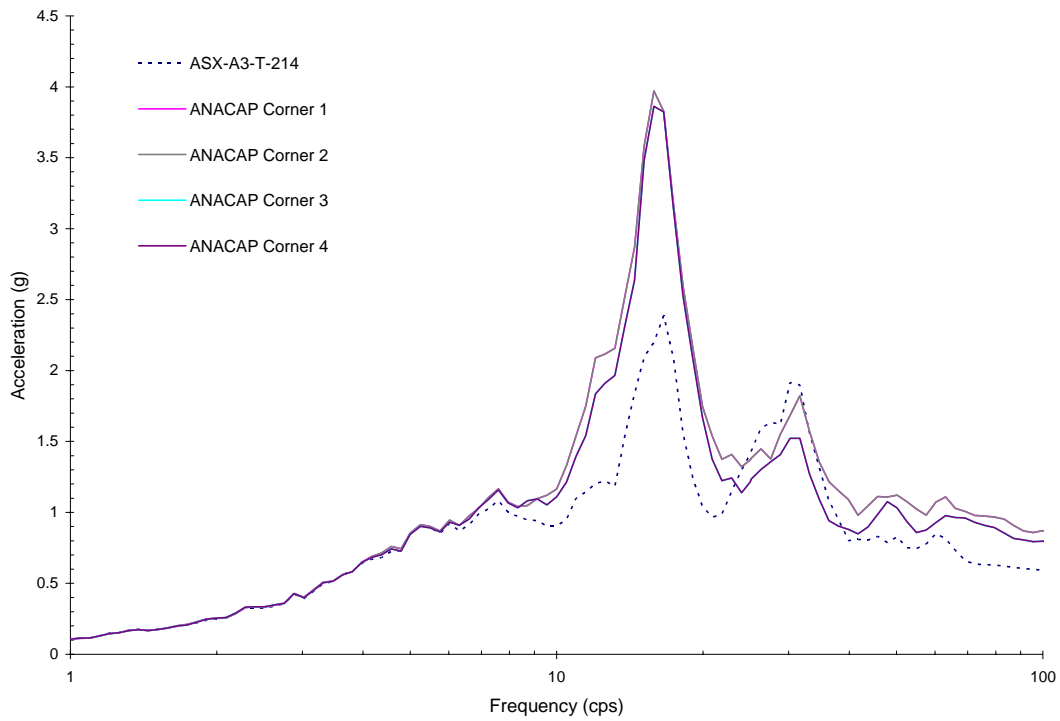


Figure 5-30 Comparison of X-Direction Response between ANACAP Analysis at Upper Corners of Shear Walls and Measured Data for Run-3

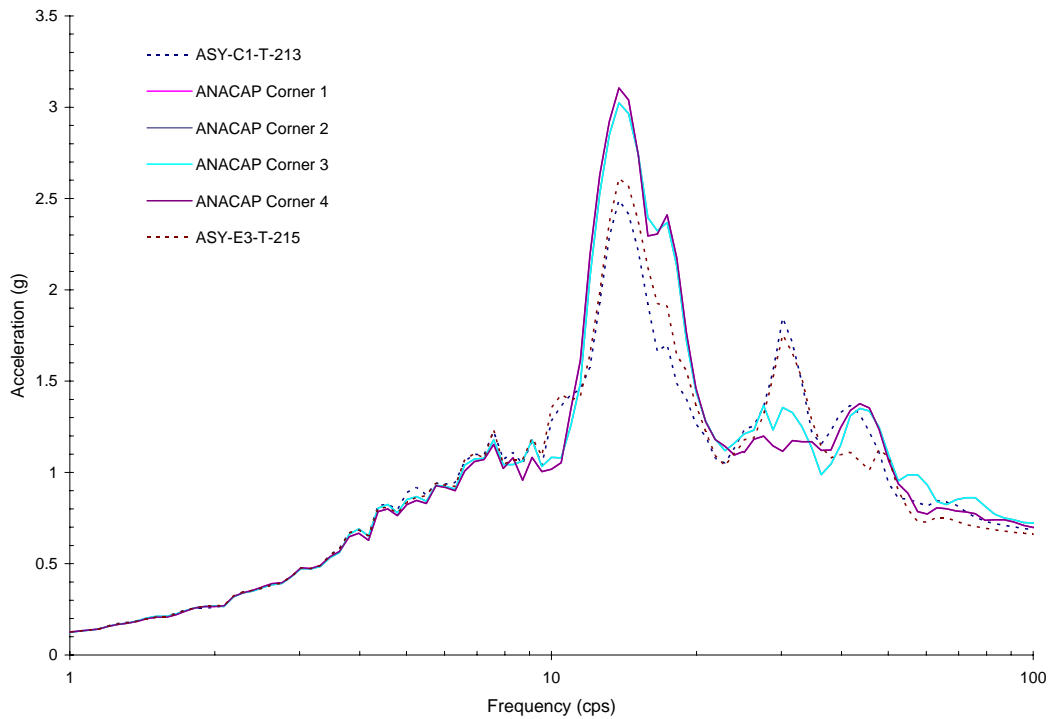


Figure 5-31 Comparison of Y-Direction Response between ANACAP Analysis at Upper Corners of Shear Walls and Measured Data for Run-3

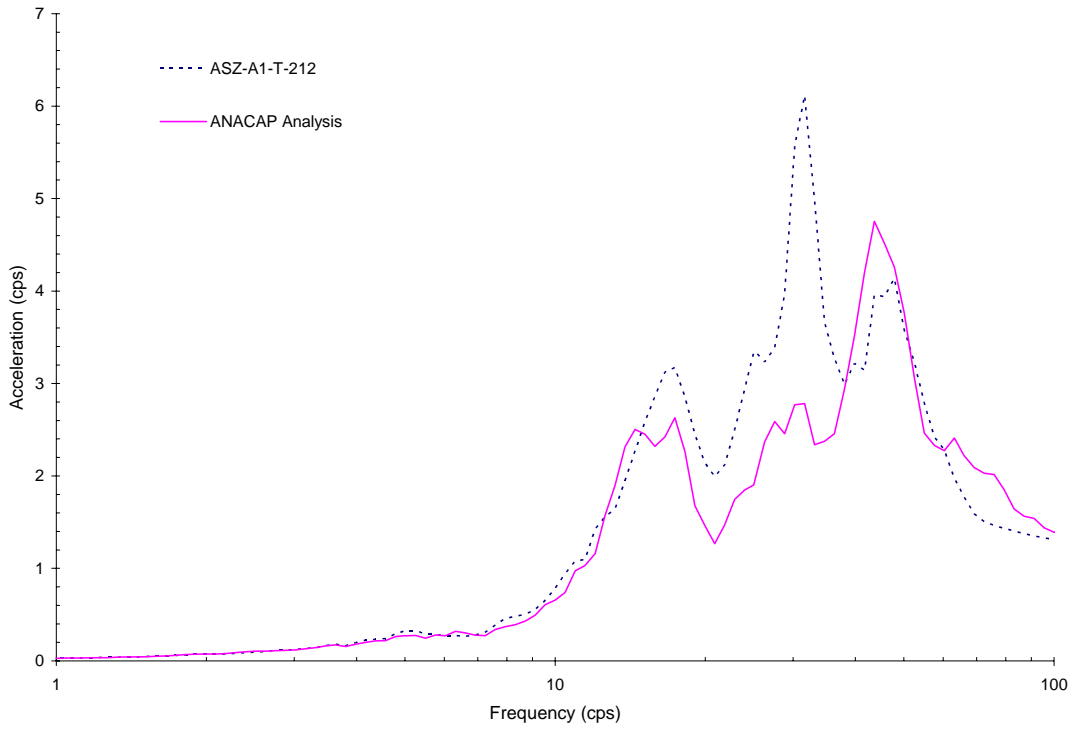


Figure 5-32 Comparison of Z-Direction Response between ANACAP Analysis at Upper Slab Corner No.1 and Measured Result for Run-3

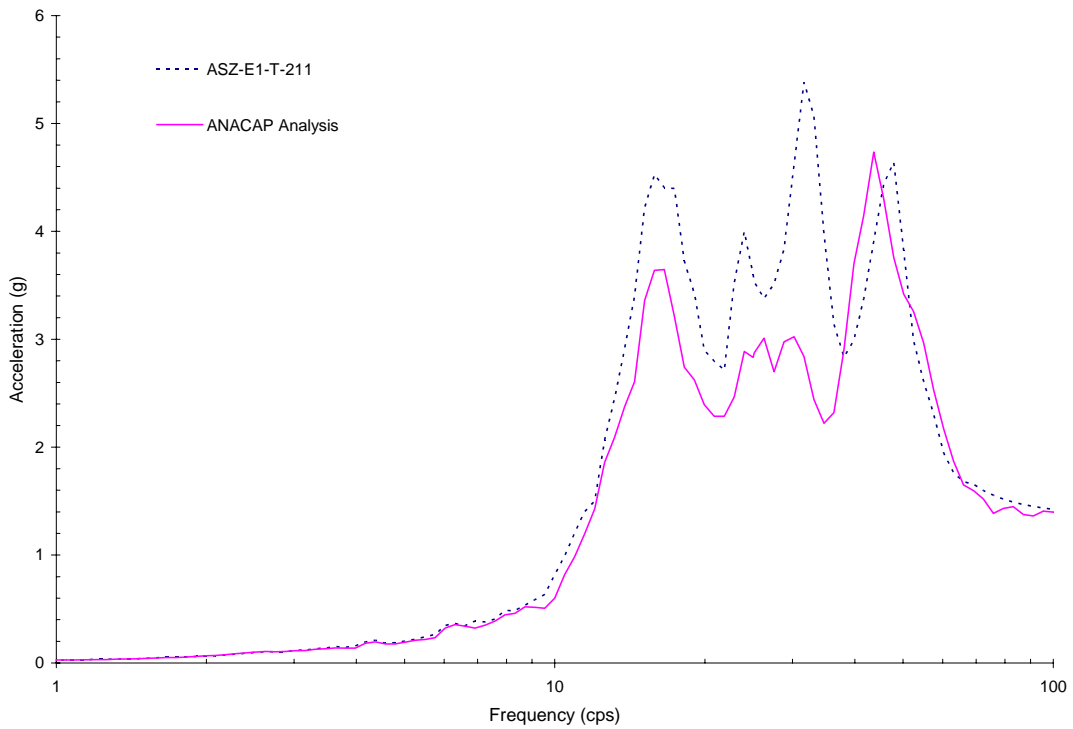


Figure 5-33 Comparison of Z-Direction Response between ANACAP Analysis at Upper Slab Corner No.2 and Measured Result for Run-3

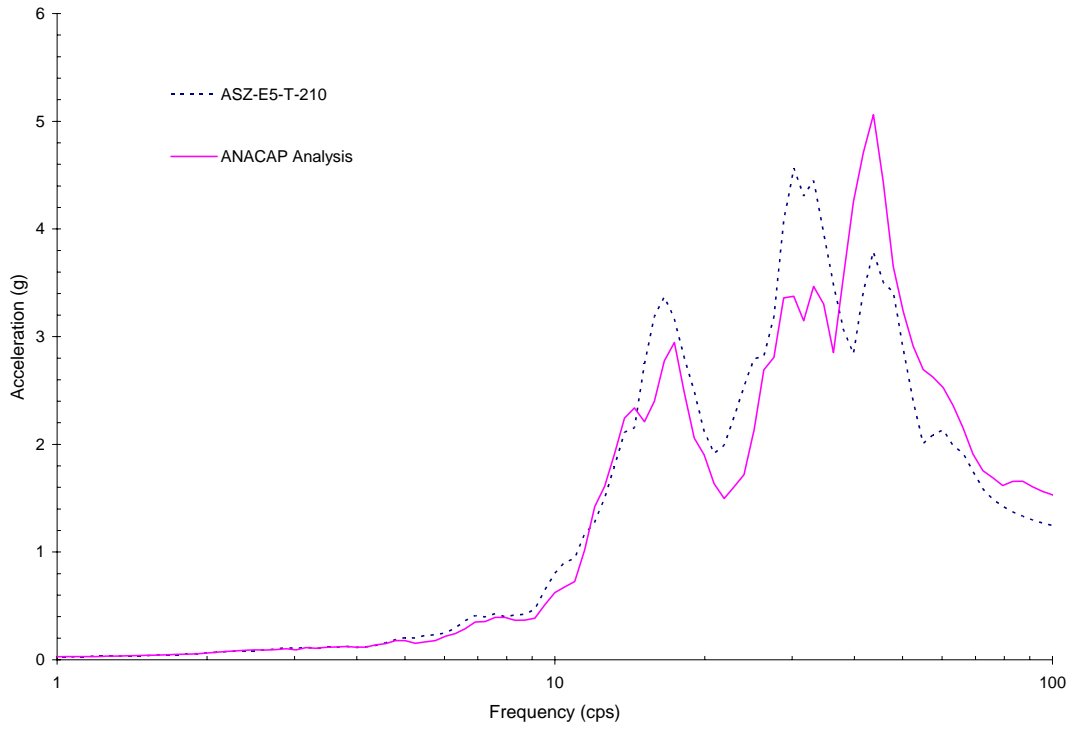


Figure 5-34 Comparison of Z-Direction Response between ANACAP Analysis at Upper Slab Corner No.3 and Measured Result for Run-3

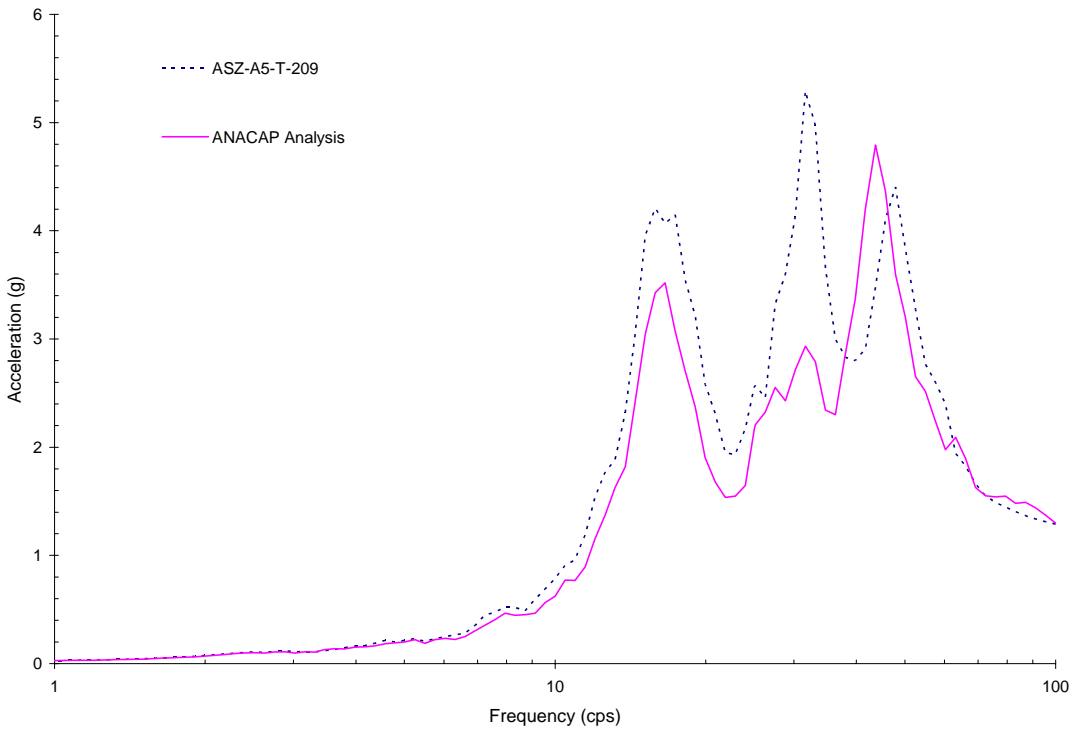


Figure 5-35 Comparison of Z-Direction Response between ANACAP Analysis at Upper Slab Corner No.4 and Measured Result for Run-3

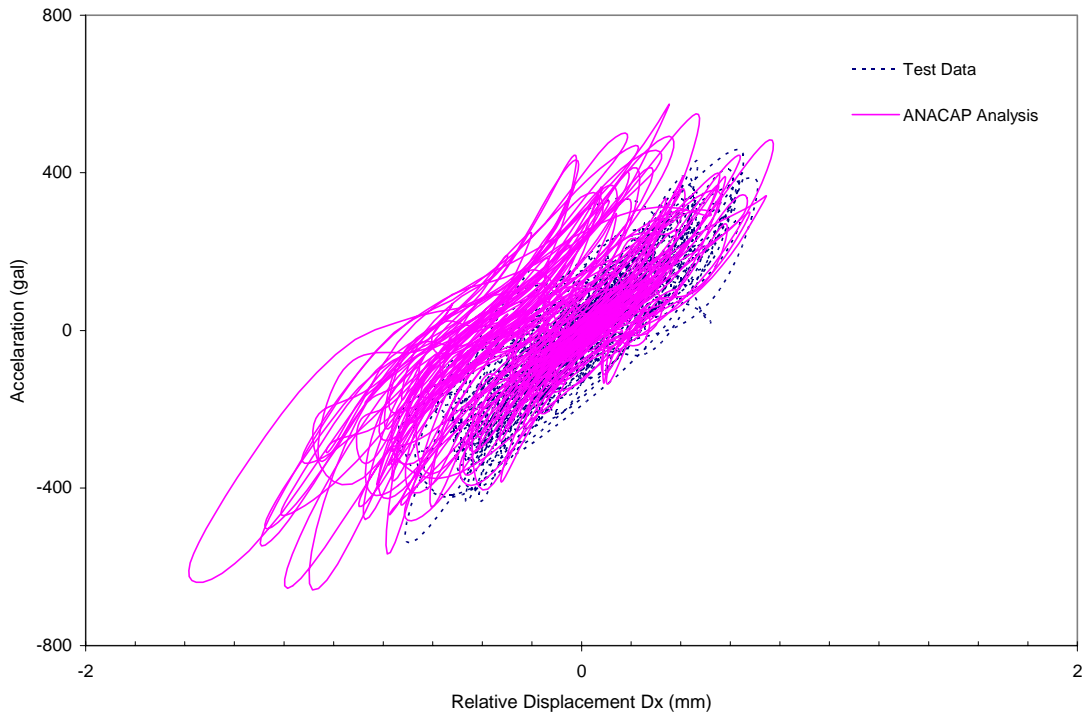


Figure 5-36 Comparison of Hysteresis Loops in X-Direction for Run-3

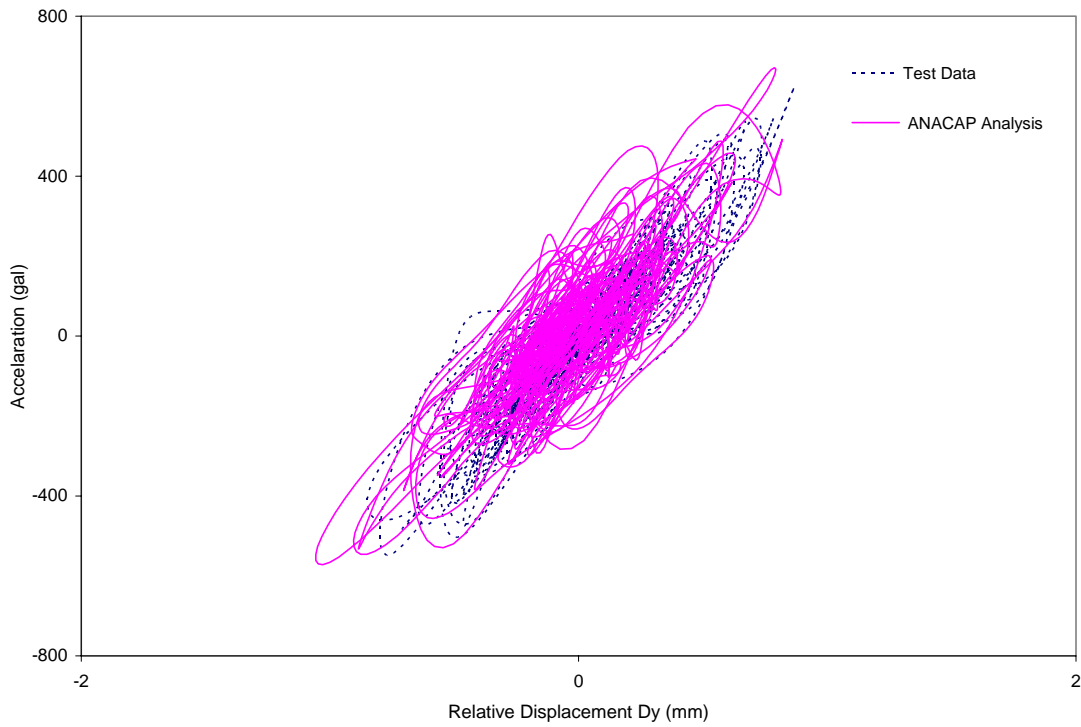


Figure 5-37 Comparison of Hysteresis Loops in Y-Direction for Run-3

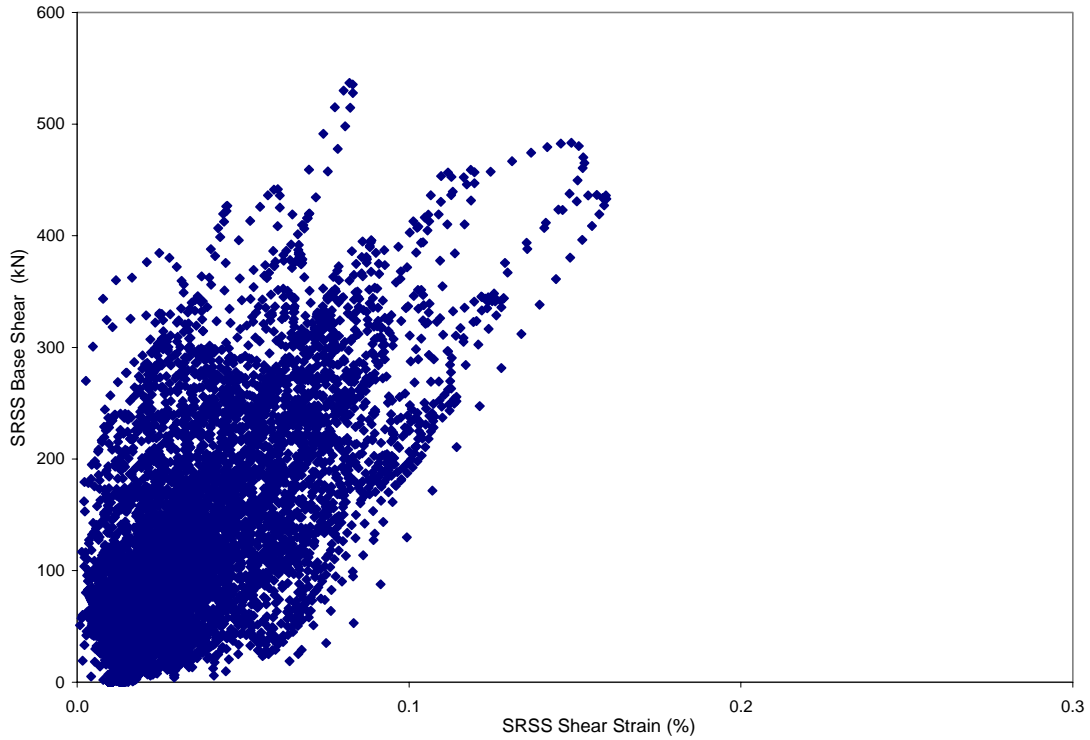


Figure 5-38 ANACAP Calculated SRSS Base Shear vs. SRSS Shear Strain for Run-3

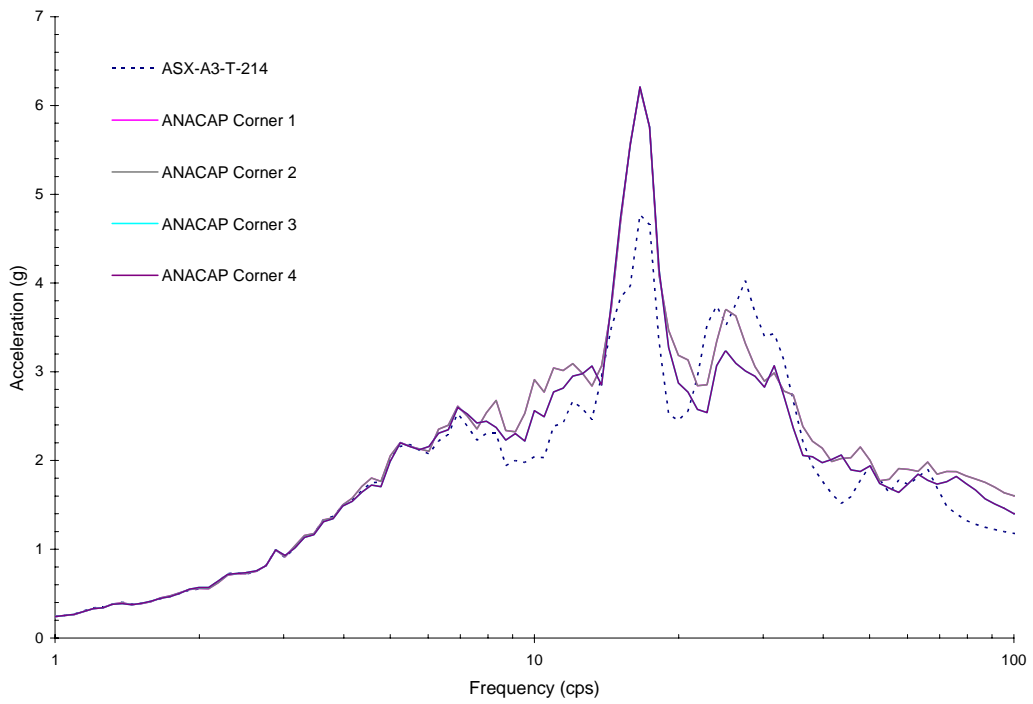


Figure 5-39 Comparison of X-Direction Response between ANACAP Analysis at Upper Corners of Shear Walls and Measured Data for Run-3'

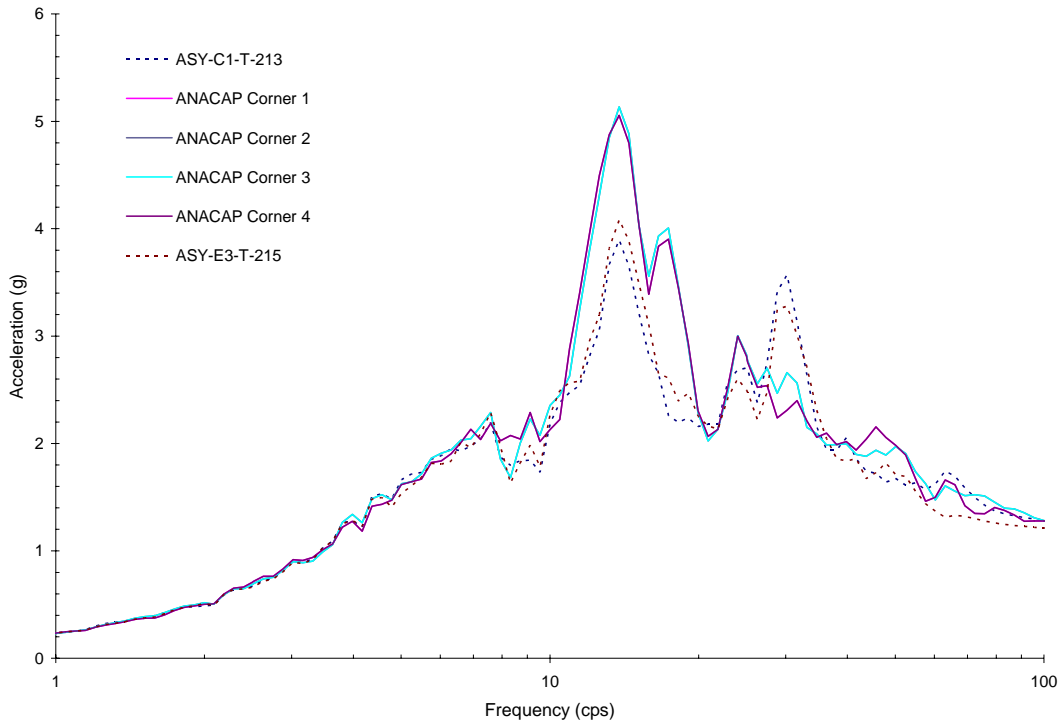


Figure 5-40 Comparison of Y-Direction Response between ANACAP Analysis at Upper Corners of Shear Walls and Measured Data for Run-3'

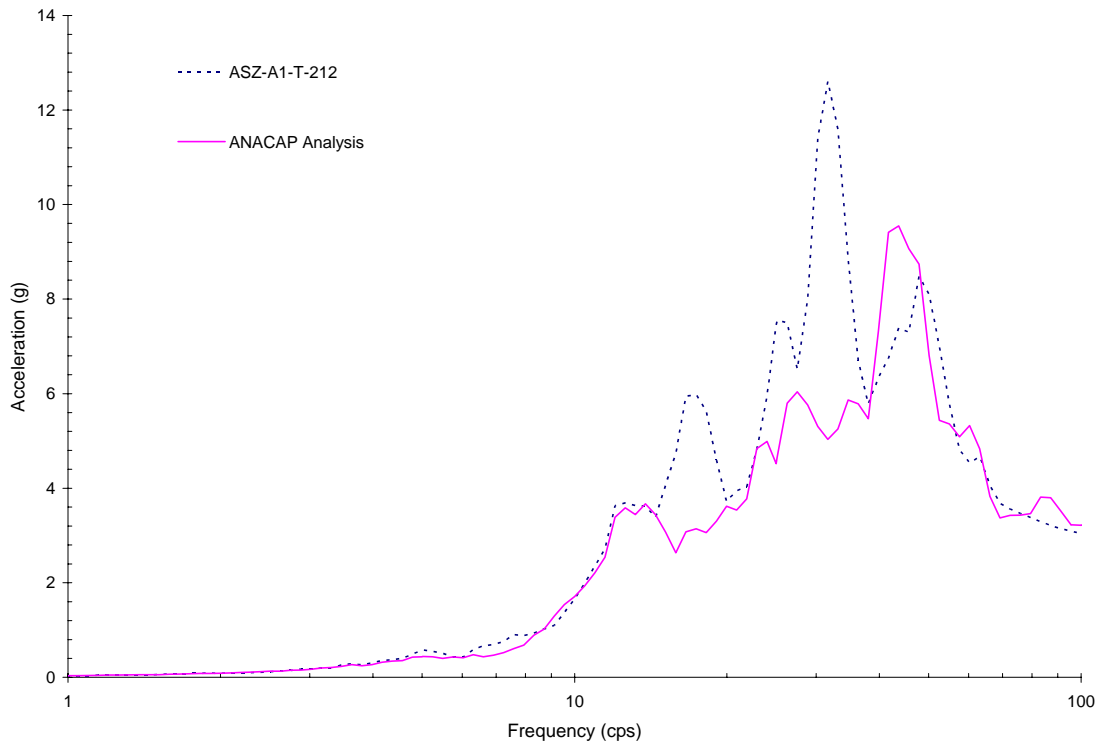


Figure 5-41 Comparison of Z-Direction Response between ANACAP Analysis at Upper Slab Corner No.1 and Measured Result for Run-3'

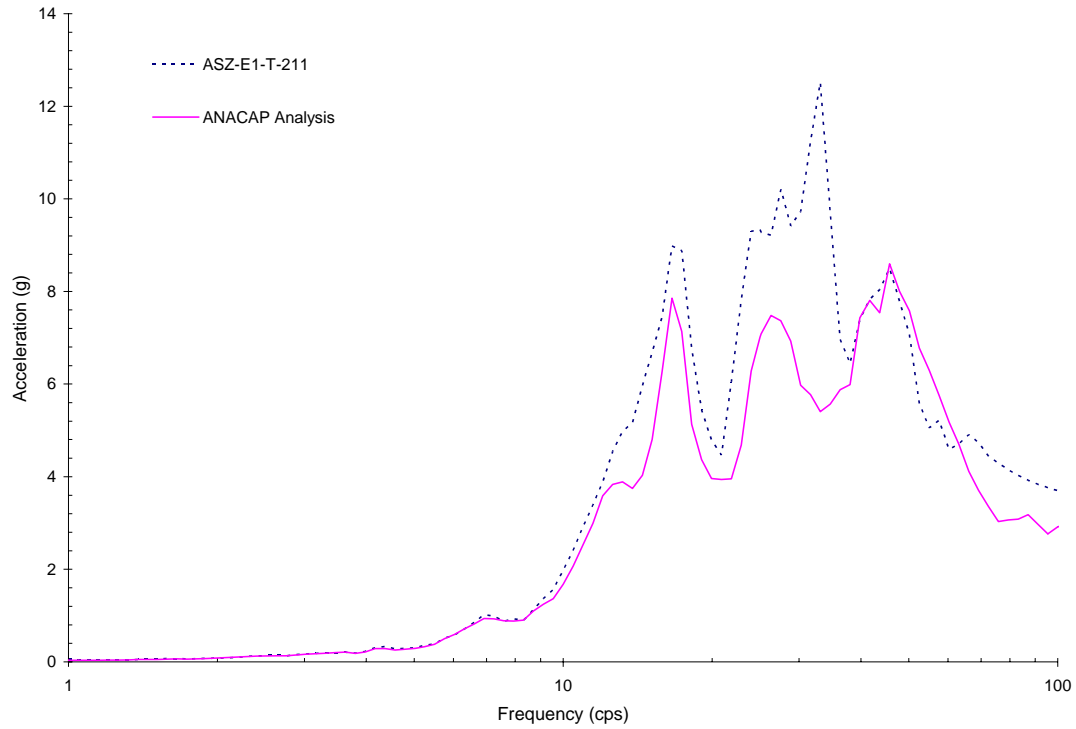


Figure 5-42 Comparison of Z-Direction Response between ANACAP Analysis at Upper Slab Corner No.2 and Measured Result for Run-3'

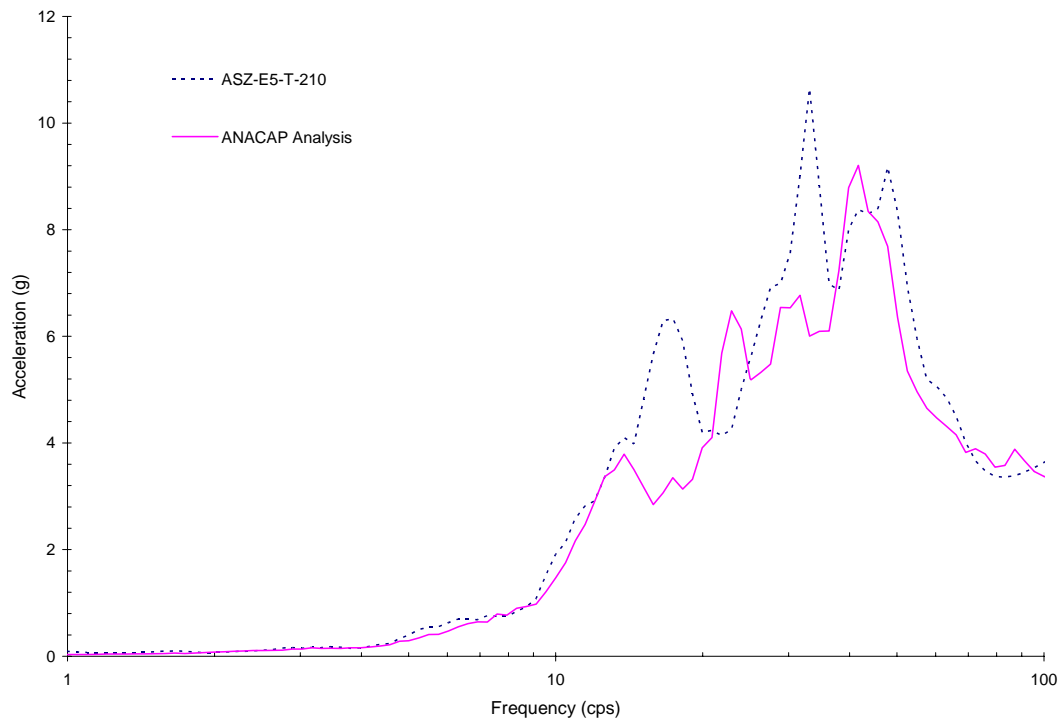


Figure 5-43 Comparison of Z-Direction Response between ANACAP Analysis at Upper Slab Corner No.3 and Measured Result for Run-3'

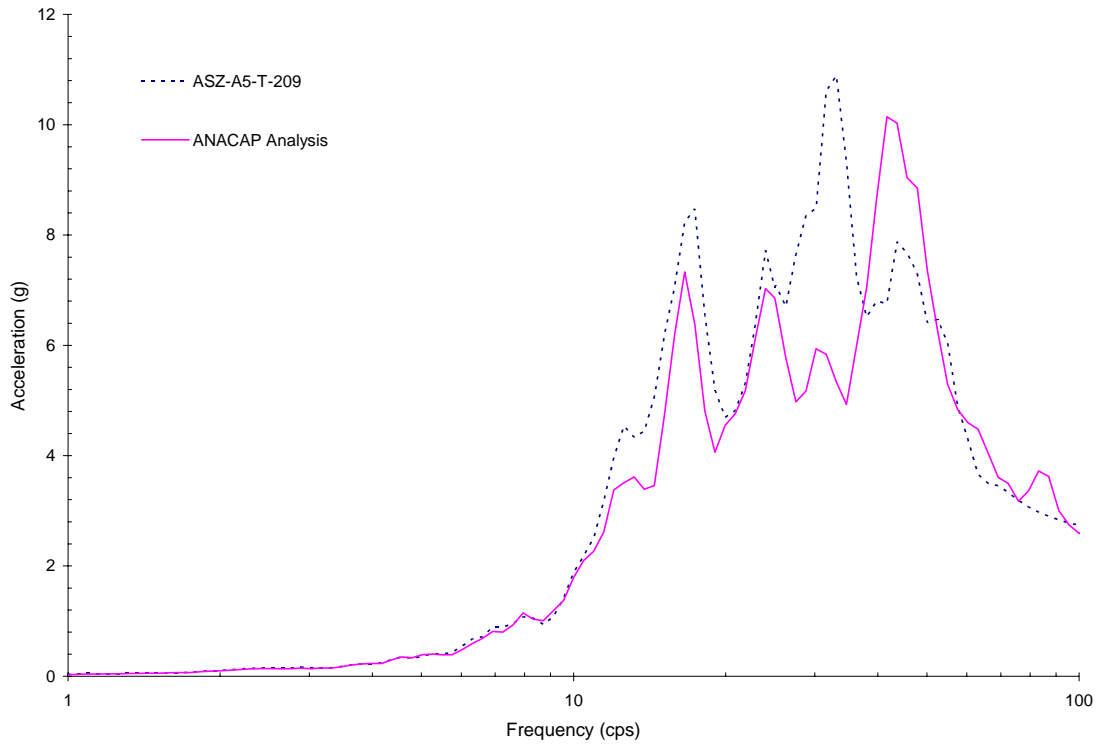


Figure 5-44 Comparison of Z-Direction Response between ANACAP Analysis at Upper Slab Corner No.4 and Measured Result for Run-3'

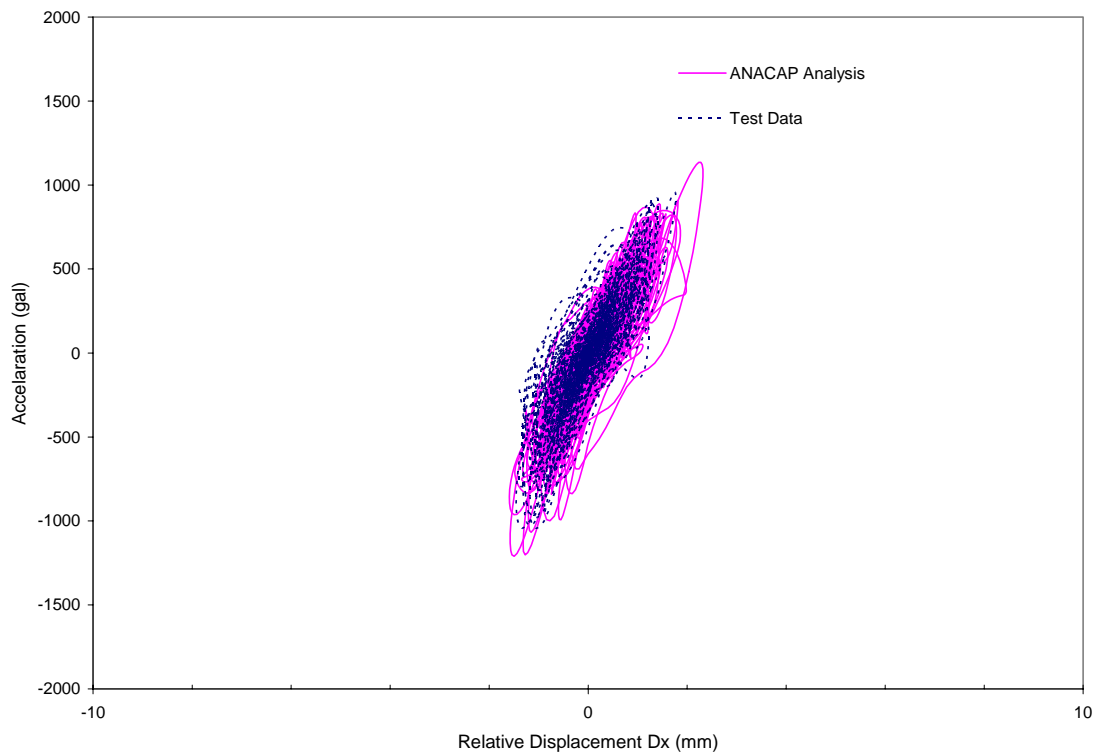


Figure 5-45 Comparison of Hysteresis Loops in X-Direction for Run-3'

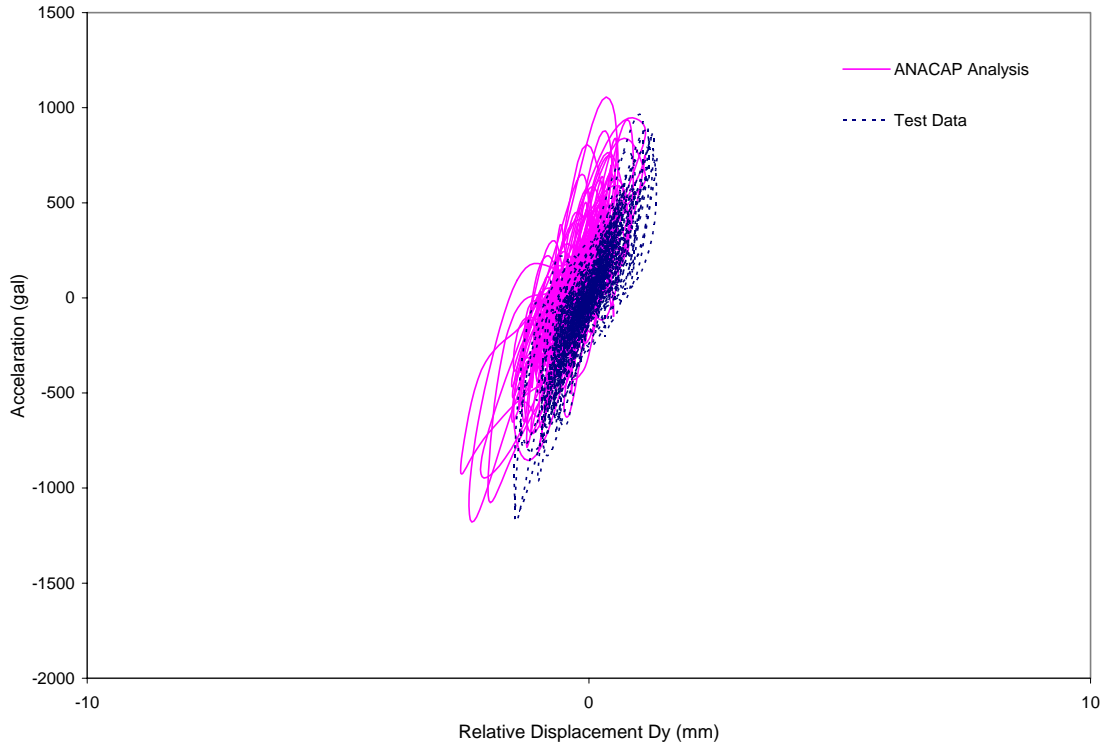


Figure 5-46 Comparison of Hysteresis Loops in Y-Direction for Run-3'

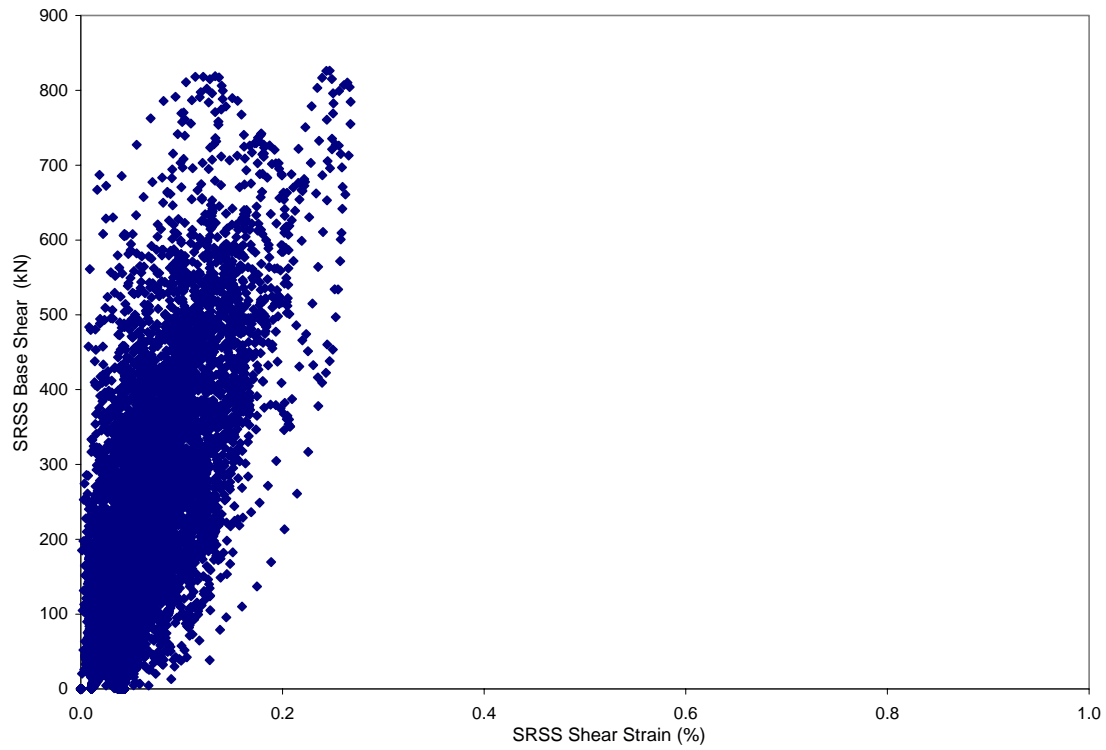


Figure 5-47 ANACAP Calculated SRSS Base Shear vs. SRSS Shear Strain for Run-3'

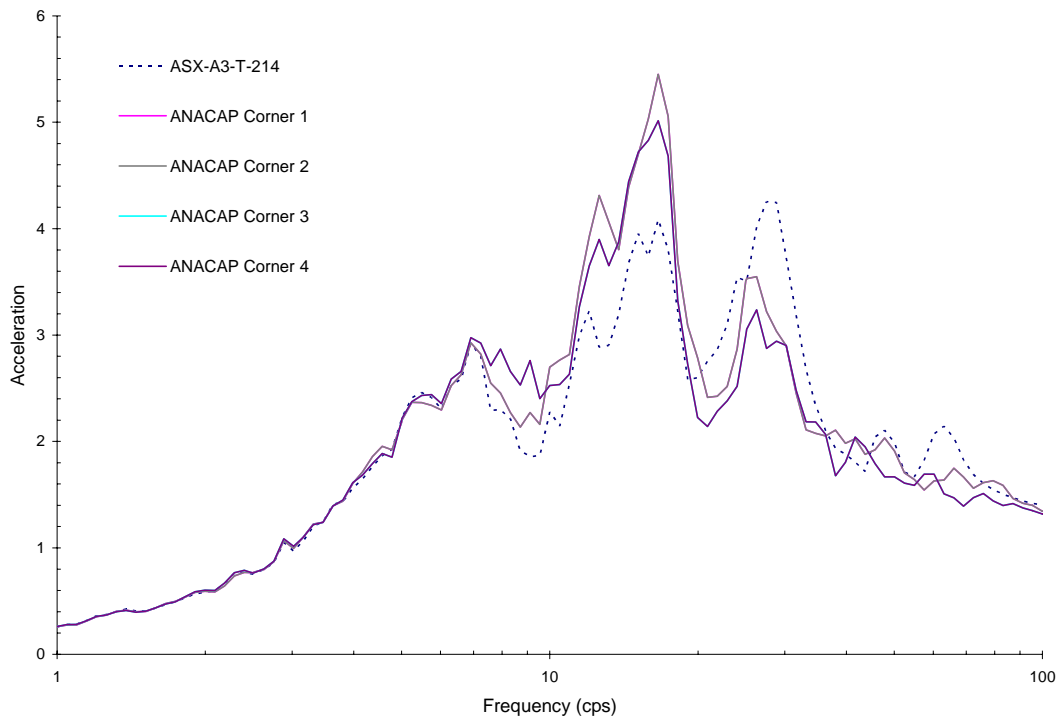


Figure 5-48 Comparison of X-Direction Response between ANACAP Analysis at Upper Corners of Shear Walls and Measured Data for Run-4

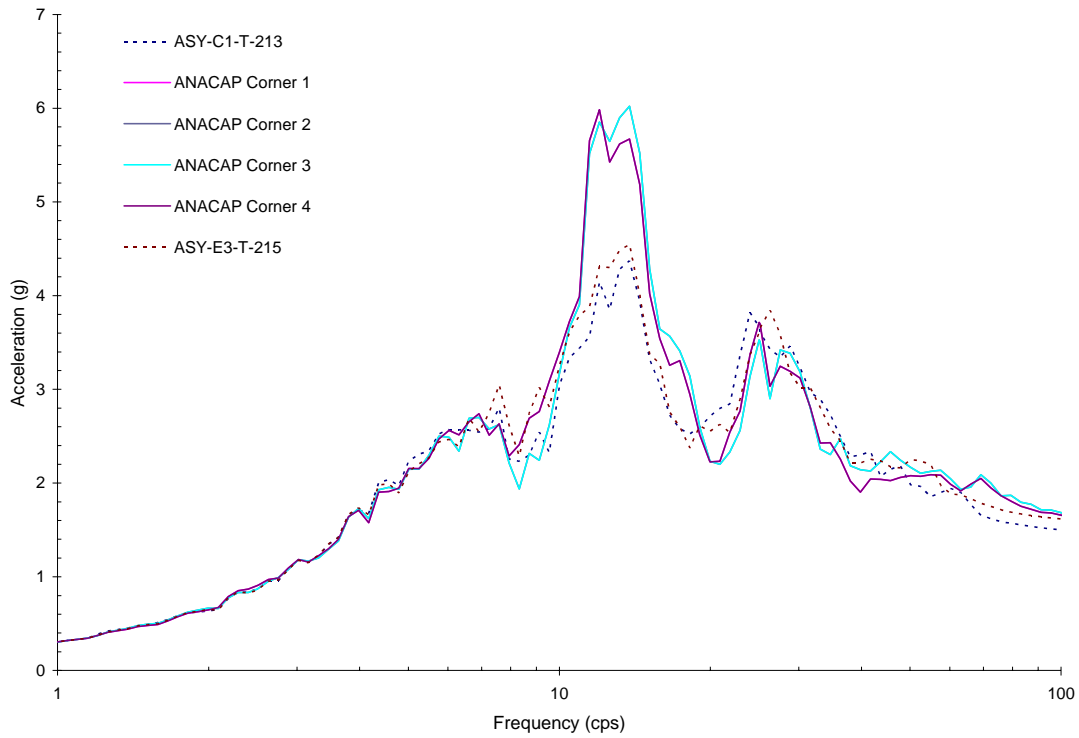


Figure 5-49 Comparison of Y-Direction Response between ANACAP Analysis at Upper Corners of Shear Walls and Measured Data for Run-4

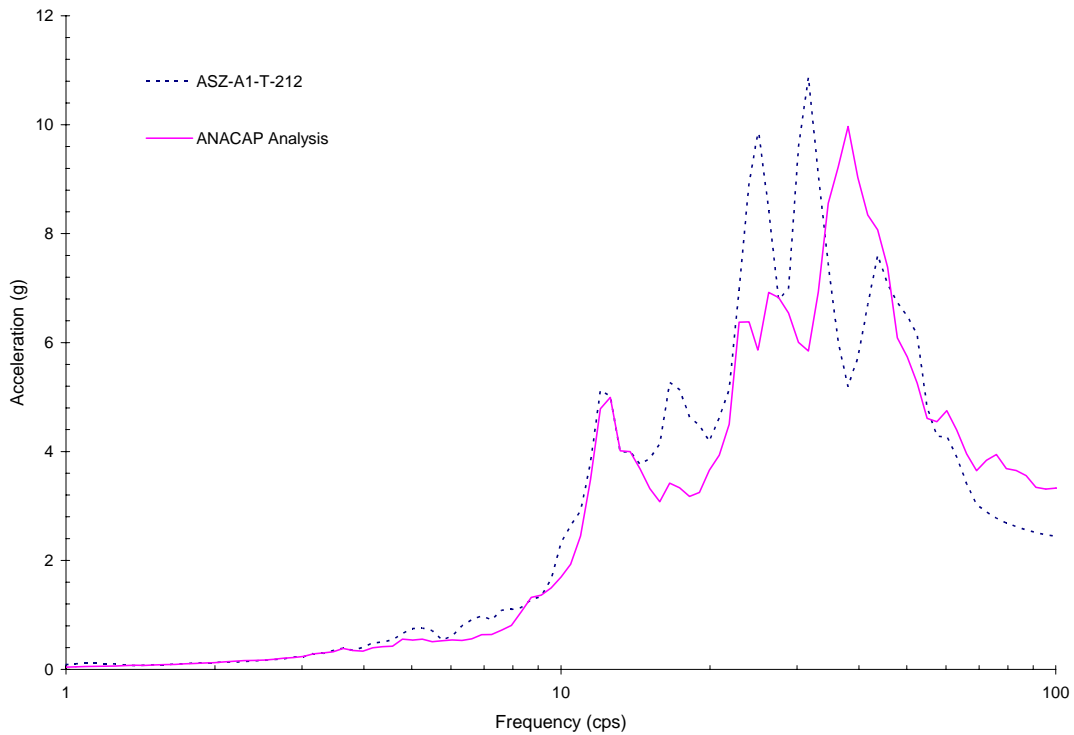


Figure 5-50 Comparison of Z-Direction Response between ANACAP Analysis at Upper Slab Corner No.1 and Measured Result for Run-4

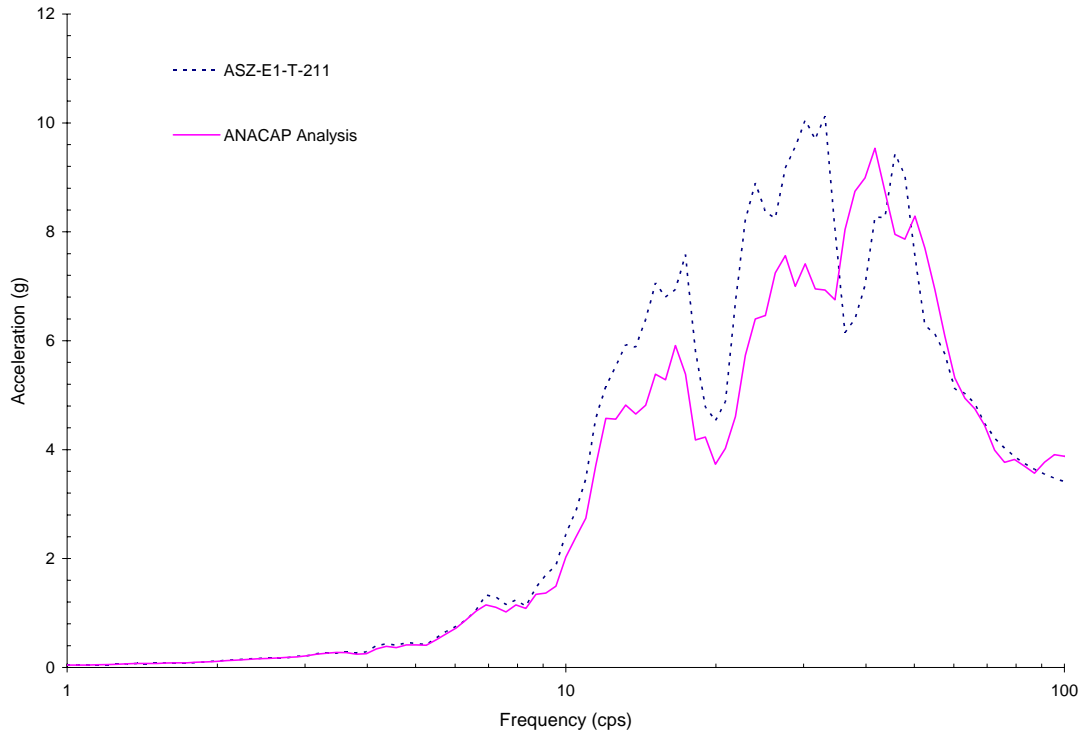


Figure 5-51 Comparison of Z-Direction Response between ANACAP Analysis at Upper Slab Corner No.2 and Measured Result for Run-4

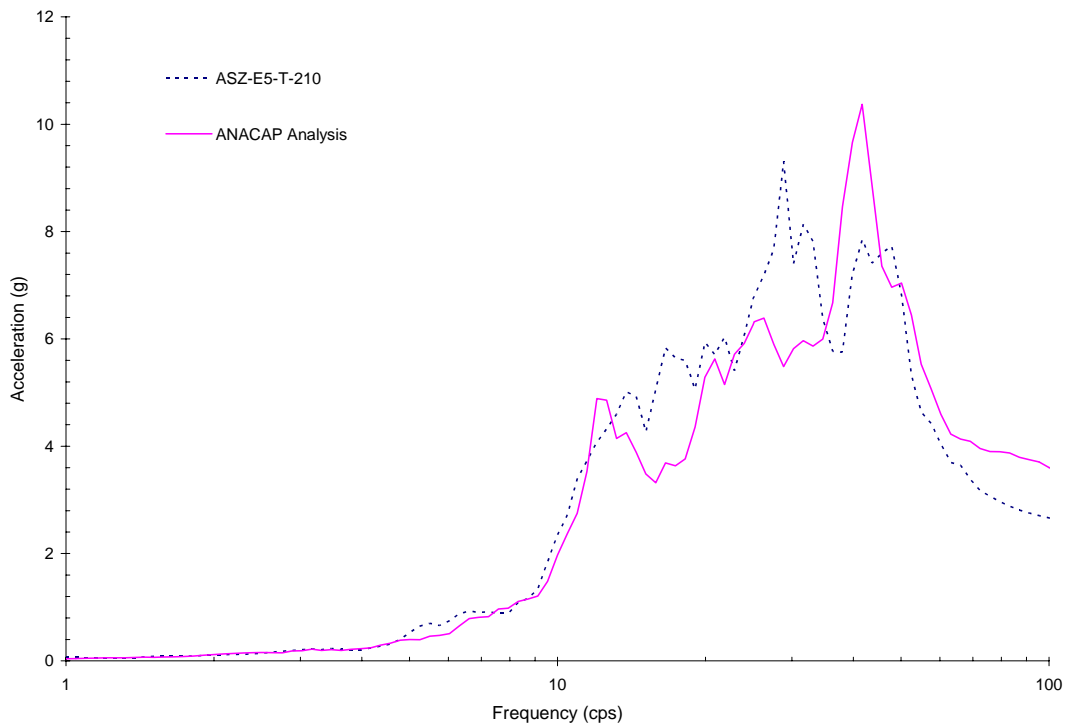


Figure 5-52 Comparison of Z-Direction Response between ANACAP Analysis at Upper Slab Corner No.3 and Measured Result for Run-4

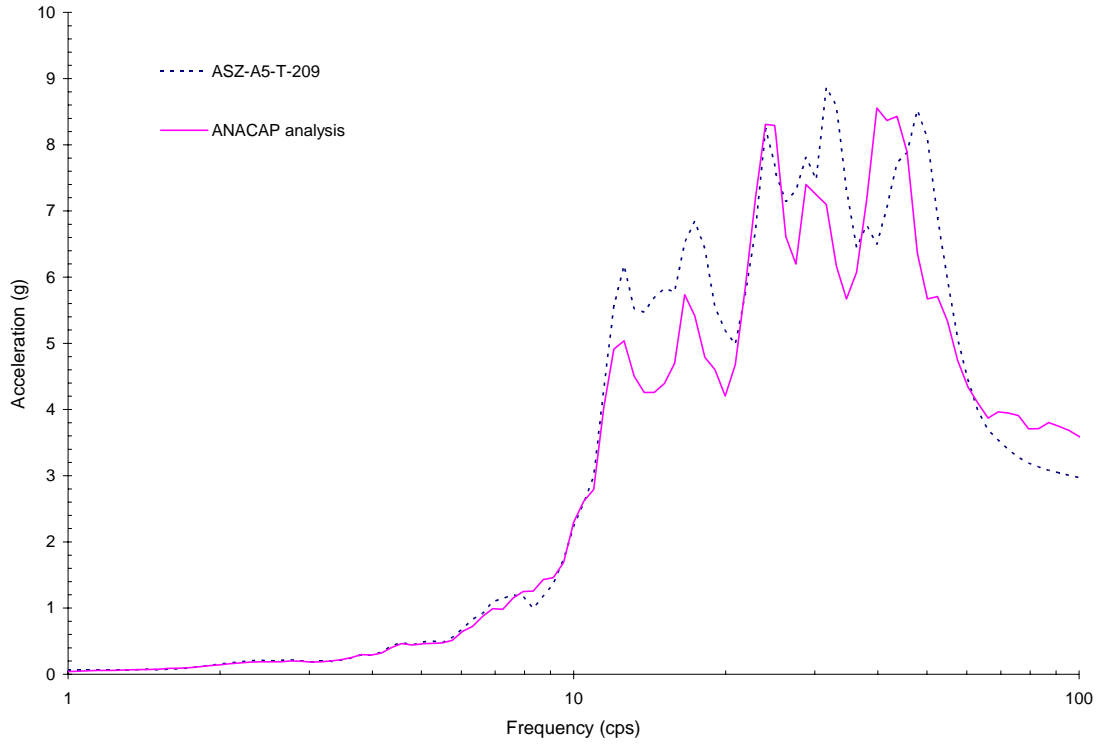


Figure 5-53 Comparison of Z-Direction Response between ANACAP Analysis at Upper Slab Corner No.4 and Measured Result for Run-4

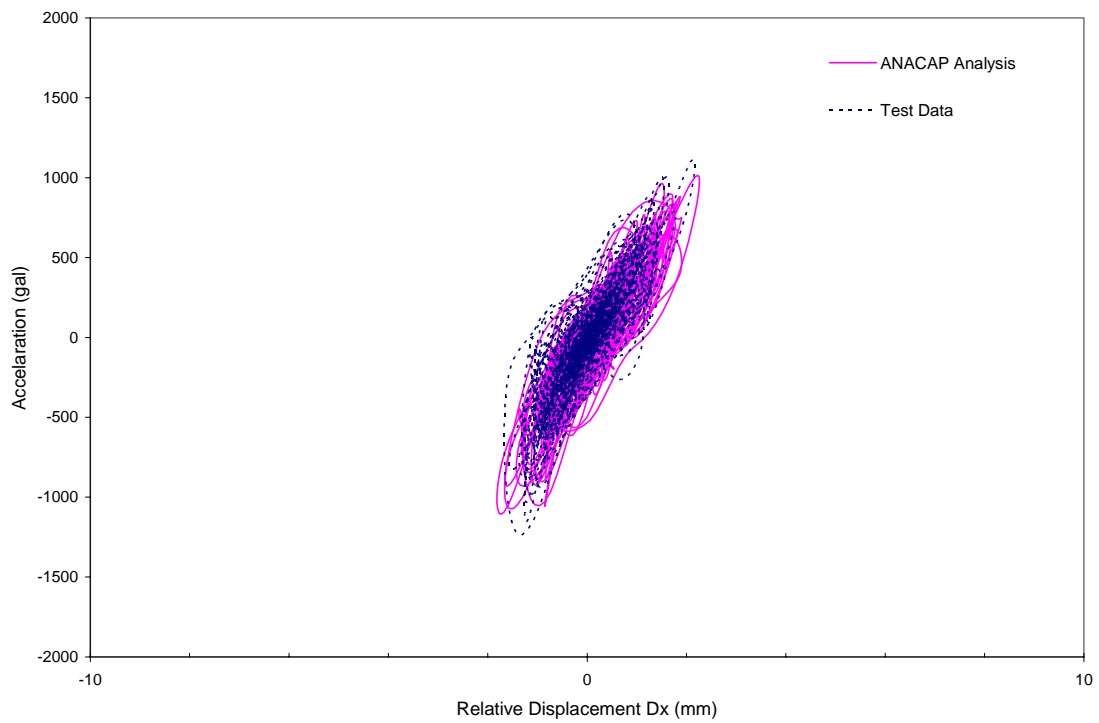


Figure 5-54 Comparison of Hysteresis Loops in X-Direction for Run-4

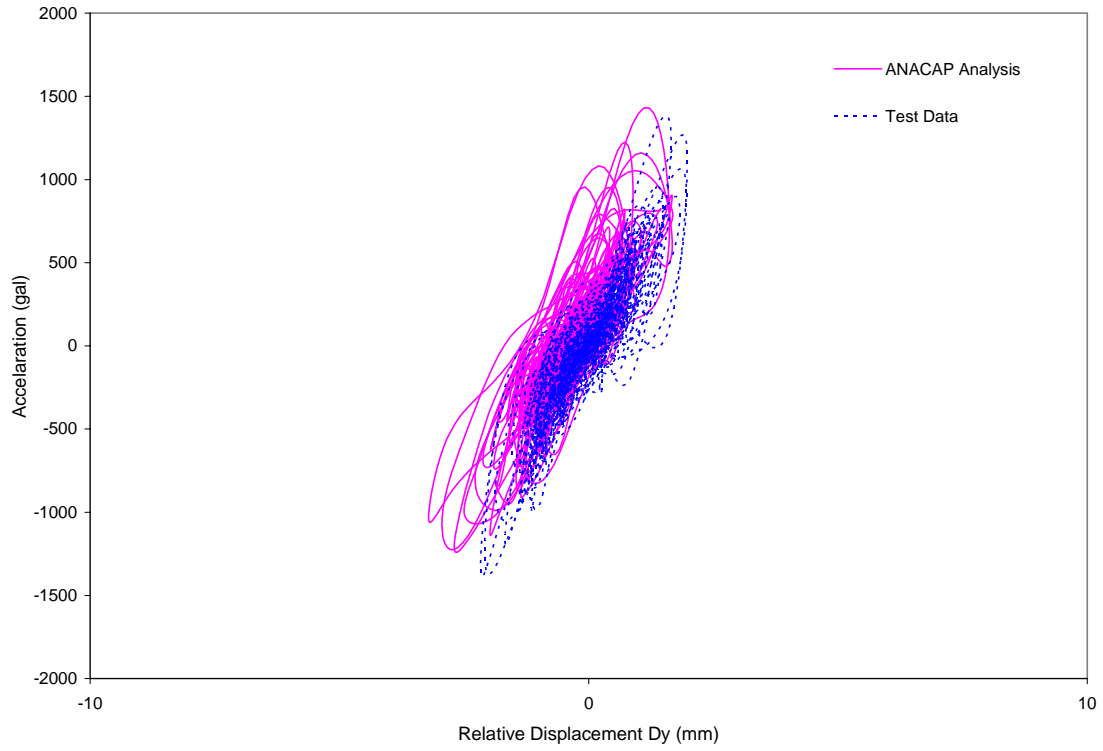


Figure 5-55 Comparison of Hysteresis Loops in Y-Direction for Run-4

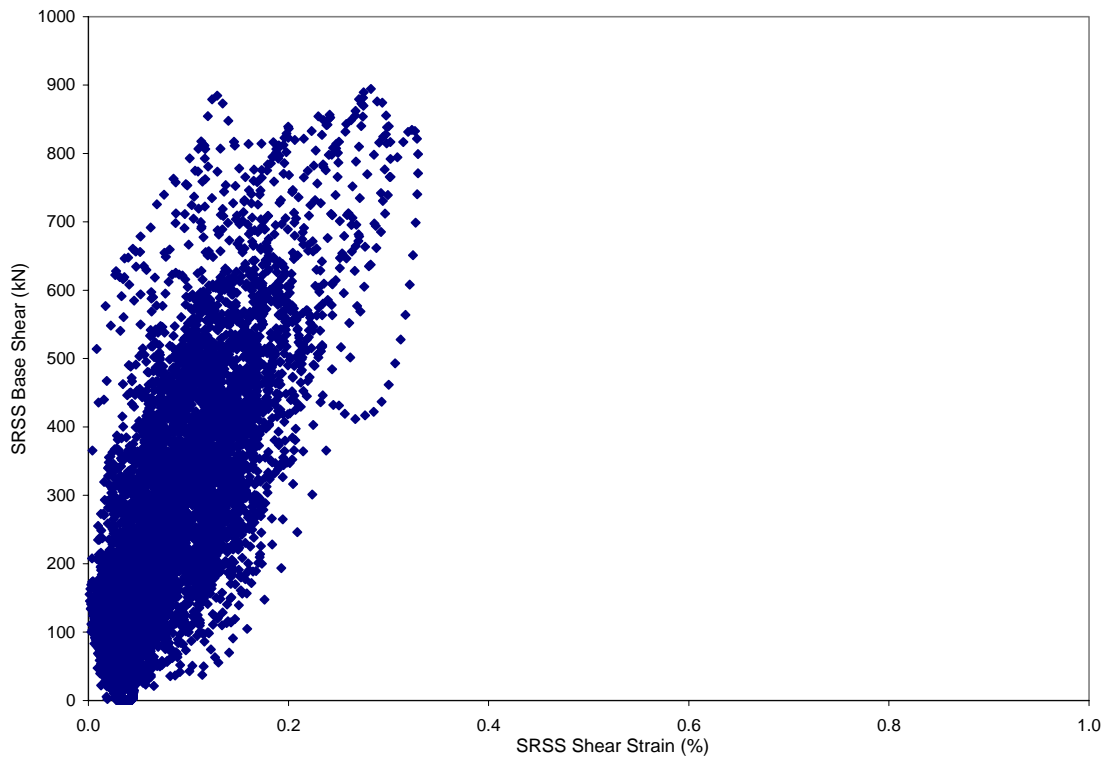


Figure 5-56 ANACAP Calculated SRSS Base Shear vs. SRSS Shear Strain for Run-4

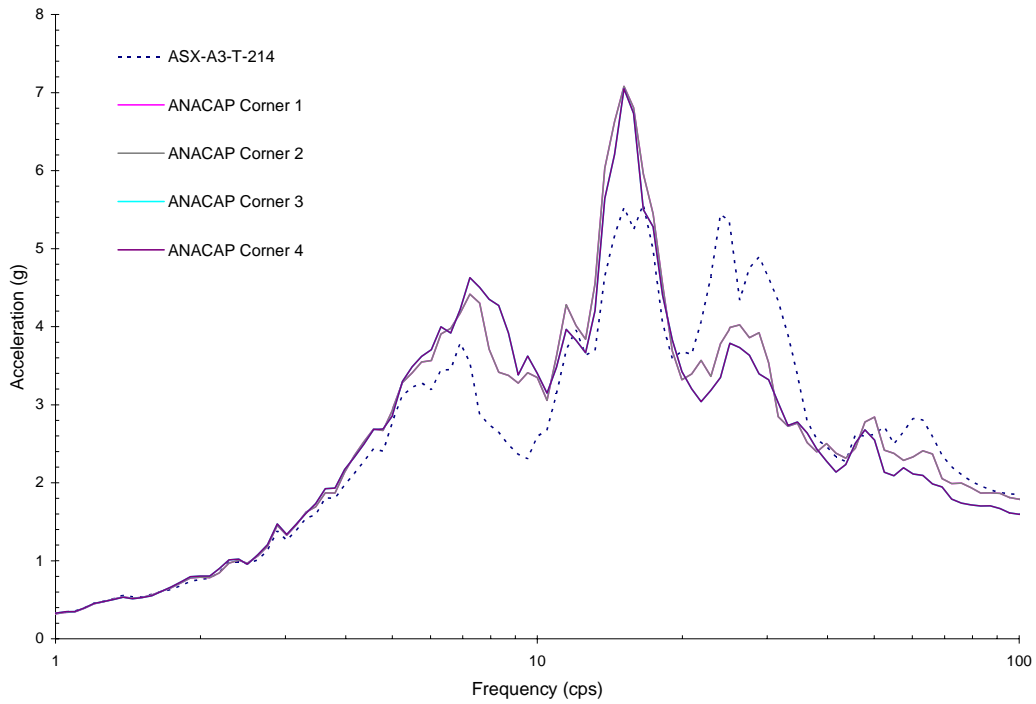


Figure 5-57 Comparison of X-Direction Response between ANACAP Analysis at Upper Corners of Shear Walls and Measured Data for Run-5

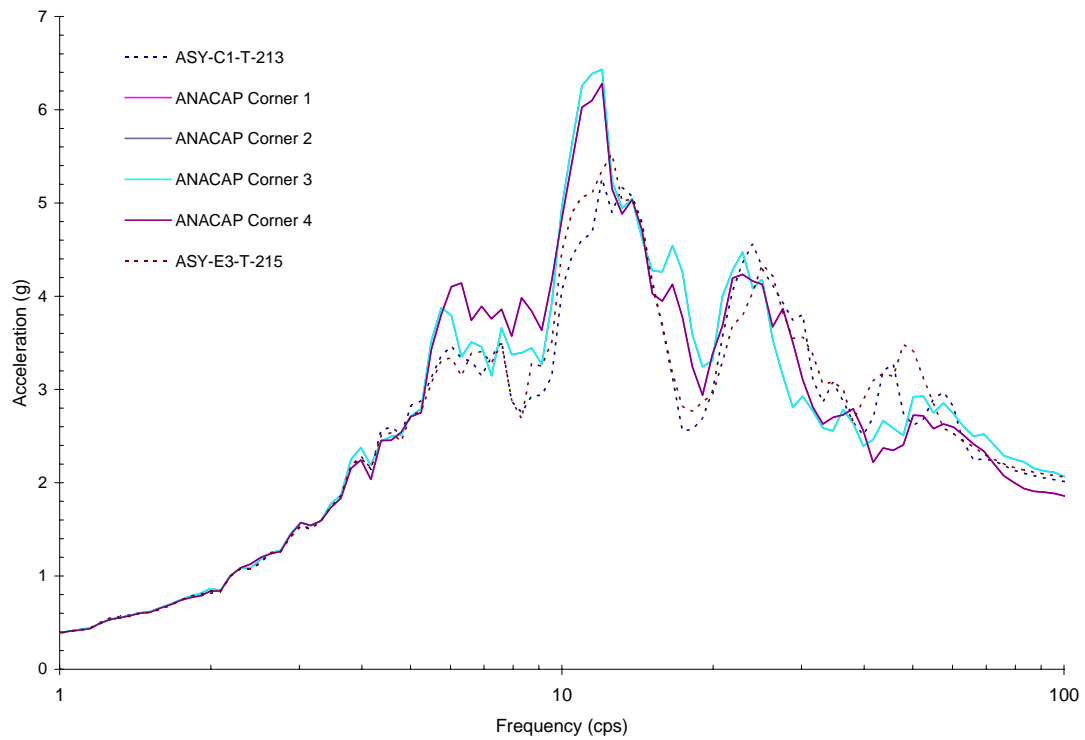


Figure 5-58 Comparison of Y-Direction Response between ANACAP Analysis at Upper Corners of Shear Walls and Measured Data for Run-5

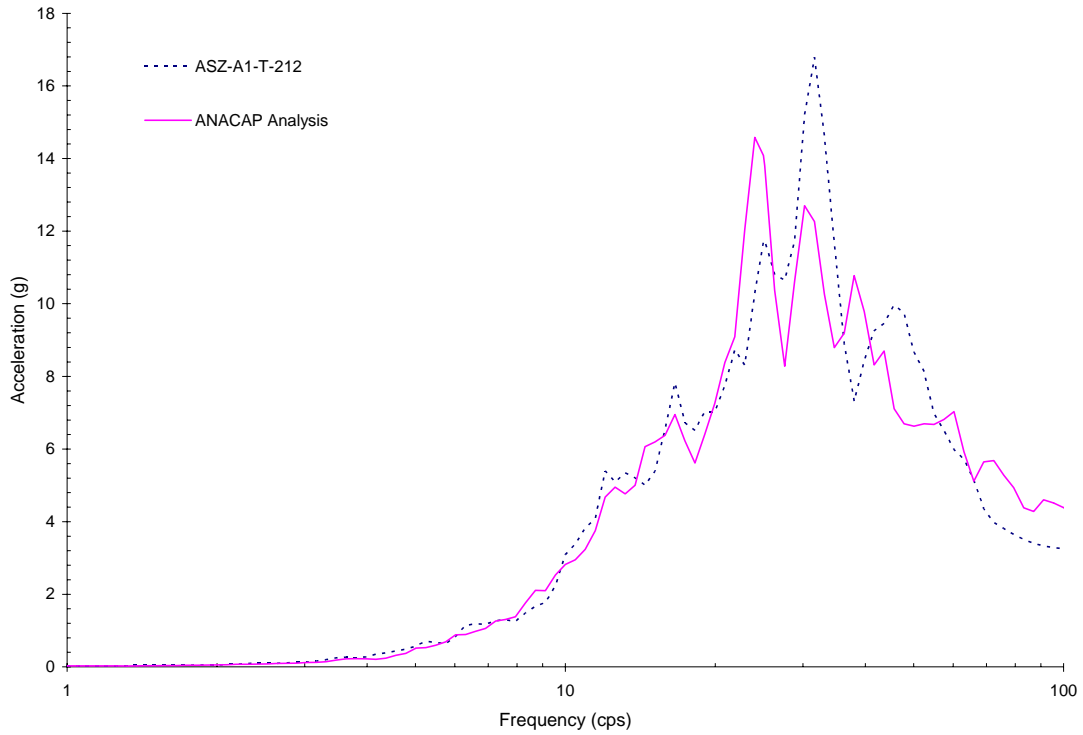


Figure 5-59 Comparison of Z-Direction Response between ANACAP Analysis at Upper Slab Corner No.1 and Measured Result for Run-5

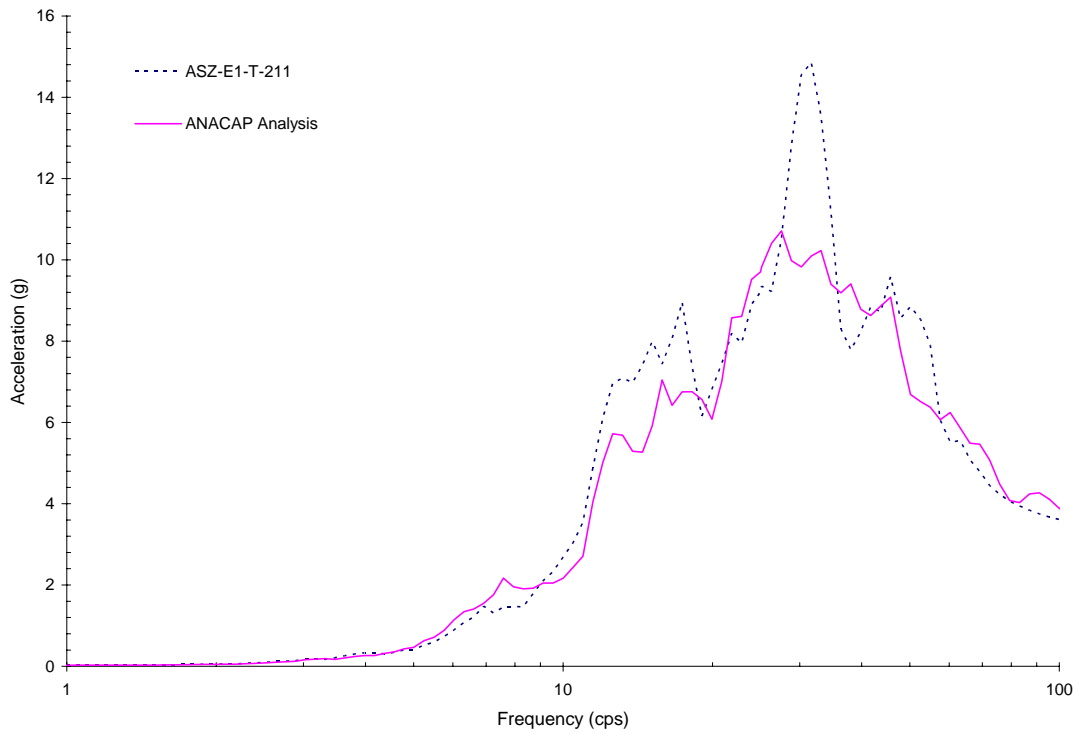


Figure 5-60 Comparison of Z-Direction Response between ANACAP Analysis at Upper Slab Corner No.2 and Measured Result for Run-5

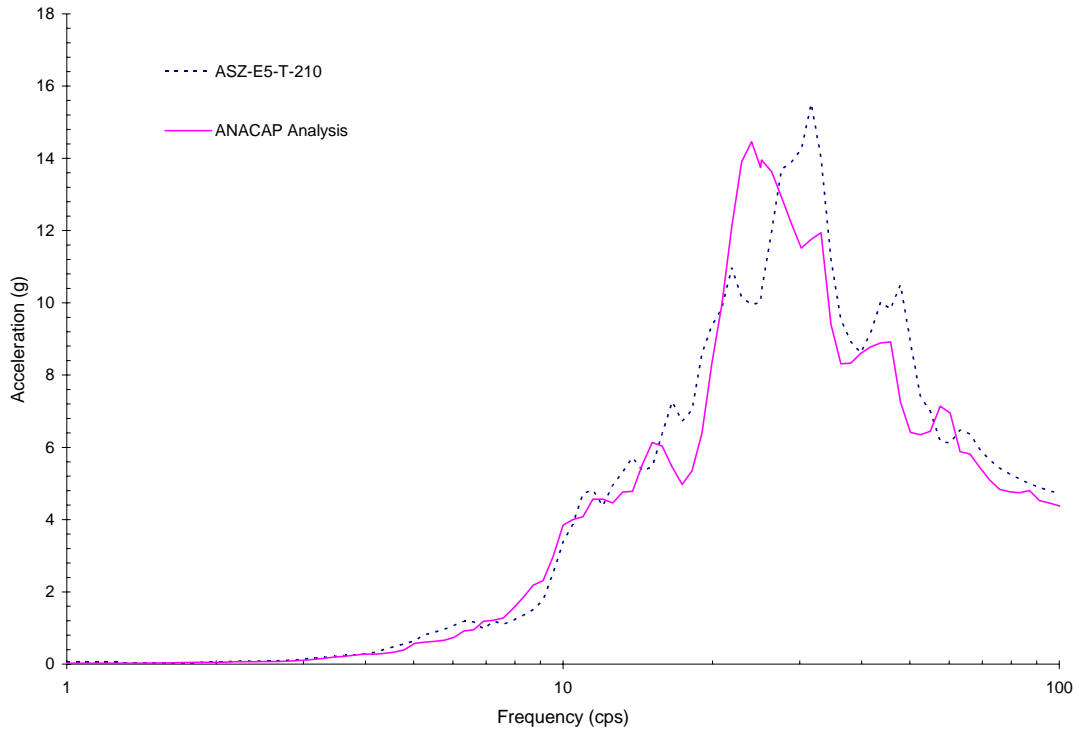


Figure 5-61 Comparison of Z-Direction Response between ANACAP Analysis at Upper Slab Corner No.3 and Measured Result for Run-5

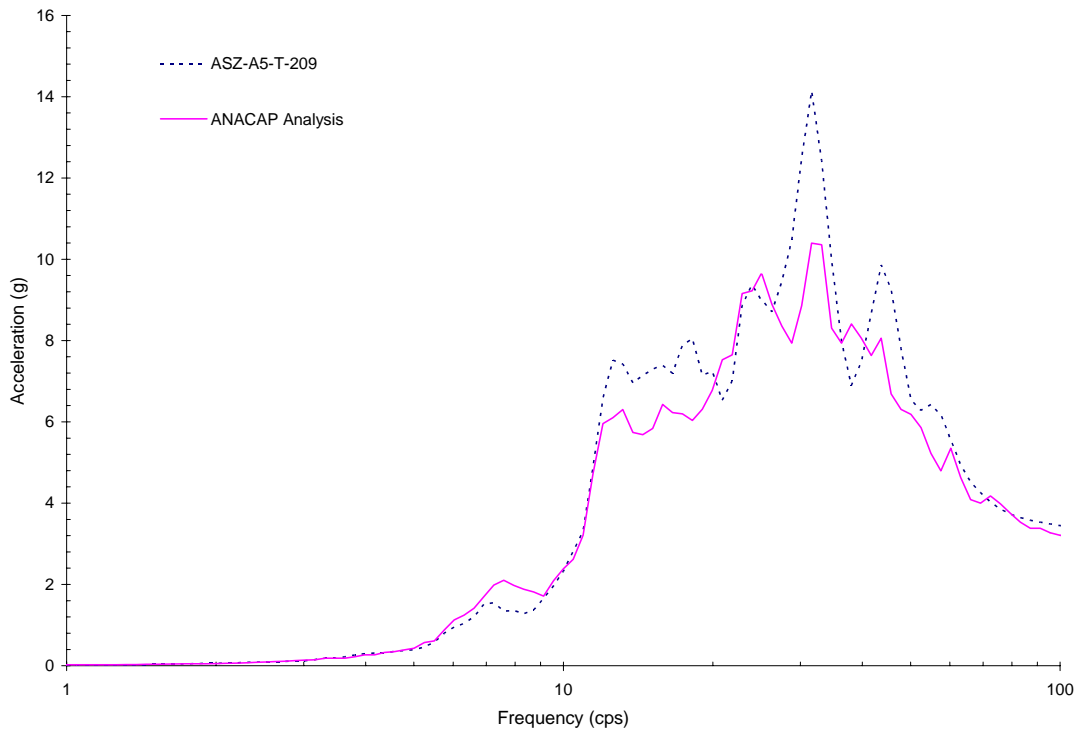


Figure 5-62 Comparison of Z-Direction Response between ANACAP Analysis at Upper Slab Corner No.4 and Measured Result for Run-5

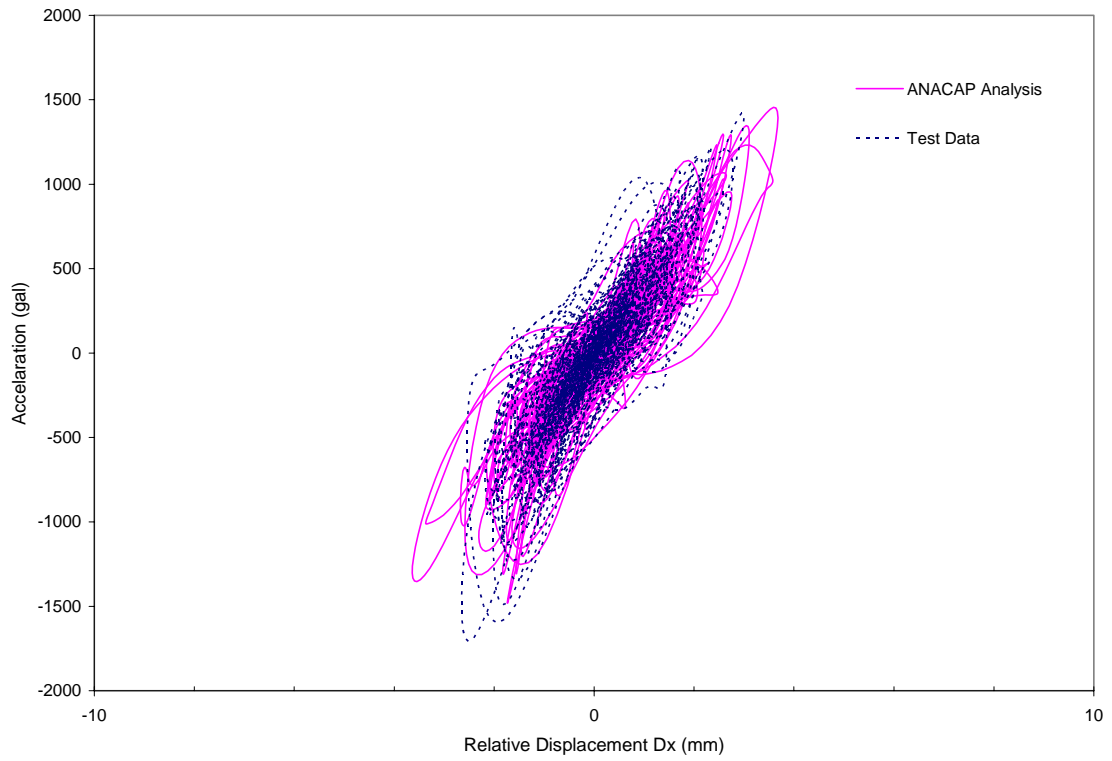


Figure 5-63 Comparison of Hysteresis Loops in X-Direction for Run-5

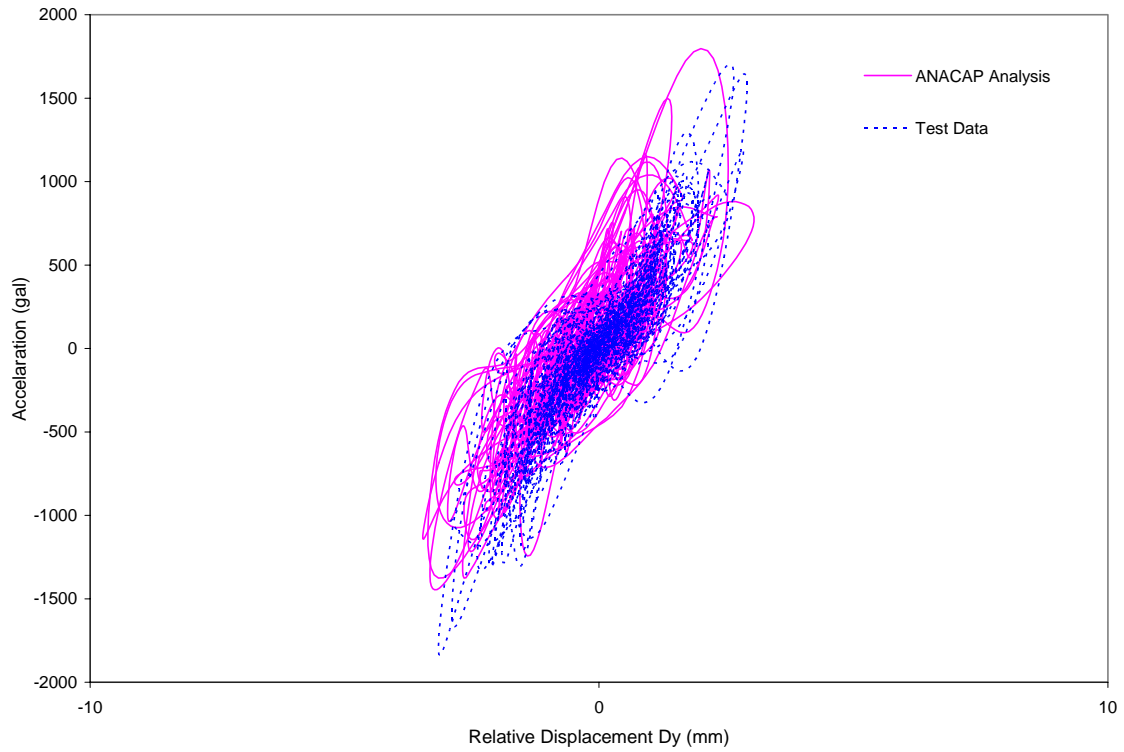


Figure 5-64 Comparison of Hysteresis Loops in Y-Direction for Run-5

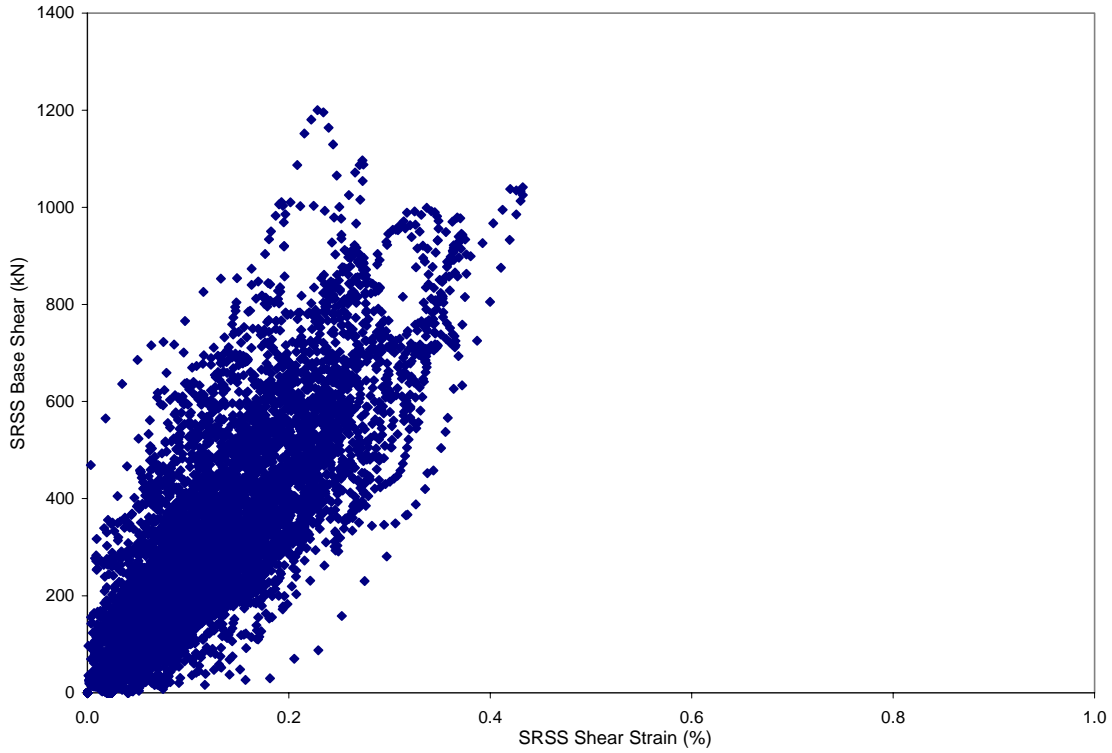


Figure 5-65 ANACAP Calculated SRSS Base Shear vs. SRSS Shear Strain for Run-5

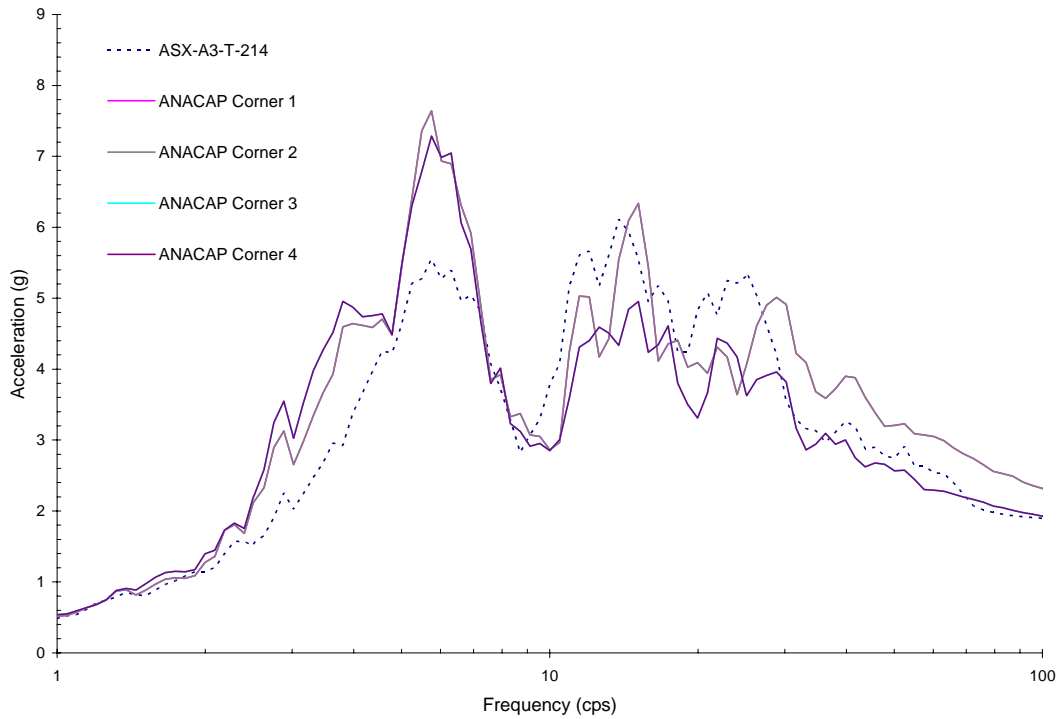


Figure 5-66 Comparison of X-Direction Response between ANACAP Analysis at Upper Corners of Shear Walls and Measured Data for Run-6

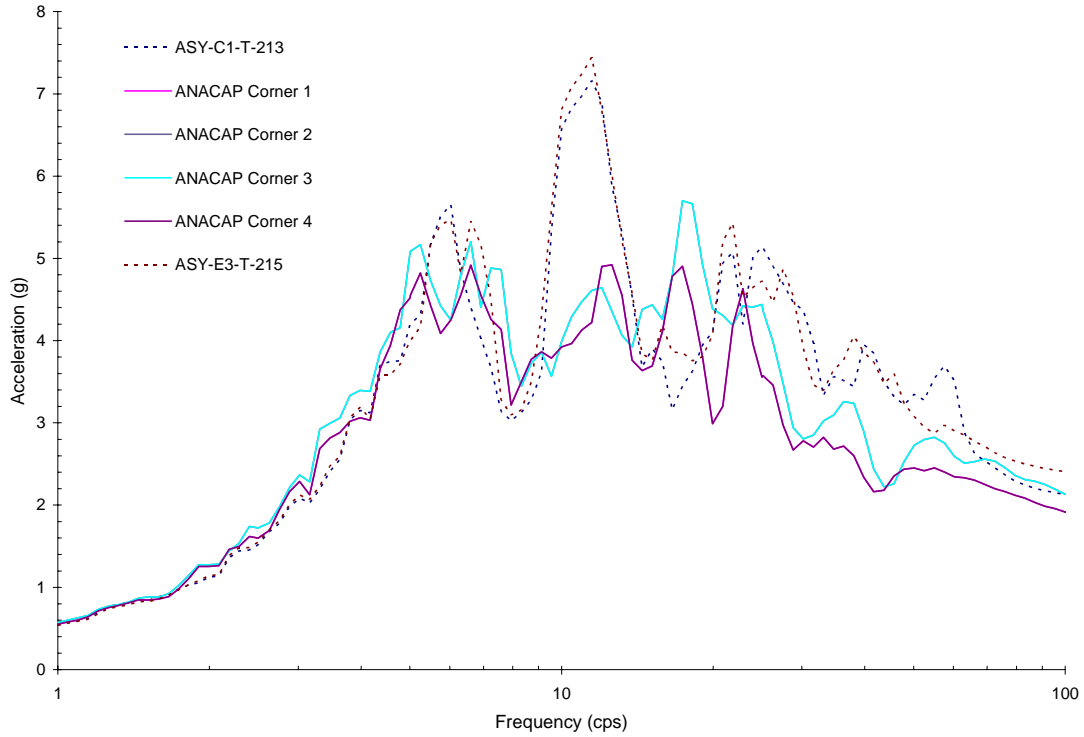


Figure 5-67 Comparison of Y-Direction Response between ANACAP Analysis at Upper Corners of Shear Walls and Measured Data for Run-6

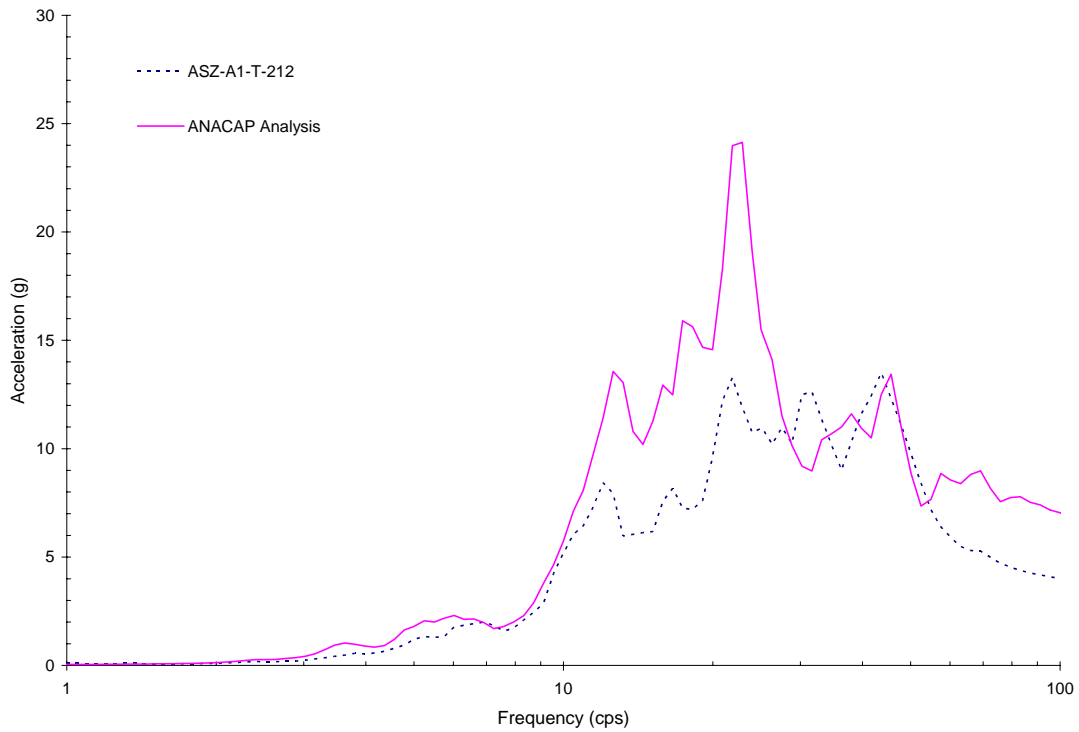


Figure 5-68 Comparison of Z-Direction Response between ANACAP Analysis at Upper Slab Corner No.1 and Measured Result for Run-6

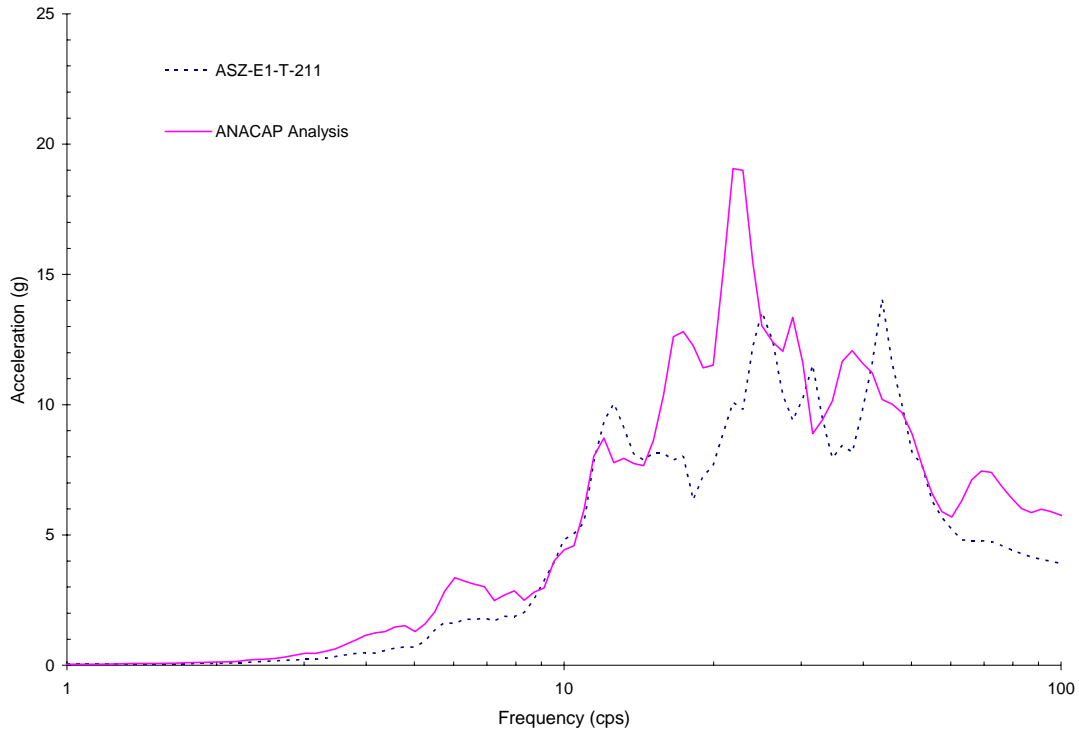


Figure 5-69 Comparison of Z-Direction Response between ANACAP Analysis at Upper Slab Corner No.2 and Measured Result for Run-6

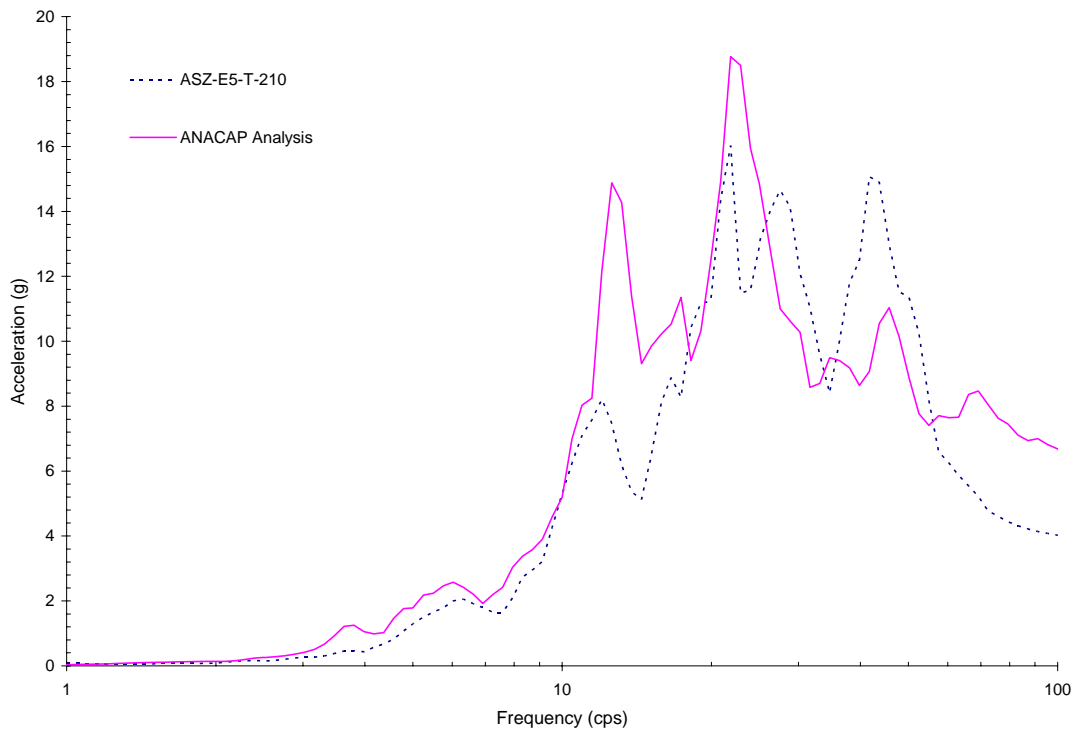


Figure 5-70 Comparison of Z-Direction Response between ANACAP Analysis at Upper Slab Corner No.3 and Measured Result for Run-6

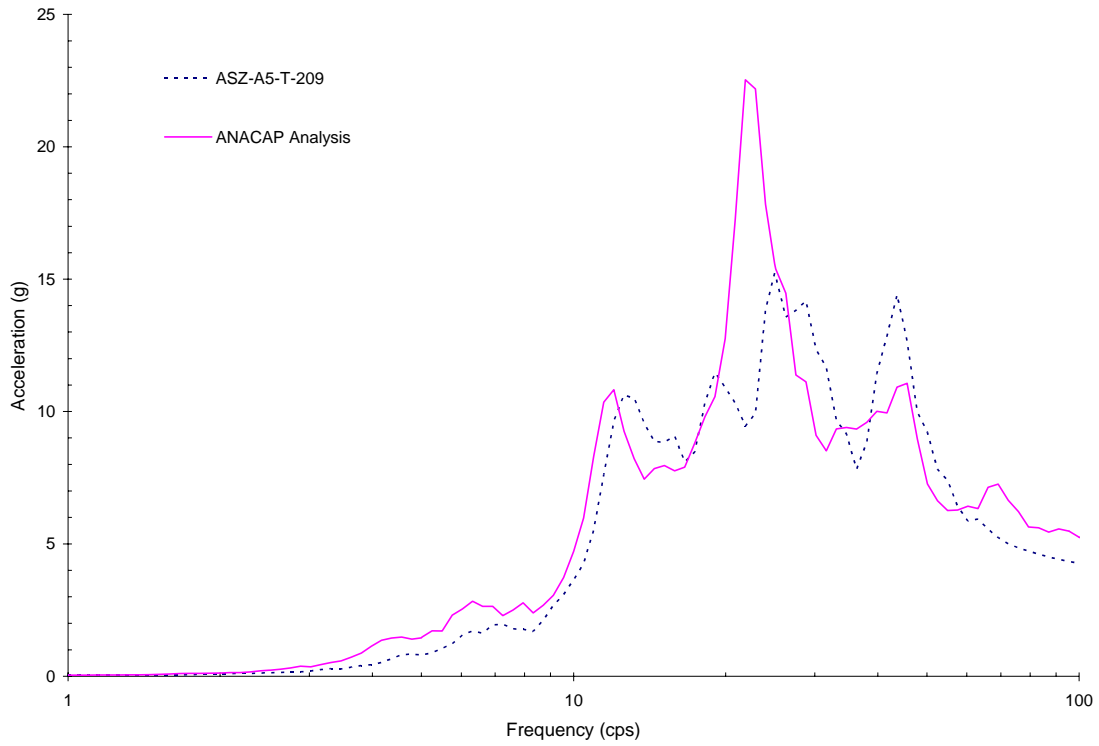


Figure 5-71 Comparison of Z-Direction Response between ANACAP Analysis at Upper Slab Corner No.4 and Measured Result for Run-6

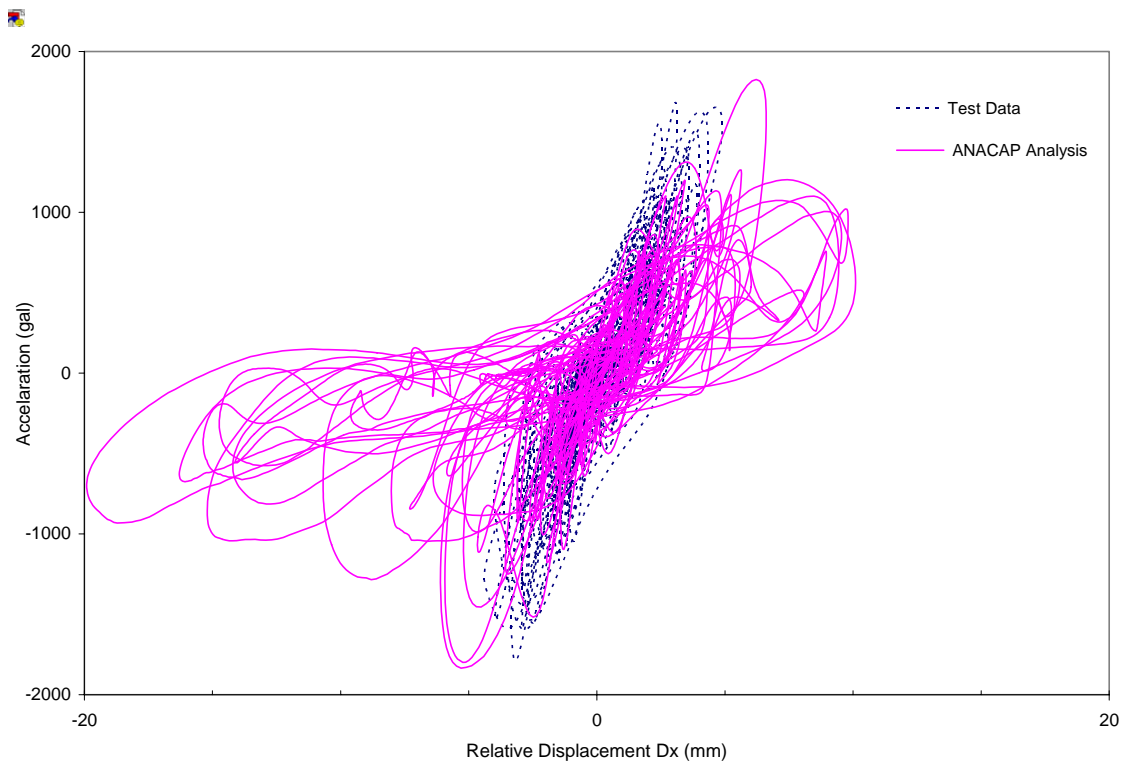


Figure 5-72 Comparison of Hysteresis Loops in X-Direction for Run-6

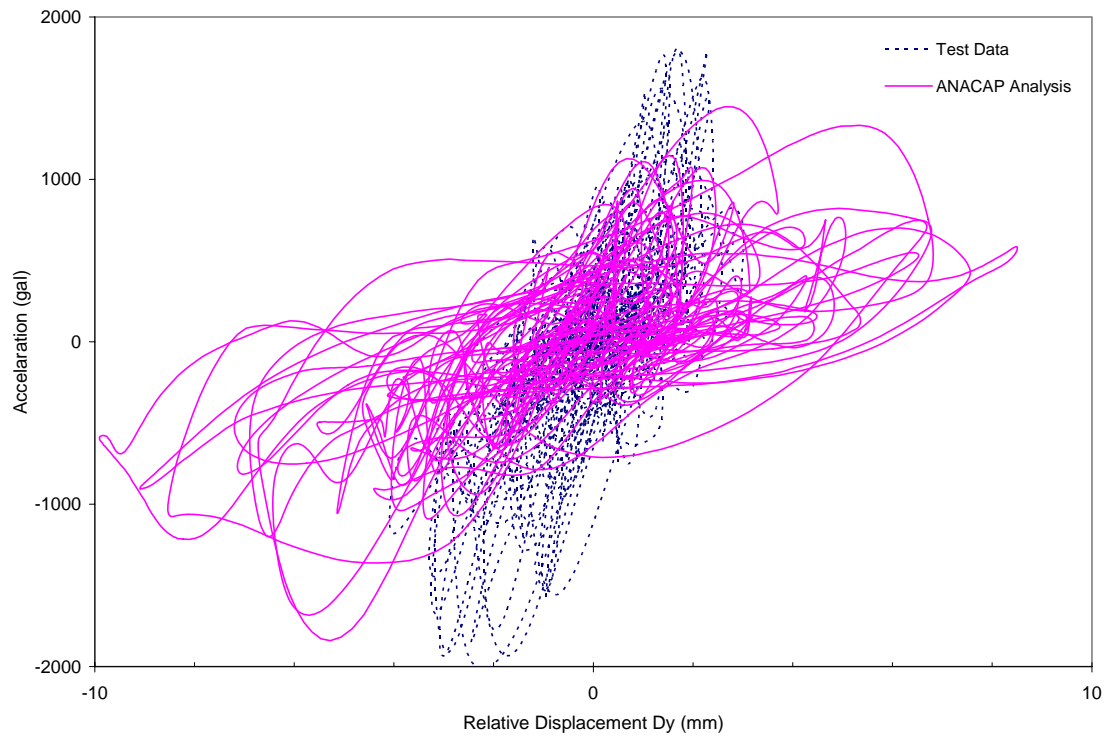


Figure 5-73 Comparison of Hysteresis Loops in Y-Direction for Run-6

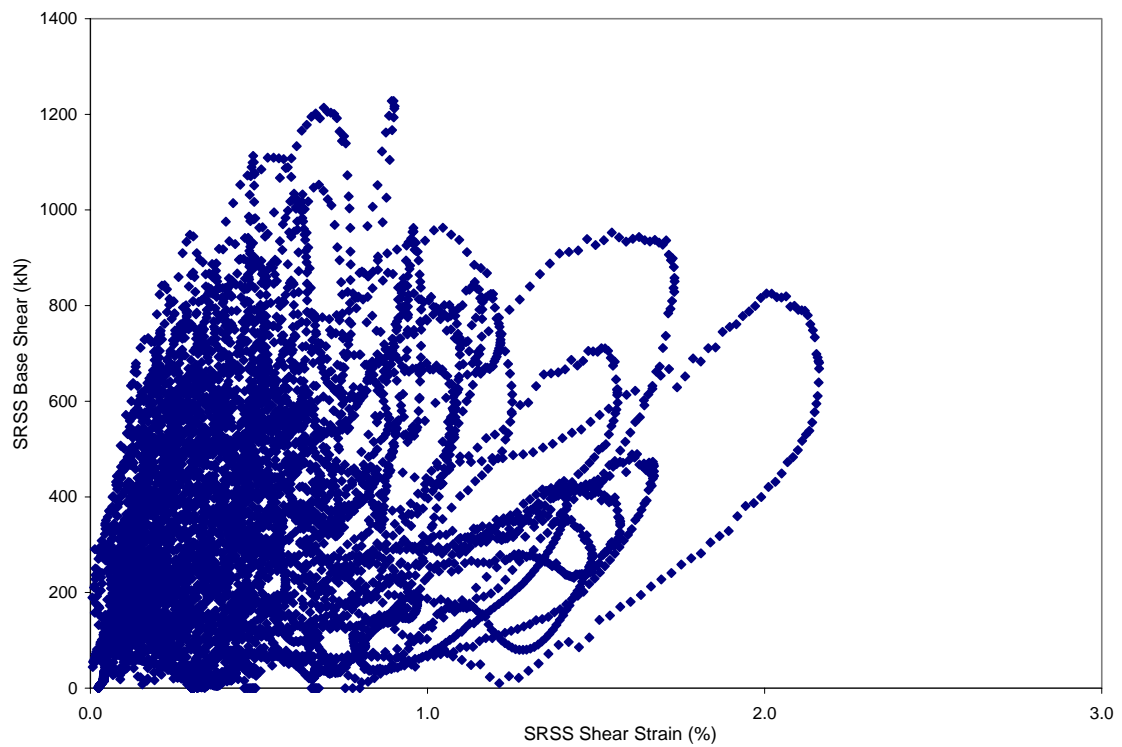


Figure 5-74 ANACAP Calculated SRSS Base Shear vs. SRSS Shear Strain for Run-6

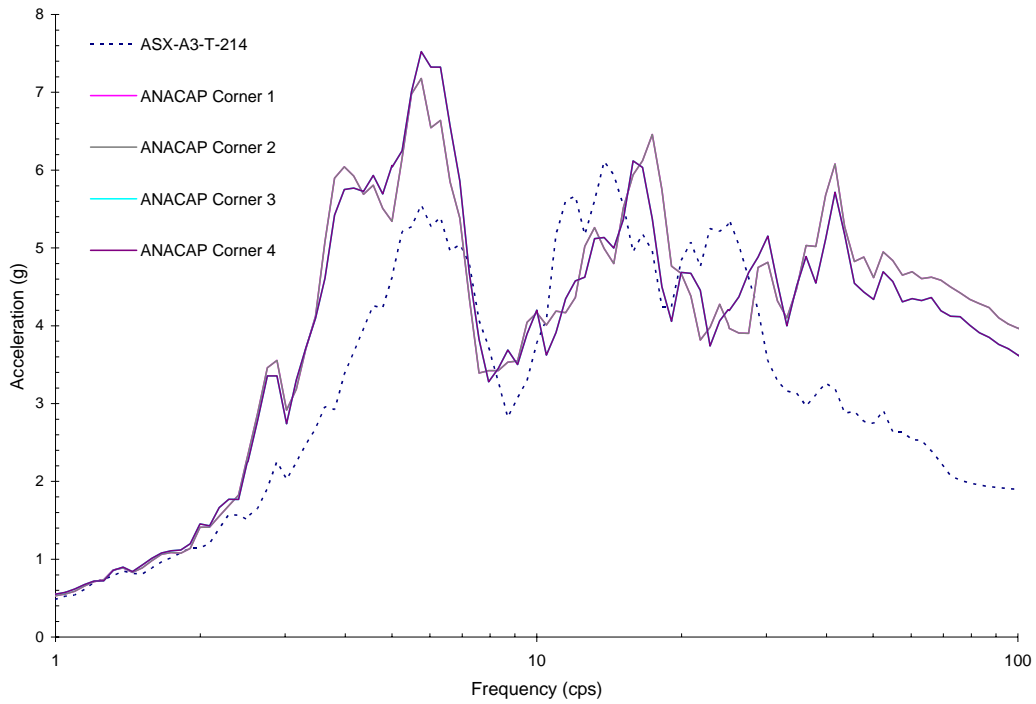


Figure 5-75 Comparison of ANACAP Analysis without Considering Prior Damages for Run-6 in X-Direction at Upper Corners of Shear Walls and Measured Data

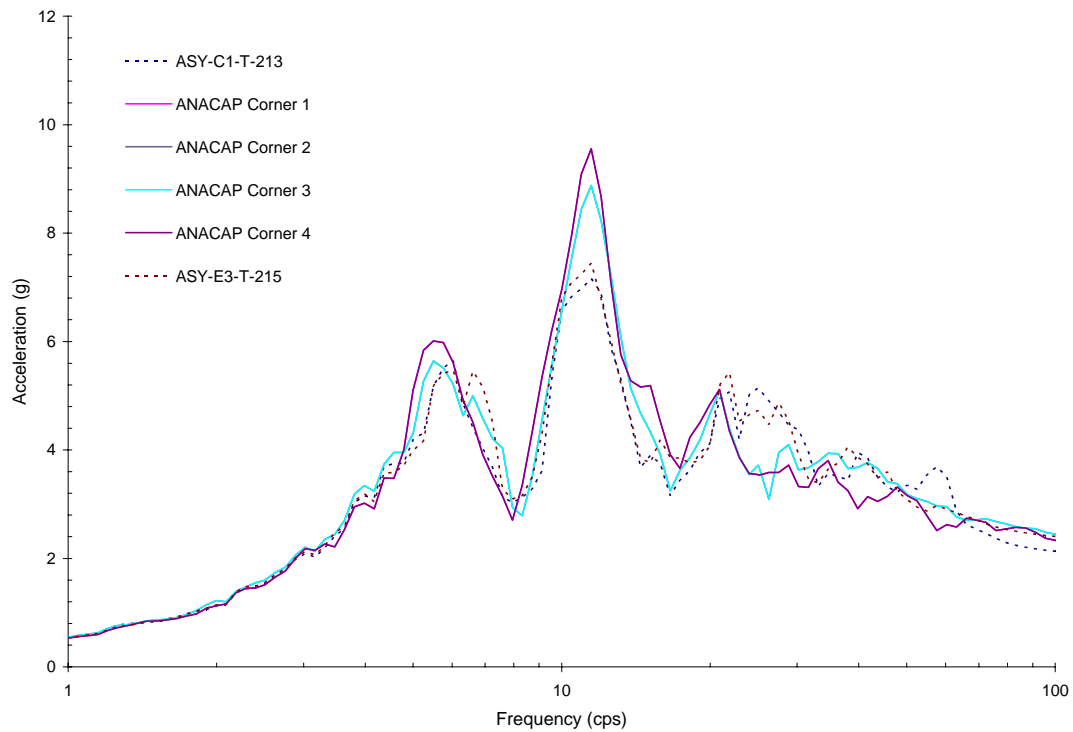


Figure 5-76 Comparison of ANACAP Analysis without Considering Prior Damages for Run-6 in Y-Direction at Upper Corners of Shear Walls and Measured Data

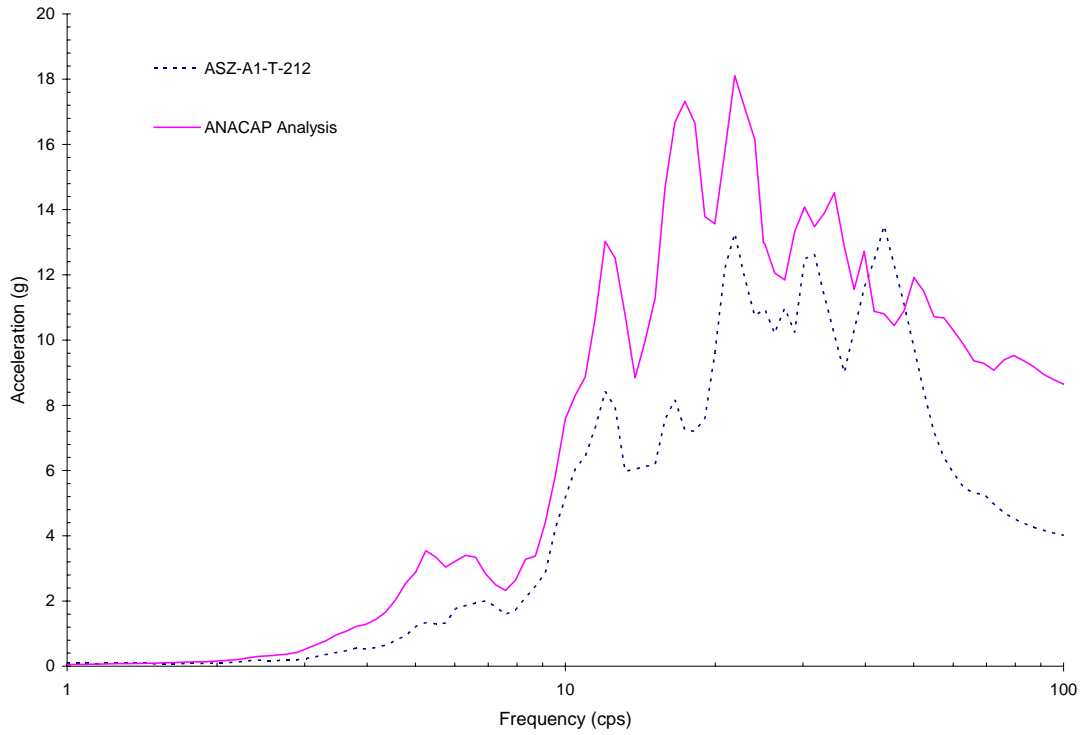


Figure 5-77 Comparison of ANACAP Analysis without Considering Prior Damages for Run-6 in Z-Direction at Upper Slab Corner No.1 and Measured Result

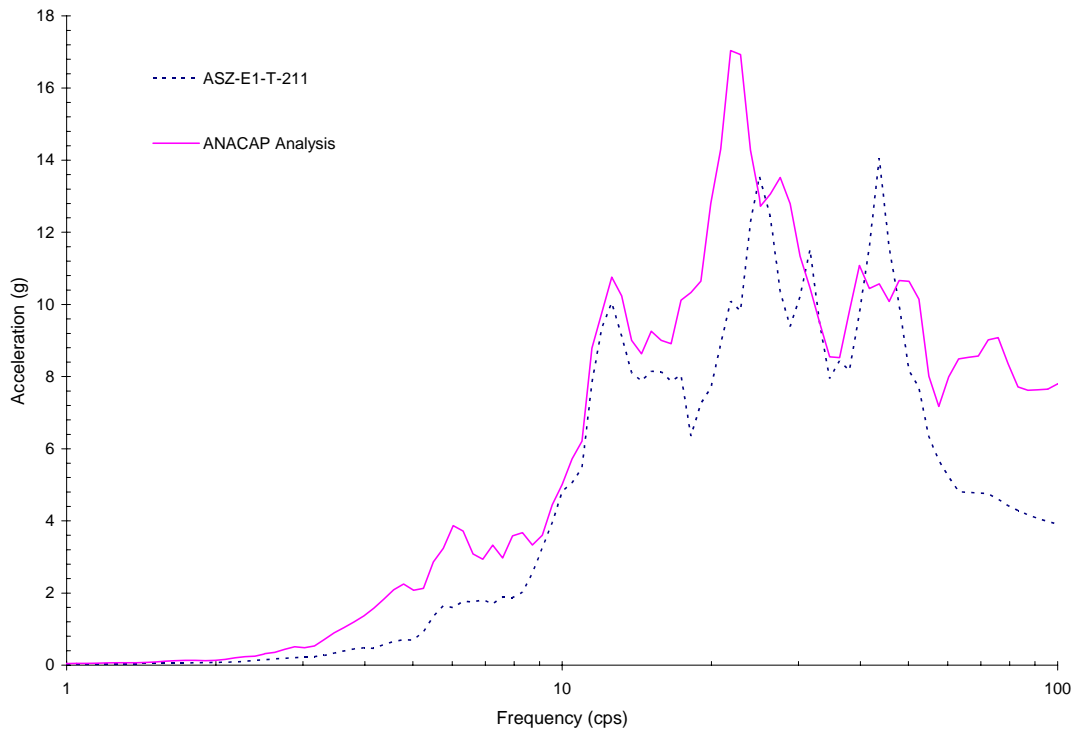


Figure 5-78 Comparison of ANACAP Analysis without Considering Prior Damages for Run-6 in Z-Direction at Upper Slab Corner No.2 and Measured Result

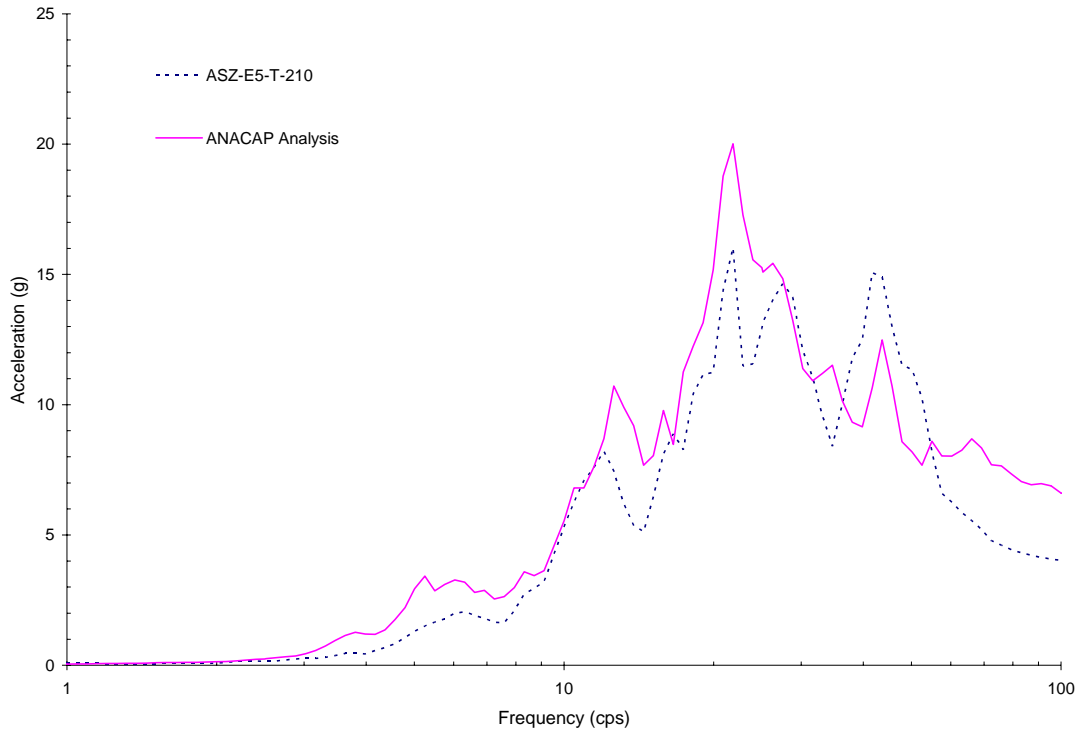


Figure 5-79 Comparison of ANACAP Analysis without Considering Prior Damages for Run-6 in Z-Direction at Upper Slab Corner No.3 and Measured Result

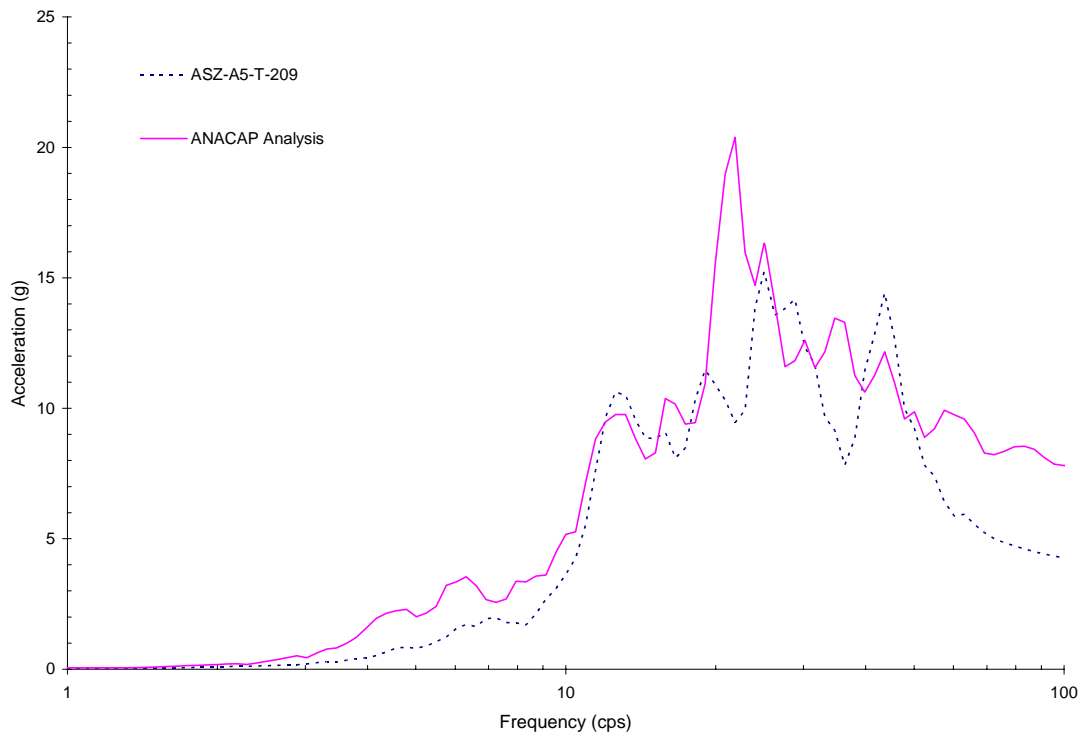


Figure 5-80 Comparison of ANACAP Analysis without Considering Prior Damages for Run-6 in Z-Direction at Upper Slab Corner No.4 and Measured Result

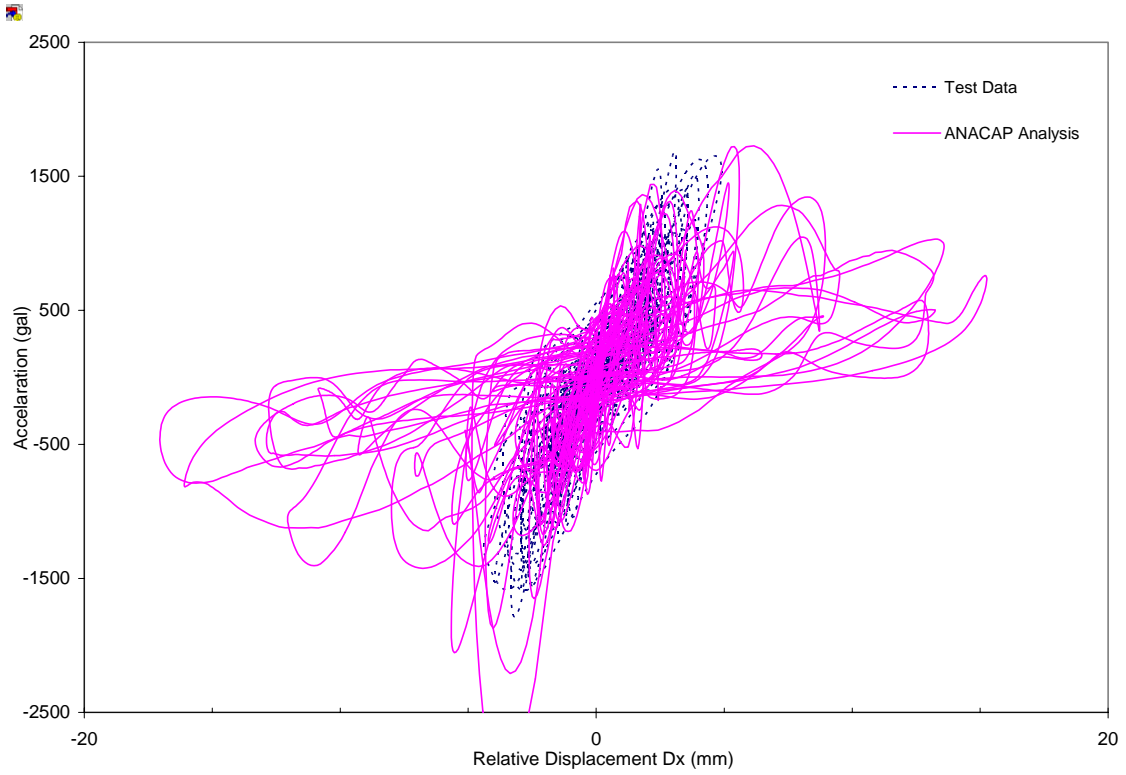


Figure 5-81 Comparison of ANACAP Hysteresis Loop without Considering Prior Damages for Run-6 in X-Direction and Test Result

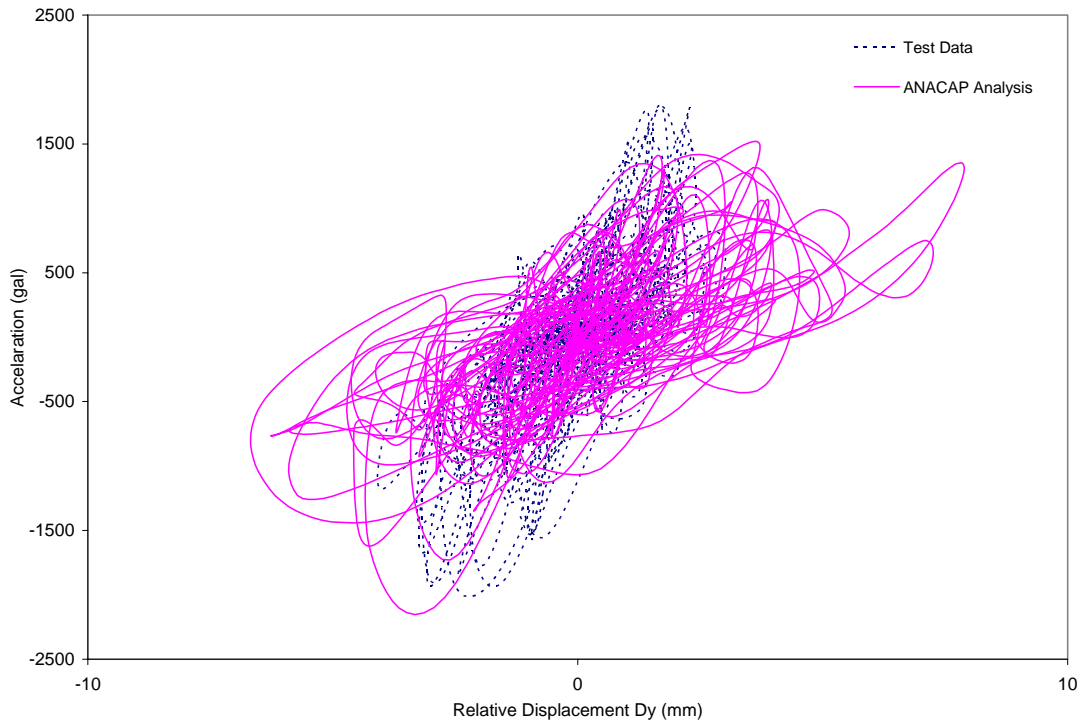


Figure 5-82 Comparison of ANACAP Hysteresis Loop without Considering Prior Damages for Run-6 in Y-Direction and Test Result

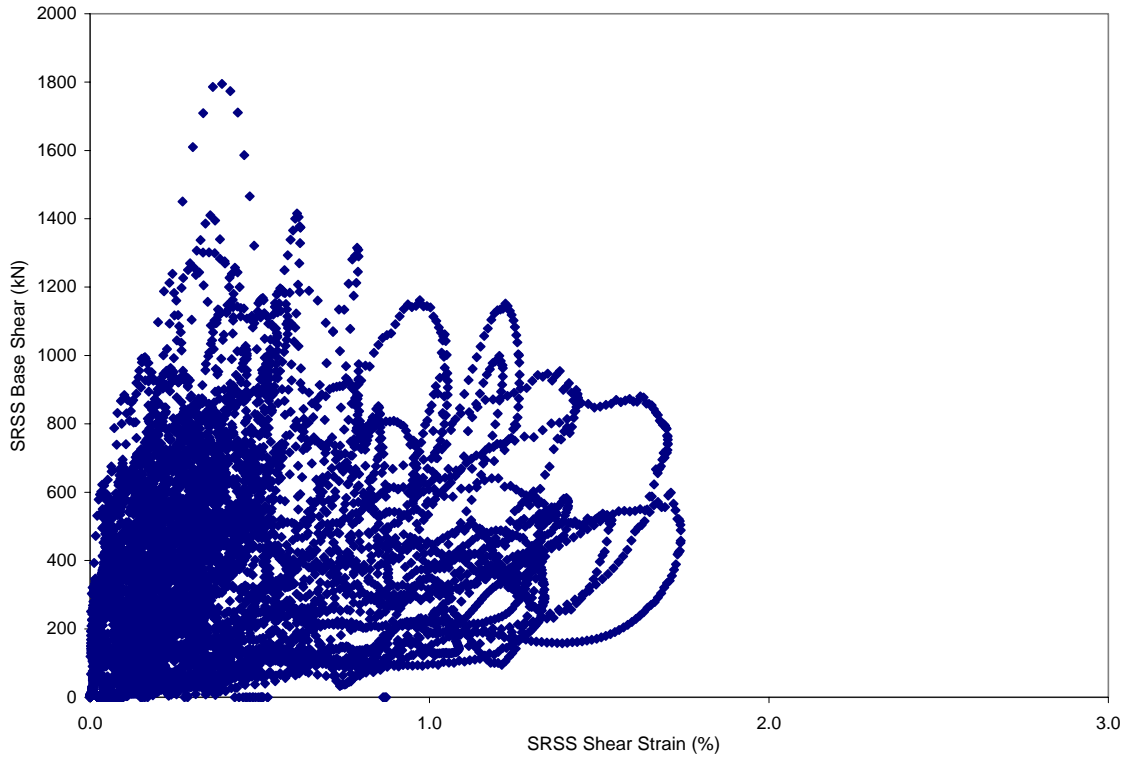


Figure 5-83 ANACAP Calculated SRSS Base Shear vs. SRSS Shear Strain without Considering Prior Damages for Run-6

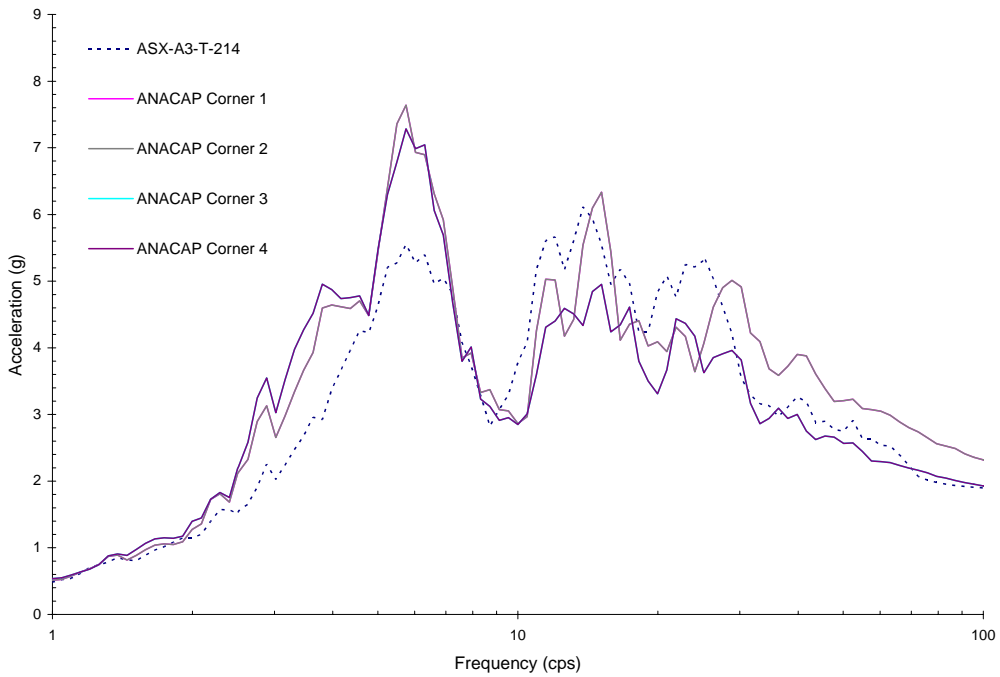


Figure 5-84 Comparison of X-Direction Response from ANACAP Analysis Considering Prior Damages but with X-Input Motion only and Test Result for Run-6

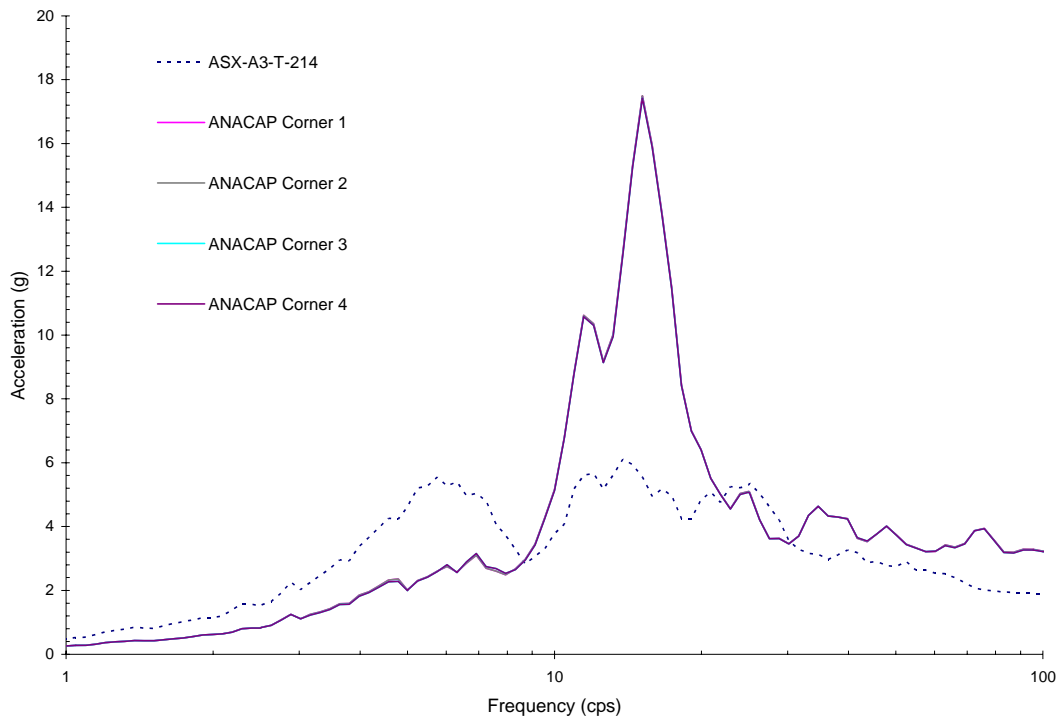


Figure 5-85 Comparison of X-Direction Response from ANACAP Analysis Considering No Prior Damages but with X-Input Motion only and Test Result for Run-6

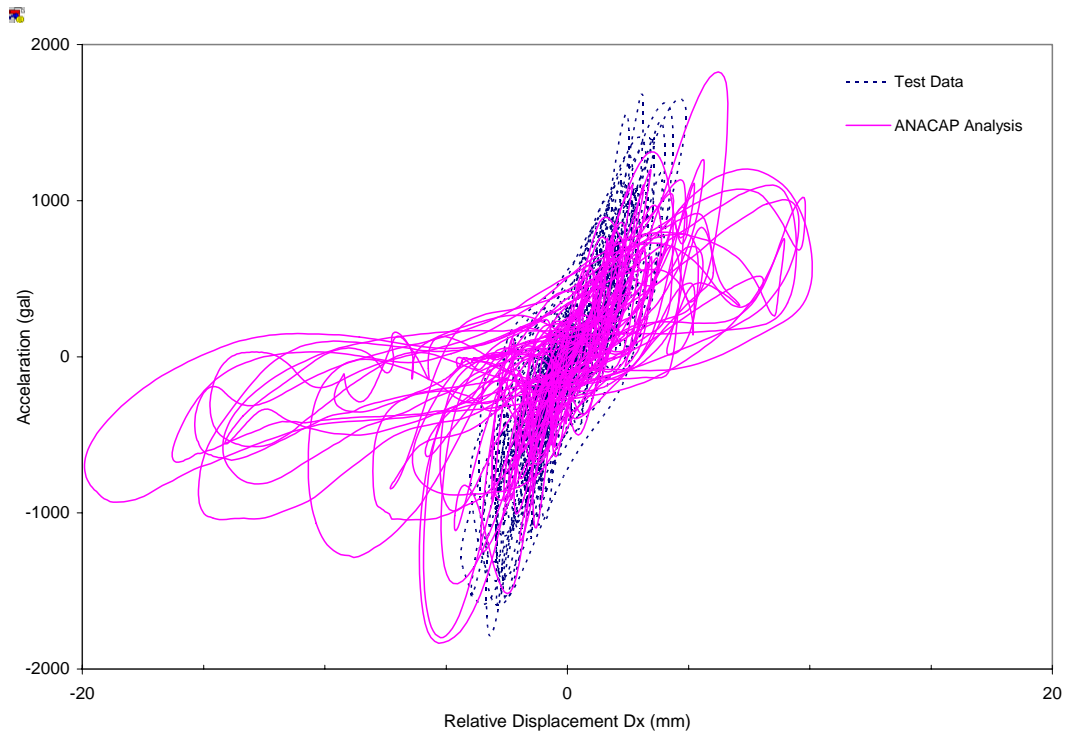


Figure 5-86 Comparison of X-Direction Hysteresis from ANACAP Analysis Considering Prior Damages but with X-Input Motion only and Test Result for Run-6

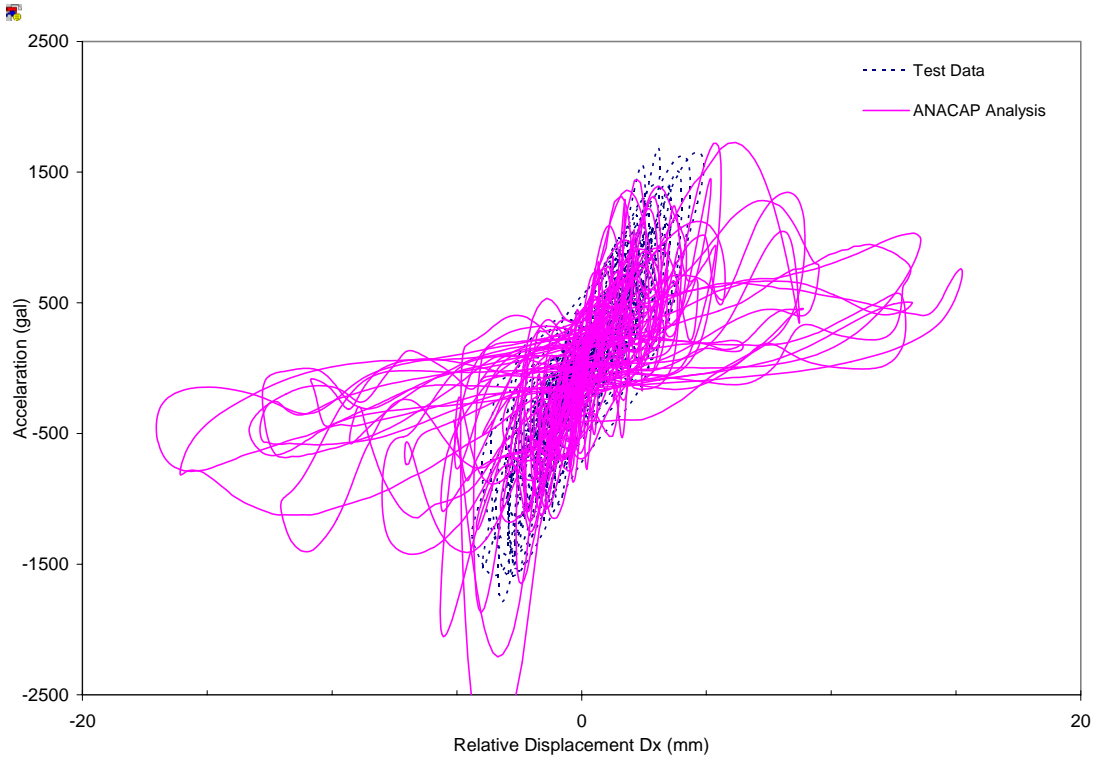


Figure 5-87 Comparison of X-Direction Hysteresis from ANACAP Analysis Considering No Prior Damages but with X-Input Motion only and Test Result for Run-6

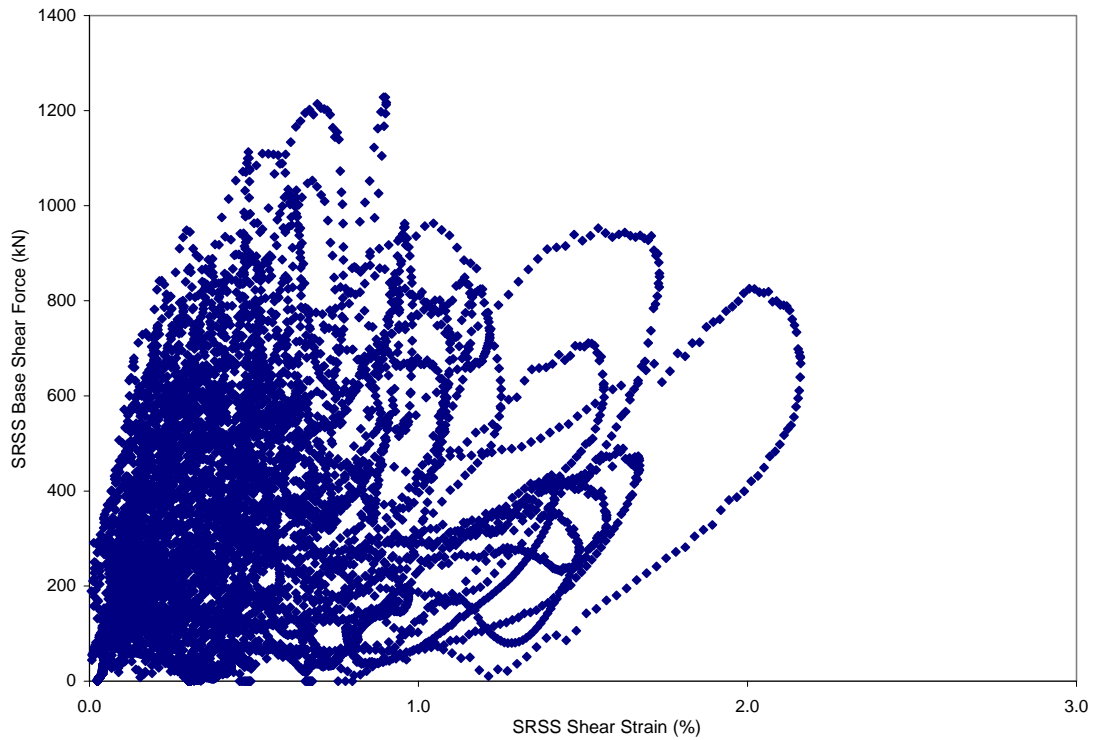


Figure 5-88 ANACAP Calculated SRSS Base Shear vs. SRSS Shear Strain Considering Prior Damages and X-Input Motion only for Run-6

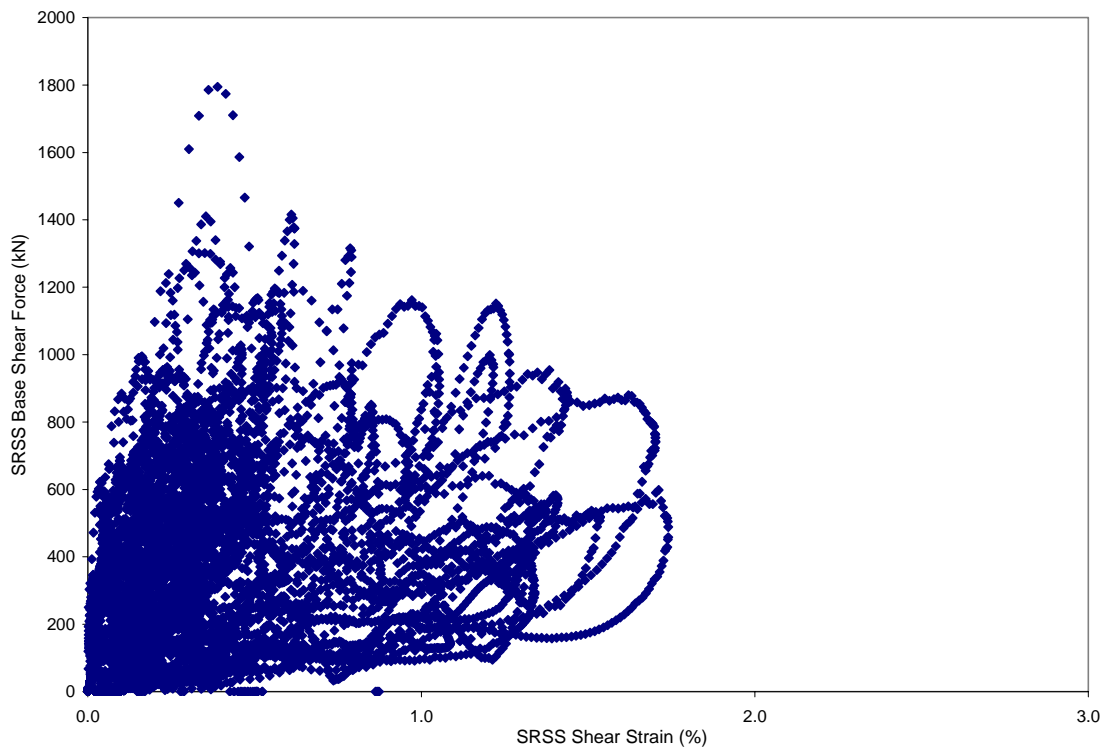


Figure 5-89 ANACAP Calculated SRSS Base Shear vs. SRSS Shear Strain Considering No Prior Damages and X-Input Motion only for Run-6

Table 5-1 Maximum Base Responses from ANACAP Simulation for Run-1

Base Response	Calculated Maximum (kN)	Test Value ^a (kN)	Relative Difference
Shear - X	243.90	316	-22.82%
Shear - Y	235.63	290	-18.75%
Vertical Force - Z	748.68	757	-1.10%

Table 5-2 Maximum Base Responses from ANACAP Simulation for Run-2

Base Response	Calculated Maximum (kN)	Test Value ^a (kN)	Relative Difference
Shear - X	512.49	630	-18.65%
Shear - Y	609.30	513	18.77%
Vertical Force	1588.79	1429	11.18%

Table 5-3 Maximum Base Responses from ANACAP Simulation for Run-2'

Base Response	Calculated Maximum (kN)	Test Value ^a (kN)	Relative Difference
Shear - X	287.33	241	19.22%
Shear - Y	238.44	224	6.44%
Vertical Force - Z	869.21	848	2.50%

6 CONCLUSIONS AND RECOMMENDATIONS

This report presented a BNL study for assessing the performance of analysis methods for computing the seismic response of shear wall structures subjected to strong ground motions and their ultimate seismic failure capacities. The analysis methods evaluated in this study include simplified (semi-empirical equations) methods for estimating seismic shear wall capacities and the finite element (FE) method for the seismic response analysis, which incorporates a detailed reinforced concrete material model as implemented in ANACAP. The study was carried out by analyzing a set of box-type shear wall test specimens (scaled shear wall structure typically encountered in commercial nuclear power plants) and comparing the analysis results with the test data provided by JNES/NUPEC as part of a collaborative agreement to study seismic issues important to the safe operation of commercial nuclear power plant (NPP) structures, systems and components (SSC). The test data utilized in the study included both single- and multi- axis cyclic box-type shear wall tests and a shaking table test of the box-type shear wall.

There are six major elements contained in the BNL study, which include: 1) the use of simplified methods to estimate the seismic failure capacities of the JNES/NUPEC shear wall specimens and to compare the analytical estimates with the seismic shear wall failure capacities inferred from the JNES/NUPEC test data for both the uni- and multi- axis cyclic tests, as well the shaking table test, 2) the development of an ANACAP static FE model for the JNES/NUPEC shear wall test specimens and the comparisons of the results from the shear wall cyclic analysis using the ANACAP static model with the JNES/NUPEC single and multi-axial cyclic test data, 3) the development of an ANACAP dynamic FE model which was used to perform a 3-D simulation analysis of the JNES shaking table test data, 4) an ANACAP analysis for Run-6 (high level motion) without considering prior damages to assess the effect of prior damage history on the FE analysis of the seismic response of shear wall structures, 5) an ANACAP analysis for Run-6 using uni-directional input to the shear wall model which has been damaged from previous test runs, and 6) same as case 5, except that the prior history of damage was not considered.

Based on the analyses performed on the shear wall test models and the comparisons made between the analysis results and the test data, the following observations and conclusions are reached:

Failure capacity estimates using simplified methods

Test results from eleven box-type RC shear wall specimens were used for assessing shear failure capacity estimated by simplified methods. These shear walls specimen having aspect ratios in the range of 0.47 – 0.87 were tested by JNES/NUPEC by applying various uni-directional and multi-axis cyclic loads. These test data offer valuable insights into the interaction effect of out-of-plane shear and moment on the in-plane shear failure, which is not considered by consensus standards for shear wall design in the U.S., and therefore provide a unique opportunity for assessing the adequacy of methods based on consensus standards for shear wall capacity estimates. To this end, shear strength of the JNES/NUPEC cyclic test specimens was computed using Chapters 11 and 21 of ACI 349-01, and ASCE 43-05 which is based on Barda et al. method. The computed shear strength was compared against the JNES/NUPEC test results and the interaction effect on the adequacy of these methods was assessed.

For the ACI methods, the computed shear strength was compared against the test results in terms of the maximum shear of the two directions and the resultant of the bi-axis shears. The comparison showed that shear strength computed by the ACI methods appear to be quite conservative as would be expected. The level of conservatism is large for smaller aspect ratios and reduces as the aspect ratio increases. In addition, the interaction intensity which measures bi-

axis interaction effect also reduces the conservative margin; however, no significant un-conservative bias is introduced when the bi-axis shear components are probabilistically combined (which is the current industry practice for seismic analysis of RC shear walls).

An extensive evaluation of the ASCE 43-05 method for estimating the capacity of RC shear walls was performed. A regression equation involving the interaction intensity and an adjustment factor was established to closely correlate the ASCE 43-05 calculated shear strength to the test data. The adjustment factor, designated in this report as F , was established as a linear function of the aspect ratio. For shear walls with small or no interaction effect (interaction intensity is approximately equal to one), the ratio of the ASCE 43-05 calculated shear strength to test data becomes simply the adjustment factor F . In this case, the use of ASCE 43-05 is very close and for most cases conservative when compared to the JNES/NUPEC test results on walls having aspect ratios in the range of 0.47 to 0.87. For walls with more significant interaction effect, the shear strength calculated based on ASCE 43-05 when corrected with the adjustment factor compares very closely to the test results. However, due to the limited range of aspect ratios for the test specimens, application of the ASCE 43-05 method should be cautioned for shear walls having aspect ratio greater than 0.9.

It was further concluded that when two horizontal components of seismic input motions are treated as being statistically independent from one another, the interaction effect could be neglected. It was demonstrated in this report that when the seismic loads in both horizontal directions are statistically uncorrelated and the shear forces are combined probabilistically in accordance with the 100-40-40 rule, the un-conservatism by neglecting the interaction effect is only 6.1% (It should be noted that the conservatism is attributed to both the interaction intensity and the adjustment factor F). Thus, no significant un-conservative bias is introduced by considering each direction independently so long as the bi-axis shear components are uncorrelated.

Assessment of methods for calculating inelastic energy absorption factors

Four methods for computing the inelastic energy absorption factor F_{μ} were selected to compare with the JNES/NUPEC shaking table test estimate of F_{μ} . These methods include: Riddell-Newmark, effective frequency/effective damping (EFED), Spectral Averaging and Secant Frequency methods. Among these methods, Riddell-Newmark conservatively bounds the test results (under predict F_{μ} by about 18 to 19% in the x and y directions) while EFED and Spectral Averaging generally over predict the test results. The reason for over-estimating F_{μ} by EFED or Spectral Averaging in this case was due to a local valley that existed in the response spectrum at the effective frequency which is higher than the secant frequency. Therefore, when a local valley exists in the response spectra at frequencies above the secant frequency, the calculation of F_{μ} should be limited to no more than that computed by the Secant Frequency Method. The calculation of F_{μ} using the Secant Frequency Method was shown to provide the best comparison to the test data (about 14% over prediction in the x direction and about 6% over prediction in the y direction). Therefore, for this specimen configuration and earthquake motion, the Secant Frequency Method provided the most accurate overall comparison to the test results.

ANACAP static cyclic analyses

To assess the performance of the ANACAP capability for modeling nonlinear cyclic characteristics of reinforced concrete shear wall structures, the ANACAP analysis results of the JNES/NUPEC cyclic test models were compared to the test data in terms of the base shear capacity, hysteresis loops of the shear force vs. displacement, and shear force orbits. The computed base shear capacities by ANACAP compare well with those of the tests with the

relative differences mostly around 10%, with one exception that results in a relative difference of 21%. These differences may be attributed to the simplifications introduced in the ANACAP models; nevertheless, the differences shown are well within the general acceptable range for reinforced concrete material.

Reasonable agreement between the analysis results and the test data were also achieved for the hysteresis loops and the shear force orbits, in terms of both the overall shape and the cycle-to-cycle comparisons. These correlations further exhibit the ANACAP capability in characterizing the reinforced concrete material behavior associated with concrete stiffening, softening, shear retention and shedding, load cycling, and rebar bond and anchorage effect. Although ANACAP does not define the final failure of the structure due to its intentional modeling strategy, the capability of the ANACAP analysis extending from the pre- to post-ultimate load bearing behaviors permits the determination of the failure capacity of the shear walls, based on a sound engineering practice.

ANACAP simulation of JNES/NUPEC shaking table tests

The ANACAP simulation analysis was performed for the JNES/NUPEC box-type shear wall shaking table test. The same ANACAP RC model as for the static cyclic analysis was used for the dynamic simulation analysis of the JNES/NUPEC shaking table tests. Eight runs with progressive increases of the shaking input motion to the RC shear wall were analyzed, and the analysis results were compared with the test data in terms of response spectra at the top of the shear wall, hysteresis loops and the base shears. The ANACAP simulation generally captured the progressive degrading behavior of the shear wall as indicated from the test data, which demonstrated the capability of the ANACAP concrete material model in characterizing the non-linear softening of RC structures. With the exception for Run-1, the simulation generally captured the frequency shifts in the response spectra comparisons with the test and the roof accelerations were reasonably matched to the test within about plus or minus 20%. The level of agreement for the in-structure response spectral peaks was about plus or minus 30% in the horizontal comparisons and about plus or minus 50% in the vertical comparisons. The largest discrepancy in the response spectra comparisons occurred in the simulation for Run-1, which has the smallest input level and the shear wall was expected to remain elastic. This discrepancy was believed to be possibly attributed to the prescribed damping for the ANACAP model. As the test runs progressed, the energy dissipation of the shear wall was gradually controlled by the hysteresis characteristics of the reinforced concrete material model; therefore, the prescribed damping became less important and the level of agreement between test and analysis results increased. Although the peaks of the calculated in-structure response spectra were not as closely matched to the test results as one might expect to achieve, the overall progressive failure behavior of the JNES/NUPEC shaking table test was reasonably captured by the simulation analysis of the ANACAP RC shear wall model.

The ANACAP capability for predicting the shaking table shear wall test was further demonstrated through the close comparisons of the hysteresis loops as presented in this report. The incipient failure of the shear wall is inferred from the calculated hysteresis loops for Run-6, which is very close to the actual failure declared for the test model.

With the exception of the vertical reaction for Run-6, base reactions were reasonably matched between test and analysis within about plus or minus 20%. The base shears predicted by ANACAP are mostly higher than test results, except for Runs 1, 4, and 5. For Runs 4 and 5, ANACAP under-predicted the base shears by approximately 3 – 8%, while ANACAP under-predicted the base shears for Run-1 by about 23%. The variability in the base shear calculations

was shown to be higher for the dynamic analysis than the static cyclic results, largely attributed to the introduced inertia effect in the dynamic analysis.

Effect of damage history and the use of uni-direction input motion

Comparisons were made in this study between the shaking table test for Run-6 and the ANACAP analysis for the same run; the analysis did not include the effect of the previous cumulative damage history. For the comparison of response spectra in the X-direction, little effect of prior damage was shown on the low frequency range (less than 30 Hz), but for frequencies greater than 30 Hz, substantially higher spectral amplitude than the test result was shown when prior damage is ignored. Similarly, higher computed spectra than the test spectra were also observed in the Y-direction when prior damage was not considered, especially near about 10 Hz. In terms of the base reactions, ignoring prior damage resulted in higher base shears than the test results, but little change in the vertical reaction calculation. The response differences between including and ignoring prior damage history demonstrated the importance of appropriately accounting for the correct boundary conditions in the seismic analysis of shear walls.

Finally, the out-of-plane effect was investigated by applying only the X-directional input motion to the ANACAP shear wall model for Run-6 and comparing the analysis results with the test data and analysis results with three directional input motions. The comparisons show that in terms of response spectra, good correlation was exhibited when prior damages are appropriately accounted for, while ignoring prior damage resulted in significantly higher spectral accelerations than the test results between 10 - 20 Hz. Furthermore, the out-of-plane effect appeared to have only increased the base shear by 9% if prior damage is appropriately included. However, when prior damage is ignored, the out-of-plane effect reduced the base shear estimate by 27%. The lesser out-of-plane effect is also an expected outcome of the fact that the seismic input motions applied to the shaking table in the three orthogonal directions are statistically independent.

In summary, the analyses presented in this report provide valuable insights into various scenarios in that important parameter considerations need to be appropriately included in the seismic response analysis of shear wall structures. The analysis methods utilized for performing the predictive analyses of the JNES/NUPEC cyclic and shaking table tests of shear walls performed well, which confirm the capability of the current technology for shear wall seismic response calculations. Based on the conclusions discussed above, it is recommended that the JNES/NUPEC cyclic and shaking table test data analyzed in this report be used as a benchmark for future validations or confirmations of the adequacy of other alternative analytical methods or computer programs for the seismic response analysis of NPP low-rise shear wall structures with comparable aspect ratios utilized for the JNES/NUPEC cyclic and shaking table tests.

7 REFERENCES

ACI 318-02, "Building Code Requirements for Structural Concrete and Commentary," American Concrete Institute, Farmington Hills, Michigan.

ACI 349-01, "Code Requirements for Nuclear Safety Related Concrete Structures," American Concrete Institute, Farmington Hills, Michigan.

ANATECH (2004). "ANACAP Version 3, User's Manual".

ASCE/SEI 43-05 (2005), "Seismic Design Criteria for Structures, Systems, and Components in Nuclear Facilities," American Society of Civil Engineers and Structural Engineering Institute.

Barda F., Hanson, J. M., and Corley, W. G. (1976), "Shear Strength of Low-Rise Walls with Boundary Elements," ACI Symposium, Reinforced Concrete Structures in Seismic Zones, SP-53, Detroit, Michigan.

Cardenas, A. E., Hanson, J. M., Corley, W. G., and Hognestad, E. (1973), "Design Provisions for Shear Walls," ACI Journal, Proceedings, Vol. 70, No. 3, pp. 221-230, March.

Cover, L. E., Bohn, M. P., Campbell, R. D., and Wesley, D. A. (1985), "Handbook of Nuclear Power Plant Seismic Fragilities," NUREG/CR-3558, Seismic Margins Research Program, Lawrence Livermore National Laboratory.

Dunham R.S. and Rashid Y.R. (2003). "ANACAP material modeling of reinforced concrete", ANA-R-03-0678, ANATECH.

Habasaki, A., Kitada, Y., Nishikawa, T., Takiguchi, K., and Torita, H. (2000), "Multi-Directional Loading Test for RC Seismic Shear Walls," 12th World Conference on Earthquake Engineering (WCEE), Auckland, New Zealand.

Hiroshi, T., Yoshio, K., Takao, N., Katsuki, T., Hideyoshi, W., and Takeyoshi, K. (2001), "Multi-Axis Loading Test on RC Shear Walls, Overview and Outline of Two Directional Horizontal Loading Test," Transactions, SMiRT 16, Washington DC.

JEAG 4601-1991 Supplement. (1991), "Japan Electric Association, Technical Guidelines for Aseismic Design of Nuclear Power Plants."

Kennedy, R. P., Short, S. A., Merz, K. L., Tokarz, F. J., Idriss, I. M., Power, M. S., and Sadigh, K., (1984), "Engineering Characterization of Ground Motion, Task 1: Characteristics of Free-Field Motion on Structural Response," NUREG/CR-3805, Structural Mechanics Associates, Inc. and Woodward-Clyde Consultants.

Kennedy, R. P., Wesley, D. A., and Tong, W. H. (1988), "Probabilistic Evaluation of the Diablo Canyon Turbine Building Seismic Capacity Using Nonlinear Time History Analyses," Report No. 1643.01, Prepared for Pacific Gas & Electric Company.

Kusama, K., Suzuki, A., Fukuda, R., Hirotani, T., and Takiguchi, K. (2003), " Simulation Analysis of Shaking Table Test for RC Seismic Shear Wall in Multi-Axis Loading Tests," SMiRT 17, Prague, Czech Republic.

Oesterle, R. G., et. al. (1979), "Earthquake Resistant Structural Walls: Tests of Isolated Walls, Phase II," Construction Technology Laboratories (Division of PCA), Skokie, Illinois.

Rashid Y.R. (1968). "Ultimate Strength Analysis of Pre-stressed Concrete Pressure Vessels", Nuclear Engineering & Design, 7, 334-344.

Riddell, R. and Newmark, N. M. (1979), "Statistical Analysis of the Response of Nonlinear Systems Subjected to Earthquakes," Civil Engineering Studies, Structural Research Series No. 468, UILU 79-2016, Department of Civil Engineering, University of Illinois at Urbana-Champaign, Urbana, Illinois.

Shiga, T., Shibata, A., and Tabahasi, J. (1973), "Experimental Study on Dynamic Properties of Reinforced Concrete Shear Walls," Proceedings, 5th World Conference on Earthquake Engineering, International Association for Earthquake Engineering, Rome.

Torita, H., Matsumoto, R., Kitada, Y., Kusama, K., and Nishikawa, T. (2004). "Shaking Table Test of RC Box-Type Shear Wall in Multi-Axes Loading," 13th World Conference on Earthquake Engineering, Vancouver, B.C., Canada.

Wang C.K. and Salmon C.G., (1979). "Reinforced Concrete Design", 3rd Edition, Harper & Row, Publishers, Inc. New York.